



TALLINNA TEHNIKAÜLIKOOL
INSENERITEADUSKOND

Department of Civil Engineering and Architecture

ASSESSMENT OF MARINE GEOID MODELS BY SHIPBORNE GNSS AND AIRBORNE LASER SCANNING PROFILES

MEREGEOIDI MUDELITE VALIDEERIMINE LAEVAL MÕÕDETUD GNSS NING
AEROLASERSKANEERIMISE KÕRGUSPROFIILIDEGA

MASTER'S THESIS

Student: Sander Varbla

Student code: 144461EATI

Supervisor: Prof. Artu Ellmann

Tallinn 2019

AUTORIDEKLARATSIOON

Olen koostanud lõputöö iseseisvalt.

Lõputöö alusel ei ole varem kutse- või teaduskraadi või inseneridiplomit taotletud. Kõik töö koostamisel kasutatud teiste autorite tööd, olulised seisukohad, kirjandusallikatest ja mujalt pärinevad andmed on viidatud.

“.....”201....a

Autor:

/ allkiri /

Töö vastab magistritööle esitatud nõuetele

“.....”201....a

Juhendaja:

/ allkiri /

Kaitsmisele lubatud

“.....”201....a

Kaitsmiskomisjoni esimees

/ nimi ja allkiri /

Ehituse ja arhitektuuri instituut

LÕPUTÖÖ ÜLESANNE

Üliõpilane: Sander Varbla, 144461EATI
Õppekava, peeriala: EATI02/09 - Teedehitus ja geodeesia
Juhendaja: Prof. Artu Ellmann, +372 620 2603

Lõputöö teema:

Meregeoidi mudelite valideerimine laeval mõõdetud GNSS ning aerolaserskaneerimise kõrgusprofiilidega
Assessment of marine geoid models by shipborne GNSS and airborne laser scanning profiles

Lõputöö põhieesmärgid:

1. Selgitada välja meregeoidi mudelite valideerimise põhimõtted ning need kirjeldada.
2. Töötada välja metoodika(d) meregeoidi mudelite valideerimiseks lähtudes kirjeldatud põhimõtetest.
3. Anda hinnang regionaalsete geoidimudelite täpsustele Soome lahes.

Lõputöö etapid ja ajakava:

Nr	Ülesande kirjeldus	Tähtaeg
1.	Lähteandmete kogumine ja andmetöötlus.	01.03.2019
2.	Tulemuste esialgne analüüs.	01.04.2019
3.	Tervikmustandi esitamine.	01.05.2019

Töö keel: inglise **Lõputöö esitamise tähtaeg:** “.....”201....a

Üliõpilane: Sander Varbla “.....”201....a
/ allkiri /

Juhendaja: Artu Ellmann “.....”201....a
/ allkiri /

Kinnise kaitsmise ja/või avalikustamise piirangu tingimused formuleeritakse pöördel

CONTENTS

PREFACE	6
List of Abbreviations and Symbols	8
List of Figures	11
List of Tables	14
INTRODUCTION	15
1 THEORETICAL PRINCIPLES OF MEAN SEA LEVEL DERIVATION FROM SHIP- AND AIRBORNE MEASUREMENTS.....	18
1.1 Effects from vessel’s attitude	18
1.2 Link between geoid surface and mean sea level	19
1.3 Determining shipborne GNSS profiles for geoid model assessment	20
1.4 Determining ALS profiles for geoid model assessment	23
2 STUDY AREA AND ITS CHARACTERISTICS.....	26
2.1 Geoid models	28
2.1.1 FAMOS2017 gravimetric data	29
2.1.2 Differences between geoid models	31
2.2 Dynamic topography data and its verification with tide gauges	33
3 SHIPBORNE GNSS PROFILES	37
3.1 The FAMOS2017 marine gravity and GNSS campaign	37
3.2 Data processing.....	39
3.2.1 GNSS post-processing	39
3.2.2 Differences between post-processing software.....	40
3.2.3 Reducing effects from vessel’s attitude and waves	42
3.2.4 GNSS profile corrections	45
3.3 Shipborne GNSS profiles compared to the geoid models	49
4 ALS PROFILES.....	57
4.1 Study area and data	57
4.2 Data processing.....	62
4.2.1 ALS grid computation.....	63
4.2.2 Data downsampling	65
4.2.3 Grid filtering.....	68
4.2.4 2013 ALS data filtering results	70
4.2.5 2018 ALS data filtering results	73

4.2.6 Combining 2018 ALS data Channels 1 and 2	77
4.2.7 Dynamic topography correction for ALS profiles	81
4.3 2013 ALS profiles compared to the geoid models.....	83
4.4 2018 ALS profiles compared to the geoid models.....	90
4.5 Cross sections of 2018 ALS grids	95
4.6 Using 2018 ALS profiles to validate hydrodynamic models.....	99
5 SHIPBORNE GNSS AND ALS PROFILES TOGETHER	102
SUMMARY	112
ABSTRACT.....	116
KOKKUVÕTE (in Estonian)	117
LIST OF REFERENCES	118
APPENDIX A	
Varbla <i>et al.</i> (2017b) – Assessment of marine geoid models by shipborne GNSS profiles	126
APPENDIX B GNSS profiles compared to geoid models	136
APPENDIX C Comparisons of 2013 ALS data filtering results	140
APPENDIX D Comparisons of 2018 ALS data filtering results	150
APPENDIX E Cross sections of 2018 ALS grids	166

PREFACE

This study was conducted within the frames of a Connecting Europe Facility (CEF) project “FAMOS (Finalising Surveys for the Baltic Motorways of the Sea) Odin” (VEU16013). The research is partly supported by the Estonian Research Council grant PRG330 „Development of an iterative approach for near-coast marine geoid modelling by using re-tracked satellite altimetry, in-situ and modelled data”.

First and foremost I would like to thank my supervisor Artu Ellmann, who has encouraged me and provided opportunities to participate in conferences and meetings. During my master’s studies, he has taught me to share my research results and findings through publications and presentations. All this has helped to shape the current thesis and my preparedness to pursue career in science.

The Estonian Maritime Agency and the Estonian Land Board are acknowledged for providing resources for carrying out the FAMOS2017 marine gravity and GNSS campaign. Jaanus Metsar from the Estonian Land Board is thanked for helping with the campaign. Anti Gruno from Datel (previously from the Estonian Land Board) processed shipborne GNSS data with NovAtel Inertial Explorer™ v8.60 software. He also provided 2013 ALS point clouds. Erkki Grünthal from the Estonian Land Board provided 2018 ALS point clouds. Karin Kollo from the Estonian Land Board provided the used GNSS-CORS data. Liisi Kaleva from Estonian Environmental Agency provided the used raw tide gauge data, which was then corrected by Karin Kollo (Kollo and Ellmann 2019). Last but not least, I am grateful to my family for supporting me in my studies.

The current thesis is partially based on the article “Assessment of marine geoid models by shipborne GNSS profiles” by Varbla *et al.* (2017b), which can be read in Appendix A. Since then, the methodology of shipborne geoid model assessment has been elaborated.

Parts of the study have been presented as poster presentations at the following international conferences:

1. Varbla, S., Ellmann, A., Märdla, S., Gruno, A. (2017). Assessment of marine geoid models by ship-borne GNSS profiles. – *The 10th International Conference "Environmental Engineering", Vilnius, Lithuania, 27-28 April 2017*. DOI: <https://doi.org/10.13140/RG.2.2.32537.11365>

2. Varbla, S. (2017). Assessment of marine geoid models by ship-borne GNSS profiles. – *ESRI User Conference, San Diego, California, 10-14 July 2017*.
3. Varbla, S., Ellmann, A. (2018). Assessment of marine geoid models by ship borne GNSS profiles in the Gulf of Finland, the Baltic Sea. – *International Symposium on Gravity, Geoid and Height Systems 2, Copenhagen, Denmark, 17-21 September 2018*. DOI: <https://doi.org/10.13140/RG.2.2.28952.03845>
4. Varbla, S., Ellmann, A. (2019). Assessment of marine geoid models by shipborne GNSS and airborne laser scanning profiles. – *EUREF 2019 Symposium, Tallinn, Estonia, 22-24 May 2019*. DOI: <https://doi.org/10.13140/RG.2.2.11335.96161>

Parts of the study have also been presented as oral presentations:

1. Varbla, S. (2017). Assessment of marine geoid models by ship-borne GNSS profiles. – *INTERGEO, Berlin, Germany, 26-28 September 2017*.
2. Varbla, S., Ellmann, A., Märdla, S., Gruno, A. (2018). Assessment of marine geoid models by ship-borne GNSS profiles – a case study for Gulf of Finland. – *Nordic Geodetic Commission (NKG) Working Group of Geoid and Height Systems meeting, Helsinki, Finland, 12-13 March 2018*.
3. Varbla, S., Ellmann, A. (2019). ALS assessment of marine geoid models in the Gulf of Finland, the Baltic Sea. – *Nordic Geodetic Commission (NKG) Working Group of Future Height Systems and Geoid meeting, Lyngby, Denmark, 12-13 March 2019*.

Additionally, relevant abstracts accepted for the forthcoming conferences:

1. Ellmann, A., Kollo, K., Varbla, S. (2019). Geodetic validation of sea level variability in offshore (poster presentation). – *27th IUGG General Assembly, Montreal, Canada, 8-18 July 2019*.
2. Varbla, S., Ellmann, A., Delpeche-Ellmann, N. (2019). Utilising airborne laser scanning and geoid model for examining marine processes (poster presentation). – *Baltic Sea Science Congress, Stockholm, Sweden, 19-23 August 2019*.

The figures of this thesis have been generated by the ArcMap 10.6, Autodesk AutoCad using a student license and Microsoft Excel.

List of Abbreviations and Symbols

Abbreviations:

3D	Three Dimensional
ALS	Airborne Laser Scanning
AVISO	Archiving, Validation and Interpretation of Satellite Oceanographic data
BSCD2000	Baltic Sea Chart Datum 2000
C1	RIEGL VQ-1560i LiDAR Scanning System Channel 1
C2	RIEGL VQ-1560i LiDAR Scanning System Channel 2
CMEMS	Copernicus Marine Environment Monitoring Service
CORS	Continuously Operating Reference Station
DB	Dynamic Bias
DT	Dynamic Topography
ESA	European Space Agency
EVRS	European Vertical Reference System
FAMOS	Finalising Surveys for the Baltic Motorways of the Sea
GGM	Global Geopotential Model
GNSS	Global Navigation Satellite System
GPS	Global Positioning System
HBM	HIROMB-BOOS
HBM-EST	Estonian implementation of the HIROMB-BOOS model
HDM	Hydrodynamic Model
HIROMB	High Resolution Operational Model for the Baltic
IDW	Inverse Distance Weighted
IGS	International GNSS Service
IMU	Inertial Measurement Unit
iSSH	Instantaneous Sea Surface Height
LiDAR	Light Detection and Ranging
LSC	Least Squares Collocation
LSMSA	Least Squares Modification of Stokes' formula with Additive corrections
MSL	Mean Sea Level
NAP	Normaal Amsterdam Peil
NEMO	Nucleus for European Modelling of the Ocean
NKG	Nordic Geodetic Commission (Nordiska Kommissionen för Geodesi)
NovAtel	NovAtel Inertial Explorer

PPP	Precise Point Positioning
R-I-R	Remove-Interpolate-Restore
RMSE	Root Mean Square Error
SA	Satellite Altimetry
SBA	Simple Bouguer' Anomaly
SSH	Sea Surface Height
TalTech	Tallinn University of Technology
TBC	Trimble Business Center
TG	Tide Gauge
TGa	Average TG correction
TGw	Weighted average TG correction
TGc	Closest two TG stations correction
UTC	Coordinated Universal Time
VRS	Virtual Reference Station

Symbols:

λ	Longitude
φ	Latitude
N	Geoid undulation
N^{GG}	Gravimetric geoid undulation
H^{GG}	Geoid model correction (location dependent constant)
MSL	Mean sea level height
$iSSH$	Instantaneous sea surface height
h	Reference point's ellipsoidal height
R, S	Reference point's height with respect to sea surface
i	Time-instance
DT_A	Actual dynamic topography height
DT_{HDM}, HDM	Hydrodynamic model derived dynamic topography height
DT_{TG}, TG	Tide gauge derived dynamic topography height
DB	Dynamic bias
ξ	Hydrodynamic model correction
DT	Calculated dynamic topography height
h^C	Corrected reference point's ellipsoidal height
C	Additional corrections (collectively)
\bar{A}	Assessment constant (for GNSS assessment)
D	Geoid model error (deviation from the assessment profile)
MSL_{ALS}	Airborne laser scanning derived mean sea level
\tilde{h}	Median values of reference point's ellipsoidal height
h^f	Double low-pass filtered reference point's ellipsoidal height
F	Fuel consumption correction
$h_{NovAtel}$	NovAtel processed and double low-pass filtered reference point's ellipsoidal height
h_{TBC}	TBC processed and double low-pass filtered reference point's ellipsoidal height
$h_C, h_{C,N}, h_{C,I}$	Combined solution of double low-pass filtered reference point's ellipsoidal height
g	A grid

List of Figures

Figure 1.1 Roll, yaw and pitch motion of a moving vessel	18
Figure 1.2 Seaborne derivation of MSL with respect to participating reference surfaces.....	20
Figure 1.3 Determination of the sea level corrections	21
Figure 1.4 Airborne derivation of MSL with respect to participating reference surfaces.....	24
Figure 2.1 Baltic Sea and the nearby countries	26
Figure 2.2 Northern coast of Estonia	26
Figure 2.3 The distribution of previously existing and new gravimetric data.....	30
Figure 2.4 Russian “Elektropribor” manufactured gravimeter Chekan-AM for marine gravimetric data acquisition.....	30
Figure 2.5 EST-GEOID2017 model.....	31
Figure 2.6 EST-GEOID2011 compared to EST-GEOID2017.....	31
Figure 2.7 NKG2015 compared to EST-GEOID2017.....	32
Figure 2.8 FAMOS GOCO05s compared to EST-GEOID2017.....	33
Figure 2.9 An example of DT from HBM-EST HDM.....	33
Figure 2.10 An example of DT from CMEMS HDM.....	35
Figure 2.11 Differences between HBM-EST and CMEMS HDM-s	36
Figure 3.1 Estonian Maritime Administration survey vessel “MS Sektori”	37
Figure 3.2 Route of the survey vessel and the used GNSS-CORS stations.....	38
Figure 3.3 Interpolation scheme and relative locations of the GNSS antennas	39
Figure 3.4 Differences between TBC and NovAtel double low-pass filtered GNSS profiles.....	41
Figure 3.5 Differences between TBC and NovAtel double low-pass filtered GNSS profiles after removing systematic bias	41
Figure 3.6. Ellipsoidal heights comparison between the three antennas and profile that has its heights calculated to the vessel’s mass centre.....	42
Figure 3.7 Methodology of double low-pass filtering of GNSS data.....	44
Figure 3.8 An example of how different double low-pass filtering windows affect the GNSS heights on the roughest conditions	44
Figure 3.9 Comparisons between HBM-EST model heights and TG station readings at Dirhami and Narva-Jõesuu TG station locations during the span of the campaign	46
Figure 3.10 Comparison between differently calculated DT	48
Figure 3.11 Direction of the vessel’s route.....	50
Figure 3.12 GNSS profile heights compared to EST-GEOID2017 at profile intersections	51
Figure 3.13 GNSS profiles excluded from the combined solution	52

Figure 3.14 Methodology of combined GNSS solution calculation in areas, where only TBC profile has been excluded.....	53
Figure 3.15 Intersections of combined GNSS profile.....	53
Figure 3.16 Combined GNSS profile heights compared to EST-GEOID2017 at profile intersections.....	54
Figure 3.17 Comparisons of EST-GEOID2011 and EST-GEOID2017 deviations from the combined GNSS profiles.....	55
Figure 3.18 Comparisons of NKG2015 and FAMOS GOCO05s deviations from the combined GNSS profiles	56
Figure 4.1 Flight paths of the survey plane during 2013 ALS campaign	58
Figure 4.2 Leica ALS50-II LiDAR System.....	58
Figure 4.3 Estonian Land Board’s survey plane Cessna Grand Caravan 208B	59
Figure 4.4 An example of noise in 2013 ALS point cloud.....	60
Figure 4.5 Flight paths of the survey plane during 2018 ALS campaign	60
Figure 4.6 RIEGL VQ-1560i LiDAR Scanning System	61
Figure 4.7 The standard workflow of ALS raw data processing.....	62
Figure 4.8 An example of a 1x1m grid (2018 ALS)	64
Figure 4.9 An example of a 1x1m grid (2013 ALS).....	65
Figure 4.10 A 5x5m grid computed from original point cloud compared to a grid computed from the same, but downsampled point cloud.....	66
Figure 4.11 Exponentially filtered grid computed from original point cloud compared to exponentially filtered grid computed from the same, but downsampled point cloud	67
Figure 4.12 Interpolation artefacts in the 5x5m grid and their average filtered results	69
Figure 4.13 Interpolation artefacts in the 5x5m grid and their exponentially filtered results.....	69
Figure 4.14 An extreme example of noise in ALS data affecting the resulting profile compared to the result of cleaned point cloud	72
Figure 4.15 Channels C1 and C2 of profile 10052018_085829 compared to FAMOS GOCO05s geoid model	75
Figure 4.16 Some filtering results of point cloud 10052018_084035 compared to the FAMOS GOCO05s geoid model	76
Figure 4.17 Some additional filtering results of point cloud 10052018_084035 compared to the FAMOS GOCO05s geoid model	76
Figure 4.18 Deformations at the ends of the profile where no-data values appear in grids.....	80
Figure 4.19 Deformations carried over to very large areas	80
Figure 4.20 Intersections of 2013 ALS profiles	83

Figure 4.21 2013 ALS profile heights compared to EST-GEOID2017 at profile intersections	84
Figure 4.22 Comparisons of EST-GEOID2011 and EST-GEOID2017 deviations from the 2013 ALS profiles	87
Figure 4.23 Comparisons of NKG2015 and FAMOS GOCO05s deviations from the 2013 ALS profiles	88
Figure 4.24 Intersections of 2013 and 2018 ALS profiles	90
Figure 4.25 2013 and 2018 ALS profile heights compared to EST-GEOID2017 at their intersections.....	91
Figure 4.26 Comparisons of EST-GEOID2011 and EST-GEOID2017 deviations from the 2018 ALS profiles	93
Figure 4.27 Comparisons of NKG2015 and FAMOS GOCO05s deviations from the 2018 ALS profiles	94
Figure 4.28 Locations of the cross sections.....	96
Figure 4.29 DT from HBM-EST and CMEMS HDM-s compared to ALS derived DT	101
Figure 4.30 TG corrected DT from HBM-EST and CMEMS HDM-s compared to ALS derived DT ...	101
Figure 5.1 Differences of heights between crossings of combined GNSS and 2018 ALS profiles ..	102
Figure 5.2 Combined GNSS and 2018 ALS profile heights compared to EST-GEOID2017 at their intersections.....	103
Figure 5.3 Comparisons of EST-GEOID2011 and EST-GEOID2017 deviations from all the profiles with corrections	104
Figure 5.4 Comparisons of NKG2015 and FAMOS GOCO05s deviations from all the profiles with corrections	105
Figure 5.5 Comparisons of EST-GEOID2011 and EST-GEOID2017 deviations (from all the profiles) as a gridded surface in the eastern side of the Gulf of Finland	106
Figure 5.6 Comparisons of NKG2015 and FAMOS GOCO05s deviations (from all the profiles) as a gridded surface in the eastern side of the Gulf of Finland	107
Figure 5.7 Comparisons of EST-GEOID2011 and EST-GEOID2017 deviations (from combined GNSS and 2018 ALS profiles) as a gridded surface in the eastern side of the Gulf of Finland	109
Figure 5.8 Comparisons of NKG2015 and FAMOS GOCO05s deviations (from combined GNSS and 2018 ALS profiles) as a gridded surface in the eastern side of the Gulf of Finland.....	110
Figure 5.9 2013 ALS profiles contribution to EST-GEOID2017 assessment	111

List of Tables

Table 2.1 Comparison between geoid modelling parameters of the assessed geoid models	29
Table 3.1 Statistics of differences between TG station readings and HBM-EST model heights at TG station locations	45
Table 3.2 Statistics of differently calculated DT applied to GNSS profiles	47
Table 3.3 Statistics of differences between GNSS profiles and geoid models	49
Table 3.4 Statistics of differences between the combined GNSS profile and geoid models	54
Table 4.1 Comparison between some Leica ALS50-II LiDAR System and RIEGL VQ-1560i LiDAR Scanning System parameters	62
Table 4.2 Comparison between averaged filtering results of 2013 ALS data	71
Table 4.3 Comparison between averaged filtering results of 2018 ALS data	73
Table 4.4 Comparison between two different methods of processing C1 and C2 ALS data together (before removing deformations)	78
Table 4.5 Comparison between two different methods of processing C1 and C2 ALS data together (after removing deformations)	79
Table 4.6 The amount of excluded profile points due to area limitations of HBM-EST HDM and profile points included in the geoid model assessment (2013 ALS)	83
Table 4.7 Statistics of differences between 2013 ALS profiles and geoid models	86
Table 4.8 Statistics of differences between revised 2013 ALS profiles and geoid models	89
Table 4.9 The amount of excluded profile points due to area limitations of HBM-EST HDM and profile points included in the geoid model assessment (2018 ALS)	90
Table 4.10 Statistics of differences between 2018 ALS profiles and geoid models	92
Table 4.11 Comparisons between the slopes of FAMOS GOCO05s geoid model and filtered 5x5m C2 grids	97
Table 4.12 HDM assessment results	100
Table 5.1 Geoid model assessment results (all the profiles)	103
Table 5.2 Geoid model assessment results (combined GNSS and 2018 ALS)	108
Table 5.3 2013 ALS data contribution in each geoid model assessment	111

INTRODUCTION

The geoid is an equipotential surface that the oceans would take at rest, being affected only by the influence of gravity and rotation of Earth. Thus, it roughly coincides with the mean sea level (MSL). Such a surface of the gravity field potential can be modelled with gravimetric data. These models are then used to transform heights between ellipsoidal and physical height systems, e.g. geoid models are needed for GNSS (Global Navigation Satellite System) based height determination.

External verification is needed for validating the accuracy of geoid models. On land, geoid models are customarily evaluated by using precise GNSS-levelling points, whereas offshore such control points cannot be established. Instead, marine geoid models can be assessed by shipborne GNSS measurements or airborne laser scanning (ALS), both of which have been proven to be effective methods.

For example, the NKG04 gravimetric geoid model (Forsberg *et al.* 2004) across the Baltic Sea was assessed using GNSS profiles by Jürgenson *et al.* (2008). Similarly, the Finnish geoid model FIN2005N00 (Bilker-Koivula 2010) and the NKG2015 quasigeoid model (Ågren *et al.* 2016) were assessed by Nordman *et al.* (2018). The latter study complemented the GNSS measurements by an inertial measurement unit (IMU) for specifying vessel's attitude. The NKG2015 model has also been assessed by Varbla *et al.* (2017b). Alternatively, Lavrov *et al.* (2015) derived geoid heights by shipborne GNSS along a river and assessed GCG2011 quasigeoid model (Jahn *et al.* 2012).

Another shipborne GNSS experiment was carried out between 2011 and 2015 along the Israeli coast (Lavrov *et al.* 2016). Four GNSS antennas were used for determining variations in vessel's attitude through calculation of a spatial rotation between two sets of coordinates. Correction from vessel's attitude was calculated for every GNSS measuring epoch. The current study uses three sets of GNSS receivers. However, instead of presenting the attitude corrections at the locations of each individual GNSS antennae, the combined GNSS height time-series are rigorously referred to the location of vessel's mass center. Such calculation has utmost effect on rough sea measurements. Also, this replaces the need for estimating vessel's attitude corrections and simplifies post-processing.

As an alternative to shipborne GNSS measurements, ALS can be utilized. Cocard *et al.* (2002), Gruno *et al.* (2013) and Julge *et al.* (2014) have all determined that ALS measurements can provide

reliable sea surface heights (SSH). Both Zlinszky *et al.* (2014) and Ellmann *et al.* (2016a) ascertained that ALS derived SSH can be used for geoid model validation.

For rigorous geoid model assessment, sea surface oscillations must be eliminated, or at the very least reduced, from both GNSS and ALS measurements. Thus, a filter is applied, which generally is a moving average low-pass filter – see e.g. Nordman *et al.* (2018) or Gruno *et al.* (2013). Varbla *et al.* (2017b) on the other hand tested a double low-pass filtering method that combines a moving median with a moving average. The same method is also used in the current study. In addition, ALS point clouds are filtered with a new methodology – a combination of gridding and three dimensional (3D) filtering.

For marine geoid validation by GNSS or ALS profiles, the dynamic topography (DT) that separates instantaneous SSH from geoid/MSL needs to be accounted for. Tide gauge (TG) records that are referenced to a particular vertical datum have been traditionally utilized for estimating SSH. However, TG-s are usually land bound, hence their data are not necessarily representative offshore. For offshore verifications, a few studies complement TG records with a regionally adapted hydrodynamic model (HDM). For instantaneous DT corrections Nordman *et al.* (2018) used the Baltic Sea Physical Analysis and Forecasting model computed at the Copernicus Marine Environment Monitoring Service (CMEMS) (Huess 2018), whereas Lavrov *et al.* (2016) used RIO2007 model, obtained from the European Space Agency (ESA) developed “Archiving, Validation and Interpretation of Satellite Oceanographic data” (AVISO).

Such models have also alternative uses. For example, Slobbe *et al.* (2018) used two regional high-resolution HDM-s, Dutch Continental Shelf model version 6 (Zijl *et al.* 2013) and Zuidelijk Noordzee model version 4 (Zijl *et al.* 2015), to connect islands and tide gauges with the national vertical datum. Similarly, a TG corrected regional HDM is tested in the present study for converting shipborne GNSS and ALS derived SSH into geoid heights. For that, the HBM-EST model (Estonian implementation of the HIROMB-BOOS model) in the Gulf of Finland is used.

The outline of the study is as follows. First, theoretical principles of determining mean sea level and its use for validating geoid models are described. Necessary prerequisites and the study area characteristics are also explored. The next chapter gives an overview of the methodology of post-processing and filtering shipborne GNSS data with the developed double low-pass filtering method. In addition, the study investigates elimination of the vessel’s attitude effects from measurements by referring the heights to the vessel’s mass centre, which is considered as the

reference point. Calculation of the corrections added to the profiles are also discussed. For DT correction, the study proposes a methodology for eliminating a dynamic bias (DB) from the HDM-s. Thereafter, the following chapter examines methodology of processing and filtering ALS data. A combination of gridding and 3D filtering of ALS point clouds is introduced. Similarly to shipborne GNSS, DT correction for ALS is discussed. Both shipborne GNSS and ALS chapters end with an examination of improvements in geoid modelling. The final chapter combines both shipborne GNSS and ALS profiles. A summary concludes the study.

1 THEORETICAL PRINCIPLES OF MEAN SEA LEVEL DERIVATION FROM SHIP- AND AIRBORNE MEASUREMENTS

The chapter examines how mean sea level (MSL) can be derived from seaborne GNSS (Global Navigation Satellite System) and airborne laser scanning (ALS) measurements. Connection between MSL and geoid heights is determined, suggesting that MSL can be used for geoid model validation. Necessary prerequisites for assessments are also discussed.

1.1 Effects from vessel's attitude

Marine geoid model assessment requires accurate GNSS profiles. Thus, vessel's movement at a time instant needs to be presented as a single reference point, especially if multiple GNSS antennae are installed on the vessel. Since the GNSS antennae are attached to continuously moving platform, then it is also necessary to consider effects from vessel's attitude, that consists of roll, pitch and yaw motions (Fig. 1.1), which can be determined by e.g. inertial measurement unit (IMU). The same principle applies to an aircraft.

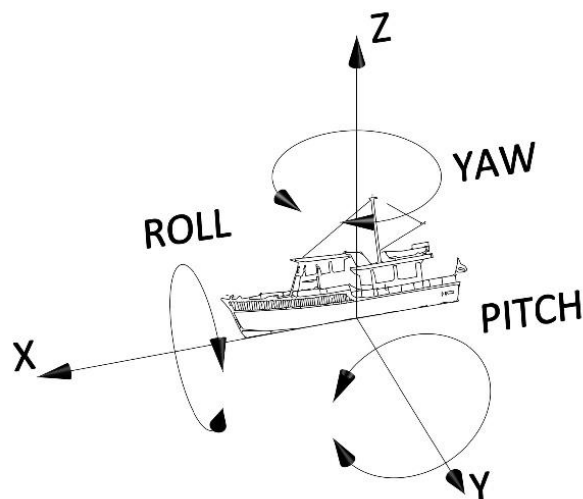


Figure 1.1 Roll, yaw and pitch motion of a moving vessel. The same motions apply to an aircraft.

In addition, the squat and heave effects, which cause a vessel to sail deeper (or sometimes higher in the case of heave) than its nominal draft, must be taken account for in the case of marine GNSS profiles. Squat is a function of vessel's velocity and its dimensions; it occurs due to a forward motion

of a vessel. Squat values can be obtained by a vessel specific squat table, calculated with a software or manually – see e.g. a book by Barrass (2004). Heave is the linear vertical motion of a vessel, e.g. due to fuel consumption the vessel would rise upwards.

The present study investigates if the calculation of heights to the vessel’s mass centre, considered as the reference point, eliminates the effects of roll and pitch. In addition, double low-pass filtering of the results is expected to remove short-term squat effect. This is needed for rigorous assessment of marine geoid models.

1.2 Link between geoid surface and mean sea level

MSL is calculated from repeated measurements that are averaged over a certain time period. Historically, MSL at selected tide gauge (TG) sites has also been adopted as the "zero" level of national/local vertical datum (Kakkuri, Poutanen 1996).

On land, high-precise GNSS-levelling points are customarily used to fit gravimetric geoid models (N^{GG}) to the national vertical datum, i.e. MSL (see e.g. a paper by Ellmann 2005). Due to a lack of such control data, the height conversion surfaces (N) over marine areas are obtained by cautious extrapolation:

$$N(\varphi, \lambda) = N^{GG}(\varphi, \lambda) - H^{GG}(\varphi, \lambda) \quad (1.1)$$

where the term H^{GG} denotes a geoid model correction, which is location dependent (polynomial) value. As deviations from the new geoid models and national vertical datum can be eliminated by fitting, possible systematic biases in offshore have supposedly been reduced also. Thus, the corrected geoid model N approximately coincides with the zero of the (historical) national vertical datum (priv. comm., Ellmann Artu, 14.02.2018):

$$MSL(\varphi, \lambda) \approx N(\varphi, \lambda) \quad (1.2)$$

However, in practice there are discrepancies caused by measurement errors, different resolutions and accuracies of reference surface models, e.g. MSL is affected by external forces, such as wind, currents, salinity, etc (see e.g. a paper by Le Provost 1990). Thus Eq. 1.2 applies only in the first

iteration – to appraise used data and corresponding acquisition technologies/methods. Also, comparing these surfaces with one another could be useful for validation of all of them (including marine geoid models). Thereafter, it could be beneficial to use these data to improve modelling of both geoid and marine processes, which is also one of the goals of the Estonian Research Council grant PRG330 „Development of an iterative approach for near-coast marine geoid modelling by using re-tracked satellite altimetry, in-situ and modelled data”.

1.3 Determining shipborne GNSS profiles for geoid model assessment

If the vertical range (R) of the reference point (e.g. vessel’s mass centre) with respect to sea surface is known, then instantaneous sea surface height ($iSSH$) can be reckoned from the geodetic reference ellipsoid, e.g. GRS-80 (Fig. 1.2):

$$iSSH(\varphi_i, \lambda_i) = h(\varphi_i, \lambda_i) - R(\varphi_i, \lambda_i) \quad (1.3)$$

where h is ellipsoidal height at a location (i.e. the reference point) with geodetic coordinates (φ, λ) and subscript i denotes an i -th time-instant of the measurement.

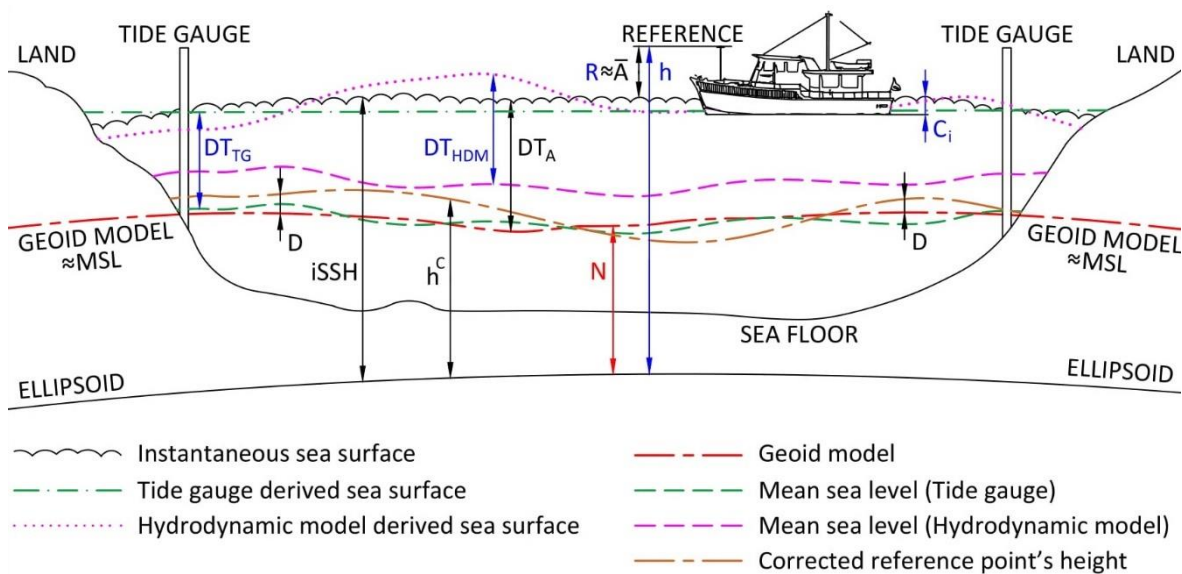


Figure 1.2 Seaborne derivation of MSL with respect to participating reference surfaces. Symbols marked blue are measurable and red are to be assessed. For the used symbols consult the text.

As $iSSH$ is affected by wind direction and speed, tidal movement, etc., then it is conventionally referred to the MSL by dynamic topography (actual, but unknown) correction DT_A :

$$MSL(\varphi, \lambda) = iSSH(\varphi_i, \lambda_i) - DT_A(\varphi_i, \lambda_i) \quad (1.4)$$

For example, dynamic topography (DT) can be estimated from nearby TG station readings at a time-instant i – see e.g. a study by Liibusk *et al.* (2013). If the coastline roughly follows parallels or meridians, the spatial interpolation of adjacent TG readings (along coast, see Fig. 1.3) allows estimation of DT as a function of only one coordinate, either longitude or latitude (priv. comm., Ellmann Artu, 05.10.2018).

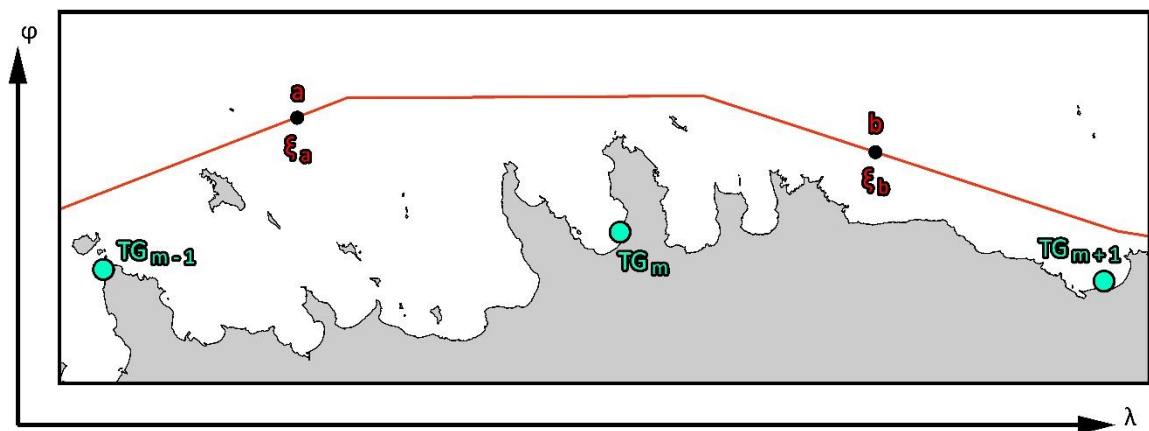


Figure 1.3 Determination of the sea level corrections. TG_{m-1} , TG_m and TG_{m+1} are the locations of tide gauge stations. a and b denote an individual GNSS profile point with coordinates $\varphi_i, \lambda_i, h_i$. ξ_a and ξ_b are the hydrodynamic model (HDM) corrections at the locations of GNSS profile points a and b .

On the other hand, as the vessel's position $(\varphi_i, \lambda_i, h_i)$ is determined at every time-instant i , it is viable to acquire sea level correction from a suitable hydrodynamic model (HDM), e.g. Baltic Sea Physical Analysis and Forecasting model computed at CMEMS (Copernicus Marine Environment Monitoring Service), NEMO (Nucleus for European Modelling of the Ocean) or HIROMB (High Resolution Operational Model for the Baltic) are available over the Baltic Sea.

However, a modelled sea level has always a dynamic bias (DB) relative to a geodetic reference system – see e.g. Allik (2014). This bias has a low-frequency part that varies from location to location and is changing slowly in time (Lagemaa *et al.* 2011). Therefore, an HDM derived MSL can deviate from the historic MSL and consequently from the vertical datum. Thus, the TG station readings can be used for determining and eliminating such a DB in the HDM.

Hence, it is recommended to use model data in conjunction with TG data. For this the following empirical method “of weights” has been developed in the present study. First, DB -s between HDM heights DT_{HDM} and TG readings DT_{TG} are calculated at locations of TG stations:

$$DB(\varphi_j, \lambda_j)_i = DT_{HDM}(\varphi_j, \lambda_j)_i - DT_{TG}(\varphi_j, \lambda_j)_i \quad (1.5)$$

where $j = 1, \dots, m - 1, m, m + 1, \dots, n$, which denotes a TG station (Fig. 1.3); n is the number of TG stations involved. Subscript i denotes an i -th time-instant.

Then, HDM correction ξ can be calculated. For example, at the location of GNSS profile point a , (Fig. 1.3) the correction is:

$$\xi_a(\varphi_i, \lambda_i) = \frac{DB(\varphi_1, \lambda_1)_i + \dots + 2*DB(\varphi_{m-1}, \lambda_{m-1})_i + 2*DB(\varphi_m, \lambda_m)_i + \dots + DB(\varphi_n, \lambda_n)_i}{n+2} \quad (1.6)$$

whereas at the location of GNSS profile point b (Fig. 1.3) the correction is:

$$\xi_b(\varphi_i, \lambda_i) = \frac{DB(\varphi_1, \lambda_1)_i + \dots + 2*DB(\varphi_m, \lambda_m)_i + 2*DB(\varphi_{m+1}, \lambda_{m+1})_i + \dots + DB(\varphi_n, \lambda_n)_i}{n+2} \quad (1.7)$$

Note that in the HDM correction calculation, the weights of DB -s depend on the location under inspection (two closest TG stations, according to distance, are weighted by two). Such a method is universal and can be used regardless of how the TG stations are located, as opposed to interpolation, which requires the coastline to roughly follow parallels or meridians.

DT can now be estimated from the HDM:

$$DT(\varphi_i, \lambda_i) = DT_{HDM}(\varphi_i, \lambda_i) - \xi(\varphi_i, \lambda_i) \quad (1.8)$$

It is expected that $DT(\varphi_i, \lambda_i)$ approximately coincides with $DT_A(\varphi_i, \lambda_i)$.

Consequently, as seen from Eqs. 1.2 and 1.4, MSL now allows geoid model assessment. However, as measuring R may be inaccurate or complicated, simpler approach can be taken (preliminarily tested by Varbla *et al.* 2017b):

$$h^C(\varphi_i, \lambda_i) = h(\varphi_i, \lambda_i) - DT(\varphi_i, \lambda_i) - C_i \quad (1.9)$$

where h^C is corrected reference point's ellipsoidal height at a location with geodetic coordinates (φ, λ) and C_i marks additional corrections at a time-instant i , e.g. correction from fuel consumption or squat. Note, that h^C in Eq. 1.9 differs from N approximately by the value R (see also Fig. 1.2).

To make h^C and N comparable, constant \bar{A} , which replaces value R , is calculated. This can be done as an average difference between the corrected reference point on the vessel (h^C) and geoid model heights N over a portion of the study area:

$$\bar{A} = \frac{1}{m} * \sum_{n=1}^m [N(\varphi, \lambda) - h^C(\varphi_i, \lambda_i)]_n \quad (1.10)$$

where subscript i denotes a time-instant of the measurement and m total amount of measurements over the same study area.

Thus, significant deviations from the geoid model at a location φ, λ may now reveal errors in the tested model:

$$[N(\varphi, \lambda) - h^C(\varphi, \lambda)] - \bar{A} = D(\varphi, \lambda) \quad (1.11)$$

where D is the geoid model deviation (i.e. error) from h^C at a location with geodetic coordinates (φ, λ) . Thus, the method allows determination of relative errors in geoid models (i.e. geoid slope errors). Similar method was used by Jürgenson *et al.* (2008) – slope errors of NKG04 gravimetric geoid model (Forsberg *et al.* 2004) were determined.

1.4 Determining ALS profiles for geoid model assessment

An ALS device (mounted on an aircraft) emits laser pulses and registers the reflections from liquid surface. The obtained range is based on time measurements. Further processing of this data results in a coordinated three dimensional (3D) *iSSH* point cloud (instead of single measurements) – such process can be simplified to an equation:

$$iSSH(\varphi_i, \lambda_i) = h(\varphi_i, \lambda_i) - S(\varphi_i, \lambda_i) \quad (1.12)$$

where D is the geoid model deviation (i.e. error) from MSL_{ALS} at a location with geodetic coordinates (φ, λ) . Thus, the method allows determination of absolute errors in geoid models. In principle, the ALS validation method is like the seaborne GNSS assessment. However, in addition to geoid slope errors, one dimensional offset in models can be determined.

2 STUDY AREA AND ITS CHARACTERISTICS

The area under investigation in this study is the Southern side of the Gulf of Finland, Northern coast of Estonia (Figs. 2.1 and 2.2).

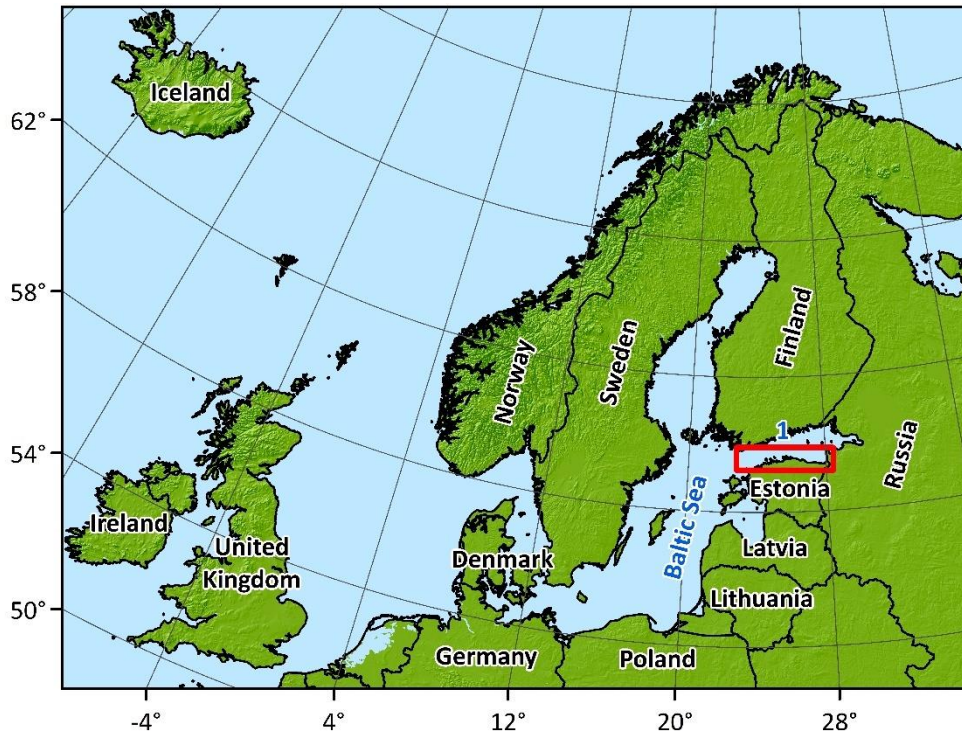


Figure 2.1 Baltic Sea and the nearby countries. Location of the study area (southern part of the Gulf of Finland) is marked on the map by the red rectangle (Fig. 2.2).

¹ The Gulf of Finland

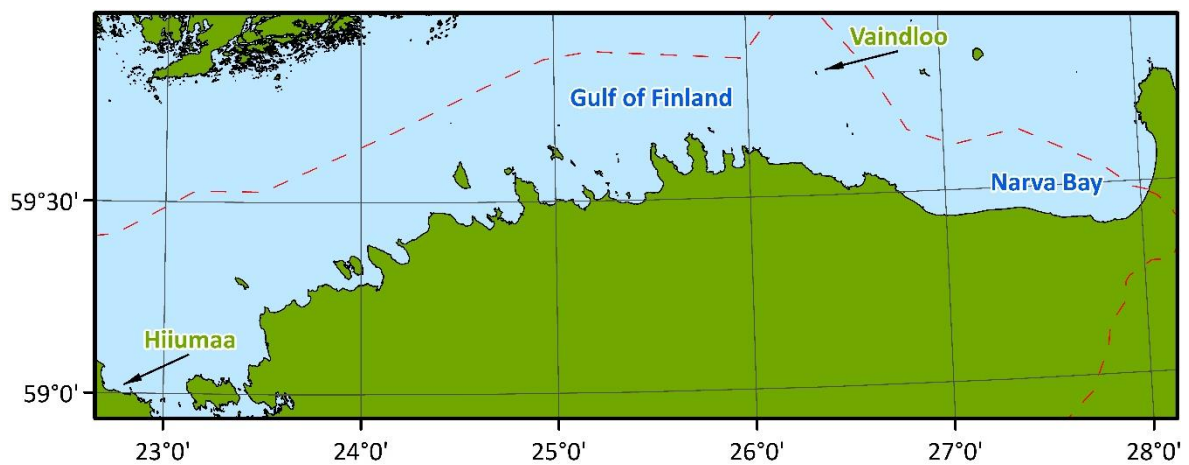


Figure 2.2 Northern coast of Estonia (location of the study area). The dashed red line depicts Estonian border.

The Gulf of Finland (Fig. 2.1) is a medium-size (covering approximately 30 000 km²) sub-basin connected with the Baltic Proper that stretches to the extreme eastern end of the Baltic Sea. It has an elongated (west-east direction) shape, with a length of approximately 400 km and width of 48...135 km. The mean depth of the Gulf of Finland is around 37 m (maximum depth is 123 m). (Alenius *et al.* 1998) Maximum cross-sectional depth decreases almost monotonically from 80...100 m at the entrance of the gulf to 20...30 m in the eastern part (Elken *et al.* 2003). The gulf is surrounded by coasts of Estonia, Finland and Russia (Fig. 2.1). The shoreline is rather disjunctive, consisting of many peninsulas, islands and small islets. The southern coast is quite steep with coastal cliffs along the banks. The main oceanographic driving forces (e.g. currents, tides, bottom friction, etc.) of dynamics of the open Baltic Sea are expected to be largely the same for the Gulf of Finland. These forces may however be modified by the mentioned geometry and sea floor topography. Latter (also the configuration of coastline) can play a major role in the forming and persistency of circulation pattern – see e.g. Myrberg and Soomere (2013).

The Gulf experiences a large spatio-temporal variability in salinity and temperature both in vertical and horizontal directions. Laterally this causes an eastward decrease in salinity, since intense water exchange on its western entrance (7 psu salinity) occurs through an open connection with the Baltic Proper, whilst on its eastern end a large amount of freshwater is entering due to a few large rivers. This decreases the salinity of the water to 0...3 psu. (Myrberg and Soomere 2013)

Due to its combination with extensive archipelago and shallow depths, the Gulf of Finland accommodates dynamical features (meso-scale eddies, fronts, specific mixing conditions, etc.) of water circulation (Andrejev *et al.* 2004a). The existing simulations (Lehmann *et al.* 2002, Andrejev *et al.* 2004a) have shown that two separate regimes of circulation may exist in the Gulf of Finland. The circulation in the uppermost layer (0...2,5 m) is mainly wind-driven and contains frequent up- and downwelling along the coast. Typical current velocities in the uppermost layer range from 5 to 10 cm/s (Andrejev *et al.* 2004b). The current motion in the sub-surface layer (depths 2,5...7,5 m) is dominated by the large scale circulation system. The maximal current velocities may reach up to 10 cm/s but stay mostly below 5 cm/s (Andrejev *et al.* 2004a). These subsurface currents are more persistent than that of the surface layer and less dependent on atmospheric conditions.

Note that all the mentioned factors have influence to the mean DT. Some general regional mean DT models were published by Poutanen (2000) and Ekman and Mäkinen (1996). Also a seasonal pattern was identified in monthly sea surface topography variations in the Gulf of Finland

(Poutanen 2000). The seasonal variations in the sea level are mainly due to large scale meteorological effects.

2.1 Geoid models

The four marine geoid models assessed in this study, by both shipborne GNSS and ALS measurements, are as follows:

- 1) EST-GEOID2011; a regional geoid model, which was the previous official Estonia quasigeoid model – see e.g. an article by Ellmann *et al.* (2016b).
- 2) EST-GEOID2017; a regional geoid model, which is the new official Estonia quasigeoid model. For more details, see Ellmann *et al.* (2019). The gridding of input gravity data is explained in Märdla *et al.* (2017).
- 3) NKG2015 quasigeoid model released by the Nordic Geodetic Commission (NKG) – see Ågren *et al.* (2016) for further details. Additional details are revealed by e.g. Sjöberg and Bagherbandi (2017).
- 4) N_unb_withDWC_FAMOSgridGOCO05s4mGal_200_2d_BLN (hitherto referred to as FAMOS GOCO05s), which is a FAMOS (Finalising Surveys for the Baltic Motorways of the Sea) quasigeoid model (gravimetric) computed at TalTech in late 2018. The used background global geopotential model (GGM) is GOCO05s (Mayer-Gürr *et al.* 2015).

All four models are computed by using Least Squares Modification of Stokes' formula with Additive corrections (LSMSA) (see e.g. Sjöberg 2003). In EST-GEOID2017 computations, the same GGM was used as a background model as in FAMOS GOCO05s computations. Differentially, in EST-GEOID2011 computations GO_CONS_GCF_2_TIM_R2 (Pail *et al.* 2011) and in NKG2015 computations GO_CONS_GCF_2_DIR_R5 (Bruinsma *et al.* 2014) were used. To fill gravity data void in the easternmost end of the Gulf of Finland (can be seen in the upper right part of Fig. 2.3), a data grid was generated from the corresponding GGM – referred to as “GoF patch” from now on. For EST-GEOID2011, the EGM2008 (Pavlis *et al.* 2012) GGM was used; in other three model computations, DIR-R4 (Bruinsma *et al.* 2013) GGM was utilized. For EST-GEOID2017 and FAMOS GOCO05s computations, new gravimetric data from FAMOS2016 (Ellmann *et al.* 2016c and Varbla *et al.* 2017b for more details) and FAMOS2017 (Varbla *et al.* 2017a for more details) campaigns are included. Geoid modelling parameters are detailed in Table 2.1. Note that over marine areas the

quasigeoid coincides with the geoid, thus for brevity the shorter term will be used in the further text.

Table 2.1 Comparison between geoid modelling parameters of the assessed geoid models.

Parameter	EST-GEOID2011	EST-GEOID2017	NKG2015	FAMOS GOCO05s
Reference GGM	GO_CONS_ GCF_2_TIM_R2	GOCO05s	GO_CONS_ GCF_2_DIR_R5	GOCO05s
GGM for GoF patch	EGM2008	DIR-R4	DIR-R4	DIR-R4
Resolution of GoF patch	0,017×0,033 arc-deg	0,1×0,2 arc-deg	0,1×0,2 arc-deg	0,1×0,2 arc-deg
FAMOS gravity data inclusion	No	Yes	No	Yes
Gravity data gridding method	SBA using kriging with anisotropic variogram model.	R-I-R using LSC. Correlation length 23 km.	R-I-R using LSC. Correlation length 15 km.	R-I-R using LSC. Correlation length 15 km.
Geoid model computation method	LSMSA	LSMSA	LSMSA (Stochastic Kernel Modification)	LSMSA
Upper degree of the geopotential model and modified harmonics	160	200	300	200
Resolution of gravity and geoid model	0,017×0,033 arc-deg	0,01×0,02 arc-deg	0,01×0,02 arc-deg	0,01×0,02 arc-deg
Geoid model fitting method	6-parameter polynomial fit	Two stage stochastic spatial prediction	1-parameter fit	No fit

Abbreviations not mentioned in the text: SBA (Simple Bouguer' Anomaly)

R-I-R (Remove-Interpolate-Restore)

LSC (Least Squares Collocation)

2.1.1 FAMOS2017 gravimetric data

A marine gravity and GNSS campaign was carried out between 03.07.2017 and 06.07.2017 (local time, UTC +3). Thanks to the campaign, large gravimetric data void areas in the Gulf of Finland were covered (Fig. 2.3). The campaign is discussed in more detail in Section 3.1 (see also a paper by Varbla *et al.* 2017a).

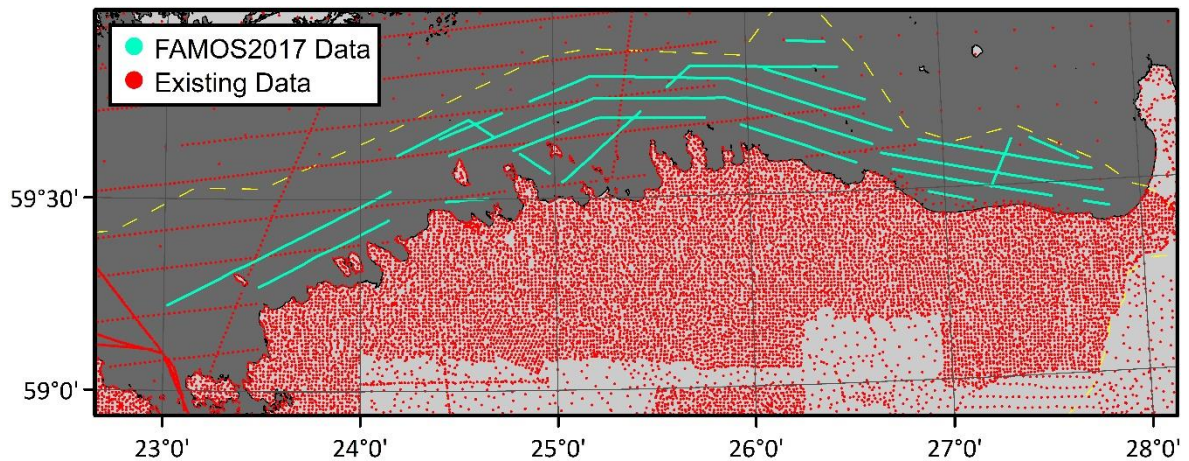


Figure 2.3 The distribution of previously existing (pre-FAMOS2017) and new (FAMOS2017) gravimetric data. North-East of Hiiumaa (see Fig. 2.2) dense lines can be seen, which is the FAMOS2016 gravimetric data (see Ellmann et al. 2016c and Varbla *et al.* 2017b). The dashed yellow line depicts Estonian border.

Gravimetric data was gathered by using a Russian “Elektropribor” manufactured marine gravimeter Chekan-AM that was mounted by the Danish Technical University team to the vessel’s cargo room (Fig. 2.4). The bottom of the gravimeter was approximately 70-80 cm below the sea level, near the mass center of the vessel.



Figure 2.4 Russian “Elektropribor” manufactured gravimeter Chekan-AM for marine gravimetric data acquisition, placed near the mass center of the vessel.

Some gravimetric data from periods with very unsettled sea (also the endings and beginnings of transit routes, i.e. parallel routes) had to be discarded (FAMOS2017 data gaps in Fig. 2.3). Crossover error analysis indicates 1 mGal or less noise in the collected data (Olesen 2017).

2.1.2 Differences between geoid models

All other three geoid models are compared to EST-GEOID2017 (Fig. 2.5). Note that all four models extend (in these comparisons) from 22° to 28,6° E and 58,6° to 60° N.

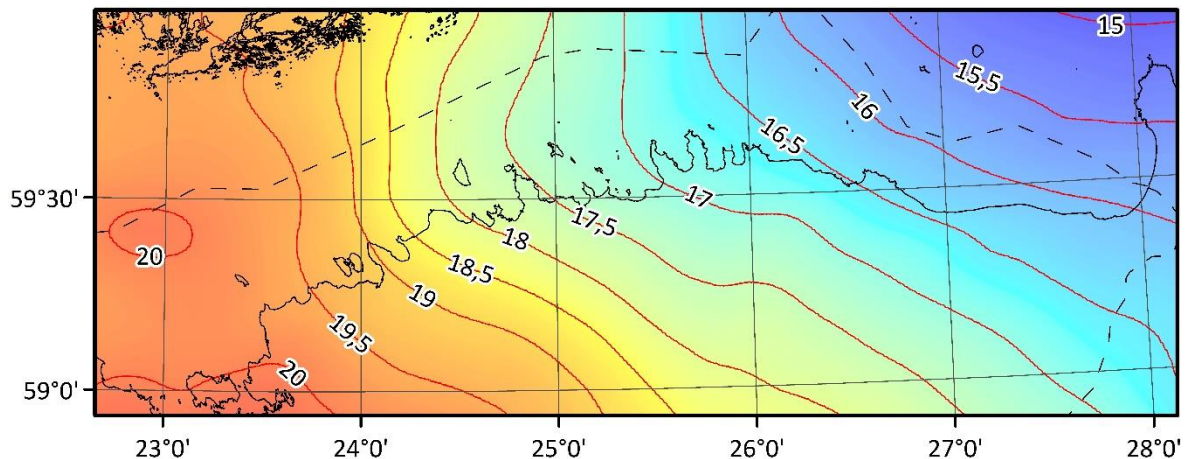


Figure 2.5 EST-GEOID2017 model depicted by red-green-blue surface and red isolines (with respect to the GRS-80 reference ellipsoid), units are in meters. The dashed black line depicts Estonian border.

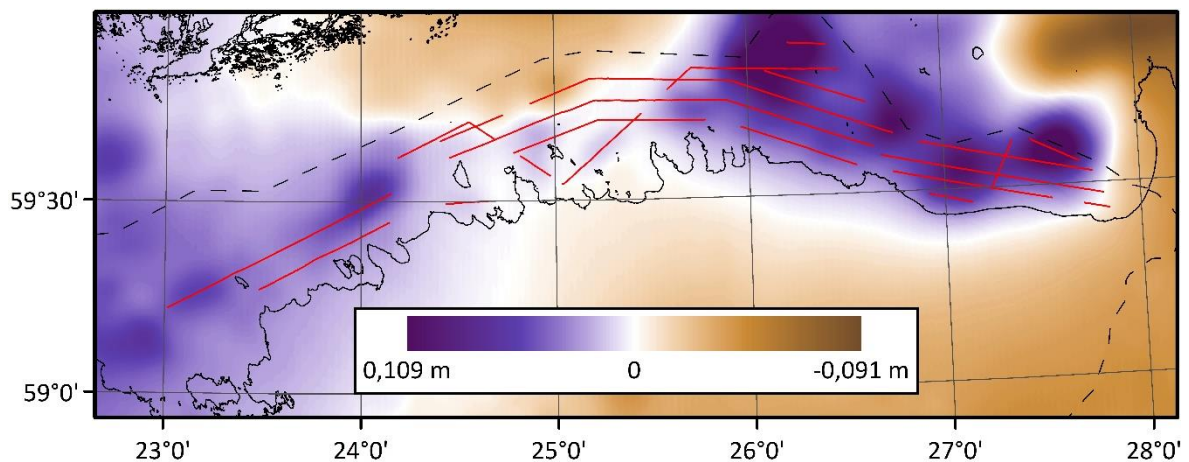


Figure 2.6 EST-GEOID2011 compared to EST-GEOID2017 (latter has been subtracted from the former). Note that the height conversion data (slightly tilted in east-westerly direction, varying from 19 to 25 cm in the study area) from BK77 to EH2000 has not been considered in the calculation (more details in the following Section 2.2). Instead, to make the surfaces more comparable, average difference of 0,2186 m (between the surfaces of two models) has been removed from the comparison. Red lines mark the FAMOS2017 gravimetric data (also see Fig. 2.3). The dashed black line depicts Estonian border.

The inclusion of newly acquired gravimetric data has significant impact to geoid modelling (Fig. 2.6). When comparing the previous official Estonia geoid model (EST-GEOID2011) and the new model (EST-GEOID2017), large differences in model surfaces can be seen in the Narva Bay and near

Vaindloo island (for location reference, see Fig. 2.2). These were also the areas with large gravimetric data voids (see Fig. 2.3).

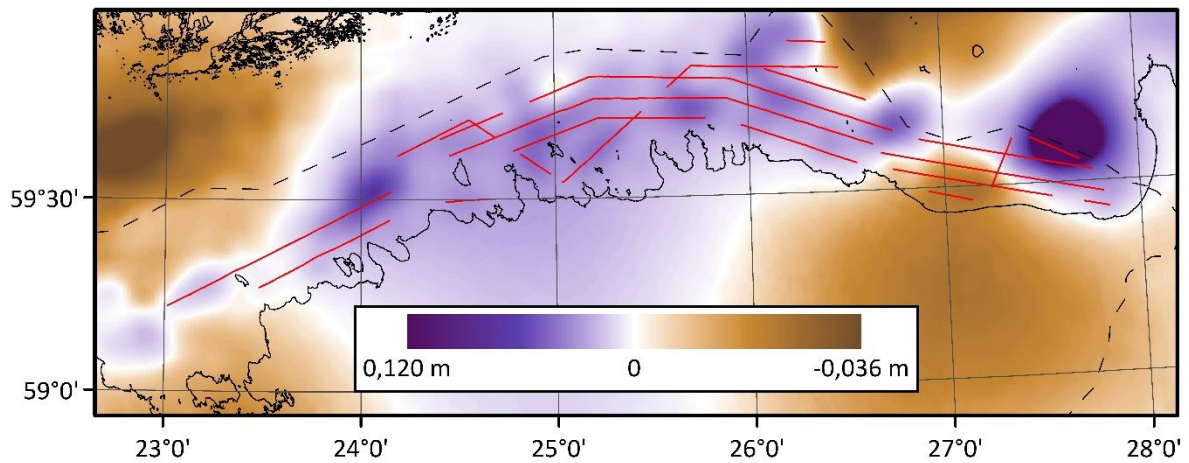


Figure 2.7 NKG2015 compared to EST-GEOID2017 (latter has been subtracted from the former). Average difference between the surfaces of two models is negligible (1,4 mm) and thus not considered. Red lines mark the gravimetric data acquired from FAMOS2017 campaign (also see Fig. 2.3), i.e. after the compilation of the NKG model. The dashed black line depicts Estonian border.

Large differences in model surfaces can also be seen when the NKG2015 geoid model is compared to the EST-GEOID2017 (Fig. 2.7). Large areas all over the Gulf of Finland differ, where new gravimetric data was acquired. However, the difference between the models is somewhat expectedly large in the Narva bay (for location reference, see Fig. 2.2).

Comparison between EST-GEOID2017 and FAMOS GOCO05s (both have FAMOS2017 gravimetric data included in the model computations, marked with red line in Fig. 2.8) shows that the differences between two models are typically around 1 cm (Fig. 2.8) (notice that the scales of Figs. 2.6 to 2.8 differ). However, a depression/bulge (EST-GEOID2017 or FAMOS GOCO05s correspondingly) exists in one of the model surfaces in the Narva Bay. Such large difference in geoid models is caused by different correlation lengths in gravity anomaly gridding (LSC method) – 23 km in the case of EST-GEOID2017 and 15 km in the case of FAMOS GOCO05s (priv. comm., Ågren Jonas and Oja Tõnis, 12.03.2019 at NKG working group meeting of Future Height Systems and Geoid in Lyngby, Denmark). In order to determine which model is the best fitting one to the investigated area, independent data is needed, such as shipborne GNSS or ALS profiles.

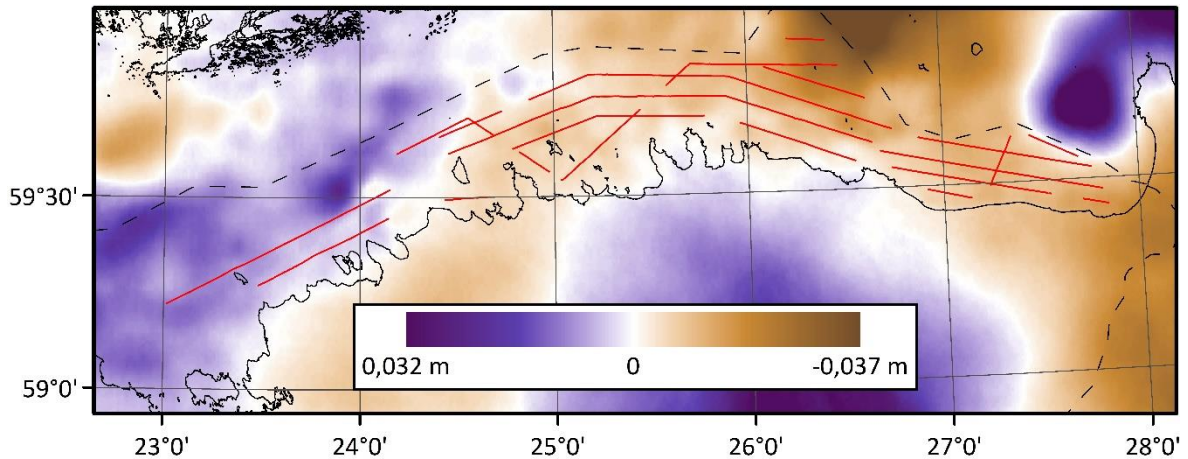


Figure 2.8 FAMOS GOCO05s compared to EST-GEOID2017 (latter has been subtracted from the former). In order to make the surfaces more comparable, average difference of 0,5822 m (between the surfaces of two models) has been removed from the comparison (FAMOS GOCO05s is gravimetric geoid and has not been fitted). Red lines mark the FAMOS2017 gravimetric data (also see Fig. 2.3). The dashed black line depicts Estonian border.

2.2 Dynamic topography data and its verification with tide gauges

The operational oceanographic forecast models have been running for the Baltic Sea since the 1990s with the primary purpose of giving short-term predictions of the sea conditions, e.g salinity, currents, wind direction and speed, sea surface elevation (i.e. DT), etc.

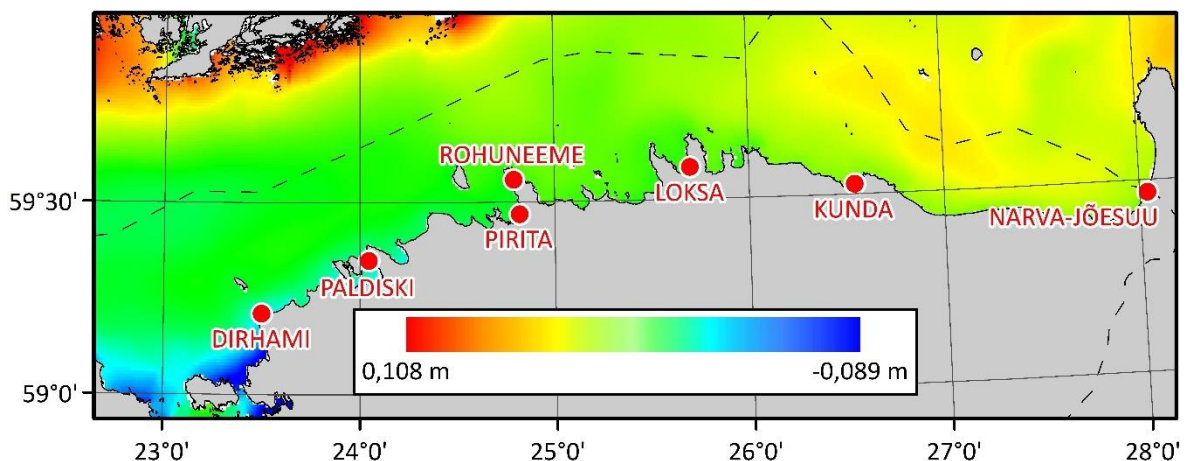


Figure 2.9 An example of DT from HBM-EST HDM on 10.05.2018 at 08:00 UTC and TG stations (denoted by red circles) used in the study. The dashed black line depicts Estonian border.

For DT correction in the current study, HBM-EST HDM (Fig. 2.9), which is an Estonian implementation of the HIROMB-BOOS model (HBM), is made use of (Lagemaa 2012; Lagemaa 2015). For every full hour, sea surface height (SSH) data with respect to MSL, from which the model is based on, can be obtained (a 24-layer NetCDF file for a single day) from Department of Marine Systems (a department of TalTech) database (for data, see <http://emis.msi.ttu.ee/allaladimine/>). Resolution of the model is 0,5 nm (i.e. approximately $0,0085 \times 0,0170$ arc-deg and thus comparable to most geoid models in use – see Table 2.1). The core of the model system is a 3D baroclinic eddy-resolving circulation model, based on the original BSHcmod (Kleine 1994) that calculates currents, temperature and salinity in the water column, and sea level. Estonian implementation of the model has been continuously developed since 2005 – more details in Lagemaa (2012). In addition to HDM data, TG station readings are utilized in the present study. Hourly data from a total of 7 TG stations are used (Fig. 2.9).

In the beginning of 2018, Estonia adopted a new EVRS (European Vertical Reference System) based height system EH2000, which is referred to the Normaal Amsterdam Peil (NAP). This change caused the previous heights (belonging to the now obsolete BK77 height system) to increase from 14 to 25 cm in a north-westerly direction (all over Estonia). In the current study area, the increase is 19 to 25 cm in an east-westerly direction. During the reconstruction of Estonian high-precision levelling network, local TG ties were re-measured and TG records corrected. Statistical analysis reveals that the new adjustment (in EH2000 height system) is more consistent than the previous one (in BK77 height system). In addition, the mean DT computed from the results agrees with earlier studies. (Kollo and Ellmann 2019)

In the current study, EST-GEOID2011 is assessed in BK77 height system (the model's corresponding height system; note that TG readings in BK77 are also corrected) and other three geoid models in EH2000 height system. The difference between height systems is taken account for within DT data, which is referred to a respective MSL. Note that DT from HBM-EST is referred to NAP and thus its MSL is supposedly in EH2000 height system. For EST-GEOID2011 assessment, DT is converted by TG readings (during elimination of DB, see Section 1.3 for more details) – then it is referred to BK77 based MSL. Expectedly, before adding the TG converted DT to the assessment, average differences between the assessment profiles and EST-GEOID2011 differ from other three geoid model assessments by approximately 20 cm due to a different height system.

However, besides conversion between height systems, the TG data are also necessary for validating and correcting HBM-EST HDM (i.e. for DB elimination). Open boundary of the model is at Danish

Straits, where DB is set near zero (referred to the NAP). Further to the east (i.e. the Gulf of Finland) and north the bias increases (priv. comm., Ellmann Artu, 06.12.2018). Note that the bias is qualitatively similar in all HDM-s. Such DB has a low-frequency part that changes slowly in time (Lagemaa *et al.* 2011) and causes the HDM derived MSL to deviate from the historic MSL and consequently from the vertical datum (i.e. EH2000). The cause for the DB is a scientifically unsolved issue. However, it is most likely caused by model inaccuracies, e.g. errors in currents, temperature, salinity, etc.

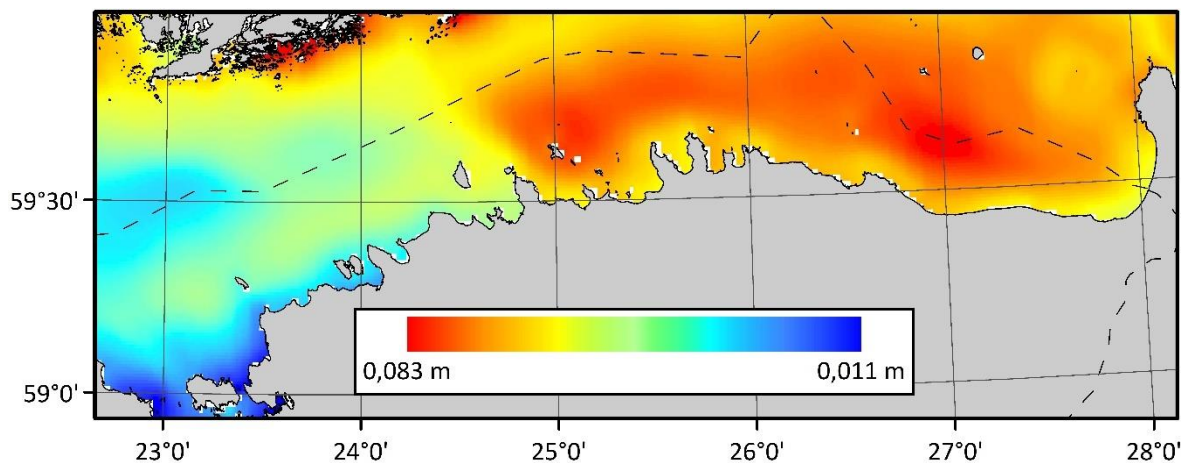


Figure 2.10 An example of DT from CMEMS HDM on 10.05.2018 at 08:00 UTC. The dashed black line depicts Estonian border.

Such inaccuracies, but also differences in model systems and algorithms, cause variability in different HDM-s. As an example, an alternative to HBM-EST is Baltic Sea Physical Analysis and Forecasting model, which is computed at CMEMS (Huess 2018) (Fig. 2.10) (notice that the scales of Figs. 2.9 and 2.10 differ) – the model is hitherto referred to as CMEMS. Similarly to HBM-EST, sea surface elevation data is available for every full hour (2x 12-layer NetCDF file for a single day). Resolution of the model is approximately 1 nm.

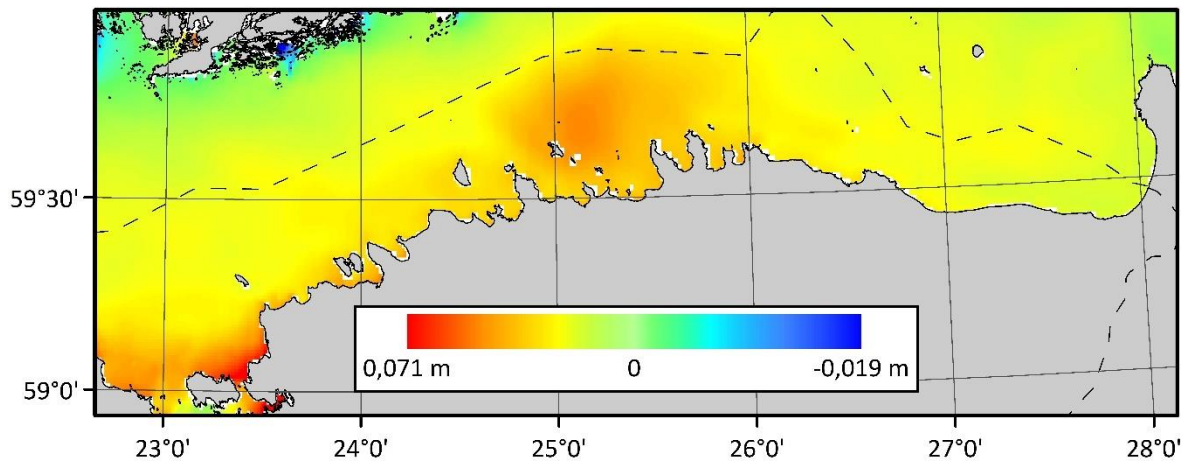


Figure 2.11 Differences between HBM-EST (Fig. 2.9) and CMEMS (Fig. 2.10) HDM-s (former has been subtracted from the latter) on 10.05.2018 at 08:00 UTC. The dashed black line depicts Estonian border.

Comparison between the two models (CMEMS was first resampled into HBM-EST grid system) shows differences of several cm (Fig. 2.11). According to the 2018 ALS profiles, the HBM-EST model derived DT appears to be more accurate (discussed later in Section 4.6) over the area of interest during ALS measurements (a timespan of slightly over an hour). Thus, CMEMS data has not been used in other calculations. However, it is important to note that this is a loose assumption (of which is more accurate model), as rigorous assessment requires data from much longer timespan (the example is brought to demonstrate possibilities of ALS data for validating different data products).

3 SHIPBORNE GNSS PROFILES

The chapter examines in detail how shipborne GNSS profiles for geoid model validation are computed – from raw data to the final product. As a conclusion, assessment results are discussed.

It is important to note that the author of this thesis participated in the FAMOS2017 campaign (discussed in the following Section 3.1) as the supervisor of the experiment. The final routes of the survey ship (can be seen in Fig. 3.2) were also designed by the author. Thus, the author has been involved with the experiment from the planning stages. Participation during the campaign has later helped to evaluate shipborne GNSS data, but also given better insight into the results of data processing. The campaign is also discussed by Varbla *et al.* (2017a).

3.1 The FAMOS2017 marine gravity and GNSS campaign



Figure 3.1 Estonian Maritime Administration survey vessel “MS Sektor”. Red arrows point to the locations of GNSS antennas (see also Fig. 3.3).

A marine gravity and GNSS campaign was carried out on board of the Estonian Maritime Administration survey vessel “MS Sektor” (Fig. 3.1) between 03.07.2017 and 06.07.2017. The campaign started right after the beginning of 3rd of July according to local time (UTC +3). 1249 km (674 nm) was covered over large areas in the Gulf of Finland (Fig. 3.2). Average speed during the

experiment was close to 8 knots. The first and most important day (GPS Days 183 and 184, Fig. 3.2), when the Narva Bay gravimetric data void was covered (Fig. 2.3, for location reference see also Fig. 2.2), had calm weather conditions. However, the last three days of the experiment (GPS Days 185-187, Fig. 3.2) were carried out on rough sea due to difficult weather conditions.

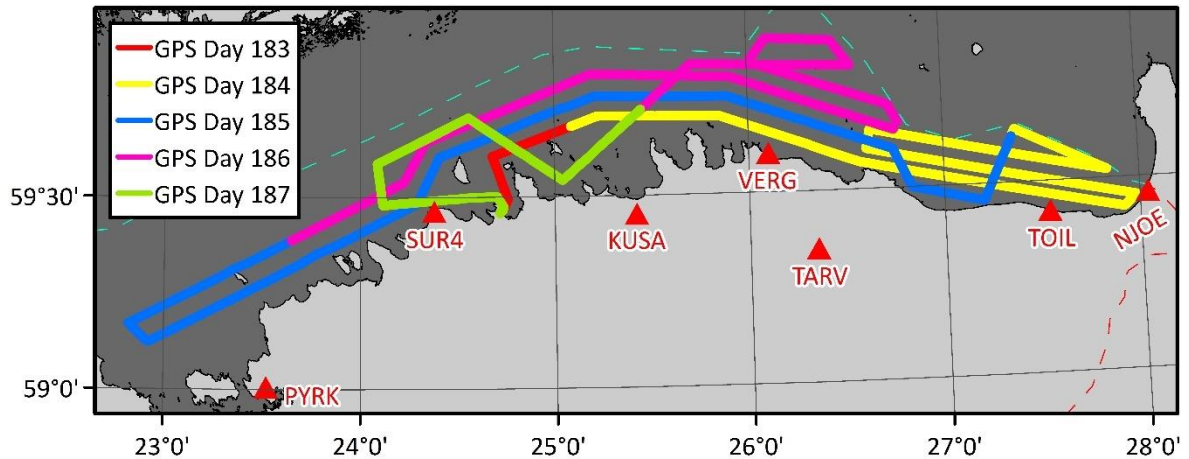


Figure 3.2 Route of the survey vessel and the used GNSS-CORS stations (denoted by red triangles and 4-letter abbreviations). The dashed cyan/red line depicts Estonian border.

Throughout the campaign, westerly winds were dominating. Wind speed on GPS Days 183 and 184 was between 1-3 m/s and during GPS Days 185-187 generally around 6-9 m/s, increasing up to 11 m/s in the second half of GPS Day 185. Wave height on GPS Days 183 and 184 was below 0,5 m, being generally around 20-30 cm. During GPS Days 185-187 on the other hand, wave height was generally around 1-1,5 m and even up to 2 m in the second half of GPS Day 185.

In addition to the gravimeter (see Subsection 2.1.1), three GNSS devices were installed on the ship (see Fig. 3.1). Two Topcon PG-A1 GNSS antennas were attached to the ship's opposite railings at bow – one to the port (antenna 5260) and the other to the starboard (antenna 5265). Third one, a Javad MarAnt+ GNSS antenna, was attached to the ship's railing on top of the captain's quarters (antenna 5312). Relative locations of the antennas are marked in the Figure 3.3.

Three Leica GRX1200 GG PRO GNSS receivers were used to collect data for profiles. The GNSS receivers sampled the 3D position with a 15 second interval (1/15 Hz) constantly from the evening of 02.07.2017 to 06.07.2017 into sequential 1h long data files. The same interval data were also received from seven Estonian GNSS-CORS (Continuously Operating Reference Station) over the same time period (see Fig. 3.2) (see e.g. an article by Metsar *et al.* 2018). This data was later used for post-processing the vessel's routes and evaluating geoid models.

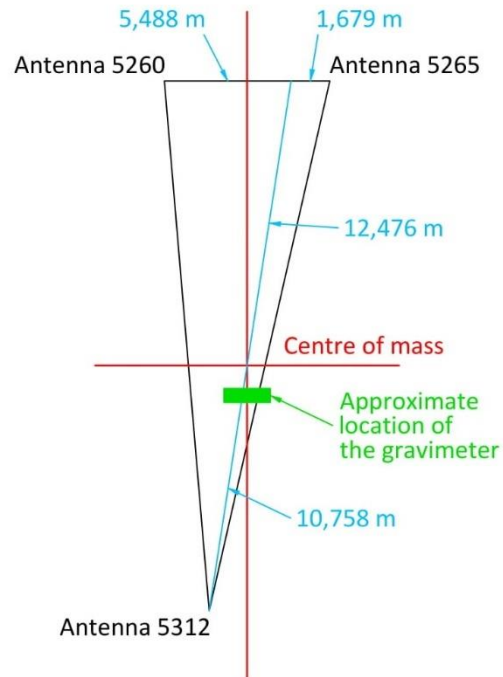


Figure 3.3 Interpolation scheme and relative locations of the GNSS antennas. View from the top. Note that vessel's bow is at the top and stern at the bottom of the figure.

3.2 Data processing

The section examines methodology of post-processing and filtering GNSS data. Calculation of the corrections added to the profiles is also discussed.

3.2.1 GNSS post-processing

The data processing revealed a large gap in GNSS data-series on July 5 from 13:00:00 to 13:31:15 UTC. All three GNSS devices were affected. The likely reason is power outage. In addition, the GNSS data-series are missing for antenna 5260 on July 6 from 12:00:00 to 12:53:00 UTC, which is believed to be due to malfunctioning of the device.

Two different commercial software were tested for post-processing kinematic GNSS data-series. These were Trimble Business Centre™ v4.00 (hitherto referred to as TBC) and NovAtel Inertial Explorer™ v8.60 (from here on NovAtel).

For TBC post-processing, each single kinematic point was calculated with respect to the closest national CORS station (see Fig. 3.2). In every section (a portion of the route closest to a single CORS station) to be processed, 2 h of precedent and subsequent CORS data and 1 h of precedent and subsequent kinematic GNSS data was included in calculations. Precise IGS (International GNSS Service) (.sp3 format) ephemerides were used. Default a priori error estimates were adopted to process the GNSS data (0,2 m + 1,0 ppm for the vertical component).

Unlike TBC, NovAtel post-processing allows multiple reference stations to be used for the entire route processing. Other post-processing parameters were by default for NovAtel post processing.

TBC post-processing resulted in 19780 GNSS positions and NovAtel in 19750 GNSS positions. NovAtel a priori error estimate is slightly more rigid (assumedly), which causes the difference in the final amount of successfully processed positions.

Varbla *et al.* (2017b) showed that as an alternative to commercial software, easy-to-use online precise point positioning (PPP) services can provide reliable GNSS post-processing results, such as Canadian CSRS-PPP (n.d.). This was not used in the present study but could be useful for open oceans where GNSS-CORS are too distant to obtain meaningful results.

3.2.2 Differences between post-processing software

When comparing double low-pass filtered TBC profile to the filtered NovAtel profile (filtering is discussed in the following Subsection 3.2.3), a systematic difference between the results occurs. NovAtel profile is by average 10,4 cm higher than that of TBC (Fig. 3.4; systematic difference can also be seen in Tables 3.2 and 3.3 by comparing constant \bar{A} values). The likely reason is that the antenna input data in NovAtel processing doesn't coincide with TBC processing – NovAtel heights are most likely calculated to the phase center of the antenna (REFERENCE!), while TBC heights are calculated to the bottom of the antenna (REFERENCE!). However, this systematic difference does

not affect geoid model assessment, as it is eliminated by the mean difference between the GNSS profile and geoid model heights (the constant \bar{A}).

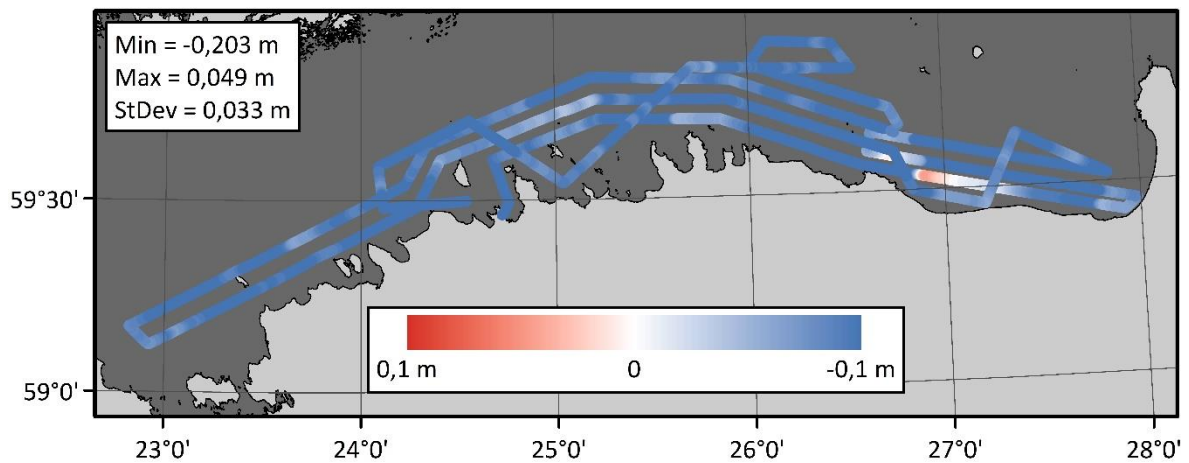


Figure 3.4 Differences between TBC and NovAtel double low-pass filtered GNSS profiles (filtering is discussed in the next subsection). Profiles calculated to the vessel's mass centre are compared. NovAtel profile heights have been subtracted from TBC profile heights.

After removing the 10,4 cm systematic difference, the results do not coincide with each other (Fig. 3.5). Generally, the differences are 2-3 cm (according to histogram). Therefore, the geoid model assessment results are highly dependent on the actual accuracy of post-processed GNSS results (and therefore on the choice of post-processing software).

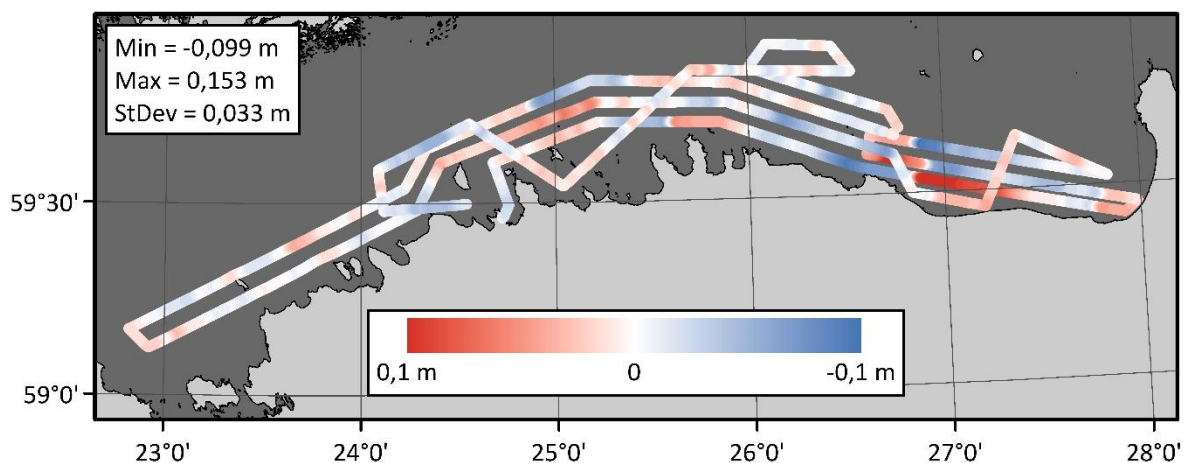


Figure 3.5 Differences between TBC and NovAtel double low-pass filtered GNSS profiles (filtering is discussed in the next subsection) after removing systematic bias 10,4 cm. Profiles calculated to the vessel's mass centre are compared. NovAtel profile heights have been subtracted from TBC profile heights.

3.2.3 Reducing effects from vessel's attitude and waves

Three GNSS profiles were obtained in both post-processing cases (one from each antenna). Comparison between the three shows how pitch and roll (see Fig. 1.1) affect the GNSS measurements (Fig. 3.6). As seen from the figure, vertical movement of antenna 5312 (closest to the vessel's centre of mass and thus the most stable out of three) is smaller than that of antenna 5260 or 5265 (both at the vessel's bow, where attitude has greater effect) – differences are caused by vessel's attitude. As the present study focuses on height determination, yaw correction can be neglected.

Exact effects from vessel's attitude are usually determined using IMU (see e.g. Nordman *et al.* 2018). However, as it was not used in the experiment, GNSS heights are instead interpolated to the vessel's mass centre according to Figure 3.3. This is done to reduce the effects of pitch and roll. Post-processed results from all three GNSS antennas are used in interpolation. The effect of interpolating heights to the vessel's mass centre can be seen in Figure 3.6.

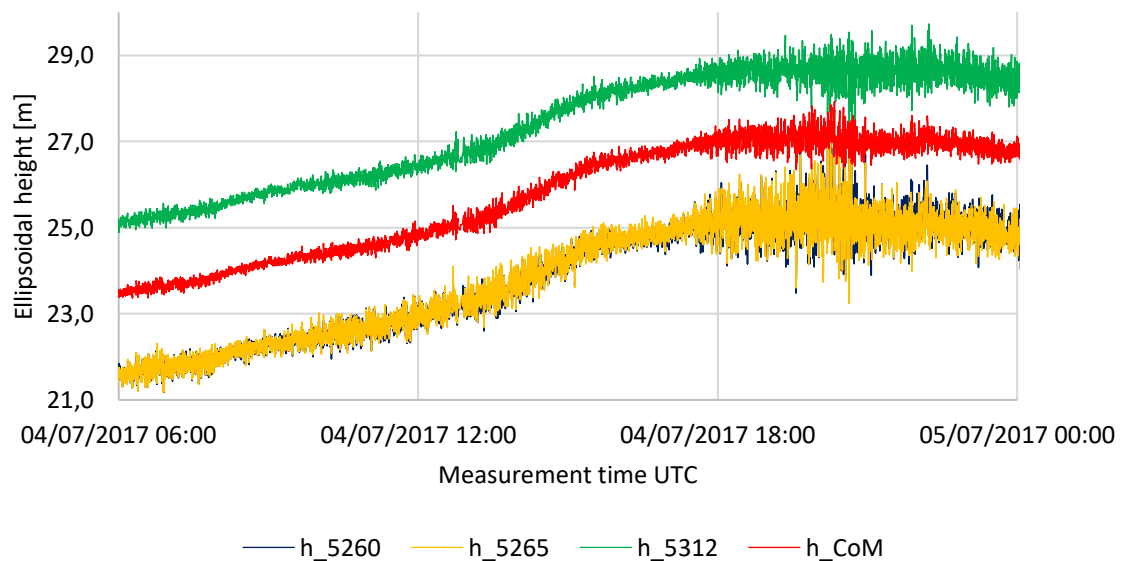


Figure 3.6. Ellipsoidal heights (TBC calculations in this example) comparison between the three antennas (h_5260, h_5265 and h_5312) and profile that has its heights calculated to the vessel's mass centre (h_CoM). Measurements on the left side of the figure are conducted on a rather calm sea, while the right side illustrates measurements on the roughest conditions the experiment was carried out on. Note that h_5260 and h_5265 are overlapping.

The figure shows that the heights interpolated to the vessel's mass centre have a smaller vertical amplitude than any of the three GNSS antennas. Therefore, it is assumed that such a calculation

has greatly reduced the effects of pitch and roll. Comparisons between raw GNSS heights (seen in Fig. 3.6) and their double low-pass filtered (discussed shortly) counterparts give the following StDev values:

- 1) Antenna 5260 (h_{5260} in Fig. 3.6) StDev = 0,180 m;
- 2) Antenna 5265 (h_{5265} in Fig. 3.6) StDev = 0,183 m;
- 3) Antenna 5312 (h_{5312} in Fig. 3.6) StDev = 0,119 m;
- 4) Vessel's mass centre (h_{CoM} in Fig. 3.6) StDev = 0,088 m.

As the results prove, heights interpolated to the vessel's mass centre are the most stable. Further calculations were conducted considering only the interpolated results (TBC and NovAtel h_{CoM} profiles are calculated separately).

A double low-pass filter was then applied to the interpolated heights for reducing the sea wave effect in GNSS data (Varbla *et al.* 2017b). Considering the average moving speed of the ship on transit routes, a moving median of 51 measurements (by average, at given 8 knots and sampling rate of 1/15 Hz, approximately 3162 m; empirically determined) was first taken:

$$\tilde{h}(i) = \text{median}(h_i[i - 25, i + 25]) \quad (3.1)$$

where h (blue line in Fig. 3.7 or 3.8) is an interpolated GNSS height component at time-instant i and \tilde{h} (purple line in Fig. 3.7) median value of it in the range of the filter, i.e. the interval from 25 epochs before time-instant i up to 25 epochs after the same time-instant i .

Taking a median allows the elimination of standalone gross errors in calculations, as well as gross errors in GNSS measurements (i.e. a priori error estimate during the GNSS post-processing can be large as the errors are eliminated through filtering). Median also removes short-term squat effect from the measurements (e.g. when the vessel slows down during turns). From the outcome, a moving average of 51 measurements was then taken:

$$h^f(i) = \frac{1}{51} \sum_{n=i-25}^{i+25} \tilde{h}(n) \quad (3.2)$$

where h^f (green line in Fig. 3.7 or yellow in Fig. 3.8) is double low-pass filtered GNSS measurement at time-instant i . Average was taken to further smoothen GNSS profiles (the expected result should be geoid-like).

Such a double low-pass filtering scheme is visualised in Figure 3.7. The green results are to be used for validating the participating geoid models.

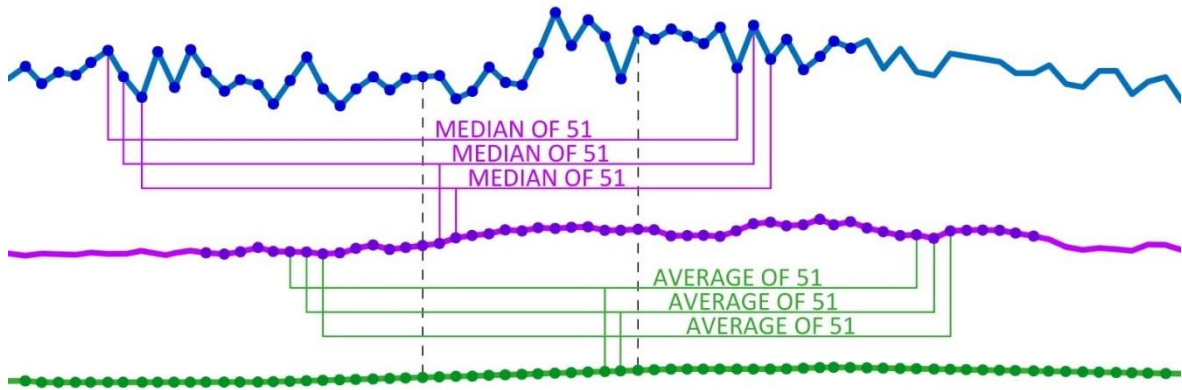


Figure 3.7 Methodology of double low-pass filtering of GNSS data (blue – raw GNSS result h_i ; purple – median values of raw GNSS result \tilde{h} ; green – low-pass filtering result h^f) (Varbla *et al.* 2017b). Note that the graphs are shifted for better readability.

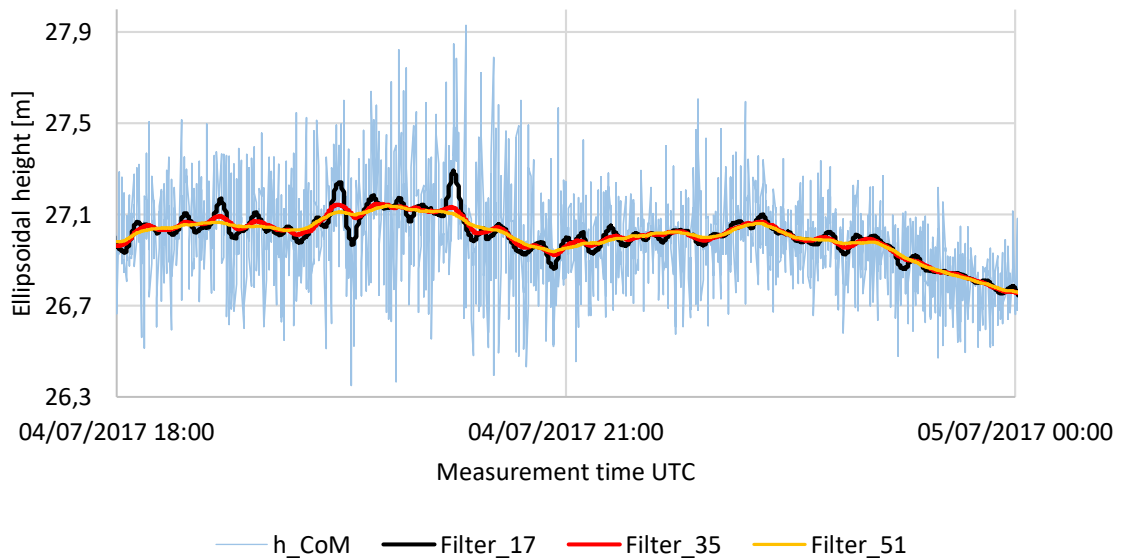


Figure 3.8 An example of how different double low-pass filtering windows affect the GNSS heights on the roughest conditions (the filter has the greatest impact on results there, as the height amplitude was largest). h_{CoM} indicates to the profile that has its heights calculated to the vessel’s mass centre (TBC calculations in this example). Number after “Filter_” indicates to the size of the double low-pass filtering window (either 17, 35 or 51 measurements). Extent of the figure (from 18:00 to 00:00) is approximately 90 km.

The effect of such filtering to the GNSS height data is shown in Figure 3.8. As seen, smaller filtering windows than 51 measurements leave unwanted vertical fluctuations into the GNSS height profile. Larger filtering windows on the other hand will not change the result much (the result would be very similar). Thus, 51 measurements is determined as an optimal filtering window. The filtering is continuous through the profile.

3.2.4 GNSS profile corrections

Corrections from DT and fuel consumption (F) have been added to the double low-pass filtered GNSS profiles. The correction from DT consists of two components – HDM component from HBM-EST and TG component (see Section 2.2). Latter is needed, as the heights of HBM-EST HDM do not coincide with the TG station readings. Statistics of differences can be seen in Table 3.1 (hourly data from 02.07.2017 21:00 UTC to 06.07.2017 08:00 UTC is considered – the entire timespan of the campaign). Visualised differences between HBM-EST and TG station readings at Dirhami and Narva-Jõesuu TG station locations (timespan of the campaign) can be seen in Figure 3.9 (see also Fig. 2.9).

Table 3.1 Statistics of differences between TG station readings (BK77 height system) and HBM-EST model heights at TG station locations (see Fig. 2.9). The results are numerically slightly different, but nevertheless similar (the phase is same), if TG station readings are in EH2000 height system. Comparison is based on 84 hourly records (the entire span of the campaign).

TG station	Avg ¹ (m)	Min ² (m)	Max ² (m)	StDev (m)
Dirhami	0,369	-0,076	0,083	0,042
Paldiski	0,351	-0,086	0,099	0,041
Rohuneeme	0,370	-0,073	0,091	0,040
Pirita	0,395	-0,074	0,089	0,039
Loksa	0,339	-0,087	0,069	0,041
Kunda	0,337	-0,112	0,072	0,050
Narva-Jõesuu	0,283	-0,161	0,088	0,059

Notes: ¹ Average difference between HDM model heights and TG station readings (HBM-EST model is higher).

² After removal of the average difference (second column).

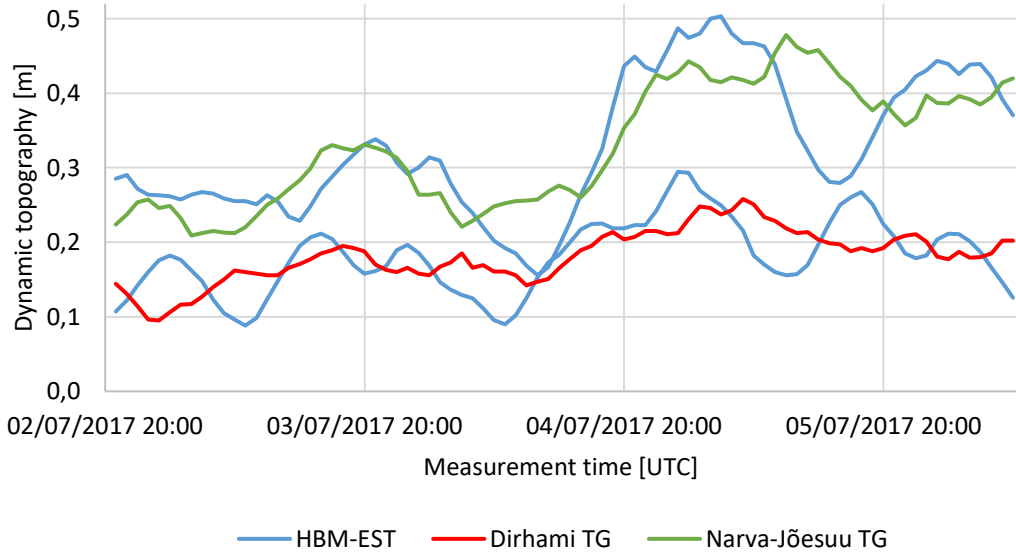


Figure 3.9 Comparisons between HBM-EST model heights and TG station readings at Dirhami and Narva-Jõesuu TG station locations (Fig. 2.9) during the span of the campaign. Note that the comparison is done after removing the bias in HBM-EST heights, which is 0,369 m and 0,283 m at Dirhami and Narva-Jõesuu TG station locations respectively (average differences shown in Table 3.1). Note that HBM-EST model is higher than TG station readings.

As seen from Table 3.1, the bias is not constant (as discussed earlier in Sections 1.3 and 2.2). However, the phases of TG readings and HDM derived DT seem to coincide (Fig. 3.9). According to the Figure 3.9, HDM tends to overestimate the local extremes in DT, which is also confirmed by Izotova (2015). The comparison illustrates near-shore dynamics. However, the same behaviour is not expected offshore. Regardless, HDM is corrected according to the TG-s in order to evaluate HBM-EST reliability.

HBM-EST model data are corrected according to seven TG stations on the Northern coast of Estonia (Fig. 2.9). The three methods tested to correct HDM data are as follows:

- 1) Average TG correction (TGa) as explained in Section 1.3, with a difference of every DB having an equal weight:

$$\xi(\varphi_i, \lambda_i) = \frac{DB(\varphi_1, \lambda_1)_i + \dots + DB(\varphi_{m-1}, \lambda_{m-1})_i + DB(\varphi_m, \lambda_m)_i + \dots + DB(\varphi_n, \lambda_n)_i}{n} \quad (3.3)$$

- 2) Weighted average TG correction (TGw) as explained in Section 1.3.

$$\xi(\varphi_i, \lambda_i) = \frac{DB(\varphi_1, \lambda_1)_i + \dots + 2 * DB(\varphi_{m-1}, \lambda_{m-1})_i + 2 * DB(\varphi_m, \lambda_m)_i + \dots + DB(\varphi_n, \lambda_n)_i}{n+2} \quad (3.4)$$

- 3) Closest two TG stations correction (TGc) as explained in Section 1.3, with a difference of only using the two DB that would have a weight of two.

$$\xi(\varphi_i, \lambda_i) = \frac{DB(\varphi_{m-1}, \lambda_{m-1})_i + DB(\varphi_m, \lambda_m)_i}{2} \quad (3.5)$$

For the used denotations, see Section 1.3. As a comparison, DT is also interpolated from TG station readings (i.e. without HDM) – it is estimated as a function of longitude. All methods are compared in Table 3.2. Differently calculated DT corrections are visualised in Figure 3.10.

Table 3.2 Statistics of differently calculated DT applied to GNSS profiles. Profiles are compared to EST-GEOID2017. All double low-pass filtered GNSS heights are considered in the comparisons (19780 profile points in TBC assessment and 19750 in NovAtel assessment).

Profile	Software	\bar{A}^1 (m)	Min ² (m)	Max ² (m)	StDev (m)
Double low-pass filtered	TBC	7,175	-0,208	0,210	0,0692
	NovAtel	7,279	-0,157	0,126	0,0676
Double low-pass with HDM DT	TBC	6,600	-0,171	0,224	0,0594
	NovAtel	6,705	-0,124	0,148	0,0568
Double low-pass with interpolated TG DT	TBC	6,725	-0,133	0,206	0,0428
	NovAtel	6,829	-0,082	0,130	0,0364
Double low-pass with HDM + TGa DT	TBC	6,721	-0,146	0,223	0,0466
	NovAtel	6,825	-0,097	0,151	0,0439
Double low-pass with HDM + TGw DT	TBC	6,720	-0,144	0,220	0,0450
	NovAtel	6,825	-0,089	0,139	0,0416
Double low-pass with HDM + TGc DT	TBC	6,718	-0,139	0,212	0,0432
	NovAtel	6,822	-0,079	0,106	0,0375

Notes: HDM is the DT from HBM-EST model; TGa/TGw/TGc is the supplementary correction for HDM data from tide gauges. Best results are highlighted in bold text.

¹ Mean difference between the GNSS profile and geoid model height.

² After removal of the mean difference (third column).

As seen from Table 3.2, the supplementary TG correction (any method out of three improves results) has a significant impact to the HDM data from HBM-EST model. Yet, the best performing DT is interpolated from TG stations, which can be interpreted as a coincidence as the coastline must stretch either along parallels or meridians for this method to be usable (the current study area is well aligned along the parallels). Thus it can be utilized rarely. The TGc correction method for HDM yields similar results. However, as the height gaps in the DT data are over several cm (e.g. Fig. 3.10 at 03.07 02:00 or 03.07 16:00) and even up to 5,5 cm at most, it is not a preferred one (height gaps are caused by changing input TG station in DT calculation). Thus, from the methodological point of view, the optimum (in terms of smoothness) correction method for HDM can be considered TGw,

which performs better than TGa correction method, yet minimizes height gaps in DT data. Also, the method is universal and can be used almost everywhere.

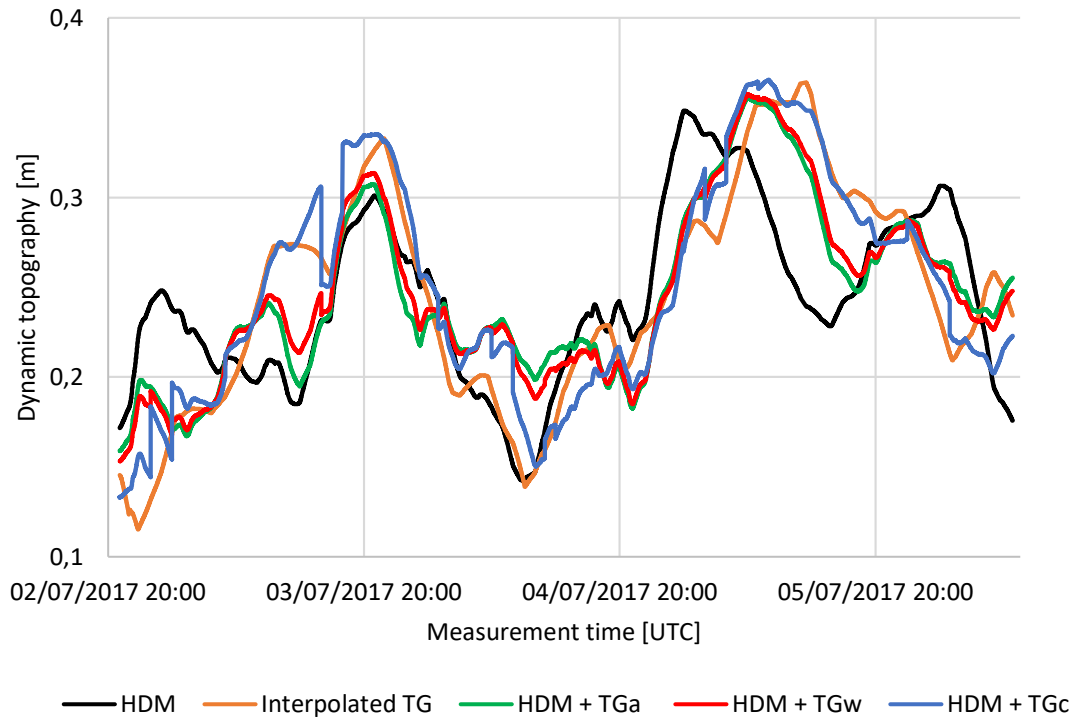


Figure 3.10 Comparison between differently calculated DT. HDM denotes HBM-EST model. For comparisons sake, HDM heights are lowered by 0,35 m (black line).

However, the shape and extension of the study area should also be considered when choosing the method for HDM correction. Whilst TGw method works best over large areas, there is no need to consider influence of distant TG stations in the calculations when investigating small areas. Thus, TGc method is suitable for investigating smaller areas, which are located between two TG stations.

To determine the correction from fuel consumption, tape measurements were conducted before and after the experiment. The change in railings height from sea surface was approximately 6 cm, which is considered as a total fuel consumption correction (F). In order to get correction F_i at time-instance i , linear function is applied along the entire route:

$$F_i = F_{i-1} + \frac{F}{n} \quad (3.6)$$

where n is the theoretical (total) amount of GNSS measurements (i.e. missing GNSS profile points are still considered in the calculation). At the initial time moment, F_1 equals 0. This correction raises artificially the ship to the initial height.

Squat correction is not considered in the current study. This can be neglected, as the vessel was moving with a constant speed and said correction can be considered within the constant \bar{A} . For a short time, the ship decelerated before taking a turn and accelerated after. However, change in squat effect during turns is eliminated by median in the low-pass filter (discussed previously).

3.3 Shipborne GNSS profiles compared to the geoid models

Double low-pass filtered GNSS profiles from both post-processing software were compared to all four geoid models. The results are presented in Table 3.3.

Table 3.3 Statistics of differences between GNSS profiles and geoid models. All double low-pass filtered GNSS heights are considered in the comparisons (19780 profile points in TBC assessment and 19750 in NovAtel assessment). Profile heights have been subtracted from the model heights. Deviations are visualised in Figures B.1 to B.8 in Appendix B (from both TBC and NovAtel corrected GNSS profiles).

Geoid model	Software	DT+F ¹	\bar{A} ² (m)	Min ³ (m)	Max ³ (m)	StDev (m)
EST-GEOID2011	TBC	No	6,917	-0,198	0,209	0,070
		Yes	6,661	-0,224	0,135	0,050
	NovAtel	No	7,022	-0,186	0,152	0,068
		Yes	6,765	-0,115	0,126	0,045
EST-GEOID2017	TBC	No	7,175	-0,210	0,208	0,069
		Yes	6,690	-0,236	0,120	0,044
	NovAtel	No	7,279	-0,126	0,157	0,068
		Yes	6,795	-0,155	0,068	0,039
NKG2015	TBC	No	7,152	-0,221	0,201	0,071
		Yes	6,667	-0,247	0,113	0,050
	NovAtel	No	7,256	-0,157	0,161	0,068
		Yes	6,771	-0,190	0,115	0,045
FAMOS GOCO05s	TBC	No	6,597	-0,211	0,211	0,071
		Yes	6,113	-0,238	0,123	0,044
	NovAtel	No	6,702	-0,130	0,155	0,069
		Yes	6,217	-0,159	0,072	0,040

Notes: HDM data is corrected with TGw method. Note that TG station readings for EST-GEOID2011 assessment are in BK77 height system, whereas for EST-GEOID2017, NKG2015 and FAMOS GOCO05s in EH2000 height system (see Section 2.2). Best results are highlighted in bold text.

¹ Marks the use of DT and fuel consumption corrections. StDev values (seventh column) of the uncorrected profiles are marked red and corrected blue.

² Mean difference between the GNSS profile and geoid model height.

³ After removal of the mean difference (fourth column).

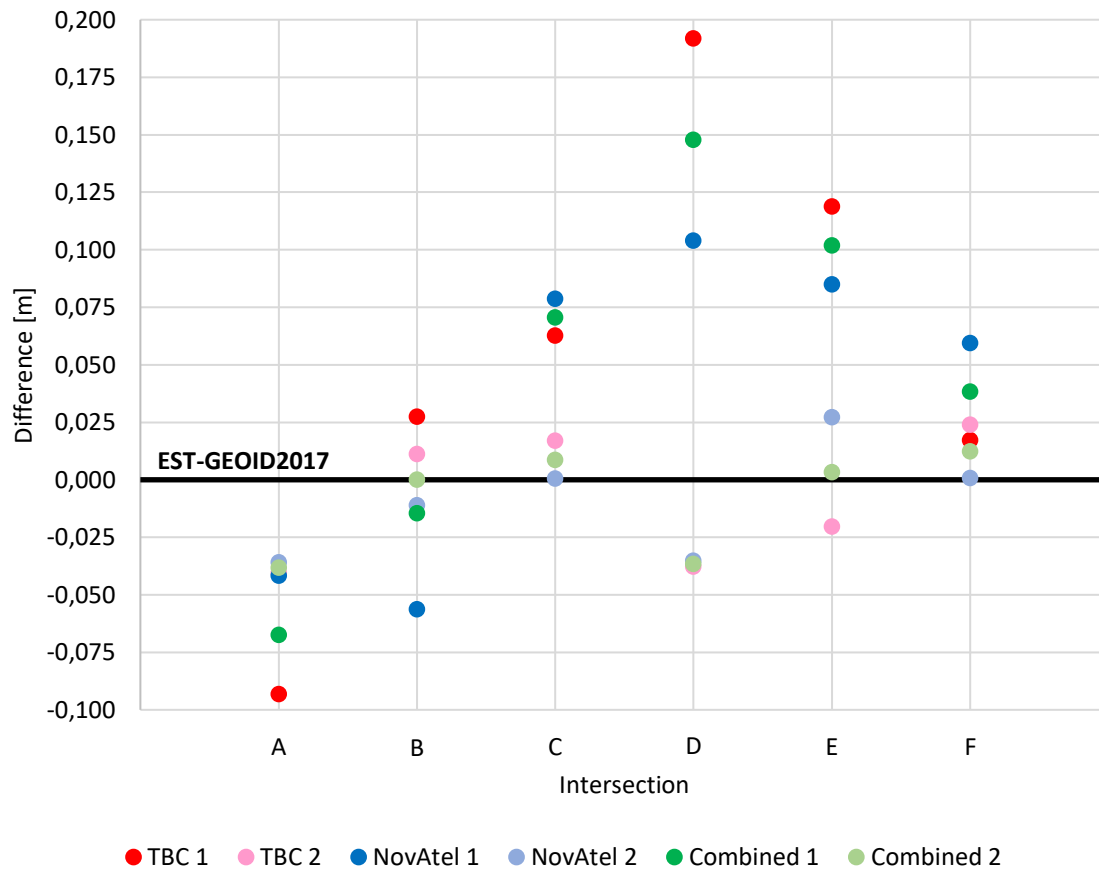


Figure 3.12 GNSS profile heights compared to EST-GEOID2017 at profile intersections (Fig. 3.11) after removing average differences: 6,6904 m from TBC, 6,7946 from NovAtel (see Table 3.3 – mean differences in bold) and 6,6904 m from the Combined profile (calculated by Eq. 3.7) heights. Double low-pass filtered profiles are compared. Corrections from DT and fuel consumption are added to the profiles before comparison. “_1” denotes the initial profile and “_2” the profile that is crossing with the initial profile (for reference, see the red arrows in Fig. 3.11). Notice the Combined solution (denoted by green dots).

However, some sections of TBC and NovAtel GNSS profiles must be excluded from the calculation (Fig. 3.13). The reason being large differences between parallel routes in the Narva Bay (see Fig. 3.5 or compare e.g. Fig. B.1 to Fig. B.2). Such differences are improbable in geoid (deviation signs are opposite; distance between the adjacent routes is 2,2 nm, the opposite-sign ones), which is why the assessment is believed to be heavily affected by errors in GNSS raw data or in GNSS post-processing (either or both). Sizeable differences between TBC and NovAtel GNSS post-processing results over said area further support that assumption (see Fig. 3.5 or 3.12). Also, the post-processing reports indicate lower estimated vertical accuracy over these areas.

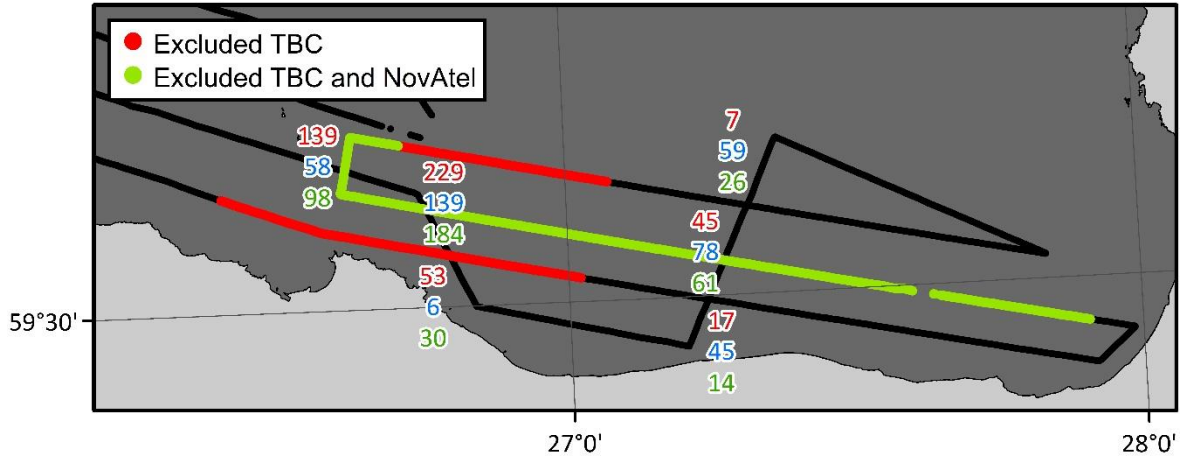


Figure 3.13 GNSS profiles excluded from the combined solution (denoted by red and green). Black portions denote usage of combined (by Eq. 3.7) GNSS data. Numbers on the map show height differences of profiles at intersections (red shows TBC, blue NovAtel and green combined GNSS profile height differences – the profile calculated by Eq. 3.7), units in mm. Double low-pass filtered profiles are compared. Corrections from DT and fuel consumption are added to the profiles before comparison.

Figures 3.5, 3.12 and Appendix B are taken into account when deciding which sections to exclude. Differences marked in Fig. 3.13 are also considered. Excluded TBC profiles span from 03.07.2017 05:07:00 to 07:34:00 UTC and 03.07.2017 17:36:15 to 19:00:00 UTC (denoted by red lines in Fig. 3.13). Both TBC and NovAtel profiles are excluded from 03.07.2017 11:53:00 to 17:36:00 UTC (denoted by green line in Fig. 3.13). In total, 2247 profile points are removed from TBC and 1326 from NovAtel GNSS profiles.

Over areas where only NovAtel profile is used (denoted by red lines in Fig. 3.13), combined solution heights ($h_{C,N}$) are calculated as follows:

$$h_{C,N}(i) = h_{NovAtel}(i) - 0,1043 \quad (3.8)$$

To avoid possible height gaps in the profile, where Eq. 3.7 switches to Eq. 3.8, interpolation is used:

$$h_{C,I}(i_s) = \frac{[h_C(i_s) * m + h_{C,N}(i_s) * (199 - m)]}{199} \quad (3.9)$$

where $m = i_s = 0,1, \dots, 198, 199$. i_s ranges from 99 measurements before the equation switch to 100 measurements after (for seamless results). $i_s = 99$ is where the equation switches. In the case, where Eq. 3.8 switches to Eq. 3.7, the formula is the same as Eq. 3.9. However, $i_s = 100$ is where the equation switches.

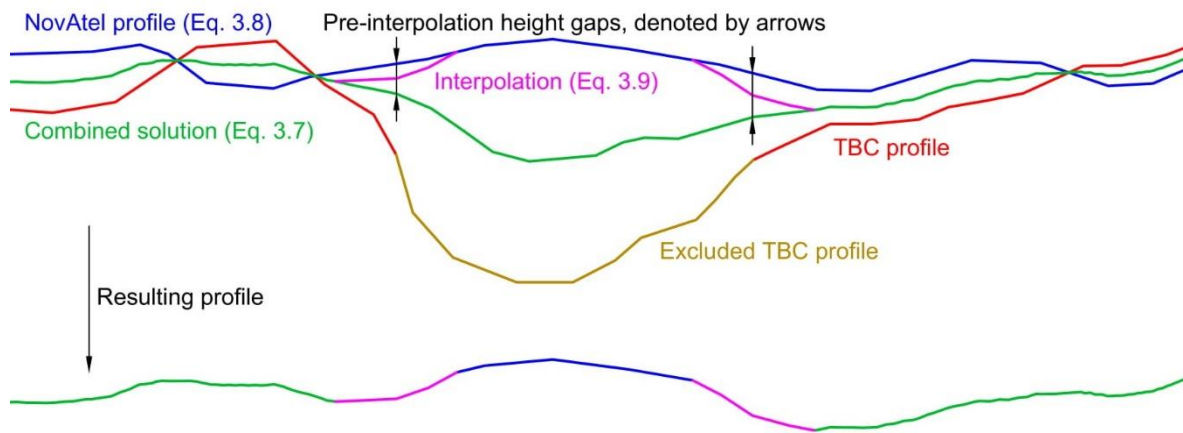


Figure 3.14 Methodology of combined GNSS solution calculation in areas, where only TBC profile has been excluded (see Fig. 3.13).

After that, h_C and $h_{C,N}$ heights in the range of interpolation are replaced with $h_{C,I}$ heights. Note that when Eq. 3.7 switches to Eq. 3.8, the first h_C height being replaced equals $h_{C,I}(0)$ and last $h_{C,N}$ height being replaced equals $h_{C,I}(199)$. When Eq. 3.8 switches to Eq. 3.7, the first $h_{C,N}$ height being replaced equals $h_{C,I}(0)$ and last h_C height being replaced equals $h_{C,I}(199)$. Such methodology is visualised in Figure 3.14. The comparison of resulting profile heights (the combined GNSS profile) at the intersections (Fig. 3.15) compared to EST-GEOID2017 is shown in Figure 3.16. As seen, the profiles coincide generally rather well with each other. Statistics of the resulting profile compared to the geoid models (the revised shipborne GNSS assessment) are presented in Table 3.4.

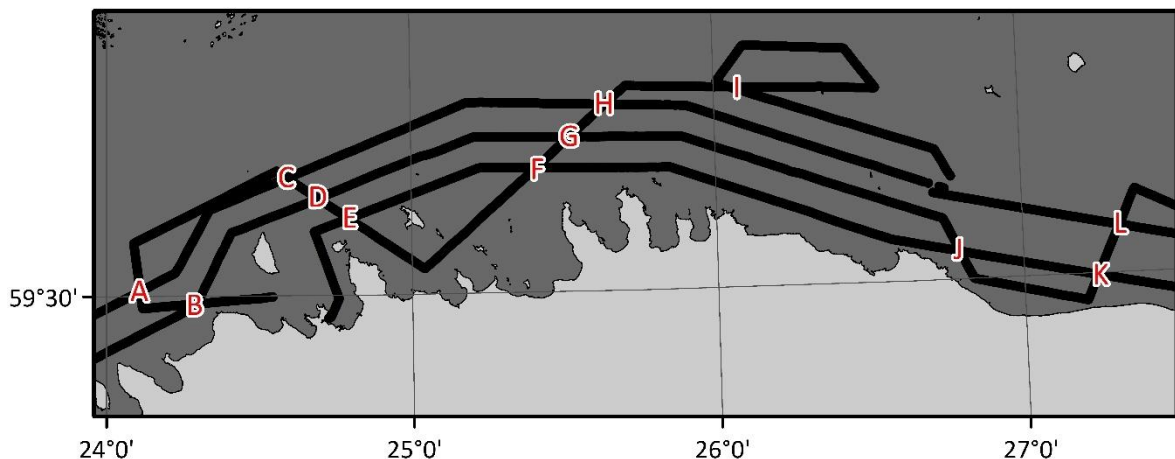


Figure 3.15 Intersections of combined GNSS profile denoted by letters in the figure.

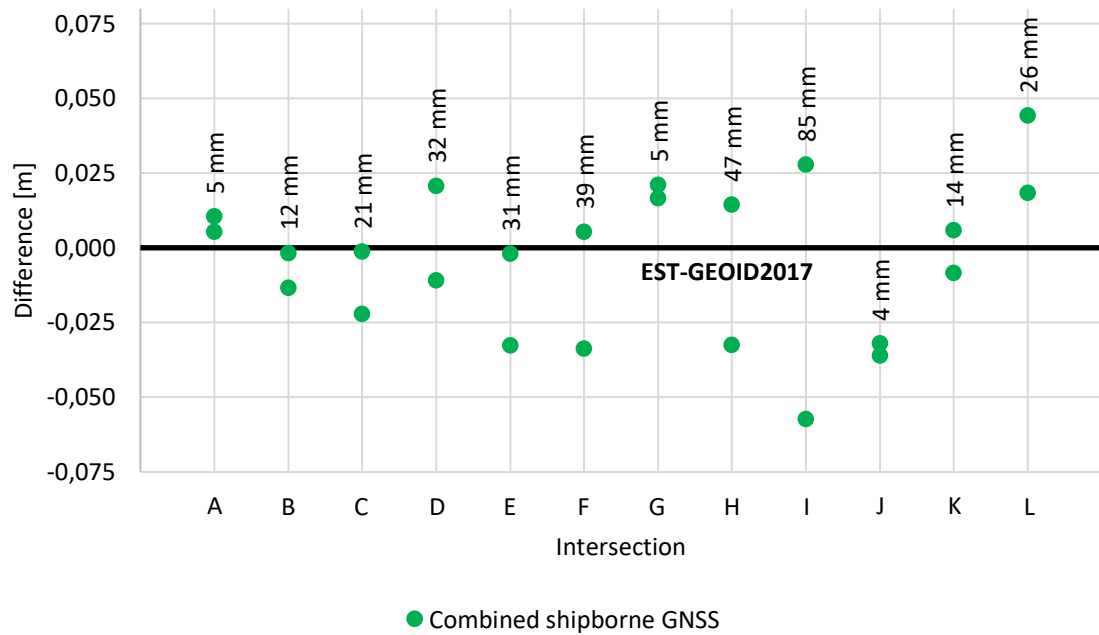


Figure 3.16 Combined GNSS profile heights compared to EST-GEOID2017 at profile intersections (Fig. 3.15) after removing average difference of 6,6844 m from profile heights (seen in Table 3.4). Double low-pass filtered profiles with corrections from DT and fuel consumption are compared. Numbers on the figure show height differences of profiles at intersections, units in mm.

Table 3.4 Statistics of differences between the combined GNSS profile and geoid models. All combined double low-pass filtered GNSS heights are considered in the comparisons (18425 profile points in total). Profile heights have been subtracted from the model heights. Deviations are visualised in Figures 3.17 and 3.18.

Geoid model	DT+F ¹	\bar{A}^2 (m)	Min ³ (m)	Max ³ (m)	StDev (m)
EST-GEOID2011	No	-6,915	-0,159	0,149	0,067
	Yes	-6,656	-0,118	0,124	0,040
EST-GEOID2017	No	-7,172	-0,121	0,156	0,065
	Yes	-6,684	-0,128	0,059	0,0278
NKG2015	No	-7,147	-0,132	0,159	0,065
	Yes	-6,660	-0,134	0,095	0,034
FAMOS GOCO05s	No	-6,594	-0,128	0,154	0,067
	Yes	-6,106	-0,112	0,061	0,0275

Notes: HDM data is corrected with TGw method. Note that TG station readings for EST-GEOID2011 assessment are in BK77 height system, whereas for EST-GEOID2017, NKG2015 and FAMOS GOCO05s in EH2000 height system (see Section 2.2). Best result is highlighted in bold text.

¹ Marks the use of DT and fuel consumption corrections. StDev values (sixth column) of the uncorrected profiles are marked red and corrected blue.

² Mean difference between the combined GNSS profile and geoid model height.

³ After removal of the mean difference (third column).

Comparing Table 3.4 to Table 3.3, significant improvements in EST-GEOID2017, NKG2015 and FAMOS GOCO05s model assessment results can be seen. The best performing geoid model in the Gulf of Finland, according to the combined GNSS profiles, is FAMOS GOCO05s, which surpasses marginally EST-GEOID2017 (Table 3.4).

Comparisons between geoid models and combined GNSS profile show significant improvements in geoid modelling over the Gulf of Finland, e.g. compare Figure 3.17a or 3.18a to Figure 3.17b or 3.18b. Largest improvements appear near Vaindloo island and in the Narva Bay (for location reference, see Fig. 2.2) – areas with largest modelling change due to FAMOS2017 gravimetric data (Subsection 2.1.1 for more information). Improvements farther from coast are larger than the ones near coastal areas (Figs. 3.17 and 3.18).

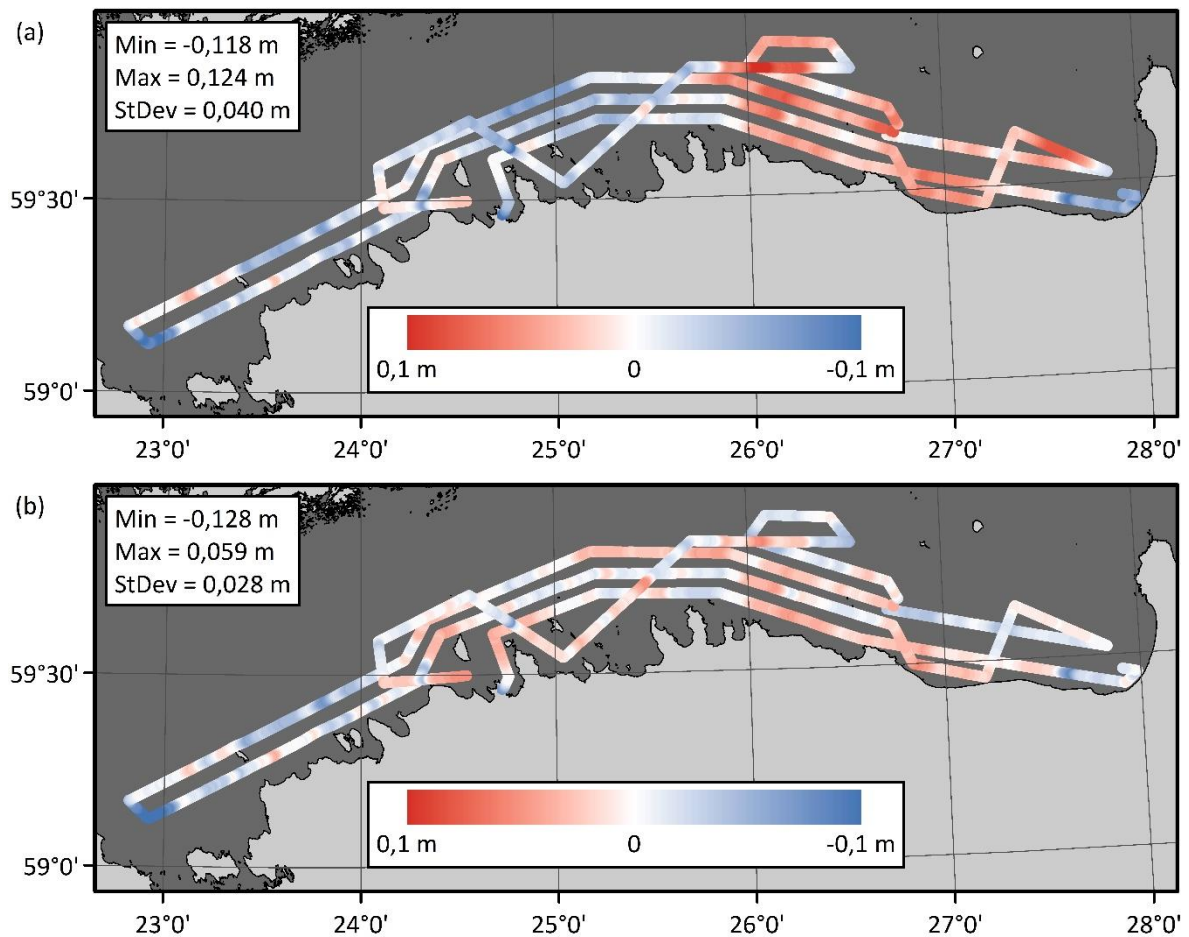


Figure 3.17 Comparisons of EST-GEOID2011 (a) and EST-GEOID2017 (b) deviations from the combined GNSS profiles. Both models are compared to the double low-pass filtered profiles with corrections from DT (TGw method) and fuel consumption.

According to the combined GNSS profiles, generalized accuracy of EST-GEOID2017 and FAMOS GOCO05s geoid models in the Gulf of Finland is approximately 2,8 cm (according to standard deviation). RMSE estimations cannot be calculated due to the nature of methodology (removal of average difference).

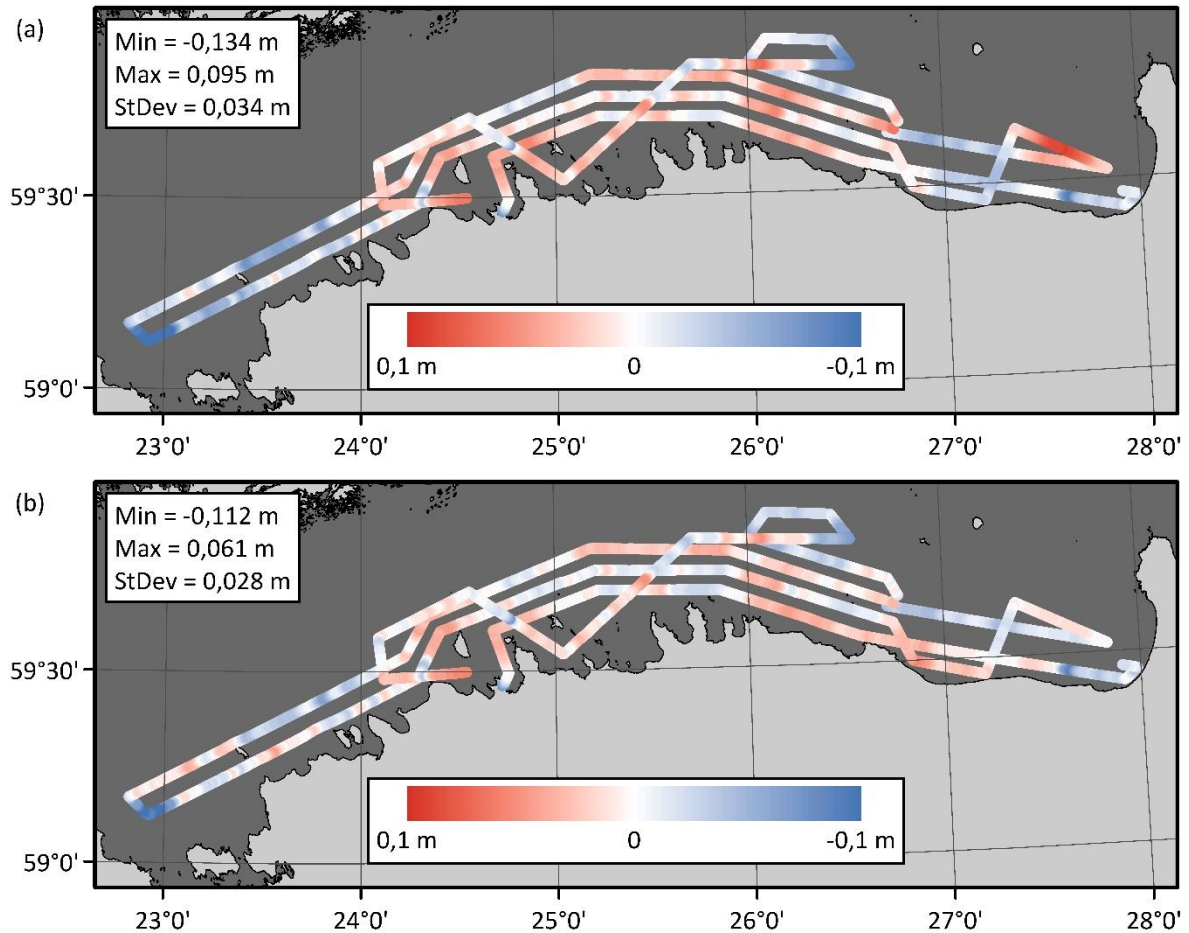


Figure 3.18 Comparisons of NKG2015 (a) and FAMOS GOCO05s (b) deviations from the combined GNSS profiles. Both models are compared to the double low-pass filtered profiles with corrections from DT (TGw method) and fuel consumption.

4 ALS PROFILES

The chapter examines in detail how ALS profiles for geoid model validation are computed – from point clouds to the final product. As a conclusion, assessment results are discussed. Also, other possibilities of ALS data usage are explored.

In brief, ALS is a remote sensing technology. A LiDAR device mounted on an aircraft emits laser pulses and registers the reflections from a surface, resulting in a 3D point cloud. Such methodology is mainly used on dry land, however reflections from the water surface can also be registered resulting in SSH point cloud. The vertical accuracy of ALS over dry land is usually estimated at 5...15 cm, depending largely on the measured surface – see e.g. papers by Huising and Gomes Pereira (1998), van der Sande *et al.* (2010) and Fowler and Kadatskiy (2011). Similar accuracy has been estimated on measurements over water as well, see e.g. papers by Cocard *et al.* (2002), Gruno *et al.* (2013) and Julge *et al.* (2014). However, less research has been conducted on the latter matter.

ALS is a more accurate and high-resolution alternative to satellite altimetry (SA) (method generally used to determine SSH), as the spatial resolution of SA data is relatively low. In addition, the SA data has poor accuracy near coastal areas due to inaccurate tidal corrections, incorrect estimations of atmospheric (wind, barometric pressure) effects on the sea surface and footprint land contaminations (Vignudelli 2005). Another advantage of ALS is the ability to monitor large areas quickly, in comparison to e.g. shipborne GNSS measurements to determine SSH/derive MSL.

4.1 Study area and data

A dedicated ALS campaign was carried out 14.05.2013 over the Gulf of Finland (see Fig. 2.1), with a test run at 08.05.2013 (Fig. 4.1). In total 9 profiles + 1 from the test run were obtained (10 point clouds in total). Scanning was done using Leica ALS50-II LiDAR System (Fig. 4.2), which was mounted on Estonian Land Board's survey plane Cessna Grand Caravan 208B (Fig. 4.3). Altitude of aircraft (above sea surface) was 2400 m when measuring point clouds 08052013_090408 and 14052013_090928. During the rest of the campaign, altitude varied between 370-450 m, and was up to 580 m when measuring point clouds 14052013_095527 (the last part, to the north) and

14052013_100143 (the first part, to the north). The total length of the ALS profiles computed from the 2013 point clouds is 373,4 km.

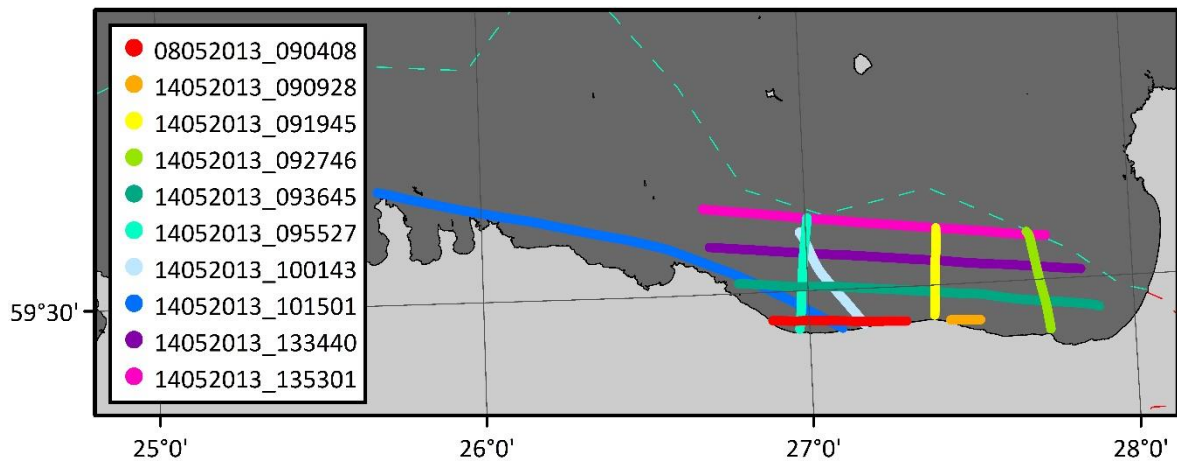


Figure 4.1 Flight paths of the survey plane (and data coverage) during 2013 ALS campaign. Numbers in the legend show flight time. The first part is the date and second GPS time of the first measurement. The dashed cyan/red line depicts Estonian border.



Figure 4.2 Leica ALS50-II LiDAR System (in the left figure) and it placed on the survey plane (the foremost instrument in the right figure; survey plane in Figure 4.3) (Aerolaserskanner 2017a; Lennuk 2016).



Figure 4.3 Estonian Land Board's survey plane Cessna Grand Caravan 208B (Lennuk 2016).

During the campaign, westerly winds were dominating. Wind speed in the morning (09:00-11:00 UTC) was between 5-8 m/s and during noon (13:00-14:30 UTC) 4-6 m/s. Wave height was generally around 10-20 cm, being slightly higher in the morning and lower at noon.

Quality of some scanning data is poor. Typically, the width of the nadir-centred data corridor is around 170-200 m. However, in some areas, it drops under 100 m. Also, the point clouds are not as dense, intensity is lower, and some areas are almost without any data coverage. Such difference in data quality is caused by changes in backscattering, which is affected by the state of sea surface during ALS measuring. More disturbed sea surface seems to give better results, as with calm sea, the laser impulses are reflected away from the LiDAR sensor (Julge *et al.* 2014). Point clouds with such poor data are:

- 08052013_090408 – very sparse and low intensity data coverage;
- 14052013_091945 – sparse and low intensity data coverage in the second half;
- 14052013_101501 – sparse data coverage in the second half and low intensity in the middle parts;
- 14052013_133440 – very sparse and low intensity data coverage, however the last third is good;
- 14052013_135301 – very sparse and low intensity data coverage throughout.

Figure 4.4 shows a typical view from the side of a low intensity point cloud. As seen, there is a lot of noise in the data. Point clouds with decent quality (the ones not listed above) have similar noise in the data, however on a much smaller scale.

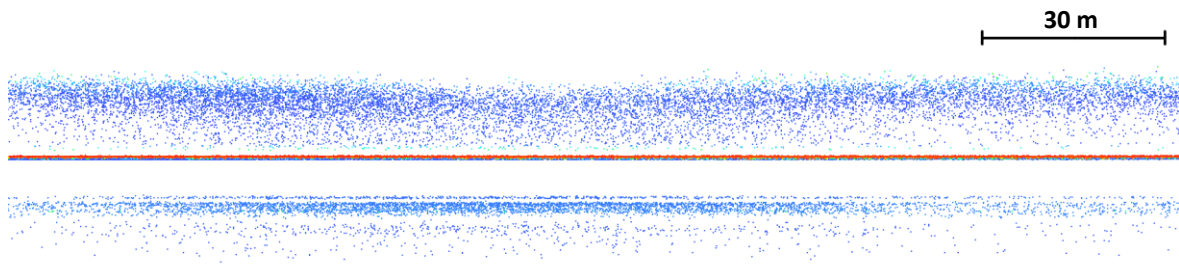


Figure 4.4 An example (cloud 14052014_133440) of noise in 2013 ALS point cloud below and above sea surface, which is identifiable in the middle as a line (coloured reddish). Note that red colours denote high and blue low intensity. Vertical scale of the figure is the same as horizontal.

Another dedicated ALS campaign was carried out 10.05.2018 (Fig. 4.5). Scanning this time was done using RIEGL VQ-1560i LiDAR Scanning System (Fig. 4.6), which replaced older Leica ALS50-II LiDAR System. In total, 14 point clouds were obtained from the experiment, as the instrument has two laser scanners (Channel 1 and Channel 2 – referred to as C1 and C2 respectively), both of which deliver straight parallel scan lines. The scan lines of two channels are separated by an 28° angle. Parameters of the two scanning systems are compared in Table 4.1.

This time, easterly winds were dominating during the campaign. Wind speed was generally around 5-8 m/s and wave height according to the weather forecast between 30-60 cm (lower in the eastern areas and higher to the west). According to the ALS measurements however, the wave height to the east was generally around 15-20 cm and to the west between 40-50 cm (discussed later in Subsection 4.2.1).

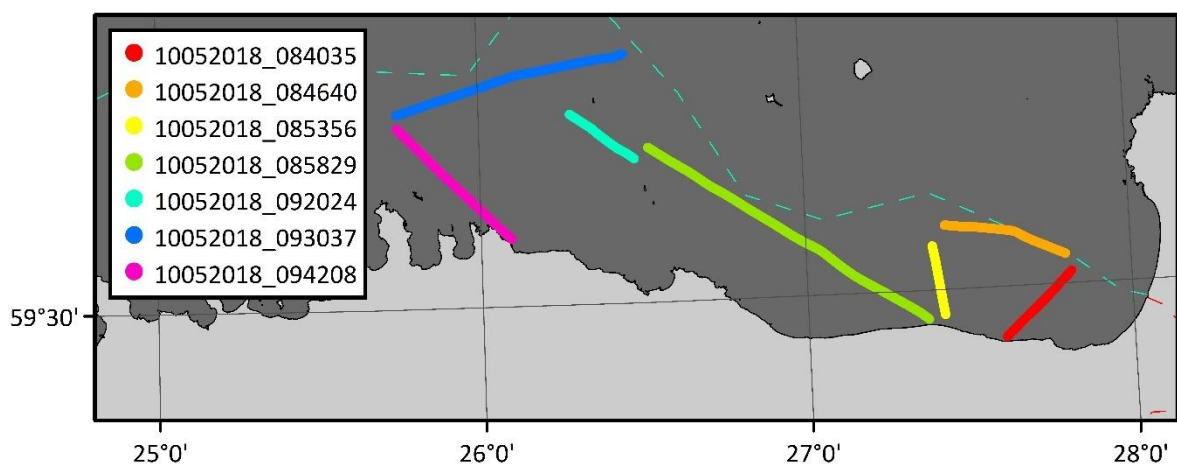


Figure 4.5 Flight paths of the survey plane (and data coverage) during 2018 ALS campaign. Numbers in the legend show flight time. The first part is the date and second UTC time of the first measurement. The dashed cyan/red line depicts Estonian border.

Quality of the 2018 ALS data is significantly better compared to the 2013 ALS data. Width of data corridor is generally between 1000 and 1200 m and data is constantly dense, i.e. differences in backscattering are not as apparent as with 2013 ALS data. Noise, as seen in Figure 4.4, is not a problem with 2018 ALS point clouds. Altitude of aircraft (above sea surface) was 1200 m during the campaign. The total length of ALS profiles computed from point clouds is 191,8 km.



Figure 4.6 RIEGL VQ-1560i LiDAR Scanning System (in the left figure) and it placed on the survey plane (in the right figure; survey plane in Figure 4.3) (Aerolaserskanner 2017b).

Table 4.1 Comparison between some Leica ALS50-II LiDAR System and RIEGL VQ-1560i LiDAR Scanning System parameters (Aerolaserskanner 2017a; Leica 2017; RIEGL n.d.).

Parameter	Leica ALS50-II	RIEGL VQ-1560i
Min range	200 m	100 m
Max range	6000 m	5800 m
Max field of view	75°	58°
Wavelength	1064 nm	1064 nm
Beam divergence	≤ 0,22 mrad	≤ 0,25 mrad
Laser pulse repetition rate	Up to 150 kHz (Multipulse ¹)	Up to 2 MHz
Scan pattern	Sinusoid-like	Parallel Crossed between channels

Notes: Multipulse (or MPiA) is a LiDAR sensor’s ability to increase survey efficiency by enabling multiple laser pulses in the air simultaneously (Parrish 2011).

4.2 Data processing

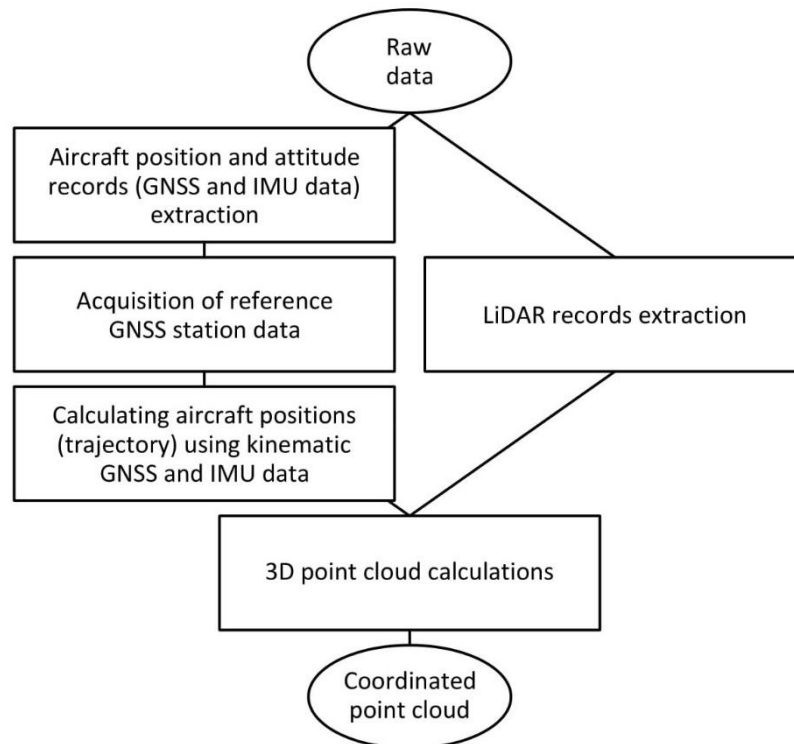


Figure 4.7 The standard workflow of ALS raw data processing based on Aerolaserskaneerimise kõrguspunktid (2019).

Estonian GNSS-CORS (for more details see an article by Metsar *et al.* 2018) belonging to a common Virtual Reference Station (VRS) network were used in the flight trajectory calculations. NovAtel Inertial Explorer™ software was used. The standard workflow of ALS raw data processing can be seen in Figure 4.7. The details of different computational stages are more thoroughly explained by Gruno *et al.* (2013). Particular care needs to be given to the GNSS-height determination of the aircraft trajectories – see e.g. Julge *et al.* (2014) for detailed discussion on general trajectory calculation issues.

The acquired ALS, GNSS, IMU data are used in calculations to produce coordinated 3D point clouds. For rigorous geoid model assessment, the obtained 3D point clouds must then be filtered (e.g. computed into profiles) to reduce sea surface oscillations, e.g. by averaging boxcar filter (Gruno *et al.* 2013). Both 2013 and 2018 ALS data are processed based on the same principles.

4.2.1 ALS grid computation

Prior to processing, all .LAS (or .LAZ for some 2013 files) data files were converted into .xyz text files (the 3D point clouds – see Sections 1.4 and 4.2 for more information). 2018 ALS data was then downsampled, meaning that every second row was deleted from the .xyz files (point clouds). All data was included while processing ALS data from 2013 campaign. Reasoning for downsampling is discussed in Subsection 4.2.2.

From the .xyz files (original files for 2013 data and downsampled for 2018 data), 5x5m and 50x50m grids were computed for every point cloud (both C1 and C2 for 2018 data). As data is dense and even (for the most part, with an exception of some 2013 point clouds), inverse distance weighted (IDW) interpolation method was used to represent sea surface. ArcMap Raster Interpolation toolset was used for the purpose.

The method assumes that data-points that are close to one another are more alike than those that are farther apart – each measured point has a local influence that diminishes with distance. IDW interpolation determines cell values using a linearly weighted combination of a set of sample points. The weight is a function of inverse distance. (How IDW works 2018)

To see how well RIEGL VQ-1560i LiDAR Scanning System has scanned the sea surface, some additional higher resolution grids (1x1m) were computed. An example can be seen in Figure 4.8. As the figure shows, sea surface has been recorded in excellent detail. Literally, the instant sea surface appears to be frozen. This data allows e.g. investigation of wave dynamics (see how the small islet diverges the waves, marked with a green arrow) and estimation of wave heights (see the graphs).

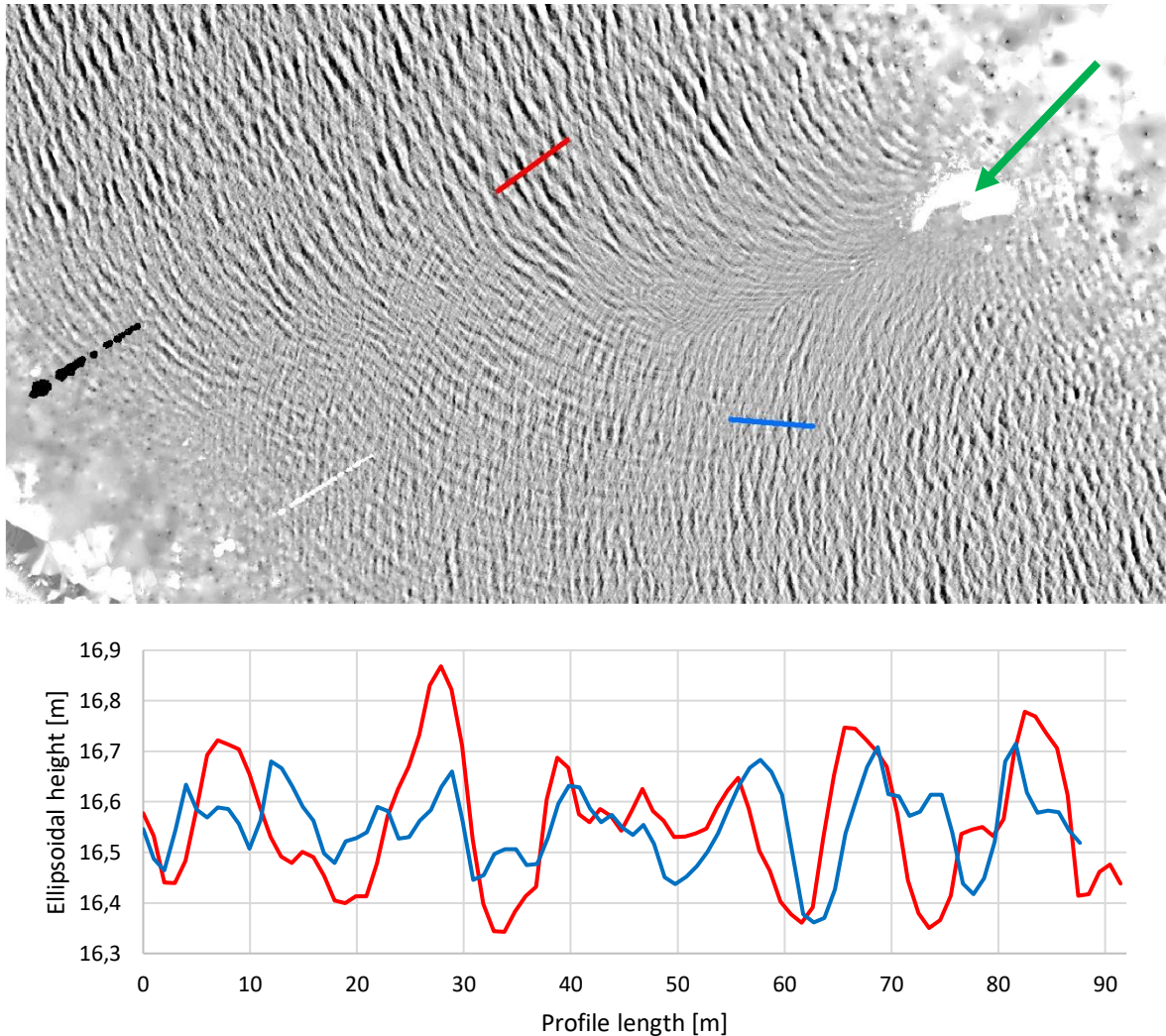


Figure 4.8 An example of a 1x1m grid computed from point cloud 10052018_094208 (C1), near coast (see Fig. 4.5). Red and blue lines show the locations of profiles visualised in the graph. The black and white areas on the lower left side are interpolation artefacts (also seen in the lower left and upper right corner). Lighter area in the upper right side is a small islet (marked with a green arrow).

Similarly, high resolution grids (1x1m) were computed from some Leica ALS50-II LiDAR System point clouds. An example can be seen in Figure 4.9 (scale of the figure is the same as in Fig. 4.8). As the figure shows, there are some identifiable wave patterns. However, the result is far worse compared to grid computed from a 2018 ALS point cloud. Also, the comparison between Figures 4.8 and 4.9

shows that there is much more noise left in gridded 2013 ALS data (see also Fig. 4.4). The graphs in Figure 4.9 indicate that too.

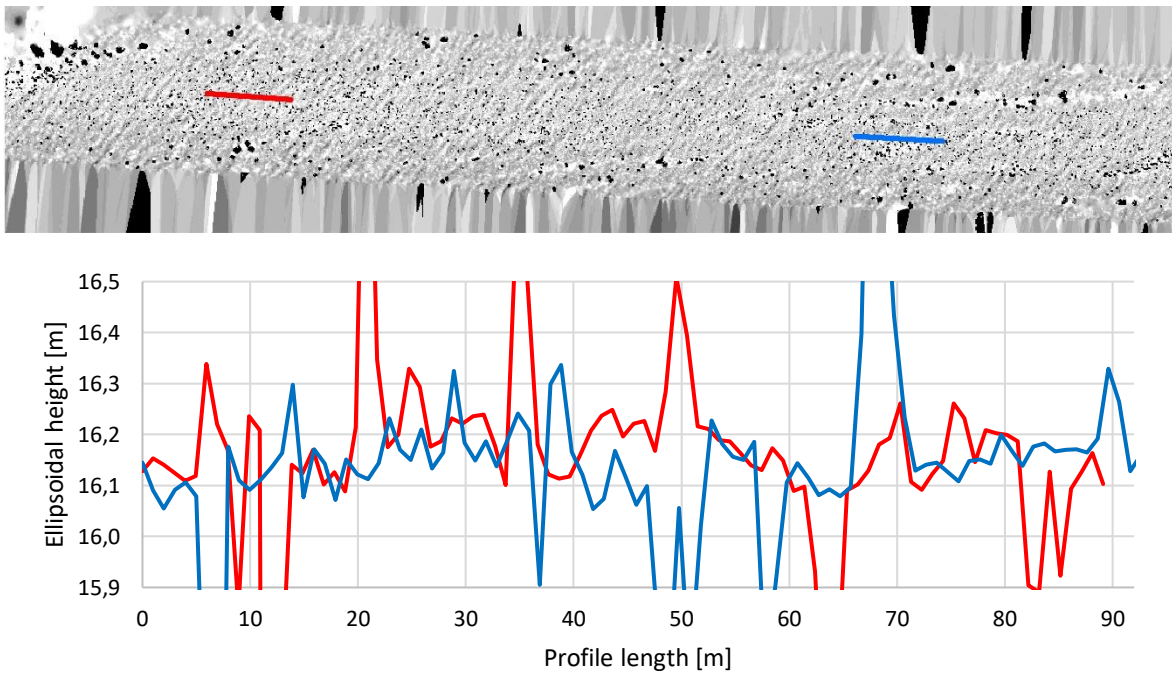


Figure 4.9 An example of a 1x1m grid computed from point cloud 14052013_093645, the middle section (see Fig. 4.1). Red and blue lines show the locations of profiles visualised in the graph. The black and white dots (which cause large fluctuations in heights seen in the graph) and lines in the upper and lower parts of the figure are interpolation artefacts.

4.2.2 Data downsampling

Before processing 2018 ALS data, point clouds were downsampled, as these were unnecessarily dense for the research purpose, but also to make processing quicker. Another reason was that some of the used software has a 2 Gb data file processing limit (the volumes of some input .xyz files exceed that limit). As data points are distributed randomly within the .xyz file, every second row was deleted from the original file. It is expected that the distribution of data points remains even after downsampling. An example of how downsampling affects the gridding result can be seen in Figure 4.10.

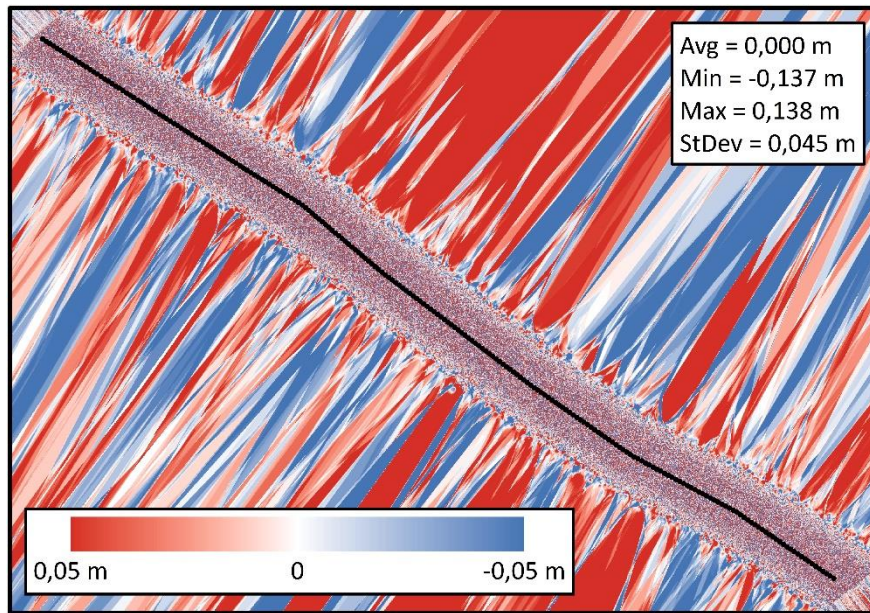


Figure 4.10 A 5x5m grid computed from original point cloud 10052018_092024 (C1) compared to a grid computed from the same, but downsampled (every other row was deleted from original .xyz file) point cloud. The black line shows the location of constructed ALS profile 10052018_092024 (explained in the further text). Statistics pertain along the profile (according to 223 profile points).

As seen from the example (Fig. 4.10), differences between grids computed from original and downsampled point clouds exceed 5 cm. Such dissimilarity would have a significant influence on the final assessment results. However, inspecting closely, the difference seems to be mainly noise – there does not appear to be any signal.

In comparison, comparing exponentially filtered (size 10 cells – see the following Subsection 4.2.3 for explanation) grids computed from original and downsampled point clouds or filtering the differences between the two grids exponentially (grid in Figure 4.10), the aforementioned dissimilarity decreases to near zero (Fig. 4.11). Differences between two solutions are sub 10^{-5} m and thus negligible. Therefore, it is expected that downsampling does not affect the signal and thus has no effect to the final geoid model assessment results.

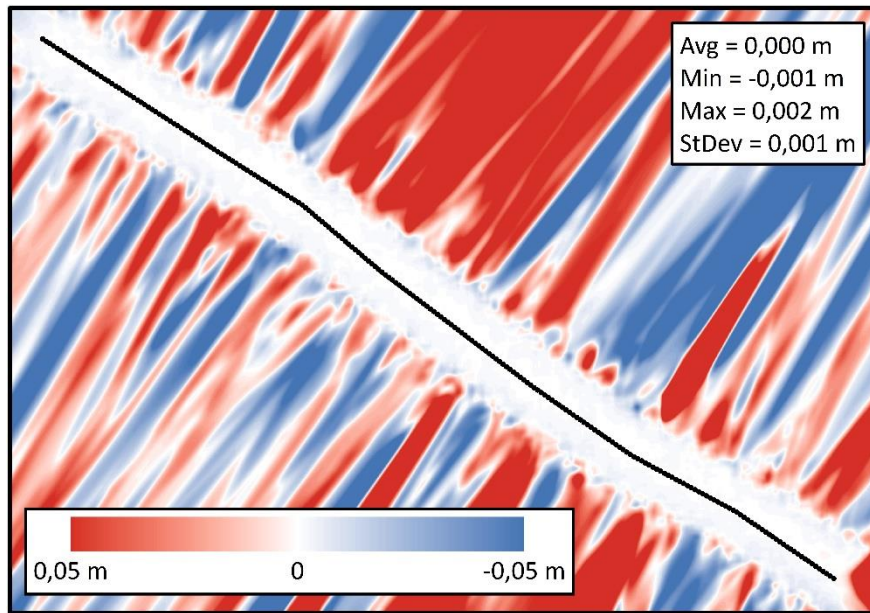


Figure 4.11 Exponentially filtered (size 10 cells) grid computed from original point cloud 10052018_092024 (C1) compared to exponentially filtered (size 10 cells) grid computed from the same, but downsampled (every other row was deleted from original .xyz file) point cloud (see the following subsection for filter explanation). Almost exact result is obtained after filtering the grid in Figure 4.10 exponentially with a size of 10 cells (differences between two solutions are sub 10^{-5} m). The black line shows the location of constructed ALS profile 10052018_092024 (explained in the further text). Statistics pertain along the profile (according to 223 profile points).

4.2.3 Grid filtering

Three different methods were tested to filter gridded ALS data. These are:

- 1) Averaging filter (SAGA-GIS version 7.1.1. was used, for details see Conrad *et al.* 2015):
Calculates a value for the target cell by averaging all cell values within the assigned Kernel radius (radius of the filter; radius 0 returns the target cell value). The filter works as a moving window, progressing from one cell to the next (all cells are assigned a new value). Mask of the filter is circular. For more details about the filter see Cimmery (2011).
- 2) Exponential filter (SAGA-GIS version 7.1.1. was used, for details see Conrad *et al.* 2015):
Applies a recursive (i.e. re-uses output data) exponential function in X and Y direction. Size of the filter shows how many cells are included in smoothing process in one direction from the target cell, i.e. size 5 filter includes a total of 11 cells in both X and Y direction (all cells are assigned a new value). For more details about the filter see Conrad (2009) and Koethe (2017).
- 3) Double low-pass filter:
After grid computations, height values were extracted at every 62 m (which is the average distance between shipborne GNSS profile points – for better comparisons sake between the two methods), approximately at plane’s nadir. Interpolation was used (surrounding cell values were considered) while extracting heights, meaning that if two points happen to be on the same cell, but at different locations, the heights are different. For 2018 data, C1 and C2 heights were extracted at the same locations.

The resulting profiles were then filtered. First, a moving median of 51 profile points (which corresponds to 3,162 km) was taken, i.e. the interval from 25 points before profile point i up to 25 points after the same profile point i . From that outcome, a moving average of 51 profile points was then taken (for more details about the filter see also Subsection 3.2.3).

3D filtering results of interpolation artefacts in the gridded sea surface (Figs. 4.12 and 4.13) show how the filters work. As seen from the two examples, if there’s an anomaly (i.e. interpolation artefact) in the computed grid, then exponentially filtered result is much more affected by it (compare white dots in Fig. 4.12 to the red circles in Fig. 4.13).

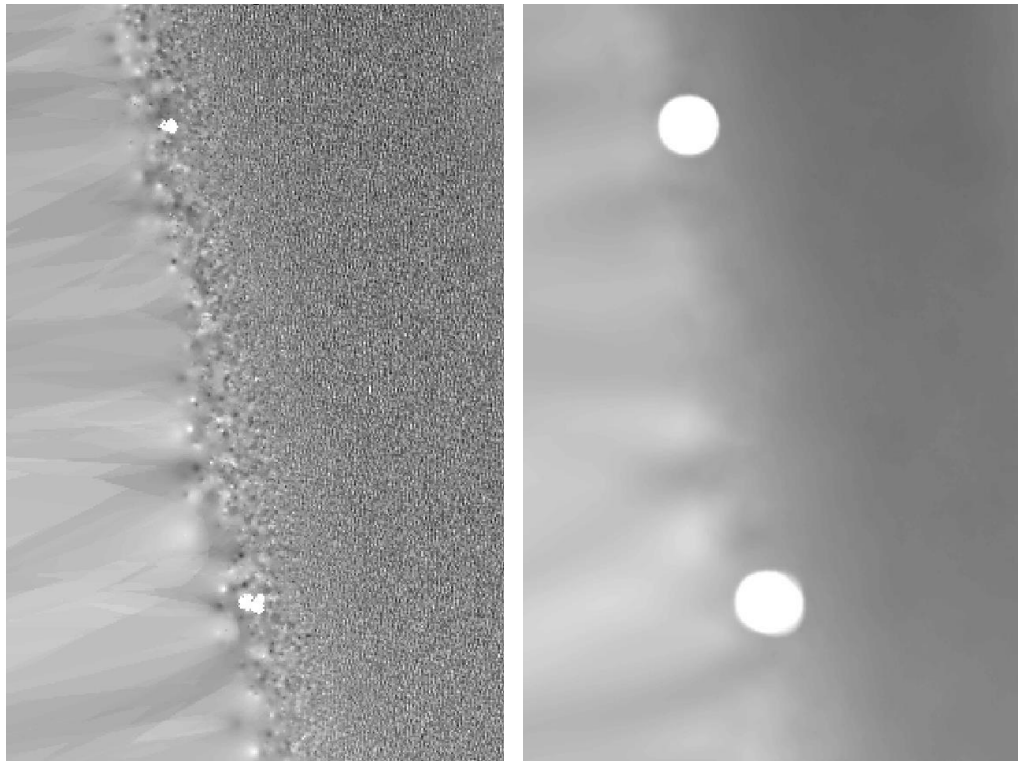


Figure 4.12 Interpolation artefacts (white dots at the edge of data corridor) in the 5x5m grid (left figure) and their average filtered results (right figure). Kernel radius of the filter is 15 cells.

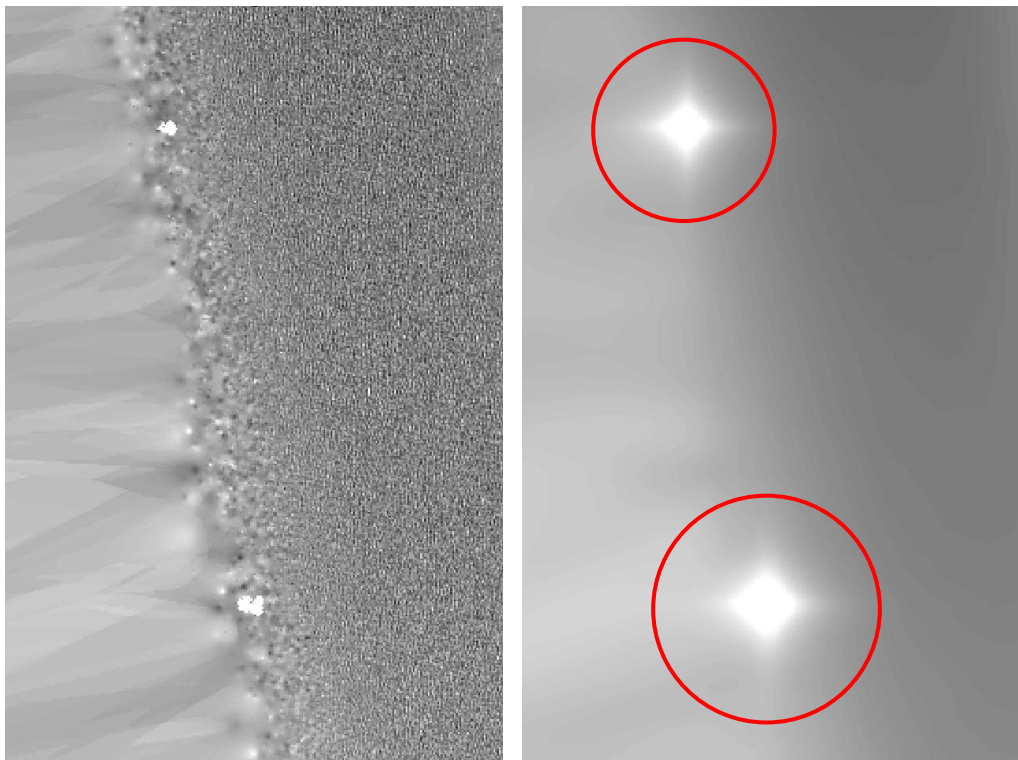


Figure 4.13 Interpolation artefacts (white dots at the edge of data corridor) in the 5x5m grid (left figure) and their exponentially filtered results (right figure). Size of the filter is 15 cells.

Due to the nature of exponential filter, the more a profile aligns with X or Y axis, the farther deformations caused by an anomaly carry over to. On the other side, exponentially filtered result represents the waveless sea more accurately than the averaging filter, assuming that no extensive anomalies exist in the input grid. Also, the exponential filter executes much faster than the averaging one.

Note that the double low-pass filter (third method) is used to filter both 5x5m and 50x50m grids. However, averaging and exponential filter (first and second method) are used only with 5x5m grids. This is because the first and second method include data from two directions, while the third one includes data from only one direction. Therefore, the width of the data corridor renders the use of 3D filters pointless with poorer resolution grids, such as the 50x50m grid.

While the extent of filtering window for averaging and exponential filter is dependent on the resolution of the grid, the extent of double low-pass filter depends solely on the distance between extracted profile points.

4.2.4 2013 ALS data filtering results

In order to find the best method for data filtering, FAMOS GOCO05s was chosen for comparison, as that model is the most accurate according to the GNSS profiles (see Table 3.4). Note that DT correction is not considered in these comparisons.

To see how noise in data affects the results, all 2013 ALS point clouds were cleaned manually (noise seen in Fig. 4.4 was removed from the point clouds), after which the resulting clouds were gridded and filtered similarly to the point clouds with noise. To compare the results of averaging and exponential filters to the double low-pass filter, height values were extracted at every 62 meters from the filtered grids (average distance between shipborne GNSS profile points), approximately at plane's nadir. Profile points that are compared, are always extracted at the very same planar location. Generalised filtering results (weighted average according to the profile lengths) are presented in Table 4.2.

Table 4.2 Comparison between averaged (weighted according to the profile lengths) filtering results of 2013 ALS data (profiles are compared to the FAMOS GOCO05s geoid model). StDev values and deviation amplitudes (maximum – minimum) from Tables C.1 – C.10 (Appendix C) are considered. The smallest StDev value and deviation amplitude are highlighted in red.

Profile type	Point clouds with noise		Cleaned point clouds	
	StDev (m)	Amplitude (m)	StDev (m)	Amplitude (m)
5x5m grid	0,6140	9,0538	0,0581	0,3958
50x50m grid	0,6299	9,8707	0,0547	0,3674
Averaging filter; Radius = 5	0,2618	1,6983	0,0363	0,1908
Averaging filter; Radius = 10	0,2310	1,3570	0,0356	0,1771
Averaging filter; Radius = 15	0,2305	1,9748	0,0357	0,1776
Exponential filter; Size = 5	0,2298	1,6341	0,0354	0,1765
Exponential filter; Size = 10	0,2248	1,9823	0,0353	0,1735
Exponential filter; Size = 15	0,2270	2,0687	0,0353	0,1706
Double low-pass filtered 5x5m grid	0,1338	0,4858	0,0294	0,1058
Double low-pass filtered 50x50m grid	0,1234	0,4482	0,0283	0,1060

Notes: Results of averaging and exponential filter are based on 5x5m grid filtering.

For double low-pass filtering results, a median of 51 profile points was taken first. From that outcome, an average of 51 profile points was then taken.

The results of clean data suggest that the double low-pass filter performs slightly better than averaging or exponential one (for detailed results of each profile see Appendix C). Also, lower resolution grids (filtered) seem to perform marginally better than using the exact same method (double low-pass filter) with higher resolution grids. Thus, in the case of 2013 ALS data, double low-pass filtered 50x50m grids (computed from cleaned point clouds) are the best option for assessment purposes. Results of 5x5m grids are similar. However, it is important to remember that computation of 5x5m grids takes remarkably longer than 50x50m grids.

In comparison, when data has a lot of noise, the double low-pass filter performs significantly better than averaging or exponential one. This is due to anomalies in the interpolated grids, which are essentially artefacts caused by noise in point clouds. Latter two filtering methods tend to amplify areas where anomalous cells appear (see Figs. 4.12 and 4.13). Double low-pass filter on the other hand eliminates these areas thanks to the median in the filter. However, if data has extreme

amount of noise (e.g. point clouds listed in Section 4.1), even the use of double low-pass filter will not improve the results (Fig. 4.14).

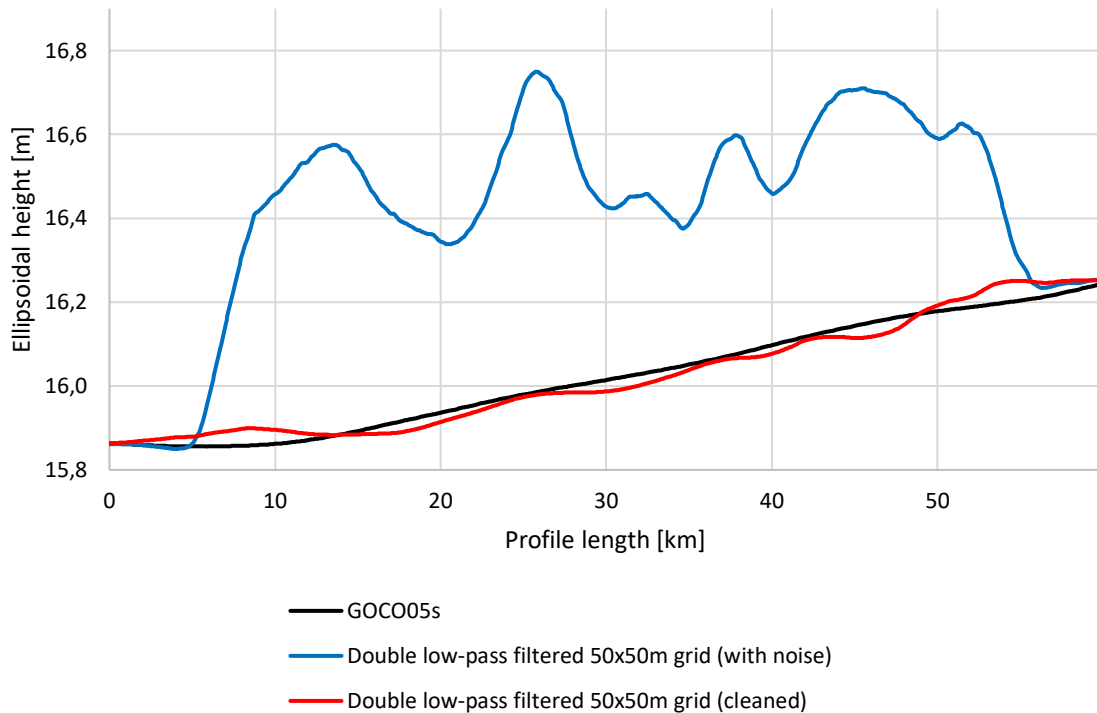


Figure 4.14 An extreme example of noise in ALS data (see Fig. 4.4) affecting the resulting profile compared to the result of cleaned point cloud (both are computed from cloud 14052013_135301, see Fig. 4.1). Double low-pass filtered profiles are compared to the GOCO05s geoid model (see also Appendix C Table C.10). Note that for comparisons sake, GOCO05s is lowered 0,415 m (average difference between the model and double low-pass filtered result of cleaned point cloud).

It seems that large filter radiuses/sizes (averaging or exponential filter correspondingly) worsen the results. This is most likely caused by the artefacts (see the left-hand side of the left Figure 4.12 or 4.13), which are an additional outcome of grid interpolation (output grid is defined by its four corners, which are determined by the farthest points in the input point cloud, not by the edges of it). This becomes very apparent with grids interpolated from lower quality data, e.g. see Appendix C Table C.10. When the width of ALS data corridor is less than 105m (which is the case with poorer quality data), filter size/radius over 10 cells (diameter of 105m) begins to include data from interpolation artefacts.

4.2.5 2018 ALS data filtering results

The methodology for finding the best filtering method for 2018 ALS data is the same as it is with 2013 ALS data. 10 profile points (620 m) in ALS profile 10052018_094208, which covered land area, had to be discarded, as these distorted the results (compare Table D.7 to D.8 in Appendix D). 2018 ALS data has not been cleaned of noise, as this does not seem to be influencing the results too much.

Table 4.3 Comparison between averaged (weighted according to the profile lengths) filtering results of 2013 ALS data (profiles are compared to the FAMOS GOCO05s geoid model). StDev values and deviation amplitudes (maximum – minimum) from Tables D.1 – D.6 and D.8 (Appendix D) are considered. Three smallest StDev values and deviation amplitudes are highlighted in red.

Profile type	StDev (m)	Amplitude (m)
5x5m grid (C1)	0,0909	0,5794
50x50m grid (C1)	0,0707	0,4942
Averaging filter; Radius = 5 (C1)	0,0119	0,0669
Averaging filter; Radius = 10 (C1)	0,0100	0,0632
Averaging filter; Radius = 15 (C1)	0,0096	0,0481
Exponential filter; Size = 5 (C1)	0,0099	0,0666
Exponential filter; Size = 10 (C1)	0,0095	0,0529
Exponential filter; Size = 15 (C1)	0,0106	0,0773
Double low-pass filtered 5x5m grid (C1)	0,0152	0,0748
Double low-pass filtered 50x50m grid (C1)	0,0145	0,0638
5x5m raster (C2)	0,0907	0,5653
50x50m grid (C2)	0,0704	0,4436
Averaging filter; Radius = 5 (C2)	0,0115	0,0699
Averaging filter; Radius = 10 (C2)	0,0093	0,0479
Averaging filter; Radius = 15 (C2)	0,00887	0,0426
Exponential filter; Size = 5 (C2)	0,0091	0,0447
Exponential filter; Size = 10 (C2)	0,0087	0,0418
Exponential filter; Size = 15 (C2)	0,0103	0,0898
Double low-pass filtered 5x5m grid (C2)	0,0147	0,0619
Double low-pass filtered 50x50m grid (C2)	0,0109	0,0474

Continuation of Table 4.3

Profile type	StDev (m)	Amplitude (m)
5x5m raster (C1 + C2)	0,0803	0,5156
50x50m grid (C1 + C2)	0,0517	0,3364
Averaging filter; Radius = 5 (C1 + C2)	0,0110	0,0650
Averaging filter; Radius = 10 (C1 + C2)	0,0093	0,0486
Averaging filter; Radius = 15 (C1 + C2)	0,00903	0,0439
Exponential filter; Size = 5 (C1 + C2)	0,0092	0,0478
Exponential filter; Size = 10 (C1 + C2)	0,00895	0,0422
Exponential filter; Size = 15 (C1 + C2)	0,0102	0,0804
Double low-pass filtered 5x5m grid (C1 + C2)	0,0136	0,0649
Double low-pass filtered 50x50m grid (C1 + C2)	0,0116	0,0519

Notes: For C1 + C2 results, each profile point is an average value of C1 and C2 heights at the same location.

Results of averaging and exponential filter are based on 5x5m grid filtering.

For double low-pass filtering results, a median of 51 profile points was taken first. From that outcome, an average of 51 profile points was then taken.

According to the results in Table 4.3, the best choice for filtering 2018 ALS data is exponential filter with a size of 10 cells (for detailed results of each profile see Appendix D), as opposed to the double low-pass filter for 2013 data. Such difference (especially large when comparing averaging and exponential filter results) between 2013 and 2018 ALS data filtering results (compare Table 4.3 to Table 4.2) is first and foremost caused by the data quality.

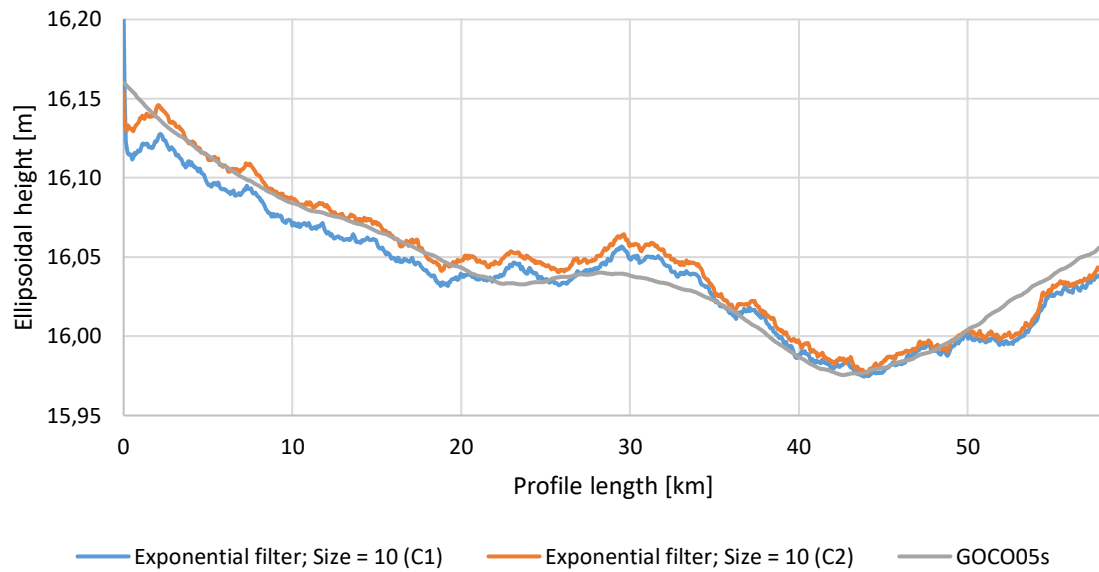


Figure 4.15 Channels C1 and C2 of profile 10052018_085829 (see Fig. 4.5) compared to FAMOS GOCO05s geoid model. As seen, the results of two channels do not coincide. Note that for comparisons sake, GOCO05s is lowered 0,559 m (average difference between the model and exponentially filtered, size 10, C1+C2 profile).

As seen from Table 4.3 and Figure 4.15, the results from channels C1 and C2 do not coincide with each other. Out of two, C2 shows generally better results than C1 (this may just be a coincidence or specific result of the current study). Also, C2 tends to surpass averaged results of C1 and C2. According to the Estonian Land Board, a combined solution is not recommended either (Aerolaserskaneerimise kõrguspunktid 2019). Therefore, the best option for 2018 ALS data filtering seems to be exponentially filtered C2, with filter size of 10 cells.

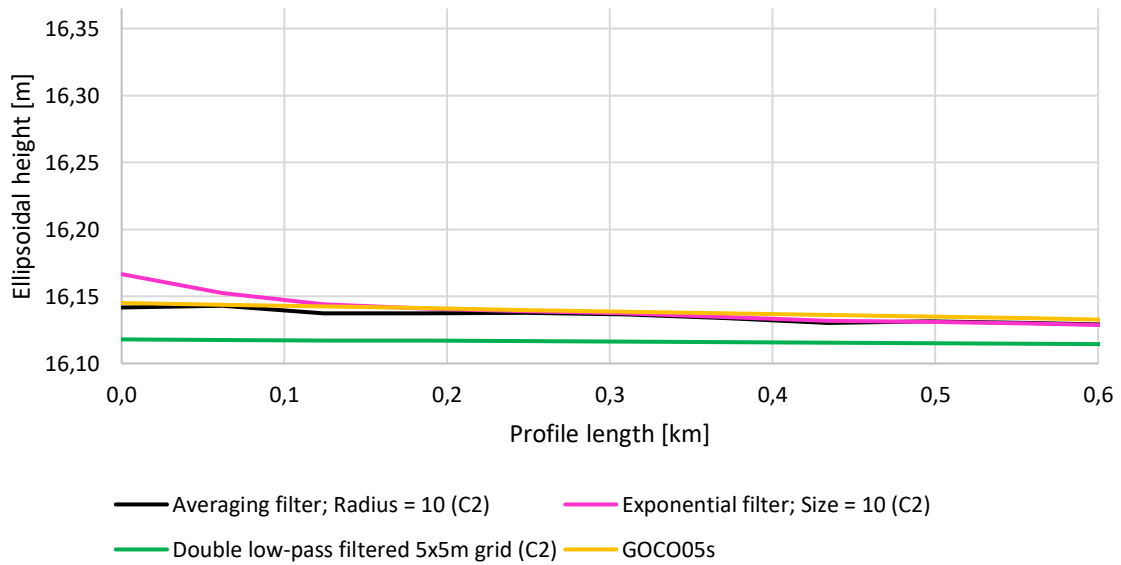


Figure 4.16 Some filtering results of point cloud 10052018_084035 compared to the FAMOS GOCO05s geoid model. For comparisons sake, FAMOS GOCO05s is lowered 0,561 m (average difference between the model and profile extracted from C2 5x5m grid). The left side of the graph (first profile point) is approximately 800 m from the shore (see also Fig. 4.5 – the southern end of the profile is near shore). Notice the result of exponential filter (size 10).

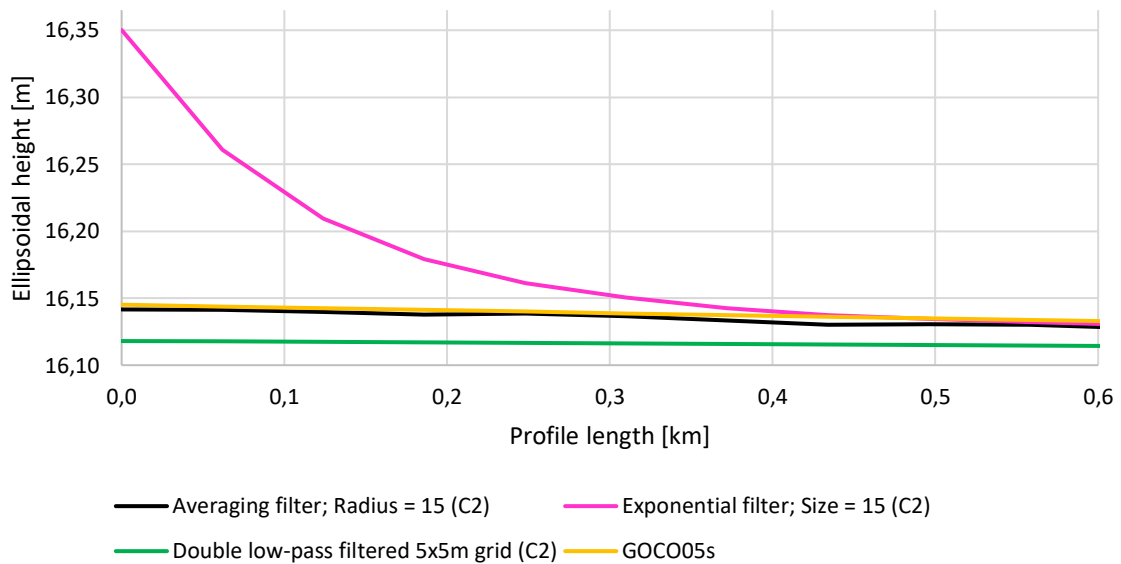


Figure 4.17 Some filtering results of point cloud 10052018_084035 compared to the FAMOS GOCO05s geoid model. For comparisons sake, FAMOS GOCO05s is lowered 0,561 m (average difference between the model and profile extracted from C2 5x5m grid). The left side of the graph (first profile point) is approximately 800 m from the shore (see also Fig. 4.5 – the southern end of the profile is near shore). Notice the result of exponential filter (size 15).

In the previous subsection, interpolation artefacts and anomalous cells/areas were briefly discussed. Figures 4.16 and 4.17 are another example of how the result of exponential filter is affected by such areas, whereas averaging and double low-pass filter work fine. In the example, the land area close to the beginning of the profile (approximately 800 m away) can be considered as a large anomaly. The extent of averaging filter in the case of Kernel radius 15 is 75 m out of those 800 m, which is why the result is not affected. However, 800 m does not seem to be enough for exponential filter (the filter is recursive). Note that the filtering result is so much affected also because the land area is large and several meters higher than the sea surface. Comparing the graphs (Figs. 4.16 and 4.17) shows how the size of exponential filter affects the extent of the anomaly.

4.2.6 Combining 2018 ALS data Channels 1 and 2

The current subsection suggests an alternative data processing method if there's a need to combine the results of two channels (as an alternative to combining point clouds before data processing) and examines the risks of it. Previously (Subsection 4.2.5) an average value was calculated from already filtered and extracted results. However, an average grid can also be calculated before filtering and extracting the profiles, which would make data processing faster.

The two methods this chapter examines are as follows:

- 1) Both C1 and C2 5x5m grids are first filtered with exponential filter with a size of 10 cells, after which a profile point is extracted from both grids at every 62 m. Then, an average value is calculated for every profile point from C1 and C2 profile points (method is used in Subsection 4.2.5).
- 2) First, C2 5x5m grid is resampled into C1 5x5m grid system by B-Spline interpolation (grid systems are slightly different). Then, a new grid is calculated according to Eq. 4.1:

$$g_n = (g_1 + g_2)/2 \quad (4.1)$$

where g_n is the new grid; g_1 and g_2 are accordingly grids calculated from C1 and C2 point clouds, i.e. a cell of output grid has an average height value of corresponding cell heights from input grids. New grid is then filtered with exponential filter with a size of 10 cells, after which a data point is extracted at every 62 m.

Exponential filter is chosen for the example as this gave the best results for 2018 ALS data filtering. As out of three filtering methods this is also the one most affected by anomalous cells, it is reasonable to test it out with resampling (to see how much data is affected by it). The results of the comparisons are in Tables 4.4 and 4.5 below.

Table 4.4 Comparison between two different methods of processing C1 and C2 ALS data together. All profiles are compared to FAMOS GOCO05s geoid model. All data is before removing deformations in grids.

Profile	Profile points	Method 1 ¹		Method 2 ²	
		StDev (m)	Amplitude (m)	StDev (m)	Amplitude (m)
10052018_084035	272	0,0058	0,0282	22,1993	336,6549
10052018_084640	356	0,0091	0,0355	51,0424	880,8796
10052018_085356	198	0,0095	0,0382	0,0576	0,5035
10052018_085829	937	0,0104	0,0545	1,6986	39,0096
10052018_092024	223	0,0072	0,0278	9,4802	129,4606
10052018_093037	664	0,0065	0,0338	0,0474	0,8654
10052018_094208	450	0,5114	7,8033	4,3897	92,2582

Notes: All data is from 5x5m grids. Filtering method is exponential filter with a size of 10 cells.

¹ Order of Method 1 is filtering C1 and C2 5x5m grids, extracting profile points from filtered grids and then calculating average value for each profile point.

² Order of Method 2 is resampling C2 grid into C1 grid system, calculating an average grid from the two, filtering the resulting grid and then extracting profile points.

Table 4.5 Comparison between two different methods of processing C1 and C2 ALS data together. All profiles are compared to FAMOS GOCO05s geoid model. All data is after removing deformations in grids.

Profile	Profile points	Method 1 ¹		Method 2 ²	
		StDev (m)	Amplitude (m)	StDev (m)	Amplitude (m)
10052018_084035	258	0,0060	0,0282	0,0060	0,0283
10052018_084640	291	0,0080	0,0322	0,0082	0,0319
10052018_085356	155	0,0067	0,0250	0,0067	0,0256
10052018_085829	916	0,0099	0,0497	0,0099	0,0501
10052018_092024	201	0,0071	0,0277	0,0071	0,0276
10052018_093037	636	0,0065	0,0338	0,0065	0,0338
10052018_094208	419	0,0117	0,0507	0,0117	0,0509

Notes: All data is from 5x5m grids. Filtering method is exponential filter with a size of 10 cells.

¹ Order of Method 1 is filtering C1 and C2 5x5m grids, extracting profile points from filtered grids and then calculating average value for each profile point.

² Order of Method 2 is resampling C2 grid into C1 grid system, calculating an average grid from the two, filtering the resulting grid and then extracting profile points.

As the results (Table 4.5) show, there is close to no statistical difference between the two methods. However, whereas the second method is faster and easier to automate, it also tends to deform data (compare Table 4.5 to Table 4.4). This is caused by resampling, which adds no-data value to cells where no grid previously existed. As no-data value is often defined by “-99999”, exponential filter considers that as a value, and thus deforms the output grid (Fig. 4.18). Also, as the filter is recursive, the deformation effect carries over to areas farther away (Fig. 4.19).

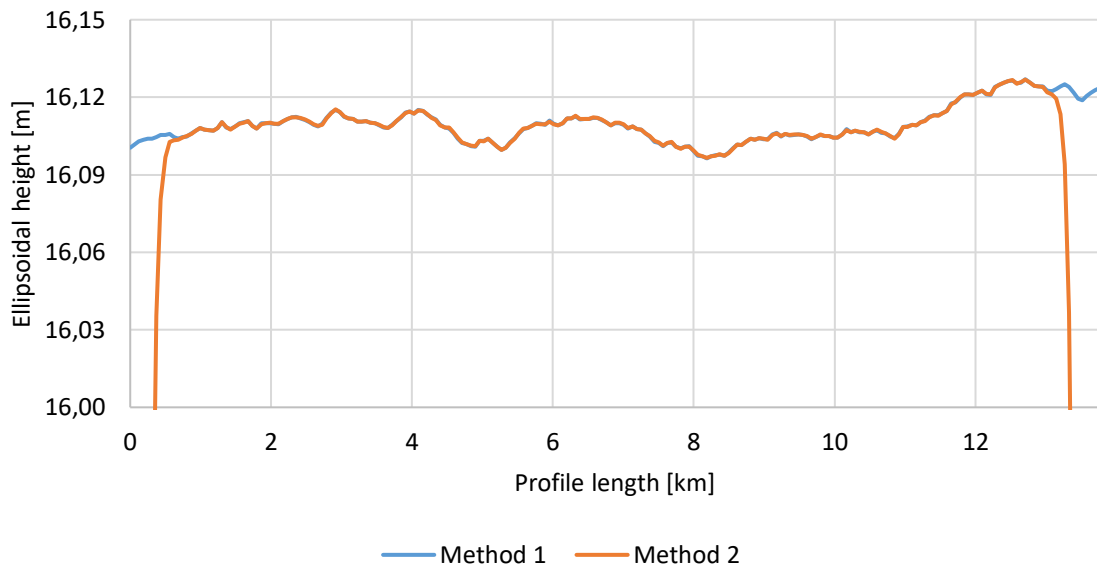


Figure 4.18 Profiles calculated from point cloud 10052018_092024. The figure shows that deformations exist at the ends of the profile, where no-data values appear in grids.

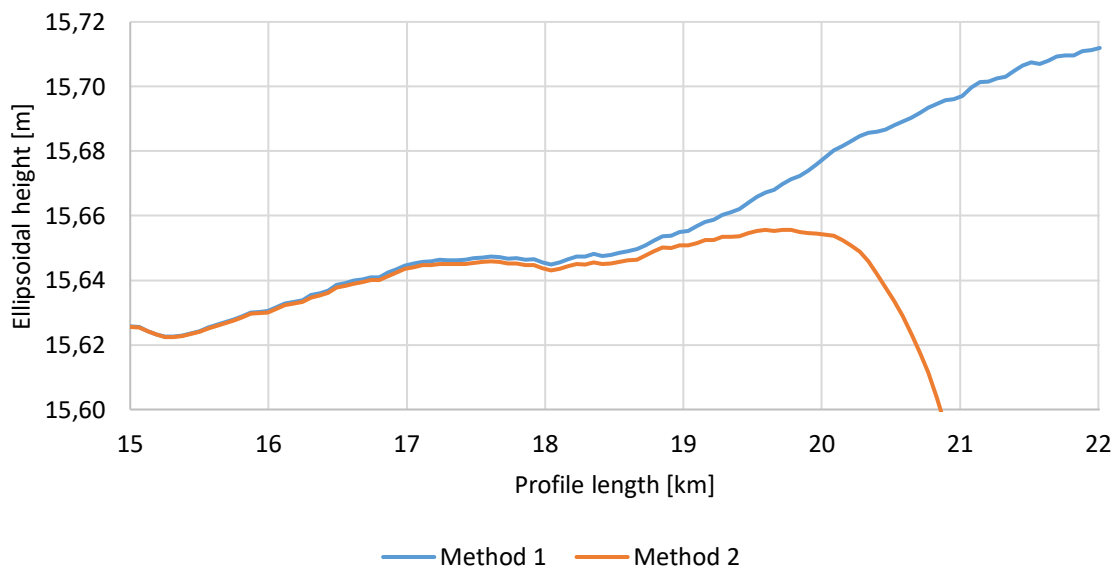


Figure 4.19 Profiles calculated from point cloud 10052018_084640. The figure shows that deformations can carry over to very large areas. Due to the nature of the exponential filter, the more a profile aligns with X or Y axis, the farther deformations carry over to.

Such deformations in grids could be avoided, if no-data values are defined as an average height of the input grid. However, this would make data processing longer (the benefit of the method is that it is faster). Using the double low-pass filter, instead of exponential one, will make it possible to avoid such deformations in output grids. Smaller size of exponential filter or use of averaging filter will reduce the area of deformations.

4.2.7 Dynamic topography correction for ALS profiles

From now on, correction from DT has been added to the filtered ALS profiles. The correction from DT consists of two components – HDM component from HBM-EST model and TG component. Note that the DT is calculated by using modified TGc method, briefly discussed in Subsection 3.2.4 – longitude as a variable has been added to the calculations (to test an alternative method, one reason being much smaller timespan). This can be done, as the northern coastline of Estonia follows roughly parallels (see also DT correction part in Section 1.3).

First, for every profile point (constructed from a point cloud), a time instant (decimal hour) is calculated:

$$i_n = i_{n-1} + \frac{i_L - i_F}{m-1} \quad (4.2)$$

where i_n is decimal hour for a profile point ($n = 1, 2, 3, \dots, m-2, m-1, m$), i_F time of the first measurement of a point cloud ($i_F = i_0$) and i_L time of the last measurement of the same point cloud ($i_L = i_m$). m is the total amount of profile points constructed from that point cloud (i_0 included, n is now $0, 1, 2, \dots, m-2, m-1, m$). Full hours (denoted by χ) are then subtracted from decimal hours.

HDM heights are extracted from the model at profile point locations (φ_n, λ_n) . As HDM data is available for every full hour, precise HDM heights must be interpolated (i_n is now a decimal part of a full hour):

$$HDM_n(\varphi_n, \lambda_n) = HDM_\chi(\varphi_n, \lambda_n) + [HDM_{\chi+1}(\varphi_n, \lambda_n) - HDM_\chi(\varphi_n, \lambda_n)] * i_n \quad (4.3)$$

where HDM_n is interpolated hydrodynamic model height at time-instance i_n . HMD_χ is the height at full hour.

Because HDM heights have an unknow DB, hourly TG station readings are used to remove it (Loksa, Kunda and Narva-Jõesuu TG stations are used – see Fig. 2.9). First, DB is calculated at the locations of two TG stations, which border the profile (only longitude is considered):

$$DB_{W,\chi} = HDM_{W,\chi} - TG_{W,\chi} \quad (4.4)$$

$$DB_{E,\chi} = HDM_{E,\chi} - TG_{E,\chi} \quad (4.5)$$

where HDM is DT from hydrodynamic model (the same as DT_{HDM} in Section 1.3) and TG tide gauge reading (the same as DT_{TG} in Section 1.3); both are full hour readings. Subscript W denotes TG station located west of the profile and E east of the profile. Note that if the profile extends outside from between two TG stations (according to longitude), parts of it are calculated separately.

For every height HDM_n , a correction is then calculated:

$$X1 = DB_{W,\chi} * (\lambda_E - \lambda_{i_n}) + DB_{E,\chi} * (\lambda_{i_n} - \lambda_W) \quad (4.6)$$

$$X2 = DB_{W,\chi+1} * (\lambda_E - \lambda_{i_n}) + DB_{E,\chi+1} * (\lambda_{i_n} - \lambda_W) \quad (4.7)$$

$$\xi_n = \frac{X1}{(\lambda_E - \lambda_W)} + \frac{X2 - X1}{(\lambda_E - \lambda_W)} * i_n \quad (4.8)$$

where ξ_n is the correction. λ_W is longitude of the western and λ_E of the eastern TG station. λ_{i_n} is longitude of the profile point for which's HDM height the correction is calculated for.

Finally, HDM heights are corrected:

$$DT_n(\varphi_n, \lambda_n) = HDM_n(\varphi_n, \lambda_n) - \xi_n \quad (4.9)$$

where DT is dynamic topography correction for filtered ALS profile point.

The difference between TGc method (discussed in Subsection 3.2.4) and this one is that the height gaps in computed DT data are eliminated (due to longitude being a variable). It is expected that the method would also improve shipborne GNSS assessment results, compared to the universal TGw method used for it (for reference compare TGc method results to TGw in Table 3.2). However, it is important to remember that the method can only be used if the coastline follows roughly parallels or meridians (Section 1.3) and has thus very limited use (compared to TGw method that can be used almost everywhere).

4.3 2013 ALS profiles compared to the geoid models

Double low-pass filtered profiles constructed from 50x50m grids (2013 ALS) with correction from DT are used to assess geoid models. However, due to area limitations of HBM-EST HDM, some profile points must be excluded from the comparison, as no DT correction can be calculated for them (there is no data close to the shore). The final amount of filtered and corrected profile points included in the model assessment is shown in Table 4.6.

Table 4.6 The amount of excluded profile points due to area limitations of HBM-EST HDM and profile points included in the geoid model assessment.

Profile	Filtered profile points	Excluded profile points	Profile points in the assessment
08052013_090408	377	9	368
14052013_090928	84	20	64
14052013_091945	246	3	243
14052013_092746	284	0	284
14052013_093645	1018	0	1018
14052013_095527	314	0	314
14052013_100143	320	4	316
14052013_101501	1375	0	1375
14052013_133440	1047	0	1047
14052013_135301	967	0	967
Σ	6032	36	5996

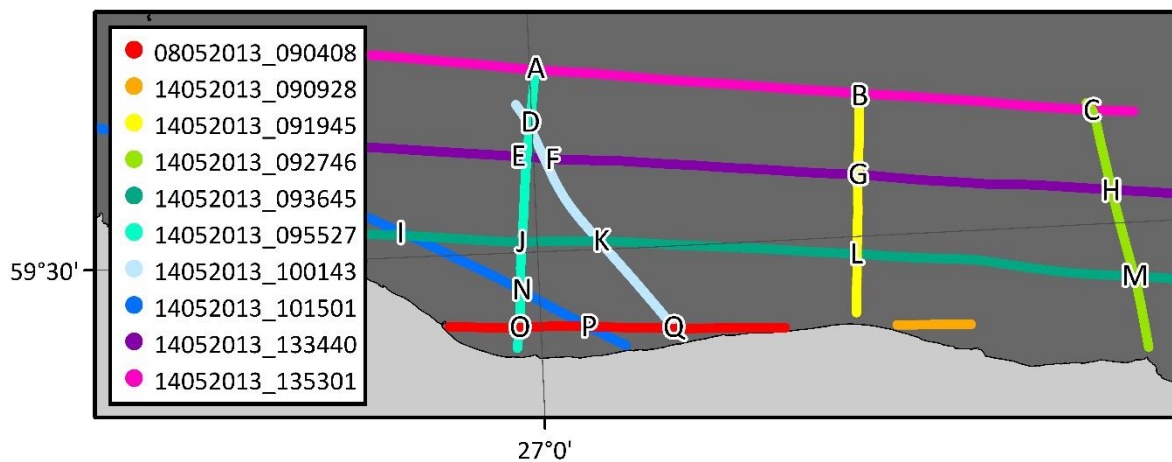


Figure 4.20 Intersections of 2013 ALS profiles denoted by letters in the figure.

Prior to assessment, the profiles were compared to each other at intersections (Fig. 4.20). EST-GEOID2017 was also added to the comparison (FAMOS GOCO05s is not suitable for this comparison, as it is a gravimetric geoid model). This revealed offsets in heights of profiles 14052013_095527 and 14052013_100143 (Fig. 4.21), which could be a trajectory or point cloud computation error. Profile 14052013_090928 cannot be checked as it does not cross with any other profile.

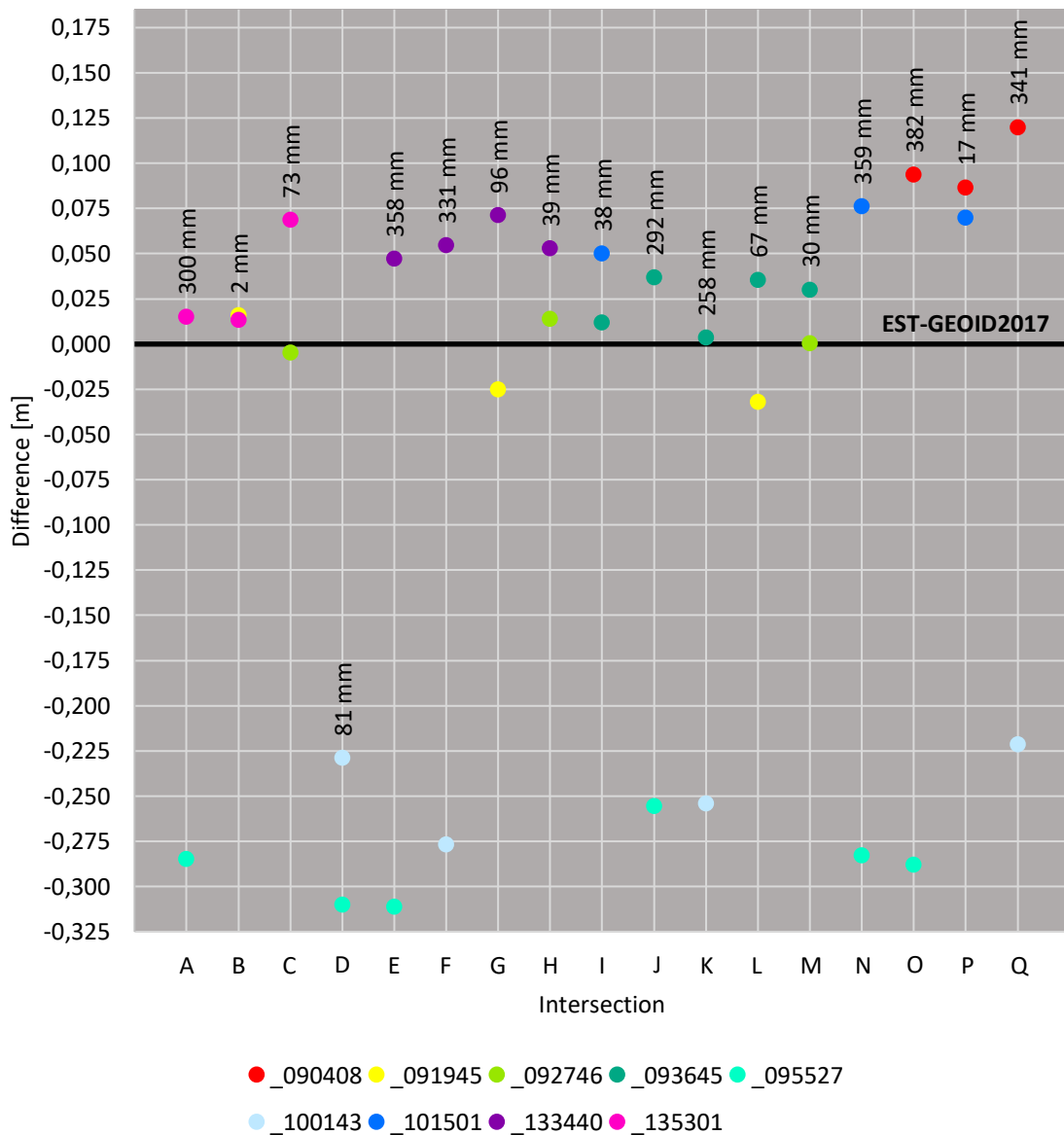


Figure 4.21 2013 ALS profile heights compared to EST-GEOID2017 at profile intersections (Fig. 4.20). Double low-pass filtered profiles constructed from 50x50m grids are compared. Correction from DT is added to the profiles before comparison. Numbers on the figure show height differences of profiles at intersections, units in mm.

Such errors in heights must be removed before assessment can be done. Thus differences between profiles were considered and the following one-dimensional offsets were calculated:

- 1) profile 14052013_095527 heights are raised $\frac{[300+358+292+359+382]}{5} = 338,2$ mm;
- 2) profile 14052013_100143 heights are raised $\frac{[331+258+341]}{3} = 310,0$ mm.

Alternatively, such data could be removed from the assessment.

Before geoid model assessment, a one-dimensional offset was also calculated for FAMOS GOCO05s geoid model, as this is a gravimetric geoid (the model is not fitted to a height system). The model was compared to EST-GEOID2017 and average difference between the models (along ALS profiles only – both 2013 and 2018 profiles were included) was used as an offset value. Thus, FAMOS GOCO05s model heights are lowered 0,5749 m. Therefore, first and foremost, geoid slope of FAMOS GOCO05s is evaluated.

To get the most accurate assessment results of geoid models, all 5996 profile points are included in the evaluation at the same time (see Table 4.6 for details of the profiles). Geoid model assessment results are presented in Table 4.7. Note that EST-GEOID2011 is assessed in BK77 height system, while EST-GEOID2017, NKG2015 and FAMOS GOCO05s are assessed in EH2000 height system (similarly to GNSS assessment) – see Section 2.2.

The results are rather unexpected. According to 2013 ALS assessment statistics, the best performing geoid model is EST-GEOID2011. However, Figures 4.22 and 4.23 indicate that there might be errors in near coast DT, i.e. approximately 10 cm errors in geoid models are not believable there (see near coast deviations in Figs. 4.22 and 4.23, longitude 27,0°-27,6°). Similarly, such large deviations are not likely westward from longitude 26,0°. An indicator of errors could also be that the DT correction does not improve assessment results (Table 4.7). These possible large scale errors affect the evaluation. Also, the average differences between geoid models and ALS profiles (see also distribution of deviations in Figs. 4.22 and 4.23) indicate a long-wavelength error, which could be caused by DT. The other possibility is that EST-GEOID2017, NKG2015 and FAMOS GOCO05s are lower than they are supposed to be in the area. In addition, the results are affected by inaccuracies in ALS data (Fig. 4.21 illustrates that).

Table 4.7 Statistics of differences between 2013 ALS profiles and geoid models (statistical values are of model deviations from the profiles). All 5996 profile points are compared at the same time. Profile heights have been subtracted from the model heights. Deviations are visualised in Figures 4.22 and 4.23.

Geoid model	Profile type	Average (m)	Min (m)	Max (m)	StDev (m)	RMSE (m)
EST-GEOID2011	(1)	-0,091	-0,216	0,006	0,041	0,100
	(2)	0,115	-0,124	0,257	0,069	0,134
	(3)	0,031	-0,105	0,140	0,043	0,053
EST-GEOID2017	(1)	-0,362	-0,459	-0,238	0,042	0,364
	(2)	-0,156	-0,366	-0,014	0,073	0,172
	(3)	-0,032	-0,143	0,126	0,045	0,055
NKG2015	(1)	-0,350	-0,473	-0,199	0,057	0,355
	(2)	-0,144	-0,381	0,053	0,081	0,166
	(3)	-0,021	-0,158	0,159	0,058	0,062
FAMOS GOCO05s	(1)	-0,360	-0,460	-0,234	0,041	0,363
	(2)	-0,154	-0,364	-0,015	0,073	0,171
	(3)	-0,031	-0,141	0,130	0,045	0,054

Notes: The final assessment results are highlighted in red.

Profiles (1) and (2) do not include height conversion between BK77 and EH2000 height systems.

Profiles: (1) – Double low-pass filtered profile, constructed from 50x50m grid.

(2) – Double low-pass filtered profile, constructed from 50x50m grid, with DT correction from HBM-EST HDM.

(3) – Double low-pass filtered profile, constructed from 50x50m grid, with DT correction from TG corrected HBM-EST HDM.

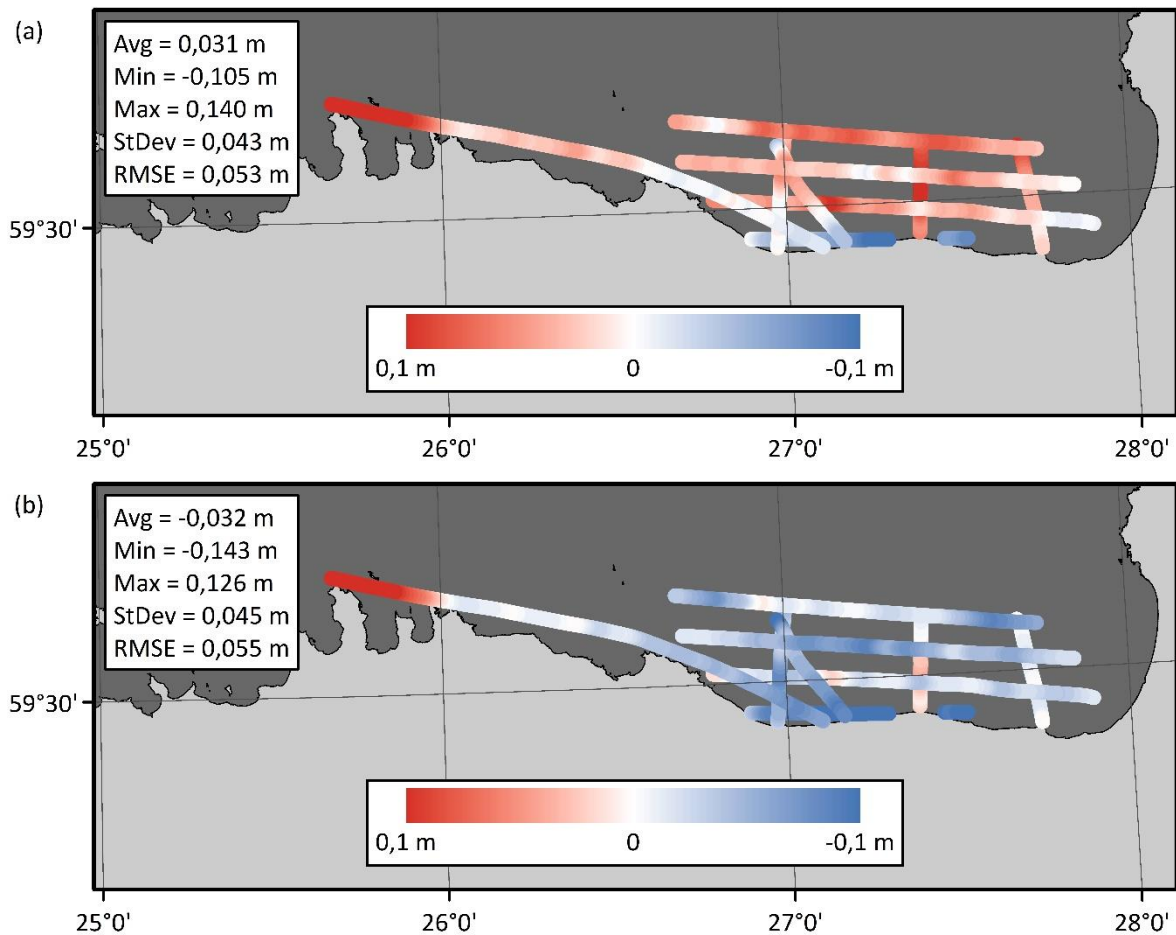


Figure 4.22 Comparisons of EST-GEOID2011 (a) and EST-GEOID2017 (b) deviations from the 2013 ALS profiles. Both models are compared to the double low-pass filtered profiles constructed from 50x50m grids, with correction from DT.

To get a better statistical representation of the geoid models' accuracies, the eastern half of profile 08052013_090408 (184 profile points), profile 14052013_090928 (64 profile points) and profile 14052013_101501 to the west from longitude 26,0° (298 profile points) were removed from the assessment. The updated results presented in Table 4.8 show significantly better StDev values (compare Table 4.8 to Table 4.7). Also, the TG corrected DT correction benefits the revised assessment. Now, according to StDev values, FAMOS GOCO05s and EST-GEOID2017 are the best fitting geoid models for the area. Accuracies of these models are correspondingly 2,9 and 3,0 cm (according to StDev). RMSE estimations are affected by the average differences between geoid models and ALS profiles – these results suggest that EST-GEOID2011 is superior to EST-GEOID2017.

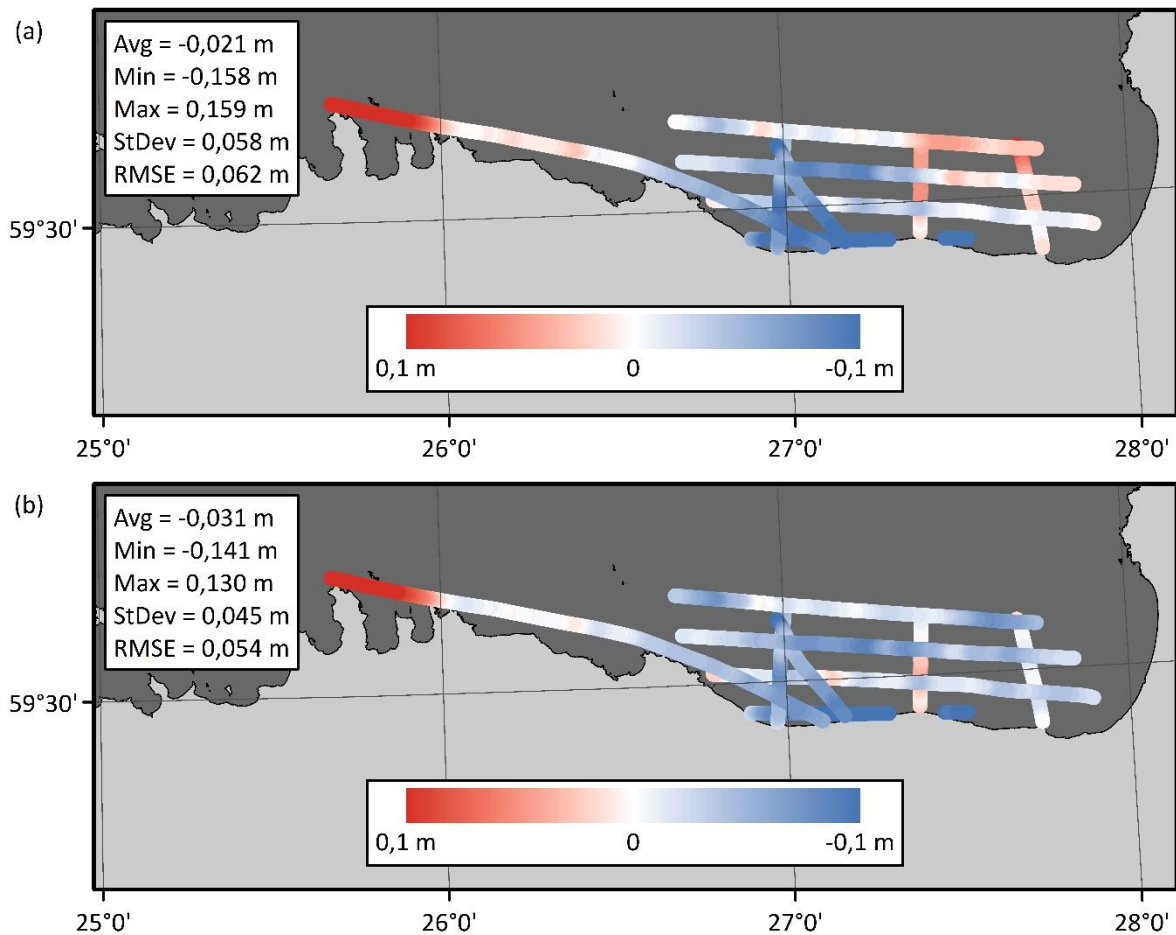


Figure 4.23 Comparisons of NKG2015 (a) and FAMOS GOCO05s (b) deviations from the 2013 ALS profiles. Both models are compared to the double low-pass filtered profiles constructed from 50x50m grids, with correction from DT.

According to the updated statistics (Table 4.8), geoid modelling has improved slightly thanks to the FAMOS2017 gravimetric data (see Subsection 2.1.1). However, it is difficult to confirm geoid modelling improvements visually. Yet one thing is certain (according to the assessment) – NKG2015 is the worst performing geoid model in the assessment area (both Table 4.7 and 4.8 suggest that).

Table 4.8 Statistics of differences between revised 2013 ALS profiles and geoid models (statistical values are of model deviations from the profiles). 5450 profile points are compared at the same time. Profile heights have been subtracted from the model heights.

Geoid model	Profile type	Average (m)	Min (m)	Max (m)	StDev (m)	RMSE (m)
EST-GEOID2011	(1)	-0,091	-0,169	0,005	0,032	0,096
	(2)	0,118	-0,070	0,257	0,057	0,131
	(3)	0,031	-0,051	0,112	0,032	0,045
EST-GEOID2017	(1)	-0,364	-0,459	-0,271	0,033	0,365
	(2)	-0,155	-0,331	-0,014	0,062	0,167
	(3)	-0,035	-0,125	0,045	0,030	0,046
NKG2015	(1)	-0,352	-0,462	-0,199	0,049	0,355
	(2)	-0,143	-0,351	0,053	0,069	0,159
	(3)	-0,023	-0,128	0,105	0,044	0,050
FAMOS GOCO05s	(1)	-0,362	-0,460	-0,272	0,032	0,364
	(2)	-0,154	-0,327	-0,015	0,061	0,166
	(3)	-0,034	-0,126	0,044	0,029	0,044

Notes: The final assessment results are highlighted in red.

Profiles (1) and (2) do not include height conversion between BK77 and EH2000 height systems.

Profiles: (1) – Double low-pass filtered profile, constructed from 50x50m grid.

(2) – Double low-pass filtered profile, constructed from 50x50m grid, with DT correction from HBM-EST HDM.

(3) – Double low-pass filtered profile, constructed from 50x50m grid, with DT correction from TG corrected HBM-EST HDM.

4.4 2018 ALS profiles compared to the geoid models

Exponentially (size 10 cells) filtered profiles constructed from 5x5m grids (2018 ALS) with correction from DT are used to assess geoid models. Similarly to 2013 ALS assessment, due to area limitations of HBM-EST HDM, some profile points must be excluded from the comparison, as no DT correction can be calculated for them (there is no data close to the shore). The final amount of filtered and corrected profile points included in the model assessment is shown in Table 4.9.

Table 4.9 The amount of excluded profile points due to area limitations of HBM-EST HDM and profile points included in the geoid model assessment. Note that previously excluded points (due to land coverage) are not included in the table (see Subsection 4.2.5).

Profile	Filtered profile points	Excluded profile points	Profile points in the assessment
10052018_084035	272	11	261
10052018_084640	356	0	356
10052018_085356	198	0	198
10052018_085829	937	6	931
10052018_092024	223	0	223
10052018_093037	664	0	664
10052018_094208	440	6	434
Σ	3090	23	3067

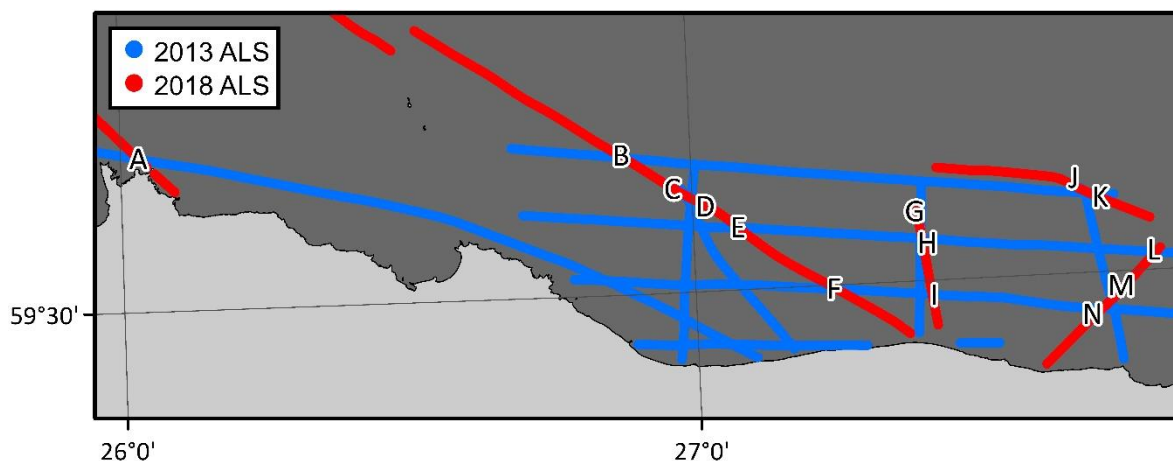


Figure 4.24 Intersections of 2013 and 2018 ALS profiles denoted by letters in the figure.

Prior to assessment, the 2018 ALS profiles were compared to the 2013 ALS profiles at their intersections (Fig. 4.24), as there are no crossings between 2018 profiles. EST-GEOID2017 was also

added to the comparison (FAMOS GOCO05s is not suitable for this comparison, as it is a gravimetric geoid model). Note that 2013 ALS profiles 14052013_095527 and 14052013_100143 had their heights raised 0,3382 and 0,3100 m correspondingly before the comparison (see previous Section 4.3 for reasoning). This affects correspondingly the crossings denoted by “D” and “C”.

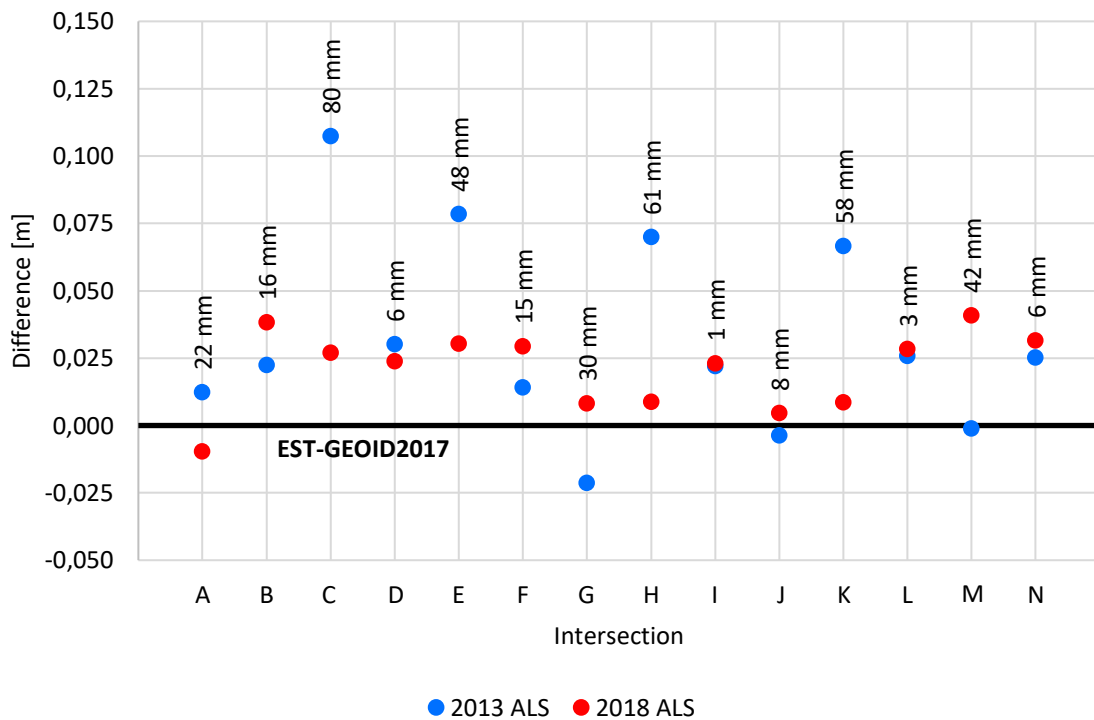


Figure 4.25 2013 and 2018 ALS profile heights compared to EST-GEOID2017 at their intersections (Fig. 4.24). Filtered profiles with correction from DT are compared. Numbers on the figure show height differences of profiles at intersections, units in mm.

From the comparison (Fig. 4.25) appears that 2018 ALS profiles coincide generally rather well with 2013 ALS profiles. However, it seems that 2018 ALS profiles are slightly more stable (i.e. there are less fluctuations between the profiles compared to 2013 ALS). Thus, the comparison suggests that there are either errors in 2013 DT or ALS data, which in turn affects the geoid model assessment results negatively, as discussed in Section 4.3.

Similarly to 2013 ALS assessment, FAMOS GOCO05s model heights are again lowered 0,5749 m. To get the most accurate assessment results of geoid models, all 3067 profile points are included in the evaluation at the same time. Note that EST-GEOID2011 is assessed in BK77 height system, while EST-GEOID2017, NKG2015 and FAMOS GOCO05s are assessed in EH2000 height system (similarly to previous assessments) – see Section 2.2.

Table 4.10 Statistics of differences between 2018 ALS profiles and geoid models (statistical values are of model deviations from the profiles). All 3067 profile points are compared at the same time. Profile heights have been subtracted from the model heights. Deviations are visualised in Figures 4.26 and 4.27.

Geoid model	Profile type	Average (m)	Min (m)	Max (m)	StDev (m)	RMSE (m)
EST-GEOID2011	(1)	0,298	0,212	0,394	0,047	0,301
	(2)	0,308	0,223	0,404	0,045	0,312
	(3)	0,063	-0,007	0,157	0,044	0,076
EST-GEOID2017	(1)	0,017	-0,041	0,079	0,033	0,037
	(2)	0,027	-0,024	0,086	0,028	0,039
	(3)	-0,005	-0,048	0,064	0,025	0,026
NKG2015	(1)	0,043	-0,044	0,139	0,049	0,065
	(2)	0,053	-0,031	0,155	0,047	0,071
	(3)	0,021	-0,057	0,123	0,043	0,048
FAMOS GOCO05s	(1)	0,015	-0,042	0,079	0,032	0,035
	(2)	0,026	-0,024	0,082	0,027	0,038
	(3)	-0,006	-0,047	0,047	0,023	0,024

Notes: The final assessment results are highlighted in red.

Profiles (1) and (2) do not include height conversion between BK77 and EH2000 height systems, which is why the average differences and RMSE values of EST-GEOID2011 are so large.

Profiles: (1) – Exponentially filtered (size 10 cells) profile.

(2) – Exponentially filtered (size 10 cells) profile with DT correction from HBM-EST HDM.

(3) – Exponentially filtered (size 10 cells) profile with DT correction from TG corrected HBM-EST HDM.

The assessment results in Table 4.10 confirm that the best fitting model in the Gulf of Finland is FAMOS GOCO05s with an accuracy of 2,3 cm, followed by EST-GEOID2017 with an accuracy of 2,5 cm (according to RMSE). Visualised deviations of the geoid models can be seen in Figures 4.26 and 4.27.

Comparisons between the results of profile types (1) and (2) show clearly that the use of HDM has great impact to the assessment (Table 4.10). However, as the average values of profiles (2) show, there tends to be a bias within the model. The use of TG stations eliminates that bias and further improves DT values – compare the results of profiles (2) to profiles (3).

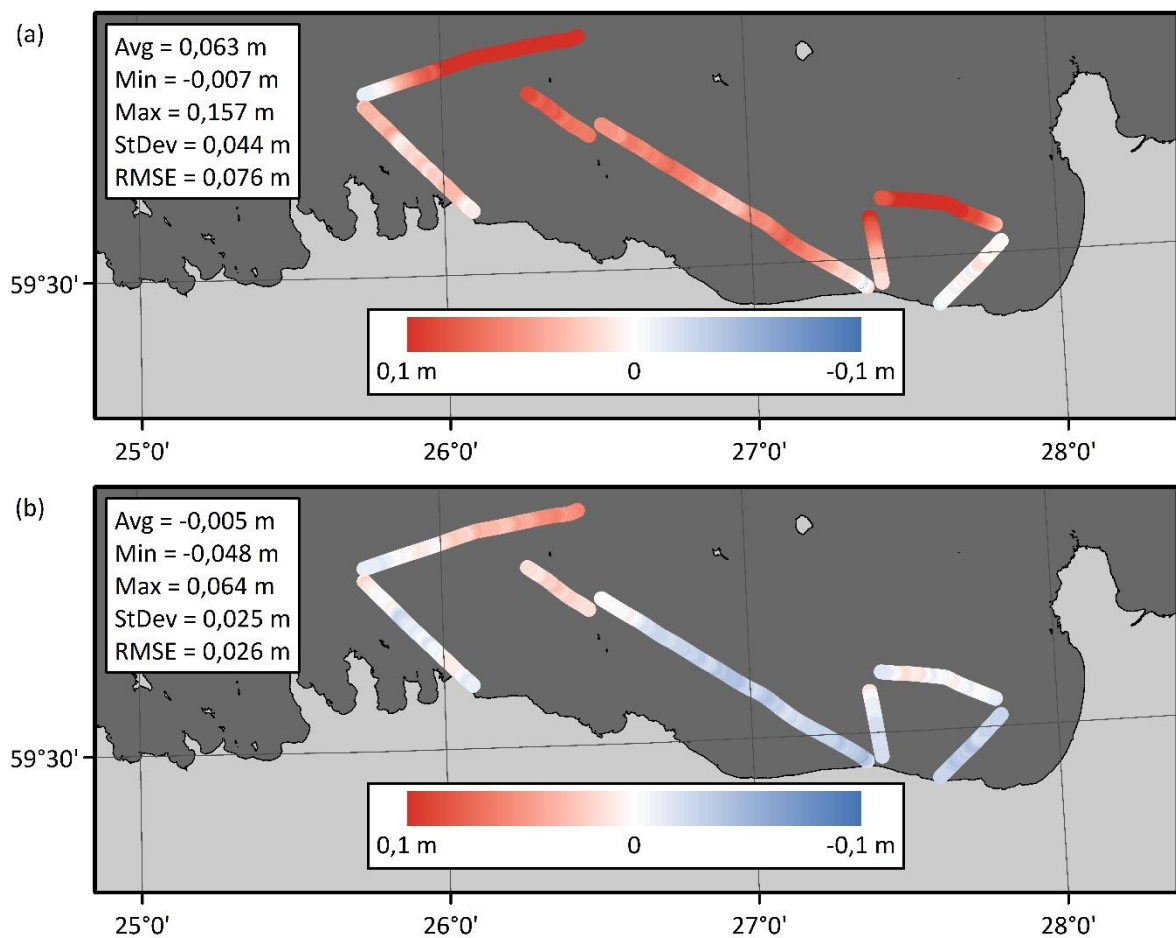


Figure 4.26 Comparisons of EST-GEOID2011 (a) and EST-GEOID2017 (b) deviations from the 2018 ALS profiles. Both models are compared to the exponentially filtered (size 10 cells) profiles with correction from DT.

What appears as an offset in EST-GEOID2011 heights (results show that by average the model is 6,3 cm higher than ALS profiles) are actually large errors in the model (over 10 cm). Such errors appear in areas where previously (before FAMOS2017 campaign) existed gravimetric data voids, e.g. areas

near Vaindloo island and in Narva Bay (Fig. 4.26a). As seen from the figure, coastal areas of the model coincide very well with ALS profiles. However, deviations grow larger farther away at sea.

Comparing EST-GEOID2017 results to EST-GEOID2011, significant improvements in geoid modelling can be seen, especially in the aforementioned areas. However, coastal areas of Narva Bay and vicinity of longitude 27° appear to be slightly lower than the profiles are (Fig. 4.26b). 2013 ALS profiles suggested that too, however on a much larger scale (the difference between profiles and geoid models was over 5 cm, see Fig. 4.22b).

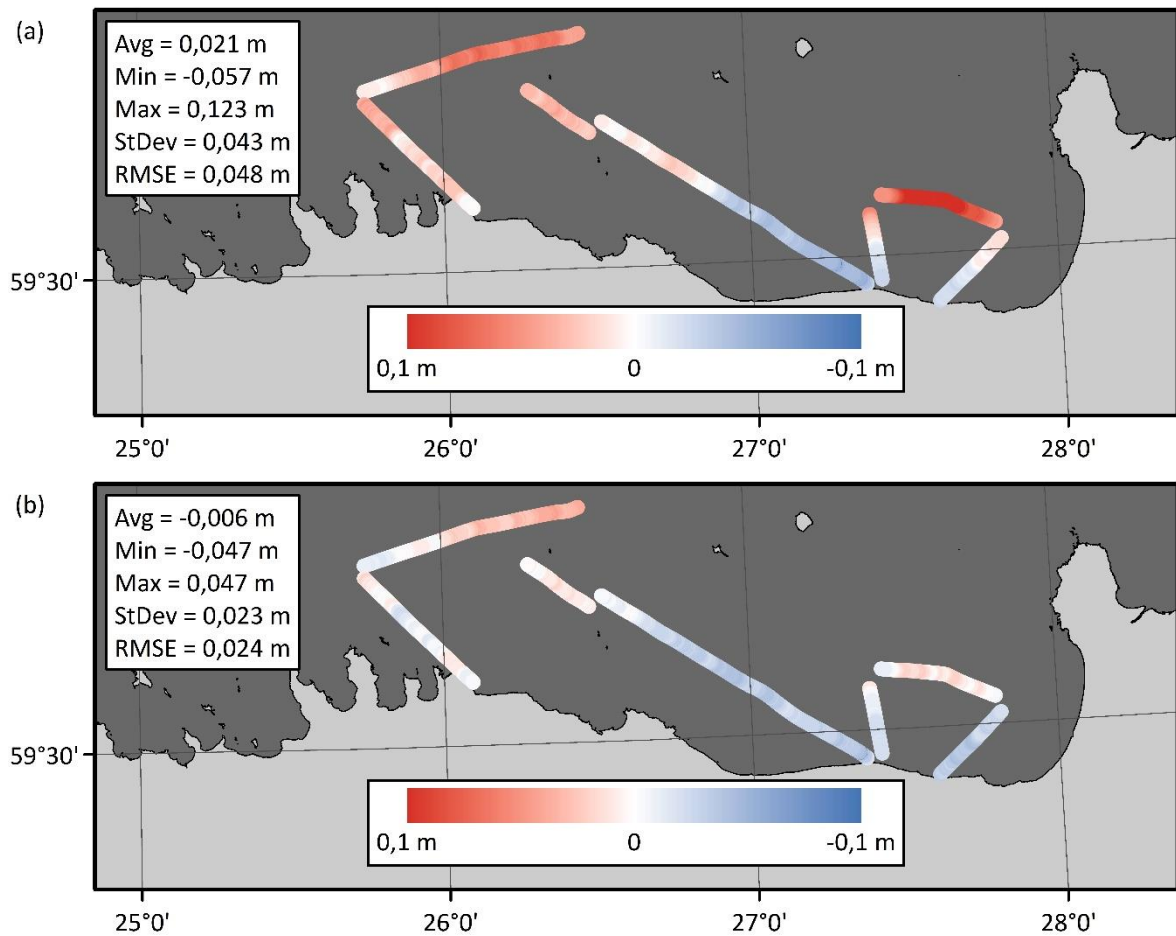


Figure 4.27 Comparisons of NKG2015 (a) and FAMOS GOCO05s (b) deviations from the 2018 ALS profiles. Both models are compared to the exponentially filtered (size 10 cells) profiles with correction from DT.

Comparison between the assessment results of NKG2015 and EST-GEOID2011 (Table 4.10; Figs. 4.26a and 4.27a; both models are computed without new gravimetric data) shows that NKG2015 performs slightly better. However, NKG2015 seems to fit worse near coastal areas.

Comparing FAMOS GOCO05s (Fig. 4.27b) to EST-GEOID2017 (both have FAMOS2017 gravimetric data included), shows that geoid modelling has further improved near Vaindloo island (FAMOS GOCO05s is newer model than EST-GEOID2017, the difference being a different gravity gridding method – see Table 2.1) – compare Figures 4.26b and 4.27b.

Although FAMOS GOCO05s is the best fitting model according to the statistics, comparison between profile 10052018_084640 (see Fig. 4.5) deviations from EST-GEOID2017 and FAMOS GOCO05s shows that the bulge in Narva Bay (Fig. 2.8) exists in FAMOS GOCO05s model surface (the profile is located on the edge of that bulging area). Such large difference in geoid models is caused by different correlation lengths in gravity anomaly gridding (discussed in Subsection 2.1.2).

4.5 Cross sections of 2018 ALS grids

As previously mentioned, the data corridor of 2018 ALS is generally between 1000 and 1200 m wide. Therefore, it can be assumed that information about sea surface is well recorded not only in the direction of flight, but also in the perpendicular direction. Thus, this data could be used for 3D assessment, e.g. grid to grid comparison.

To control such assumption, three cross sections were constructed from each point cloud's C2 grid. First cross section is located on the 1/10, second in the middle and third on the 9/10 of the grid. 10052018_094208 is an exception – third cross section is located on the 8/10 of the grid, as the end part of it is too close to the shore. Exponential filter with a size of 10 cells and averaging filter with a Kernel radius of 10 cells are tested. Locations of the cross sections can be seen in Figure 4.28 (numbers grow in the direction of flight) and all profiles are presented in Appendix E (all figures are drawn facing the direction of flight).

As seen in Appendix E Figures E.1 to E.21, the edges of the data corridor curve upward, typically around 10-15 cm (or more in some places) compared to the middle section. This systematic error in measurements is the so-called SMILE effect caused by over-reporting of scanner mirror angles, i.e. a scanner scale error (Parrish 2011). Such error can be eliminated or at least reduced by calibration. More details about the scale error can be read in Morin (2002).

The scale error is also the likely reason why exponential filter with a size of 15 cells performs worse than a filter of size 10 (see Table 4.3) – the curving up affects middle section (see Figs. 4.16 and 4.17 for an analogy).

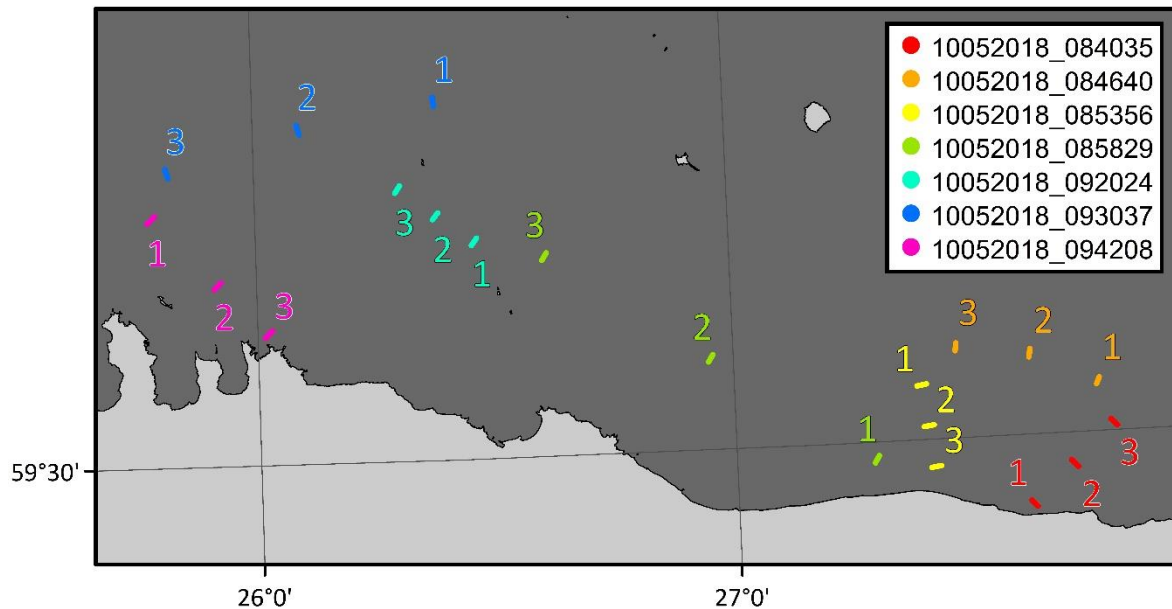


Figure 4.28 Locations of the cross sections. Numbers grow in the direction of flight. Cross section profiles are presented in Appendix E (all figures are drawn facing the direction of flight).

However, in the middle of data corridor tends to be a 200-300 m wide, relatively flat surface, which could be used for model assessment purposes. Therefore, slopes of these areas are further investigated. For the purpose, 200 m wide sections are selected (100 m mark is approximately at plane’s nadir). No DT correction is calculated as the slope of DT from HDM is typically much smaller compared to geoid’s. Therefore, for brevity’s sake it is expected that DT correction does not affect the assessment greatly (not enough to change tendencies). The results are presented in Table 4.11.

Investigation of figures in Appendix E and results in Table 4.11 show that there tends to be some correlation between the slopes of the FAMOS GOCO05s geoid model and computed cross sections (generally stronger correlation with exponential filter solution indicates that it is superior to averaging filter solution). However, there are also areas with strong negative correlation (i.e. the slope of geoid is inclined opposite to a cross section) or areas without any correlation. It is expected that the results would improve slightly when using DT correction.

Table 4.11 Comparisons between the slopes of FAMOS GOCO05s geoid model and filtered 5x5m C2 grids. For the locations of the cross sections, see Figure 4.28. Cross section numbers grow in the direction of flight. Profiles of listed cross sections are presented in Appendix E (all figures are drawn facing the direction of flight).

Profile	Cross section	FAMOS GOCO05s slope	Slope of 5x5m grid; Averaging filter (radius 10)	Slope of 5x5m grid; Exponential filter (size 10)	Correlation between FAMOS GOCO05s and averaging filter solution	Correlation between FAMOS GOCO05s and exponential filter solution
10052018_084035	1	0,0135	0,0161	-0,0016	0,6444	-0,3597
	2	0,0132	0,0280	-0,0060	0,4320	-0,2588
	3	0,0127	-0,0174	-0,0079	-0,4887	-0,4812
10052018_084640	1	-0,0214	-0,0018	0,0052	0,1349	-0,7160
	2	-0,0207	0,0082	-0,0089	-0,5094	0,7632
	3	-0,0206	-0,0169	-0,0232	0,4309	0,8235
10052018_085356	1	0,0122	-0,0338	-0,0270	-0,7306	-0,8876
	2	0,0109	-0,0538	-0,0465	-0,9221	-0,9854
	3	0,0104	-0,0127	-0,0165	-0,5462	-0,9312
10052018_085829	1	-0,0231	-0,0423	-0,0416	0,9092	0,9843
	2	-0,0225	-0,0287	-0,0525	0,6925	0,9722
	3	-0,0231	-0,0516	-0,0436	0,8047	0,9347

Continuation of Table 4.11

Profile	Cross section	FAMOS GOCO05s slope	Slope of 5x5m grid; Averaging filter (radius 10)	Slope of 5x5m grid; Exponential filter (size 10)	Correlation between FAMOS GOCO05s and averaging filter solution	Correlation between FAMOS GOCO05s and exponential filter solution
10052018_092024	1	-0,0218	-0,0606	-0,0468	0,8904	0,9926
	2	-0,0196	-0,0437	-0,0442	0,7468	0,9845
	3	-0,0203	-0,0623	-0,0367	0,9032	0,9721
10052018_093037	1	-0,0130	-0,0323	-0,0517	0,6940	0,9804
	2	-0,0078	-0,0353	-0,0675	0,5628	0,9942
	3	-0,0028	-0,0512	-0,0717	0,8583	0,9828
10052018_094208	1	0,0126	-0,0644	-0,0660	-0,7331	-0,9772
	2	0,0171	-0,0714	-0,0762	-0,7777	-0,9780
	3	0,0189	-0,0590	-0,0523	-0,8326	-0,9902

Notes: Correlation coefficients exceeding 0,8 are highlighted in red. Correlation coefficients exceeding -0,8 are highlighted in blue.

Nevertheless, the results more likely confirm that grid to grid assessment is possible. Middle parts (at least 200 m wide) of computed grids (from point clouds) can be used directly in the assessment, alternatively to extracting profiles out of these (the method used in the current study).

The areas with negative correlation may indicate to errors in geoid model (errors in ALS data are also likely). For example, in the FAMOS GOCO05s geoid model, there is a slight depression between 10052018_084035 and 10052018_085356 point clouds (for reference, see Fig. 4.28). However, cross sections of said area seem to indicate that:

- a) depression is wider in actual geoid or more to the west;
- b) there is no depression.

Another area where differences are seen is the coast around longitude 26°. FAMOS GOCO05s shows that slope is towards sea. However, computed ALS grids indicate a slope to the opposite direction.

4.6 Using 2018 ALS profiles to validate hydrodynamic models

According to all assessments (GNSS, 2013 ALS and 2018 ALS), the most accurate geoid model in the Gulf of Finland is FAMOS GOCO05s (the model is fitted to EH2000 height system as in Sections 4.3 and 4.4). Thus, for the assessment of HDM-s, the model is chosen as a reference surface (note that the assessment tendencies are the same, regardless of the chosen geoid model). ALS profiles used in the assessment are extracted from exponentially filtered (size 10 cells) 5x5m grids.

By subtracting geoid model heights from ALS profile heights, ALS derived DT can be obtained. This data is then compared to HDM model derived DT, which allows the assessment of HDM-s.

The two HDM-s under investigation are HBM-EST and CMEMS (see Section 2.2 for more details). As the resolutions of the models are different, CMEMS was first resampled into HBM-EST grid system (resolution of CMEMS is approximately 1 nm, while the resolution of HBM-EST is 0,5 nm). The results of the assessment are presented in Table 4.12.

The amount of used profile points is slightly different, as the extents of the models are different. CMEMS HDM does not extend as close to the shore, as HBM-EST does. Therefore, less data and thus less profile points are available for CMEMS assessment.

Table 4.12 HDM assessment results. All profile points are compared at the same time. Statistics are of ALS derived DT compared to HDM derived DT (former has been subtracted from the latter). An example of differences between the models is shown in Figure 2.11.

HDM	Profile type	Profile points	Average (m)	Min (m)	Max (m)	StDev (m)	RMSE (m)
HBM-EST	(1)	3067	0,026	-0,024	0,082	0,027	0,038
	(2)		-0,006	-0,047	0,047	0,023	0,024
CMEMS	(1)	2997	0,079	0,028	0,143	0,031	0,085
	(2)		-0,010	-0,052	0,041	0,023	0,025

Notes: The most important assessment results (that should be compared) are highlighted in red.

Profiles: (1) – ALS derived DT compared to HDM derived DT.

(2) – ALS derived DT compared to TG corrected HDM derived DT (Subsection 4.2.7 explains TG correction used for this comparison).

As seen from the results, HBM-EST is more accurate according to 2018 ALS profiles. However, it is important to note that the timespan of the assessment is slightly over an hour. For definitive answer of which of the two models is more accurate, the timespan should be at least several months (if not a year or more).

From the comparison becomes evident also the importance of TG correction – before correction, the results differ more than they do after introducing the TG correction (Table 4.12, Figs. 4.29 and 4.30). What is interesting, however, is that near shore HBM-EST and CMEMS models coincide with ALS better before TG correction (compare Fig. 4.29 to Fig. 4.30 at 08:42 and 08:57). However, this could just be a coincidence, as the data from 09:49 is close to the shore too.

Comparison between Figures 4.29 and 4.30 suggests that the assessed models are more accurate than the results presented in e.g. Table 4.10. It seems that a large portion of the error is caused by DT. Thus, the method for DT calculation has an utmost importance to geoid model assessment results.

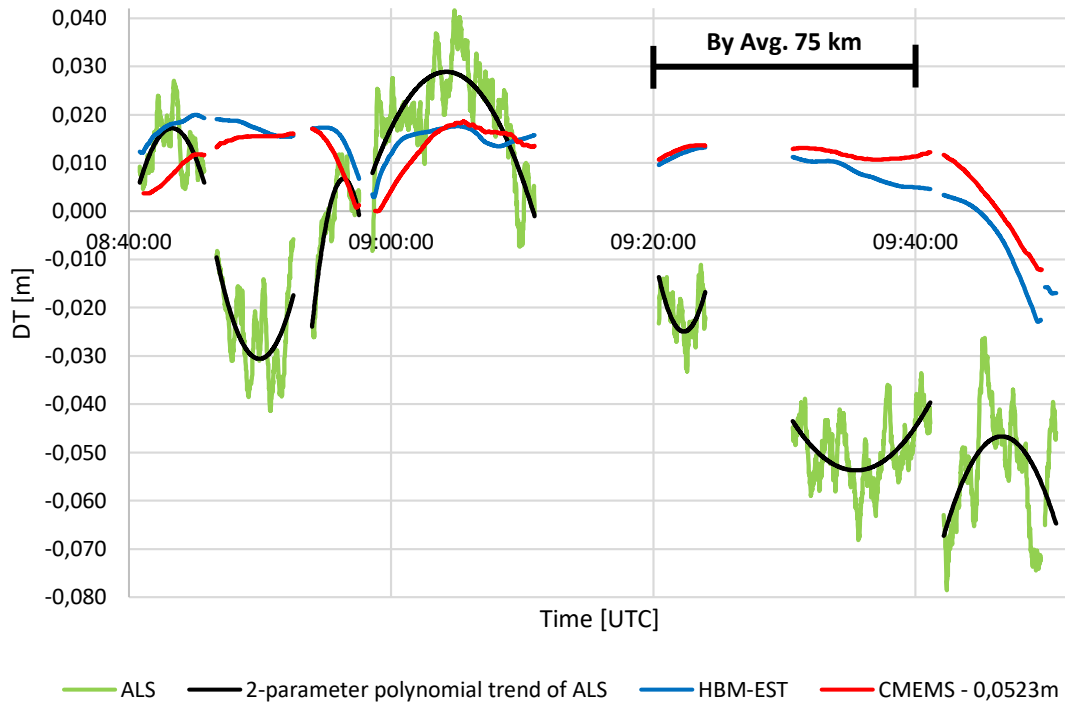


Figure 4.29 DT from HBM-EST and CMEMS HDM-s compared to ALS derived DT. For comparisons sake, CMEMS has been lowered 0,0523 m.

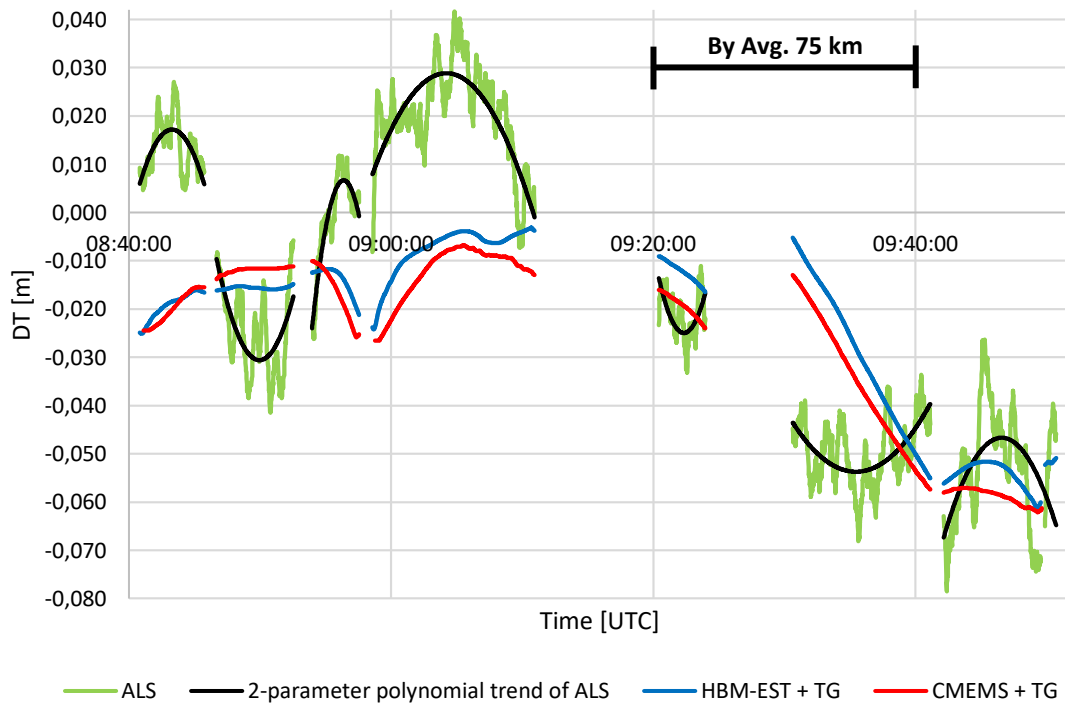


Figure 4.30 TG corrected DT from HBM-EST and CMEMS HDM-s compared to ALS derived DT (TG correction is explained in Subsection 4.2.7).

5 SHIPBORNE GNSS AND ALS PROFILES TOGETHER

The final Combined GNSS profile with corrections from DT and fuel consumption and both 2013 (final profiles without the eastern half of profile 08052013_090408, profile 14052013_090928 and profile 14052013_101501 to the west from longitude 26,0°) and 2018 ALS profiles with correction from DT are compared to the geoid models together. Shipborne GNSS and 2013 ALS profiles are double low-pass filtered; 2018 ALS profiles are exponentially filtered (size of the filter is 10 cells).

Before assessment, shipborne GNSS profiles were fitted according to 2018 ALS profiles (2018 ALS seems to perform better than 2013 ALS – see Sections 4.3 and 4.4). The average difference between profiles at crossings is 6689 mm (Fig. 5.1). Recall that this is the reference point’s (vessel’s) separation from geoid/MSL. This value is subtracted as a constant from every combined GNSS profile point height. Also, a one-dimensional offset was calculated for FAMOS GOCO05s geoid model (similarly to previous ALS assessments). The model was compared to EST-GEOID2017 and average difference between the models (along Combined GNSS, 2013 and 2018 ALS profiles) was used as an offset value. Thus, FAMOS GOCO05s model heights are lowered 0,5771 m.

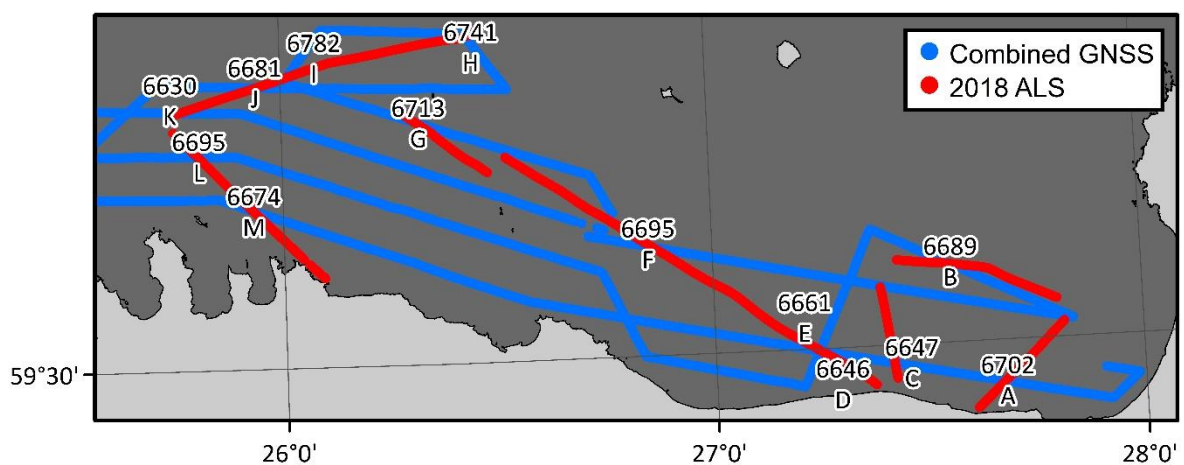


Figure 5.1 Differences of heights between crossings of combined GNSS and 2018 ALS profiles, units in mm (average difference is 6689 mm). Letters in the figure denote the intersections. GNSS profile is double low-pass filtered with corrections from DT and fuel consumption. ALS profiles are exponentially filtered (filter size is 10 cells) with DT correction. ALS profile heights are subtracted from GNSS profile heights.

After removing the difference of 6689 mm from Combined GNSS heights, the profile was compared to the 2018 ALS profiles at their intersections (Fig. 5.1). EST-GEOID2017 was also added to the comparison. It appears that the Combined GNSS profile coincides generally rather well with 2018 ALS profiles (Fig. 5.2) with some exceptions farther from the coast (e.g. intersections “I” and “H”).

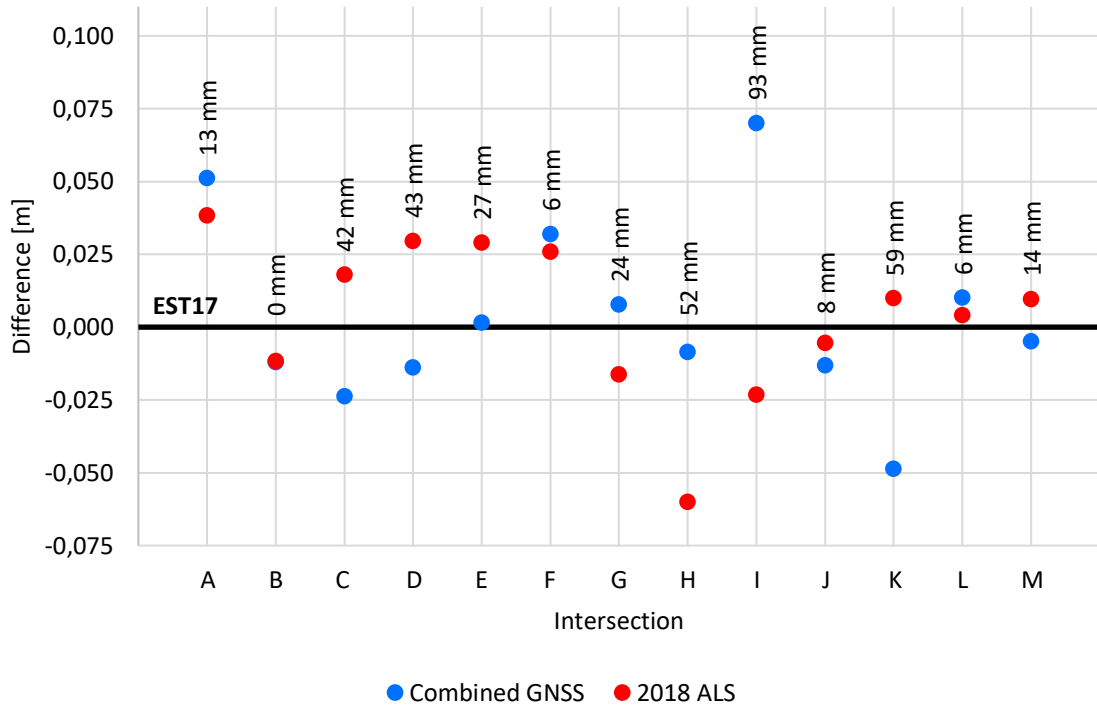


Figure 5.2 Combined GNSS (after removing average difference 6689 mm) and 2018 ALS profile heights compared to EST-GEOID2017 (abbreviated to EST17) at their intersections (Fig. 5.1). GNSS profile is double low-pass filtered with corrections from DT and fuel consumption. ALS profiles are exponentially filtered (filter size is 10 cells) with DT correction. Numbers on the figure show height differences of profiles at intersections, units in mm.

In the model evaluation, all 26942 profile points are included at the same time. Note that EST-GEOID2011 is assessed in BK77 height system, while EST-GEOID2017, NKG2015 and FAMOS GOCO05s are assessed in EH2000 height system (similarly to all previous assessments) – see Section 2.2. The results are presented in Table 5.1 and Figures 5.3 to 5.6.

Table 5.1 Geoid model assessment results (statistical values are of model deviations from the profiles). 26942 profile points are compared at the same time (combined GNSS, 2013 ALS and 2018 ALS, all with previously described corrections). Profile heights have been subtracted from the model heights. Deviations are visualised in Figures 5.3 and 5.4.

Geoid model	Average (m)	Min (m)	Max (m)	StDev (m)	RMSE (m)
EST-GEOID2011	0,043	-0,075	0,168	0,040	0,059
EST-GEOID2017	0,003	-0,125	0,075	0,034	0,0346
NKG2015	0,025	-0,128	0,134	0,045	0,052
FAMOS GOCO05s	0,003	-0,128	0,078	0,035	0,0347

According to the statistics presented in Table 5.1, the best performing geoid models are EST-GEOID2017 and FAMOS GOCO05s, the former being slightly better.

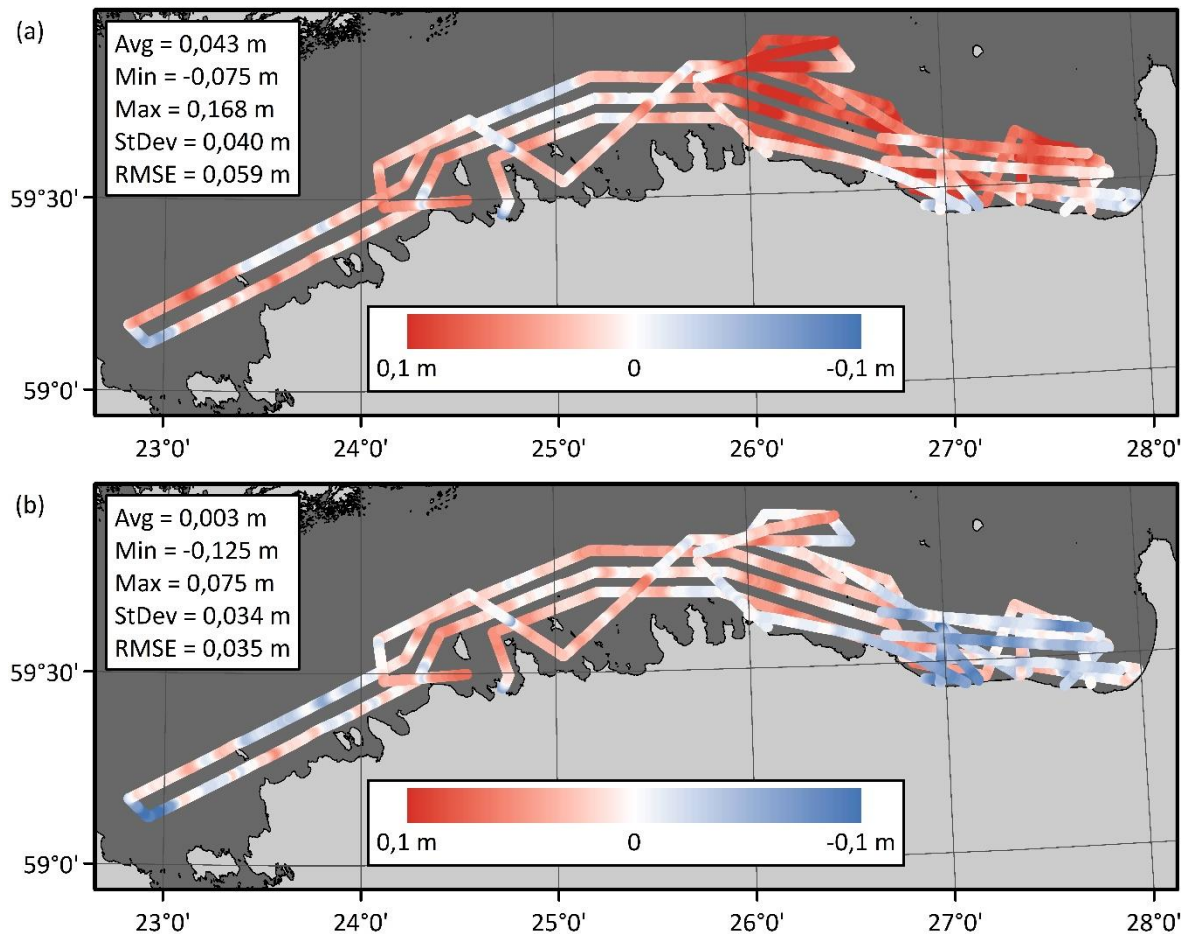


Figure 5.3 Comparisons of EST-GEOID2011 (a) and EST-GEOID2017 (b) deviations from all the profiles (combined GNSS, 2013 ALS and 2018 ALS) with corrections.

Comparison between Figures 3.17 and 5.3, 3.18 and 5.4 shows that in the initial shipborne GNSS assessment (Section 3.3), one-dimensional offsets were excluded from the assessments within the removed average differences. Thus, deviations presented in Figures 5.3 and 5.4 seem to represent geoid model errors more accurately. For example, EST-GEOID2011 deviations presented in Figure 5.3a correlate with the surface in Figure 2.6 more than the ones presented in Figure 3.17a (EST-GEOID2017 is considered as the reference surface in Fig. 2.6). The same can be said about NKG2015 geoid model (Figs. 2.7, 3.18a and 5.4a correspondingly). Therefore, if model deviations (i.e. errors) are to be visualised as accurately as possible, it is important to derive absolute MSL not relative as is done in shipborne GNSS assessment.

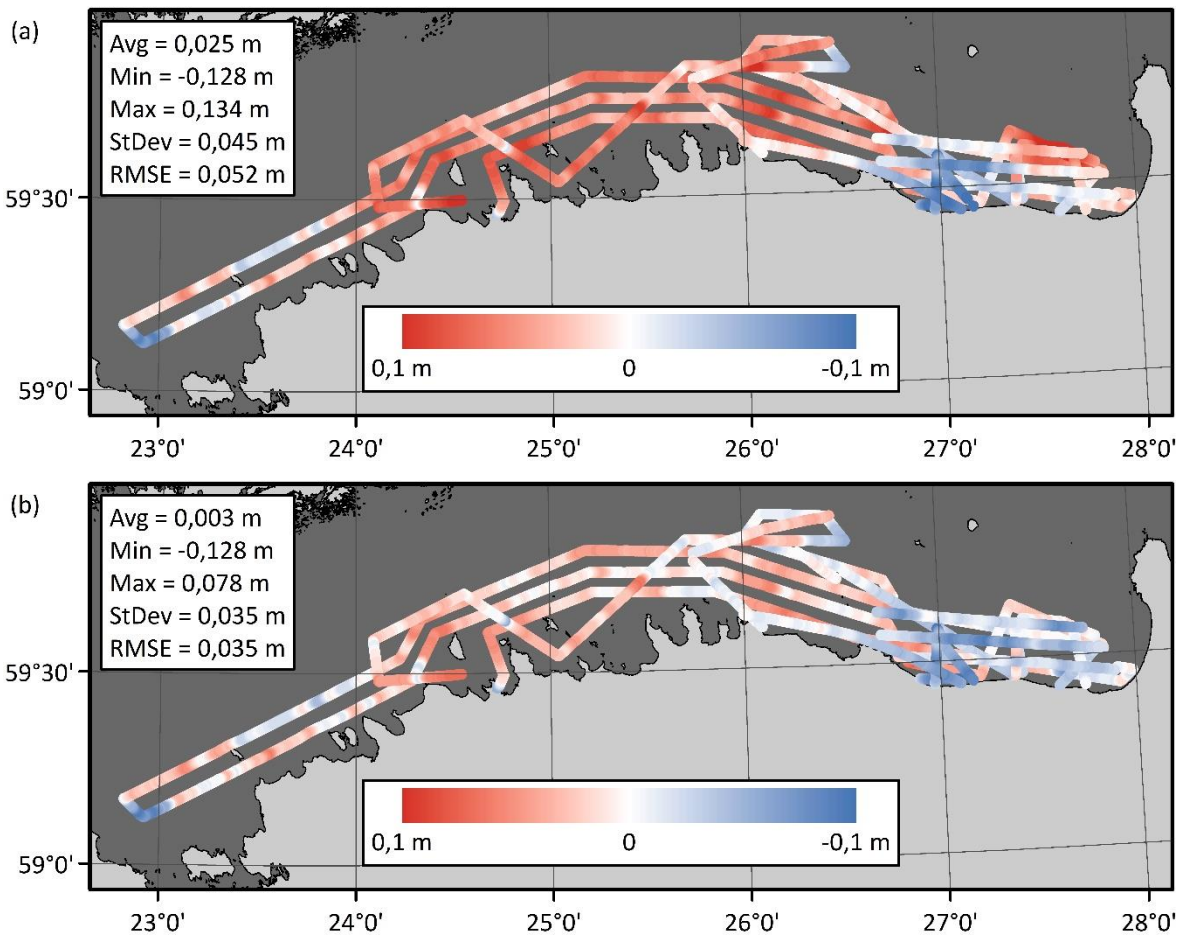


Figure 5.4 Comparisons of NKG2015 (a) and FAMOS GOCO05s (b) deviations from all the profiles (combined GNSS, 2013 ALS and 2018 ALS) with corrections.

From deviations presented in Figures 5.3 and 5.4, surfaces were generated by gridding with IDW interpolation method (see Subsection 4.2.1). Only the eastern side of the Gulf of Finland is considered, as data there are denser than to the west. The resulting grids can be seen in Figures 5.5 and 5.6. Such gridding reveals a long-wavelength error (Figs. 5.5b and 5.6b), which could be caused by errors in DT instead of errors in geoid model's themselves (2013 ALS contributes most to this; see also the discussion in Section 4.3). Note that the scales in the Figures 5.5 and 5.6 differ.

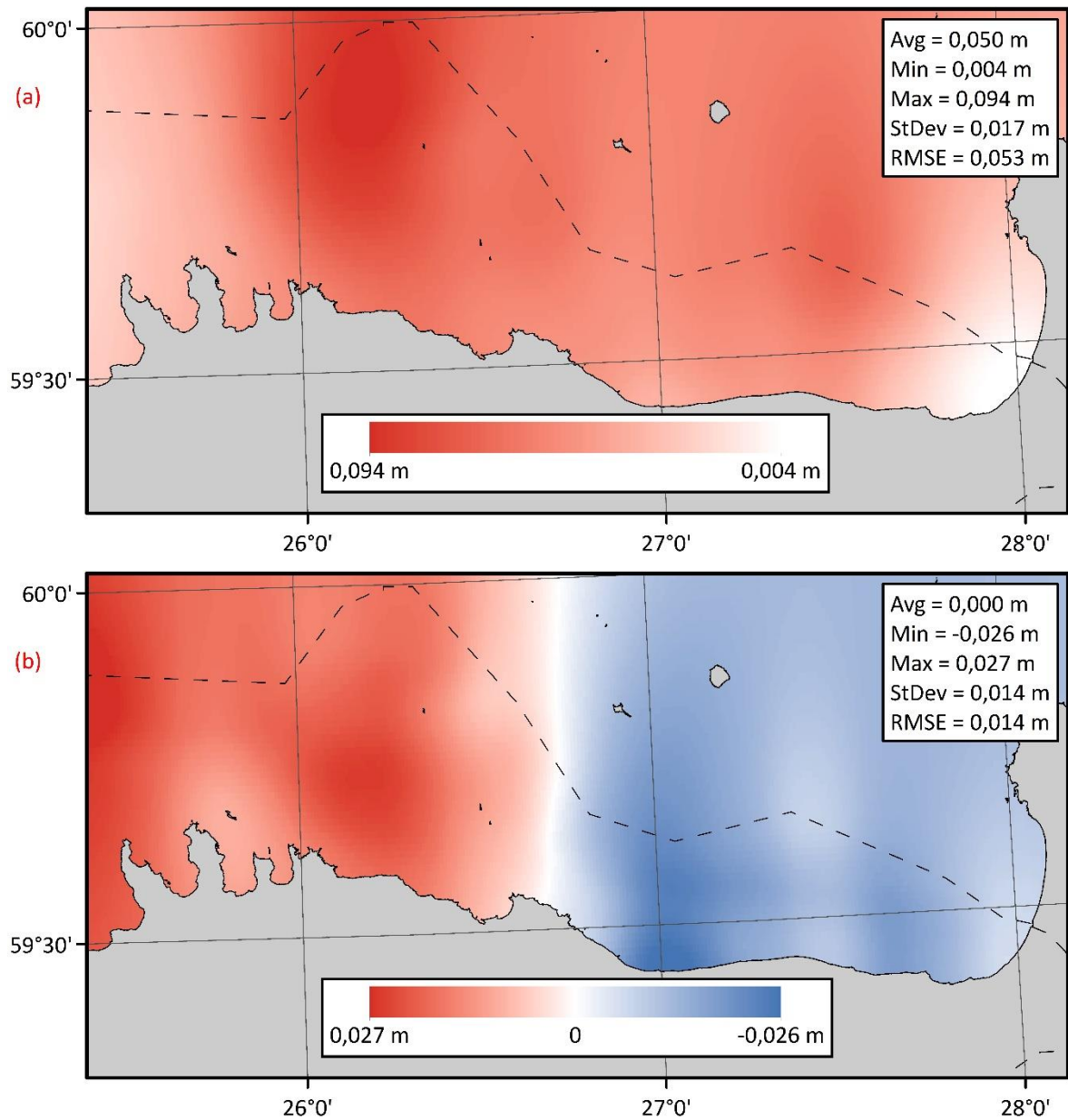


Figure 5.5 Comparisons of EST-GEOID2011 (a) and EST-GEOID2017 (b) deviations (Fig. 5.3) as a gridded surface in the eastern side of the Gulf of Finland (all profiles are included). The dashed black line depicts Estonian border.

Similarly to previously mentioned comparisons, surface in Figure 5.5a correlates with the one in Figure 2.6 and surface in Figure 5.6a correlates with the one in Figure 2.7. Such correlation also shows the improvements in geoid modelling and better fit of EST-GEOID2017 (to which EST-GEOID2011 and NKG2015 are compared to in Figs. 2.6 and 2.7; EST-GEOID2017 is considered as a reference surface in the example).

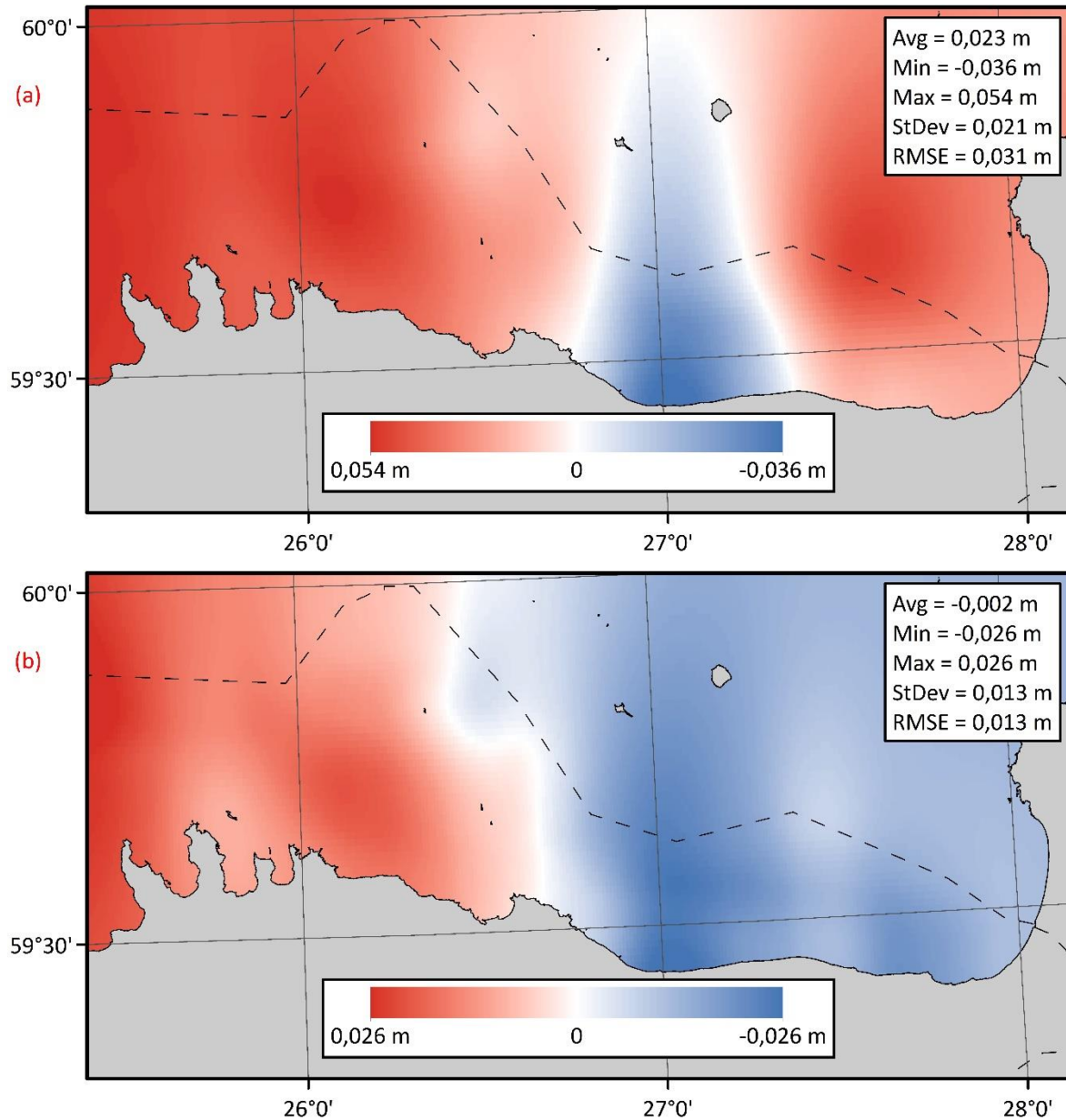


Figure 5.6 Comparisons of NKG2015 (a) and FAMOS GOCO05s (b) deviations (Fig. 5.4) as a gridded surface in the eastern side of the Gulf of Finland (all profiles are included). The dashed black line depicts Estonian border.

A slight bulge can be determined in both EST-GEOID2017 (Fig. 5.5b) and FAMOS GOCO05s (Fig 5.6b) model surfaces in the eastern side of the Narva Bay (whitish areas near Estonian border, longitude 27,5°). However, the bulge is slightly more apparent in FAMOS GOCO05s surface (approximately 2 mm). This suggests that the large difference between the models seen in Figure 2.8 (a bulge in the Narva Bay) is indeed in the surface of FAMOS GOCO05s geoid model. Regardless, according to the assessment, EST-GEOID2017 too seems to be locally higher in the area than the actual geoid itself.

For the sake of argument, a comparison is also done without 2013 ALS profiles, i.e. shipborne GNSS and 2018 ALS profiles are compared to the geoid models together. The results are presented in Table 5.2.

Table 5.2 Geoid model assessment results (statistical values are of model deviations from the profiles). 21492 profile points are compared at the same time (combined GNSS and 2018 ALS with previously described corrections). Profile heights have been subtracted from the model heights.

Geoid model	Average (m)	Min (m)	Max (m)	StDev (m)	RMSE (m)
EST-GEOID2011	0,046	-0,075	0,168	0,041	0,062
EST-GEOID2017	0,013	-0,113	0,075	0,0284	0,0311
NKG2015	0,037	-0,094	0,134	0,036	0,052
FAMOS GOCO05s	0,013	-0,096	0,077	0,0283	0,0310

Interestingly, EST-GEOID2011 accuracy according to the assessment worsens, however accuracies of other three geoid models increase (compare Table 5.2 to Table 5.1). The deviations (seen in Figs. 5.3 and 5.4) were also gridded (with IDW interpolation method) without including 2013 ALS data. Gridding results can be seen in Figures 5.7 and 5.8. Note that the scales in the Figures 5.7 and 5.8 differ.

From these comparisons the previously present long-wavelength error (see Figs. 5.5b and 5.6b) is gone. This suggests that the 2013 ALS profiles are indeed greatly affected by errors, e.g. in DT as discussed in Section 4.3.

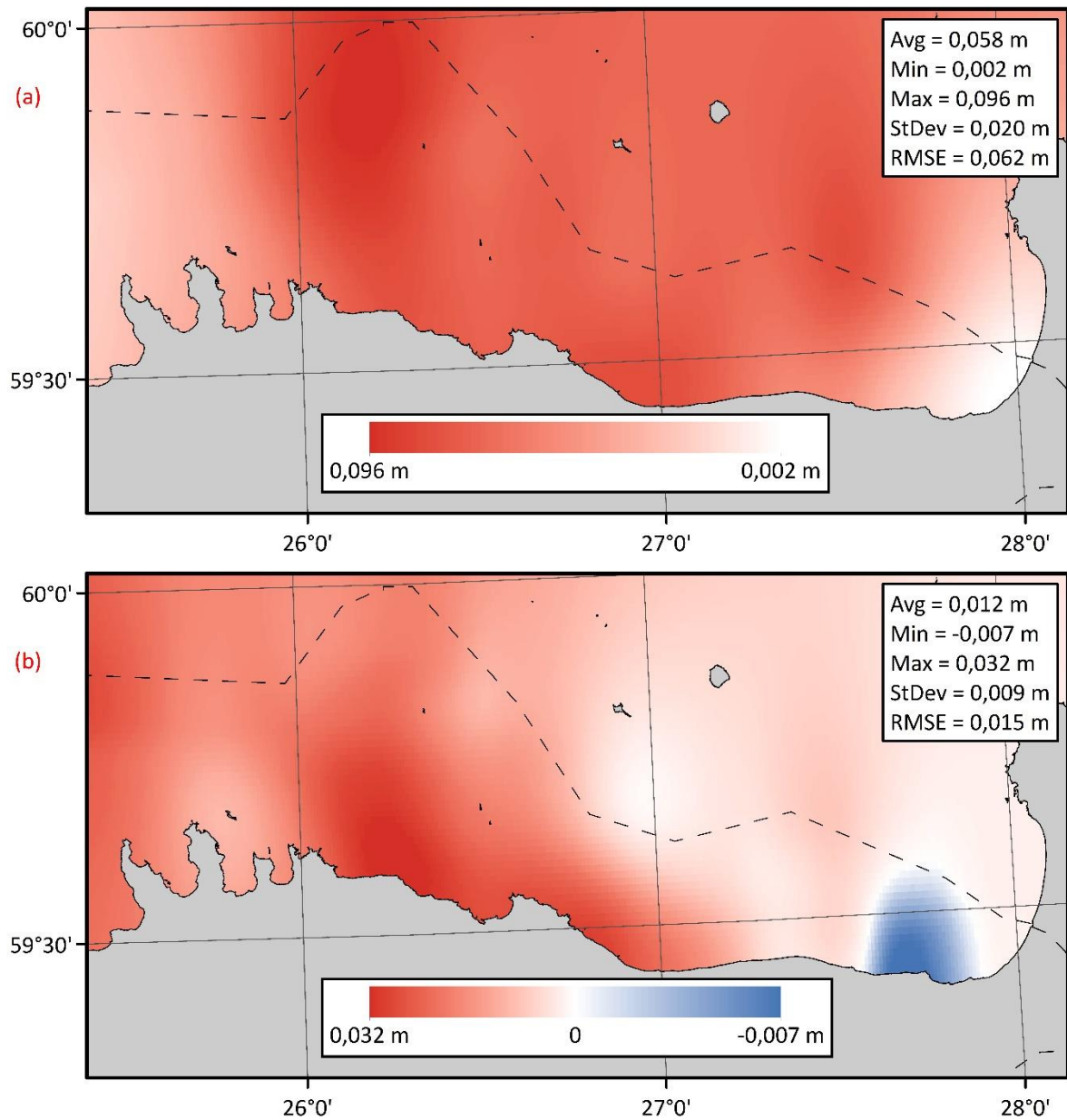


Figure 5.7 Comparisons of EST-GEOID2011 (a) and EST-GEOID2017 (b) deviations (from combined GNSS and 2018 ALS profiles) as a gridded surface in the eastern side of the Gulf of Finland. The dashed black line depicts Estonian border.

Surface in Figure 5.7a correlates with the one in Figure 2.6 more than the surface in Figure 5.5a. Similarly, surface in Figure 5.8a correlates with the one in Figure 2.7 more than the surface in Figure 5.6a. This is another indicator that 2013 ALS profiles have either internal errors or the DT correction is insufficient.

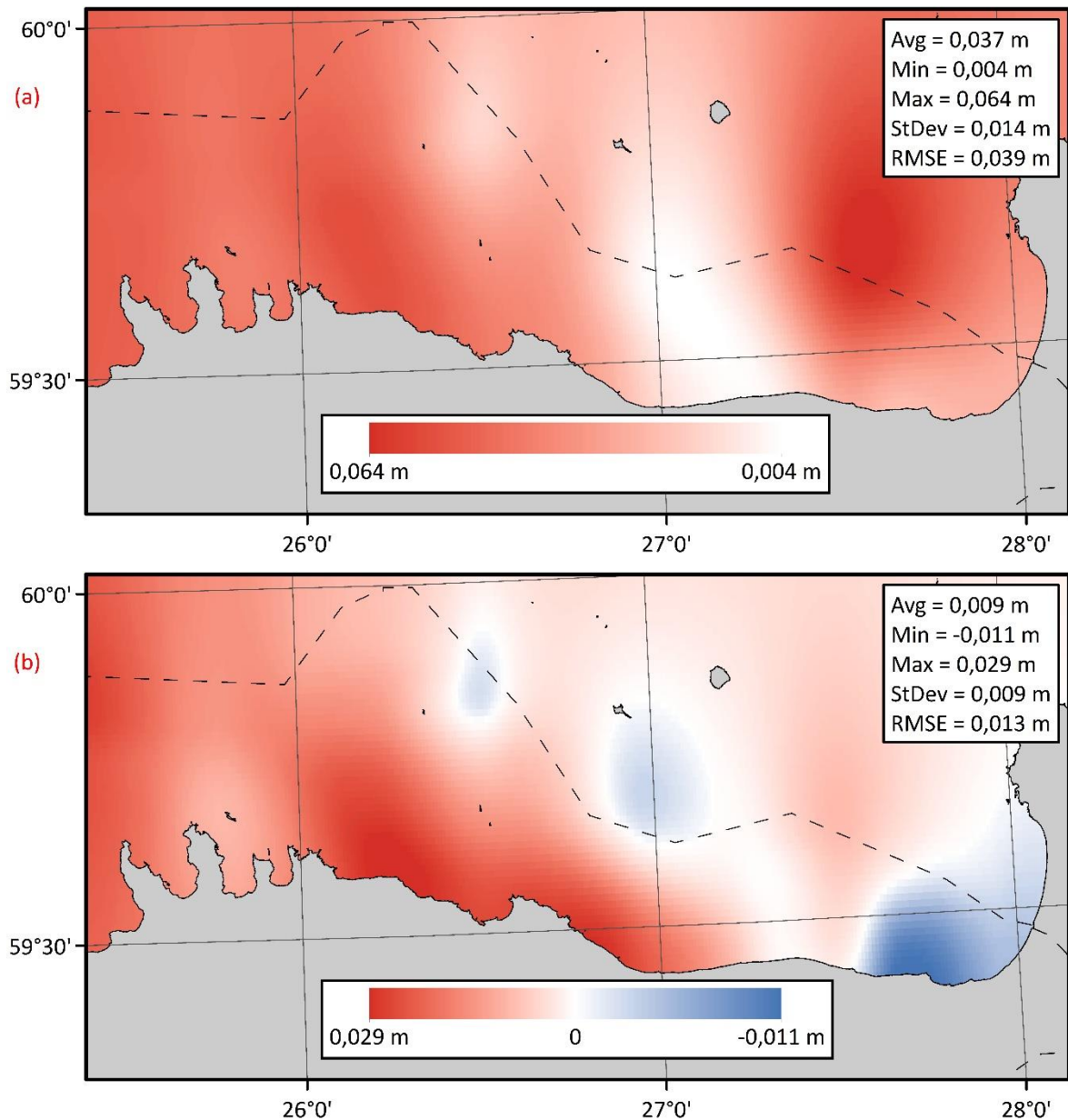


Figure 5.8 Comparisons of NKG2015 (a) and FAMOS GOCO05s (b) deviations (from combined GNSS and 2018 ALS profiles) as a gridded surface in the eastern side of the Gulf of Finland. The dashed black line depicts Estonian border.

Gridded surfaces with and without deviations from 2013 ALS profiles were compared too. 2013 ALS data contribution to the assessments (according to the differences between gridded surfaces) is presented in Table 5.3 for each individual geoid model evaluation. An example of contribution to EST-GEOID2017 assessment can be seen in Figure 5.9. All other comparisons (EST-GEOID2011, NKG2015 and FAMOS GOCO05s) are visually very similar, however differ slightly statistically as seen in Table 5.3.

Table 5.3 2013 ALS data contribution in each geoid model assessment. Gridded surface without 2013 ALS data has been subtracted from the surface with said data.

Geoid model	Average (m)	Min (m)	Max (m)	StDev (m)	RMSE (m)
EST-GEOID2011	-0,008	-0,044	0,003	0,009	0,012
EST-GEOID2017	-0,012	-0,048	0,000	0,010	0,015
NKG2015	-0,014	-0,051	0,000	0,011	0,017
FAMOS GOCO05s	-0,012	-0,046	0,000	0,009	0,015

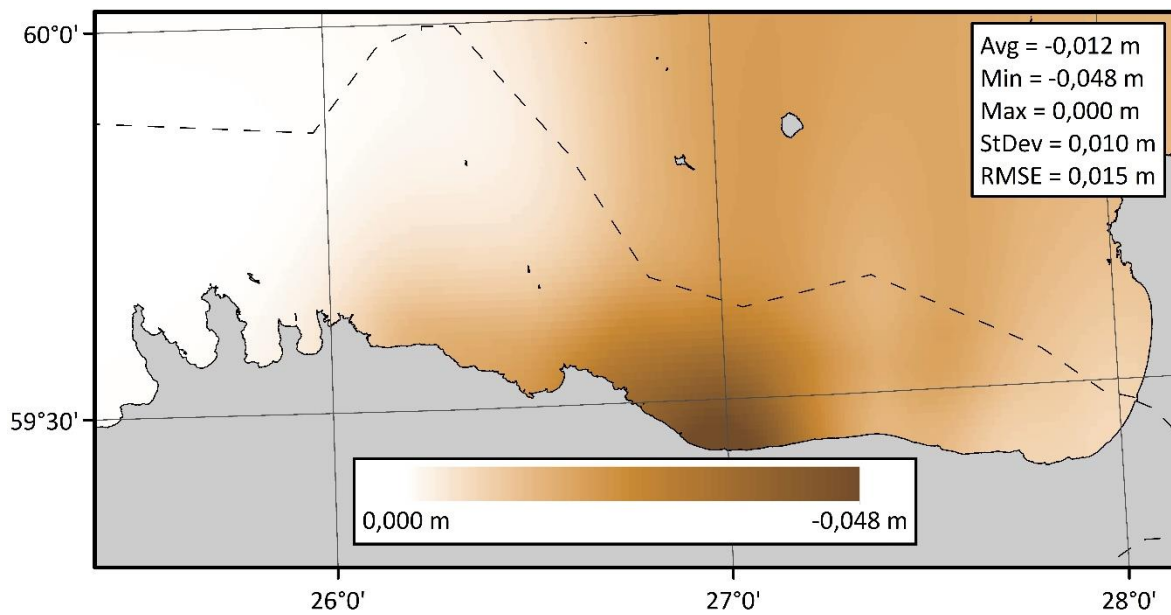


Figure 5.9 2013 ALS profiles contribution to EST-GEOID2017 assessment (according to the gridded surfaces). The dashed black line depicts Estonian border.

These comparisons show that the least affected by 2013 ALS profiles was the EST-GEOID2011 assessment. NKG2015 on the other hand was affected the most.

SUMMARY

Shipborne GNSS (Global Navigation Satellite System) and airborne laser scanning (ALS) profiles were used as an external verification for validating the accuracies of geoid models. The models were assessed in the Gulf of Finland, where new gravity data gathered during FAMOS2017 shipborne gravity and GNSS campaign, carried out on board of the Estonian Maritime Administration survey vessel “MS Sektori” between 03.07.2017 and 06.07.2017, had largest effect to geoid modelling. GNSS data gathered during the campaign was used in the current study for assessment purposes.

Two different commercial software were tested for post-processing kinematic GNSS data-series: Trimble Business Centre™ v4.00 and NovAtel Inertial Explorer™ v8.60. It was found that the GNSS post-processing results of these two software differ generally 2-3 cm. Thus, the choice of software has a large impact to the assessment results. In order to minimize such an effect, a Combined GNSS solution was calculated after data filtering.

Filtering the post-processed GNSS data-series is important for eliminating, or at the very least reducing, sea surface oscillations (i.e. waves). Shipborne GNSS profiles, however, are also affected by vessel’s own attitude. Both influence the assessment results and thus must be taken account for.

The current study used three sets of GNSS devices. Two antennas were attached to the ship’s opposite railings at bow – one to the port and the other to the starboard. Third one was attached to the ship’s railing on top of the captain’s quarters. The Combined GNSS height time-series from three devices were rigorously referred to the location of vessel’s mass center. The calculation has utmost effect on rough sea measurements, reducing effects of pitch and roll. Such method replaces the need for estimating vessel’s attitude corrections, e.g. the use of inertial measurement unit (IMU), thus simplifying also post-processing.

A double low-pass filter was applied to the GNSS data time-series referred to the vessel’s mass center. The filter consists of a moving median and a moving average. The median within the filter reduces sea surface oscillations and short-term changes in squat. The average then smoothens out the outcome, resulting in a geoid-like profile that can be used in model assessment.

For marine geoid validation, the dynamic topography (DT) that separates instantaneous sea surface heights (iSSH) from geoid/MSL needs to be accounted for. The HBM-EST (Estonian implementation of the HIROMB-BOOS model) hydrodynamic model (HDM) in conjunction with readings from 7 tide gauge (TG) stations on the northern coast of Estonia were used. These were Dirhami, Paldiski, Pirita, Rohuneeme, Loksa, Kunda and Narva-Jõesuu TG stations.

TG station readings are necessary as a modelled sea level has always a dynamic bias (DB) relative to a geodetic reference system, which varies from location to location and changes slowly in time. Therefore, a HDM-s mean sea level (MSL) can deviate from the historic MSL and consequently from the vertical datum. The TG station readings were thus used for determining and eliminating such a DB in the HBM-EST HDM. In addition to DT correction, a correction from vessel's fuel consumption was added to the profiles.

As an alternative to shipborne GNSS, ALS assessment was also tested in the current study. The point clouds used were obtained from dedicated ALS campaigns that took place at 14.05.2013 and 10.05.2018. Leica ALS50-II LiDAR System was used during the first airborne campaign, and during the second campaign, RIEGL VQ-1560i LiDAR Scanning System was utilized.

Similarly to shipborne GNSS data processing, sea surface oscillations (i.e. waves) must be eliminated from the ALS point clouds. For the purpose, a combination of gridding and filtering was tested. First, 5x5m and 50x50m grids were computed from ALS point clouds with inverse distance weighted (IDW) interpolation method. 5x5m grids were then filtered with three dimensional (3D) filters, such as averaging filter and exponential filter, which apply a corresponding function to the grid. Profiles were then extracted from the filtered grids. Additionally, profiles were extracted from yet to be filtered grids (from both 5x5m and 50x50m resolution grids), which were then filtered with the previously mentioned double low-pass filter – a two dimensional filter.

It was found that the results are highly dependent on the input point cloud data quality. 3D filters yield great results and surpass double low-pass filter when point clouds are even and dense. Also, a wide data corridor improves the results. On the other hand, if data quality is poor, decent results can be obtained with double low-pass filtering. In these cases, 3D filters will not work, and the results are substandard.

In terms of data quality, the point clouds obtained with RIEGL VQ-1560i LiDAR Scanning System clearly surpass these of obtained with Leica ALS50-II LiDAR System. Thus, the extracted profiles

from gridded point clouds of the first campaign were filtered with the double low-pass filter and gridded point clouds from the second campaign were filtered with the exponential filter, which surpasses averaging filter according to the current study. Similarly to shipborne GNSS assessment, DT correction was then added to the ALS profiles.

It should be noted that the point clouds obtained during the 2013 ALS campaign could be affected by internal errors. However, it is also likely that the DT data during that time period is insufficient, which in turn affects the geoid model assessment results.

The study also tested alternative uses for RIEGL VQ-1560i LiDAR Scanning System obtained point clouds. It was found that 3D filtered grids computed from the point clouds allow grid to grid assessment. Also, the data can be used for HDM assessment, similarly to marine geoid model assessment. The two HDM-s assessed were previously mentioned HBM-EST and Baltic Sea Physical Analysis and Forecasting model computed at the Copernicus Marine Environment Monitoring Service (CMEMS). According to the profiles computed from RIEGL obtained point clouds, the HBM-EST HDM surpasses the CMEMS model. The results also suggest that the marine geoid model assessment is affected by errors in DT.

The main difference between shipborne GNSS and ALS assessments in the current study is that the first one is a relative and the second an absolute assessment method. With ALS, ellipsoidal height of the sea surface is obtained. However, determination of the distance between GNSS antenna and sea surface was difficult and inaccurate during shipborne assessment. Thus the method is relative. This can be done however, e.g. if the vessel itself is coordinated.

Four geoid models were then assessed with the resulting shipborne GNSS and ALS profiles. These were EST-GEOID2011, EST-GEOID2017, NKG2015 and a FAMOS (Finalising Surveys for the Baltic Motorways of the Sea) geoid model referred to as FAMOS GOCO05s. EST-GEOID2017 and FAMOS GOCO05s are the models that have FAMOS2017 gravity data included in their computations. Accuracies of these four geoid models along various profiles and surfaces (Combined GNSS, 2018 ALS, final 2013 ALS profiles and gridded deviation surfaces) are as follows:

- 1) EST-GEOID2011 – 1,7...4,4 cm according to StDev and 4,5...7,6 cm according to RMSE;
- 2) EST-GEOID2017 – 0,9...3,4 cm according to StDev and 1,4...4,6 cm according to RMSE;
- 3) NKG2015 – 1,4...4,5 cm according to StDev and 3,1...5,2 cm according to RMSE;
- 4) FAMOS GOCO05s – 0,9...3,5 cm according to StDev and 1,3...4,4 cm according to RMSE.

According to the results, the best performing geoid model in the Gulf of Finland is FAMOS GOCO05s, followed by EST-GEOID2017. The worst performing model on the other hand is EST-GEOID2011.

The study did not manage to answer or do everything and some of these matters could be topics for future studies. Some of these are as follows:

1. An investigation of pitch and roll motion during seaborne GNSS measurements. How large are the differences between pitch and roll determined by using IMU and referring the GNSS height time-series (from multiple antennas) to the location of vessel's mass center?
2. ALS grid to grid assessment of geoid models. The current study determined that it is possible but did not go on with it. What are the benefits over profile-wise assessment?
3. A dedicated study to evaluating HDM-s using ALS data (and shipborne GNSS profiles?).
4. A dedicated study to investigate the resulting sea surface from the RIEGL VQ-1560i LiDAR Scanning System obtained point clouds.

As a conclusion to the thesis, the author has a couple of recommendations for future experiments:

1. When choosing a vessel for shipborne GNSS campaigns, already coordinated one should be preferred. Otherwise it is recommended to coordinate the vessel pre-experiment.
2. If GNSS data are used for absolute assessment, it is absolutely necessary to pay attention to the antenna reference (during measurements and post-processing).
3. The choice of GNSS post-processing software has utmost importance to the results. It would be wise to test different software.
4. When gravimetric data too are being collected during a shipborne campaign, it is absolutely necessary to remember that even slow accelerations and decelerations may corrupt the data. Thus, a constant speed should always be kept.
5. When planning routes for either shipborne GNSS or ALS campaigns, intersections should be included. This allows internal validation of collected data. Intersections are also necessary when gravimetric data is being collected.
6. DT correction calculation requires great attention, as this is the likely source of errors. The choice of HDM will also affect the assessment results.
7. ALS measurements should be carried out with slightly disturbed sea surface – this will improve the resulting point clouds.

ABSTRACT

The geoid is an equipotential surface that the oceans would take at rest, being affected only by the influence of gravity and rotation of Earth. Thus, it roughly coincides with the mean sea level. A modelled surface of the gravity field potential requires an external verification for validating its accuracy. On land, geoid models are customarily evaluated by using precise GNSS-levelling points, whereas offshore such control points cannot be established. Instead, marine geoid models can be assessed by shipborne GNSS measurements or airborne laser scanning (ALS). Emphasis of the study is on principles of using the shipborne GNSS and ALS profiles for validation of existing geoid models. Methods for elimination of sea surface oscillations (i.e. data filtering) are investigated. Tide gauge records in conjunction with a regional hydrodynamic model are used for accounting sea level dynamics. It is concluded that both shipborne GNSS and ALS profiles have a potential in providing complementary constraints in problematic geoid modelling areas.

KOKKUVÕTE (in Estonian)

Geoidiks nimetatakse ekvipotentsiaalpinna, mis ühtib ligikaudu Maa gravitatsiooni ja pöörlemise poolt vormitud ookeanide häirimata veepinnaga ehk keskmise meretasemega. Selleks, et säärase gravitatsioonivälja mudeldatud potentsiaalpinna täpsust kontrollida, on vaja sõltumatuid andmeid. Maismaal kasutatakse selleks reeglina GNSS-nivelleerimise kontrollpunkte, mida aga merel ei ole võimalik üles seada. Selle asemel võib meregeoidi mudelite hindamiseks kasutada laeval mõõdetud GNSS või aerolaserskaneerimise (ALS) kõrgusprofiile. Antud töö keskendubki meregeoidi mudelite hindamise printsiipide väljaselgitamisele ning nende rakendamisele. Näiteks on äärmiselt oluline mõõdistusandmetest lainetuse mõju elimineerida, mille tarbeks töötati välja vastavad filtreerimis-metoodikad. Selleks, et võtta arvesse merepinna dünaamikast tulenevad muutused, on töös rakendatud regionaalset hüdrodünaamika mudelit ning kohalike veemõõdujaamade andmeid. Võib öelda, et nii laeval mõõdetud GNSS kui ka ALS kõrgusprofiilid annavad väärtusliku infot problemaatiliste alade kohta meregeoidide mudelites.

LIST OF REFERENCES

1. Aerolaserskaneerimise kõrguspunktid. (2019). Estonian Land Board Geoportal <https://geoportaal.maaamet.ee/est/Andmed-ja-kaardid/Topograafilised-andmed/Korgusandmed/Aerolaserskaneerimise-korguspunktid-p499.html> (21.03.2019)
2. Aerolaserskanner Leica ALS50-II (2008-2016). (2017a). Estonian Land Board Geoportal <https://geoportaal.maaamet.ee/est/Andmed-ja-kaardid/Ortofotod/Tootmislugu/Aerolaserskanner-Leica-ALS50-II-2008-2016-p336.html> (21.03.2019)
3. Aerolaserskanner Riegl VQ-1560i. (2017b). Estonian Land Board Geoportal <https://geoportaal.maaamet.ee/est/Andmed-ja-kaardid/Ortofotod/Tootmislugu/Aerolaserskanner-Riegl-VQ-1560i-p561.html> (21.03.2019)
4. Ågren, J., Strykowski, G., Bilker-Koivula, M., Omang, O., Märdla, S., Forsberg, R., Ellmann, A., Oja, T., Liepinš, I., Paršeliūnas, E., Kaminskis, J., Sjöberg, L., Valsson, G. (2016). The NKG2015 gravimetric geoid model for the Nordic-Baltic region. – *1st Joint Commission 2 and IGFS Meeting International Symposium on Gravity, Geoid and Height Systems, Thessaloniki, Greece, 19-23 September 2016, Proceedings*. International Association of Geodesy Symposia, DOI: <https://doi.org/10.13140/RG.2.2.20765.20969>
5. Alenius, P., Myrberg, K., Nekrasov, A. (1998). The physical oceanography of the Gulf of Finland: A review. – *Boreal Environment Research*, 3(2), 97–125. Boreal Environment Research Publishing Board <http://www.borenv.net/BER/pdfs/ber3/ber3-097-125.pdf> (24.04.2019)
6. Allik, A. (2014). Satelliitaltimeetria mõõtmiste integreerimine meretaseme prognoosimudeliga (The integration of satellite altimetry and sea level forecast model, thesis in Estonian) : Bachelor's thesis. Tallinn : Tallinn University of Technology. – *TTÜR Digikogu / TUT Press* <https://digi.lib.ttu.ee/i/?7017> (04.04.2019)
7. Andrejev, O., Myrberg, K., Alenius, P., Lundberg, P. A. (2004a). Mean circulation and water exchange in the Gulf of Finland – a study based on three-dimensional modelling. – *Boreal Environment Research*, 9(1), 1–16. Boreal Environment Research Publishing Board <http://www.borenv.net/BER/pdfs/ber9/ber9-001.pdf> (24.04.2019)
8. Andrejev, O., Myrberg, K., Lundberg, P. A. (2004b). Age and renewal time of water masses in a semi-enclosed basin – application to the Gulf of Finland. – *Tellus A: Dynamic Meteorology and Oceanography*, 56(5), 548-558. Taylor and Francis Online, DOI: <https://doi.org/10.3402/tellusa.v56i5.14435>

9. Barrass, C. B. (2004). *Ship Design and Performance for Masters and Mates*. Oxford : Elsevier Butterworth-Heinemann.
10. Bilker-Koivula, M. (2010). Development of the Finnish Height Conversion Surface FIN2005N00. – *Nordic Journal of Surveying and Real Estate Research*, 7(1), 76-88.
11. Bruinsma, S. L., Förste, C., Abrikosov, O., Lemoine, J.-M., Marty, J.-C., Mulet, S., Rio, M.-H., Bonvalot, S. (2014). ESA's satellite-only gravity field model via the direct approach based on all GOCE data. – *Geophysical Research Letters*, 41(21), 7508–7514. American Geophysical Union Publications, DOI: <https://doi.org/10.1002/2014GL062045>
12. Bruinsma, S. L., Förste, C., Abrikosov, O., Marty, J.-C., Rio, M.-H., Mulet, S., Bonvalot, S. (2013). The new ESA satellite-only gravity field model via the direct approach. – *Geophysical Research Letters*, 40(14), 3607–3612. American Geophysical Union Publications, DOI: <https://doi.org/10.1002/grl.50716>
13. Cimmery, V. (2011). Simple Filter https://sourceforge.net/p/saga-gis/wiki/grid_filter_0/ (29.04.2019)
14. Cocard, M., Geiger, A., Kahle, H.-G., Veis, G. (2002). Airborne laser altimetry in the Ionian Sea, Greece. – *Global and Planetary Change*, 34(1-2), 87-96. Elsevier ScienceDirect, DOI: [https://doi.org/10.1016/S0921-8181\(02\)00107-8](https://doi.org/10.1016/S0921-8181(02)00107-8)
15. Conrad, O. (2009). SAGA-GIS Tool Library Documentation (v6.4.0), Tool Smoothing (ViGrA) http://www.saga-gis.org/saga_tool_doc/6.4.0/imagery_vigra_0.html (29.04.2019)
16. Conrad, O., Bechtel, B., Bock, M., Dietrich, H., Fischer, E., Gerlitz, L., Wehberg, J., Wichmann, V., Böhner, J. (2015). System for Automated Geoscientific Analyses (SAGA) v. 2.1.4. – *Geoscientific Model Development*, 8(7), 1991-2007. European Geosciences Union Publications, DOI: <https://doi.org/10.5194/gmd-8-1991-2015>
17. CSRS-PPP. (n.d.). Available: <https://webapp.geod.nrcan.gc.ca/geod/tools-outils/ppp.php> (25.04.2019)
18. Ekman, M., Mäkinen, J. (1996). Mean sea surface topography in the Baltic Sea and its transition area to the North Sea: A geodetic solution and comparisons with oceanographic models. – *Journal of Geophysical Research*, 101(C5), 11993-11999. American Geophysical Union Publications, DOI: <https://doi.org/10.1029/96JC00318>
19. Elken, J., Raudsepp, U., Lips, U. (2003). On the estuarine transport reversal in deep layers of the Gulf of Finland. – *Journal of Sea Research*, 49(4), 267-274. Elsevier ScienceDirect, DOI: [https://doi.org/10.1016/S1385-1101\(03\)00018-2](https://doi.org/10.1016/S1385-1101(03)00018-2)

20. Ellmann, A. (2005). Two deterministic and three stochastic modifications of Stokes's formula: a case study for the Baltic countries. – *Journal of Geodesy*, 79(1-3), 11-23. Springer-Verlag, DOI: <https://doi.org/10.1007/s00190-005-0438-1>
21. Ellmann, A., Julge, K., Gruno, A., Liibusk, A. (2016a). Airborne laser scanning validation of marine geoid models. – *1st Joint Commission 2 and IGFS Meeting International Symposium on Gravity, Geoid and Height Systems, Thessaloniki, Greece, 19-23 September 2016, Proceedings*. International Association of Geodesy Symposia: <http://gghs2016.com/presentation-info/?presentation=728>
22. Ellmann, A., Märdla, S., Oja, T. (2019). The 5 mm geoid model for Estonia computed by the least squares modified Stokes's formula. – *Survey Review*. Taylor and Francis Online, DOI: <https://doi.org/10.1080/00396265.2019.1583848>
23. Ellmann, A., Oja, T., All, T., Jürgenson, H., Kall, T., Liibusk, A. (2016b). Raskuskiirenduse anomaalvälja ja geoidi mudelpinna täpsustamine Eestis (Enhanced gravity field and geoid models over Estonia, article in Estonian). – *Publicationes Geophysicales Universitatis Tartuensis*, 51, 152-164. Tartu Ülikooli Kirjastus / University of Tartu Press http://www.maaamet.ee/data/files/Ellmann_etal_metobs_150_2016.pdf (24.04.2019)
24. Ellmann, A., Väling, P., Oja, T. (2016c). Meregravimeetritelised mõõdistused Lääne-Eesti vetes FAMOS projekti raames (The FAMOS marine gravity surveys in West-Estonian waters, article in Estonian). – *Geodeet*, 45/46(69/70), 80-82.
25. Forsberg, R., Strykowski, G., Solheim, D. (2004). NKG-2004 Geoid of the Nordic and Baltic Area. – *Gravity, Geoid and Satellite Gravity Missions, Porto, Portugal, 30 August – 3 September 2004, Proceedings on CD-ROM from the International Association of Geodesy*.
26. Fowler, A., Kadatskiy, V. (2011). Accuracy and error assessment of terrestrial, mobile and airborne lidar. – *ASPRS 2011 Annual Conference, Milwaukee, Wisconsin, 1-5 May 2011, Proceedings*. American Society for Photogrammetry and Remote Sensing http://www.asprs.org/a/publications/proceedings/Milwaukee2011/files/Fowler_1.pdf (04.05.2019)
27. Gruno, A., Liibusk, A., Ellmann, A., Oja, T., Vain, A., Jürgenson, H. (2013). Determining sea surface heights using small footprint airborne laser scanning. – *Remote Sensing of the Ocean, Sea Ice, Coastal Waters, and Large Water Regions 2013, Dresden, Germany, 23 September 2013, Proceedings*. Spie - International Society for Optical Engineering, DOI: <https://doi.org/10.1117/12.2029189>
28. How inverse distance weighted interpolation works. (2018). ArcGIS Pro Help <https://pro.arcgis.com/en/pro-app/help/analysis/geostatistical-analyst/how-inverse-distance-weighted-interpolation-works.htm> (21.03.2019)

29. Huess, V. (2018). Product User Manual for Baltic Sea Physical Analysis and Forecasting Product BALTICSEA_ANALYSIS_FORECAST_PHY_003_006 <http://cmems-resources.cls.fr/documents/PUM/CMEMS-BAL-PUM-003-006.pdf> (26.03.2019)
30. Huising, E. J., Gomes Pereira, L. M. (1998). Errors and accuracy estimates of laser data acquired by various laser scanning systems for topographic applications. – *ISPRS Journal of Photogrammetry and Remote Sensing*, 53(5), 245-261. Elsevier ScienceDirect, DOI: [https://doi.org/10.1016/S0924-2716\(98\)00013-6](https://doi.org/10.1016/S0924-2716(98)00013-6)
31. Izotova, J. (2015). Operatiivsete meremudelite valideerimine ja võrdlus Läänemere idaosas (Validation of Operational Ocean Models in The Eastern Baltic Sea, thesis in Estonian) : Bachelor's thesis. Tallinn : Tallinn University of Technology. – *TTÜR Digikogu / TUT Press* <https://digi.lib.ttu.ee/i/?2677> (18.04.2019)
32. Jahn, C.-H., Ihde, J., Liebsch, G., Richter, B., Sacher, M., Schirmer, U., Habrich, H., Wilmes, H. (2012). EUREF National Report of Germany 2012. – *EUREF Symposium 2012, Paris, France, 6-8 June 2012, Proceedings*.
33. Julge, K., Gruno, A., Ellmann, A., Liibus, A., Oja, T. (2014). Exploring sea surface heights by using Airborne Laser Scanning. – *2014 IEEE/OES Baltic International Symposium (BALTIC), Tallinn, Estonia, 27-29 May 2014, Proceedings*. IEEE Xplore Digital Library, DOI: <https://doi.org/10.1109/BALTIC.2014.6887853>
34. Jürgenson, H., Liibus, A., Ellmann, A. (2008). Geoid profiles in the Baltic Sea determined using GPS and sea level surface. – *Geodezija Ir Kartografija / Geodesy and Cartography*, 34(4), 109–115. Taylor and Francis Online, DOI: <https://doi.org/10.3846/1392-1541.2008.34.109-115>
35. Kakkuri, J., Poutanen, M. (1996). Geodetic determination of the surface topography of the Baltic Sea. – *Marine Geodesy*, 20(4), 307-316. Taylor and Francis Online, DOI: <https://doi.org/10.1080/01490419709388111>
36. Kleine, E. (1994). Das Operationelle Modell des BSH für Nordsee und Ostsee. Konzeption und Übersicht, Bundesamt für Seeschifffahrt und Hydrographie (manuscript report in German).
37. Koethe, U. (2017). Smooth an image using Recursive convolution functions: smooth.cxx http://ukoethe.github.io/vigra/doc-release/vigra/smooth_8cxx-example.html (29.04.2019)
38. Kollo, K., Ellmann, A. (2019). Geodetic reconciliation of tide gauge network in Estonia. – *Geophysica*, accepted for publication.

39. Lagemaa, P., Elken, J., Kõuts, T. (2011). Operational sea level forecasting in Estonia. – *Estonian Journal of Engineering*, 17(4), 301–331. Estonian Academy Publishers, DOI: <https://doi.org/10.3176/eng.2011.4.03>
40. Lagemaa, P. (2012). Operational forecasting in Estonian marine waters : PhD thesis. Tallinn : Tallinn University of Technology. – *TTÜR Digikogu / TUT Press* <https://digi.lib.ttu.ee/i/?714> (25.03.2019)
41. Lagemaa, P. (2015). Operatiivne meremudel HBM-EST Tehniline juhend (Technical manual for HBM-EST operational forecasting model, article in Estonian) https://www.kik.ee/sites/default/files/uuringud/operatiivne_meremudel_hbm-est.pdf (26.03.2019)
42. Lavrov, D., Even-Tzur, G., Reinking, J. (2015). Extraction of geoid heights from shipborne GNSS measurements along the Weser River in northern Germany. – *Journal of Geodetic Science*, 5(1). De Gruyter, DOI: <https://doi.org/10.1515/jogs-2015-0014>
43. Lavrov, D., Even-Tzur, G., Reinking, J. (2016). Expansion and improvement of the Israeli geoid model by shipborne GNSS measurements. – *Journal of Surveying Engineering*, 143(2). ASCE Library, DOI: [https://doi.org/10.1061/\(ASCE\)SU.1943-5428.0000204](https://doi.org/10.1061/(ASCE)SU.1943-5428.0000204)
44. Lehmann, A., Krauss, W., Hinrichsen, H.-H. (2002). Effects of remote and local atmospheric forcing on circulation and upwelling in the Baltic Sea. – *Tellus A: Dynamic Meteorology and Oceanography*, 54(3), 299-316. Taylor and Francis Online, DOI: <https://doi.org/10.3402/tellusa.v54i3.12138>
45. Leica ALS50-II LIDAR. (2017). The Natural Environment Research Council Airborne Research Facility Data Analysis Node <https://nerc-arf-dan.pml.ac.uk/trac/wiki/Sensors/LeicaLIDAR> (06.04.2019)
46. Lennuk – Cessna Grand Caravan 208B. (2016). Estonian Land Board Geoportal <https://geoportaal.maaamet.ee/est/Andmed-ja-kaardid/Ortofotod/Tootmislugu/Lennuk-Cessna-Grand-Caravan-208B-p71.html> (21.03.2019)
47. Le Provost, C. (1990). The Geoid and Mean Sea Level. – *International Hydrographic Review*, 67(1), 171-175. International Hydrographic Organization Monaco <https://journals.lib.unb.ca/index.php/ihr/article/viewFile/23325/27100> (04.05.2019)
48. Liibus, A., Ellmann, A., Kõuts, T., Jürgenson, H. (2013). Precise Hydrodynamic Levelling by Using Pressure Gauges. – *Marine Geodesy*, 36(2), 138-163. Taylor and Francis Online, DOI: <https://doi.org/10.1080/01490419.2013.771594>

49. Mayer-Gürr, T., Pail, R., Gruber, T., Fecher, T., Rexer, M., Schuh, W.-D., Kusche, J., Brockmann, J.-M., Rieser, D., Zehentner, N., Kvas, A., Klinger, B., Baur, O., Höck, E., Krauss, S., Jäggi, A. (2015). The combined satellite gravity field model FAMOS GOCO05s. – *European Geosciences Union General Assembly, Vienna, Austria, 12-17 April 2015, Proceedings*. DOI: <https://doi.org/10.13140/rg.2.1.4688.6807>
50. Metsar, J., Kollo, K., Ellmann, A. (2018). Modernization of the Estonian National GNSS Reference Station Network. – *Geodesy and Cartography*, 44(2), 55–62. Vilnius Gediminas Technical University Press, DOI: <https://doi.org/10.3846/gac.2018.2023>
51. Morin, K. W. (2002). Calibration of Airborne Laser Scanners : Master’s thesis. Calgary : University of Calgary. – *Governors of the University of Calgary* https://www.ucalgary.ca/engo_webdocs/NES/02.20179.KrisMorin.pdf (03.05.2019)
52. Märdla, S., Ågren, J., Strykowski, G., Oja, T., Ellmann, A., Forsberg, R., Bilker-Koivula, M., Omang, O., Paršeliūnas, E., Liepinš, I., Kaminskis, J. (2017). From Discrete Gravity Survey Data to a High-resolution Gravity Field Representation in the Nordic-Baltic Region. – *Marine Geodesy*, 40(6), 416-453. Taylor and Francis Online, DOI: <https://doi.org/10.1080/01490419.2017.1326428>
53. Myrberg, Kai., Soomere, T. (2013). The Gulf of Finland, Its Hydrography and Circulation Dynamics. In: Soomere, T., Quak, E. (eds). *Preventive Methods for Coastal Protection*, 181-222. Springer, Heidelberg, DOI: https://doi.org/10.1007/978-3-319-00440-2_6
54. Nordman, M., Kuokkanen, J., Bilker-Koivula, M., Koivula, H., Häkli, P., Lahtinen, S. (2018). Geoid Validation on the Baltic Sea Using Shipborne GNSS Data. – *Marine Geodesy*, 41(5), 457-476. Taylor and Francis Online, DOI: <https://doi.org/10.1080/01490419.2018.1481160>
55. Olesen, A. V. (2017). Marine gravity onboard MS Sektori July 2017, processing report. Danish Technical University (DTU).
56. Pail, R., Bruinsma, S., Migliaccio, F., Förste, C., Goiginger, H., Schuh, W.-D., Höck, E., Reguzzoni, M., Brockmann, J. M., Abrikosov, O., Veicherts, M., Fecher, T., Mayrhofer, R., Krasbutter, I., Sansò, F., Tscherning, C. C. (2011). First GOCE gravity field models derived by three different approaches. – *Journal of Geodesy*, 85(11), 819–843. Springer-Verlag, DOI: <https://doi.org/10.1007/s00190-011-0467-x>
57. Parrish, C. (2011). Lidar 101. – *Lidar and Height Mod Workshop, Silver Spring, Maryland, 18 August 2011, Proceedings*. National Oceanic and Atmospheric Administration’s National Geodetic Survey https://www.ngs.noaa.gov/corbin/class_description/Parrish_Lidar_and_Height_Mod_Presentation.pdf (03.05.2019)

58. Pavlis, N. K., Holmes, S. A., Kenyon, S. C., Factor, J. K. (2012). The development and evaluation of the Earth Gravitational Model 2008 (EGM2008). – *Journal of Geophysical Research: Solid Earth*, 117(B4). American Geophysical Union Publications, DOI: <https://doi.org/10.1029/2011JB008916>
59. Poutanen, M. (2000). Sea Surface Topography and Vertical Datums Using Space Geodetic Techniques : PhD thesis. Helsinki : University of Helsinki. – *Publications of the Finnish Geodetic Institute*.
60. RIEGL VQ-1560i. (n.d.). Mena3D GmbH
http://www.mena3d.com/pdf/Riegl_Brochures/VQ-1560i.pdf (06.04.2019)
61. Sjöberg, L. E. (2003). A computational scheme to model the geoid by the modified Stokes formula without gravity reductions. – *Journal of Geodesy*, 77(7), 423–432. Springer-Verlag, DOI: <https://doi.org/10.1007/s00190-003-0338-1>
62. Sjöberg, L. E., Bagherbandi, M. (2017). Applications and Comparisons of LSMSA and RCR. In: Sjöberg, L. E., Bagherbandi, M. (eds). *Gravity Inversion and Integration*, 181-202. Springer, Cham, DOI: https://doi.org/10.1007/978-3-319-50298-4_6
63. Slobbe, D. C., Klees, R., Verlaan, M., Zijl, F., Alberts, B., Farahani, H. H. (2018). Height system connection between island and mainland using a hydrodynamic model: a case study connecting the Dutch Wadden islands to the Amsterdam ordnance datum (NAP). – *Journal of Geodesy*, 92(12), 1439–1456. Springer Berlin Heidelberg, DOI: <https://doi.org/10.1007/s00190-018-1133-3>
64. Zijl, F., Verlaan, M., Gerritsen, H. (2013). Improved water-level forecasting for the northwest European shelf and North Sea through direct modelling of tide, surge and non-linear interaction. – *Ocean Dynamics*, 63(7), 823-847. Springer Berlin Heidelberg, DOI: <https://doi.org/10.1007/s10236-013-0624-2>
65. Zijl, F., Sumihar, J., Verlaan, M. (2015). Application of data assimilation for improved operational water level forecasting on the northwest European shelf and North Sea. – *Ocean Dynamics*, 65(12), 1699-1716. Springer Berlin Heidelberg, DOI: <https://doi.org/10.1007/s10236-015-0898-7>
66. Zlinszky, A., Timár, G., Weber, R., Székely, B., Briese, C., Ressler, C., Pfeifer, N. (2014). Observation of a local gravity potential isosurface by airborne lidar of Lake Balaton, Hungary. – *Solid Earth*, 5, 355-369. Copernicus Publications, DOI: <https://doi.org/10.5194/se-5-355-2014>

67. van der Sande, C., Soudarissanane, S., Khoshelham, K. (2010). Assessment of Relative Accuracy of AHN-2 Laser Scanning Data Using Planar Features. – *Sensors*, 10(9), 8198-8214. Multidisciplinary Digital Publishing Institute, DOI: <https://doi.org/10.3390/s100908198>
68. Varbla, S., Ellmann, A., Metsar, J., Oja, T. (2017a). Meregravimeetrilised mõõdistused Soome lahel projekti FAMOS raames (The FAMOS marine gravity survey on the Gulf of Finland, article in Estonian). – *Geodeet*, 47(71), 39-43.
69. Varbla, S., Ellmann, A., Märdla, S., Gruno, A. (2017b). Assessment of marine geoid models by shipborne GNSS profiles. – *Geodesy and Cartography*, 43(2), 41-49. Vilnius Gediminas Technical University Press, DOI: <https://doi.org/10.3846/20296991.2017.1330771>
70. Vignudelli, S., Cipollini, P., Roblou, L., Lyard, F., Gasparini, G. P., Manzella, G., Astraldi, M. (2005). Improved satellite altimetry in coastal systems: Case study of the Corsica Channel (Mediterranean Sea). – *Geophysical Research Letters*, 32(7), n/a–n/a. American Geophysical Union Publications, DOI: <https://doi.org/10.1029/2005GL022602>

APPENDIX A

Copyright © 2017 Vilnius Gediminas Technical University. Reprinted from:

Varbla, S., Ellmann, A., Märdla, S., Gruno, A. (2017b). Assessment of marine geoid models by shipborne GNSS profiles. – *Geodesy and Cartography*, 43(2), 41-49. Vilnius Gediminas Technical University Press, DOI: <https://doi.org/10.3846/20296991.2017.1330771>

ASSESSMENT OF MARINE GEOID MODELS BY
SHIP-BORNE GNSS PROFILESSander VARBLA¹, Artu ELLMANN², Silja MÄRDLA³, Anti GRUNO⁴^{1, 2, 3}*Department of Civil Engineering and Architecture, Tallinn University of Technology,
Ehitajate tee 5, 19086 Tallinn, Estonia*⁴*Estonian Land Board, Mustamäe tee 51, 10621 Tallinn, Estonia**E-mails: ¹sander.varbla@ttu.ee (corresponding author); ²artu.ellmann@ttu.ee;**³silja.mardla@ttu.ee; ⁴anti.gruno@maaamet.ee**Received 21 April 2017; accepted 10 May 2017*

Abstract. Even though the entire Baltic Sea is included in previous geoid modelling projects such as the NKG2015 and EGG07, the accuracy of contemporary geoid models over marine areas remains unknown, presumably being offshore around 15–20 cm. An important part of the international cooperation project FAMOS (Finalising Surveys for the Baltic Motorways of the Sea) efforts is conducting new marine gravity observations for improving gravimetric quasigeoid modelling. New data is essential to the project as the existing gravimetric data over some regions of the Baltic Sea may be inaccurate and insufficiently scarce for the purpose of 5 cm accuracy geoid modelling. Therefore, it is important to evaluate geoid modelling outcome by independent data, for instance by shipborne GNSS measurements. Accordingly, this study presents results of the ship-borne marine gravity and GNSS campaign held on board the Estonian Maritime Administration survey vessel “Jakob Prei” in West-Estonian archipelago in June/July 2016. Emphasis of the study is on principles of using the GNSS profiles for validation of existing geoid models, post-processing of GNSS raw data and low-pass filtering of the GNSS results. Improvements in geoid modelling using new gravimetric data are also discussed. For example, accuracy of geoid models including the new marine gravity data increased 11 mm as assessed from GNSS profiles. It is concluded that the marine GNSS profiles have a potential in providing complementary constraints in problematic geoid modelling areas.

Keywords: ship-borne GNSS, marine gravimetry, sea surface topography, FAMOS, Baltic Sea.

Introduction

An international cooperation project FAMOS (Finalising Surveys for the Baltic Motorways of the Sea) has been initiated to improve the gravimetric quasigeoid model that will be needed for the realisation of the Baltic Sea Chart Datum 2000 (BSCD2000) as the new common height reference system for the Baltic Sea hydrographic surveying and nautical charts (FAMOS 2017). The goal is to improve the accuracy of GNSS (Global Navigation Satellite System) supported bathymetric measurements and navigation by computing a new 5 cm accuracy marine geoid (note that over marine areas the quasigeoid coincides with the geoid, thus for brevity the shorter term will often be used in the text) model over the entire Baltic Sea.

The existing gravimetric data over some regions of the Baltic Sea appear to be too sparse and inaccurate for the purpose of 5 cm geoid modelling (FAMOS 2017). It is estimated that the accuracy of contemporary geoid models over marine areas could often be no better than 15–20 cm, especially in the gravity data void areas. For instance, some earlier studies have indicated that the precision of geoid models in coastal areas can suffer due to heterogeneity of regional gravity data (Liibusk, Ellmann 2015; Märdla *et al.* 2017). This could also yield systematic offsets in marine geoid models over certain marine areas (Ellmann 2010).

External verification is thus needed for validating the accuracy of geoid models. On land, geoid models are customarily evaluated by using precise GNSS-levelling points, whereas offshore such control points

cannot be established. Instead, marine geoid models can be assessed by ship-borne GNSS measurements. For instance, the NKG04 gravimetric geoid model (Forsberg *et al.* 2004) was assessed by Jürgenson *et al.* (2008). Another similar experiment was carried out between 2011 and 2015 along Israeli coast (Lavrov *et al.* 2016). The purpose of the study was to determine suitability of ship-borne GNSS measurements for complementing geoid modelling. Results showed indeed, that the data obtained were sufficiently accurate for fulfil this task.

Different approaches have been tested in the region of interest of the present study – the Baltic Sea. In 2013, during gravity surveys on ice, GNSS data-points were acquired to determine geoidal heights (Märdla *et al.* 2015), see also a study by Liibus *et al.* (2014). The results showed that high accuracy GNSS positioning on the sea ice possesses a potential for enhancing geoid modelling results. Airborne laser scanning measurements (in conjunction with GNSS-IMU trajectory computations) in 2012 demonstrated further possibilities for determining sea surface heights (Gruno *et al.* 2013) and subsequent validation of marine geoid models.

The present study also aims at assessing improvements in geoid models due to inclusion of new marine gravity data, collected on-board of a hydrographic survey vessel in and around West-Estonian Archipelago in 2016.

The outline of the paper is as follows. First, theoretical principles of determining sea surface height and their use for validating geoid models are described. Theoretical background of processing kinematic GNSS data with precise point positioning solutions is also described briefly. The next sections give an overview of the methodology used during the marine gravity experiment and post-processing of GNSS and gravimetric data. Thereafter improvements in geoid modelling are examined and discussed. A brief summary concludes the paper.

1. Theoretical principles

1.1. Determining sea surface heights, interrelations with geoid

The position of the on-board antenna (most relevantly, the height) is determined by GNSS. At the moment of the GNSS measurement, instantaneous sea surface height (SSH_i) is obtained (accounting also for the separation between the GNSS antenna and vessel's waterline). Thus, if the height of the antenna with respect to sea surface is known, GNSS measurements provide instantaneous SSH_i reckoned from the surface of geodetic reference ellipsoid at a location with geodetic coordinates φ, λ (Fig. 1):

$$SSH_i(\varphi, \lambda) = h_i(\varphi, \lambda) - R_i(\varphi, \lambda), \quad (1)$$

where h_i is the height of the GNSS antenna with respect to the reference ellipsoid (e.g. GRS-80) and R_i is the range between the GNSS antenna and the sea surface (e.g. determined by tape measurements), both at the same time-instant (i).

As the instantaneous sea surface height (SSH_i) is affected by tidal movement, wind direction and speed etc., then conventionally SSH_i is referred to the mean sea level (MSL) by (cf. Fig. 1):

$$MSL(\varphi, \lambda) = SSH_i(\varphi_i, \lambda_i) - H_i(\varphi_i, \lambda_i), \quad (2)$$

where H_i is the sea level correction (e.g. estimated from nearby tide gauge (TG) station readings at the same time instant i , see e.g. a study by Liibus *et al.* (2013); or using a suitable hydrodynamic model).

MSL is calculated from repeated measurements that are averaged over a certain time period (decades). MSL in open sea can be obtained by averaging satellite altimetry results and in coastal areas by averaging the TG time series. Historically, MSL at selected TG sites has been adopted as the “zero” level of national/local vertical datums.

On land high-precise GNSS-levelling points are customarily used to fit gravimetric geoid models (N^{GG})

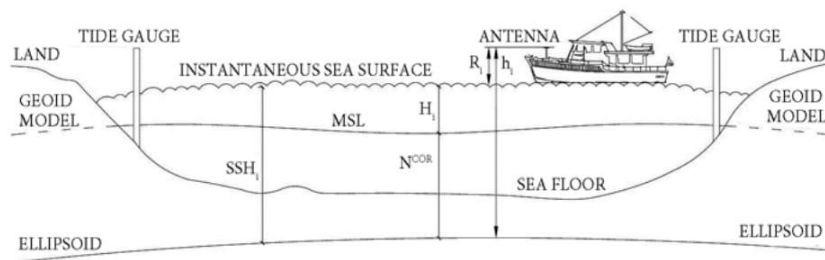


Fig. 1. Seaborne determination of sea surface heights (SSH) with respect to participating reference surfaces. The used symbols and abbreviations are explained in the text

Note: Figures have been generated using ArcGIS Desktop 10.5, Excel and GMT (Wessel *et al.* 2013) software.

to the national vertical datum. For eliminating possible systematic biases a multi-parameter polynomial fit was often applied (see e.g. Ellmann (2002, 2005) and references therein) to achieve 1–3 cm post-fit accuracy for resulting height conversion surfaces in the past. Due to lack of such GNSS-levelling control data the height conversion surfaces (N^{COR}) over marine areas were obtained by extrapolation, i.e.:

$$N^{COR}(\varphi, \lambda) = N^{GG}(\varphi, \lambda) - H^{GG}(\varphi, \lambda), \quad (3)$$

where the term H^{GG} denotes the location dependent (polynomial) geoid correction term, i.e. the bias between the tested geoid model and the national vertical datum.

Certainly, the quality of the resulting height conversion surfaces remains dubious offshore. However, nowadays, as a result of the Nordic Geodetic Commission NKG2015 geoid modelling project (Ågren *et al.* 2015, 2016) (which contain extensive data improvements, see e.g. Mårdla *et al.* 2017) systematic biases in new geoid models over the region of interest have largely been eliminated. An important result is that the deviations from the new geoid models and national vertical datum can be eliminated by one-dimensional fit, i.e. in this case the term H^{GG} in Eq. (3) appears to be a constant. This suggest also that the possible systematic biases in offshore have been reduced. Thus, the corrected geoid model N^{COR} approximately coincides with the vertical datum (based on the historical mean sea level determination):

$$MSL(\varphi, \lambda) \approx N^{COR}(\varphi, \lambda). \quad (4)$$

We want to establish link between the geoid model and SSH_i . Considering Eq. (2), then Eq. (4) becomes:

$$N^{COR}(\varphi, \lambda) \approx SSH_i(\varphi_i, \lambda_i) - H_i(\varphi_i, \lambda_i). \quad (5)$$

Note that the first term in the right-hand side is measured, whereas the second term need to be estimated by using a network of tide gauges or suitable hydrodynamic model.

Nowadays, different global or regional hydrodynamic models have been compiled by using oceanographic data, satellite altimetry or geodetic measurements. For example, the HIROMB (High Resolution Operational Model for the Baltic) or NEMO (Nucleus for European Modelling of the Ocean) are available over the Baltic Sea. The common disadvantage of these models is that their accuracy may often be poorer (especially in the coastal areas) than that of actual sea level observations. A note of warning on quality of TG readings is also due. Sometimes TG data may

be unreliable or contaminated by systematic biases. Also, extrapolation from TG-s is needed in estimating H_i for most of the offshore GNSS-profile points. In other words, in such a case the sea level correction would be a time-dependent quantity over the entire study area.

However, arguably the magnitude of formal inequality in Eq. (5) is numerically comparable with the uncertainties in GNSS measurements, in the term H_i and geoid model to be validated. Therefore, in the present study we use a simplified geoid validation method, where the offshore H_i will be estimated as a mean value \bar{H} (within a time period of couple hours) between ship-borne GNSS-derived SSH_i and N^{COR} of a geoid model being assessed. Thus, significant deviations from the mean (especially the one-sign ones, over a sequence of the route) may reveal errors in the tested geoid model. Comparing different concurrent geoid models enables determination of the best fit geoid model.

1.2. GNSS precise point positioning

Traditionally, costly commercial or sophisticated scientific software are used for post-processing ship-borne GNSS data. Instead, applicability of an alternative solution is tested in the present study. More specifically, recently easy-to-use online (PPP) services have become more popular as they give relatively good results (see, e.g. Ocalan *et al.* 2013).

PPP uses ionosphere-free combinations of dual-frequency GNSS pseudorange (P) and carrier-phase observations (Φ) related to user position, clock, troposphere and ambiguity parameters according to the following simplified observation equations (Héroux, Kouba 2001):

$$P = \rho + C(dt - dT) + T_r + \varepsilon_p; \quad (6)$$

$$\Phi = \rho + C(dt - dT) + T_r + N\lambda + \varepsilon_\Phi, \quad (7)$$

where: P – ionosphere-free combination of L1 and L2 pseudoranges ($2.55P_1 - 1.55P_2$); Φ – ionosphere-free combination of L1 and L2 carrier-phases ($2.55\Phi_1 - 1.55\Phi_2$); ρ – geometrical range computed as a function of satellite and station coordinates; C – vacuum speed of light; dt – station clock offset from GNSS time; dT – satellite clock offset from GNSS time; T_r – signal path delay due to the neutral-atmosphere; λ – carrier, or carrier-combination, wavelength; N – ambiguity of the carrier-phase ionosphere-free combination; ε_p , ε_Φ – relevant measurement noise components, including multipath.

Then the GNSS antennae 3D positions are computed with respect to GNSS-CORS (Continuously Operating Reference Station) stations. The online-PPP services usually rely upon a limited number of internationally recognized GNSS-CORS rather than using nearby national/commercial ones. For this study, several innovative online-PPP services were tested, the corresponding results were compared to the results obtained by traditional algorithms as adopted in many commercial software and with respect to nearby located national GNSS-CORS.



Fig. 2. Baltic Sea and the surrounding countries. The location of the study area is marked on the map by the red rectangle

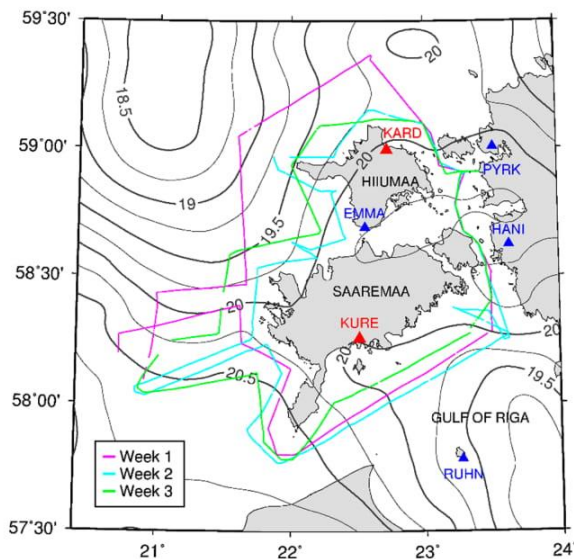


Fig. 3. Transit routes of the survey vessel and the used GNSS-CORS stations (denoted by colored triangles and 4-letter abbreviations) in West-Estonian Archipelago. The isolines depict the NKG2015 quasigeoid model in the study area. Units in metres

2. Study area, data acquisition and geoid models

A marine gravity experiment was carried out on board the Estonian Maritime Administration survey vessel “Jakob Prei” (JP) between 27.06.2016 and 15.07.2016. The vessel was deployed for hydrographic surveys over large areas West of Saaremaa in the central part of the Baltic Proper and the Gulf of Riga, cf. Figures 2 and 3.

However, our current research interest focuses mostly in transit routes, which were conducted around the islands of Saaremaa and Hiiumaa in West-Estonian archipelago (Fig. 3). The ship was offshore on all three weeks from Monday to Friday, returning to the base harbour for week-ends.

Gravimetric data were also gathered by using a Russian Elektropribor manufactured marine gravimeter Chekan-AM that was mounted by the Danish Technical University (DTU) team. The gravity survey post-processing revealed a precision better than 1 mGal (Olesen, Kasenda 2016).

Additionally, a standard Javad GNSS antenna was attached to the starboard of ship’s railing. A dual frequency Javad Delta GPS/GLONASS receiver was used to collect GNSS data for profiles. The GNSS receiver sampled the 3D position with a 5 second interval (1/5 Hz) constantly from 24.06.2016 to 15.07.2016 into sequential 24h long data files. The same interval data were also received from six Estonian GNSS-CORS (see Fig. 3) over the same time period. These data were later used for precise post-processing the vessel’s routes and for evaluating geoid models.

Three marine geoid models to be assessed by ship-borne GNSS profiles are as follows: (i) The official NKG2015 quasigeoid model released by the Nordic Geodetic Commission (NKG), see Ågren *et al.* (2016) for further details; (ii) Model 1 – a preliminary NKG2015 quasigeoid model computed at Tallinn University of Technology (TTÜ) in 2016; (iii) Model 2 – another preliminary quasigeoid model computed similarly to Model 1, but including the newly acquired marine gravity data. Note that the two first models do not contain the gravimetric data collected during the marine gravity experiment. However, all known systematic biases in terrestrial gravity data (see e.g. Ellmann *et al.* 2009) have been removed from the NKG gravity database prior the computations. The resulting geoid models were evaluated by the Estonian high-precision GNSS-levelling control points, yielding a sub-centimetre accuracy (in terms of StDev). For more details see Märdla *et al.* (2017).

Models 1 and 2 have been computed similarly to the NKG2015 geoid model, i.e. by using Least Squares Modification of Stokes' formula (e.g. Sjöberg 2003) and the GO_CONS_GCF_2_DIR_R5 (Bruinsma *et al.* 2014) global geopotential model as the reference surface. All the models have a spatial resolution of 0.01×0.02 arc-deg (approximately 1.1×1.1 km within the study area). The gravity data, the applied gridding strategies and quality assurance methods are explained in Märdla *et al.* (2017).

3. The GNSS results

The data processing revealed multiple gaps in GNSS data-series (e.g. see Fig. 4 from 20:58 to 21:19). Some of these lasted over 10 minutes, corresponding up to ca 3.5 km in transit routes. The likely reason is malfunctioning of the used GNSS receiver.

Two different commercial software were used for post-processing kinematic GNSS data-series. These were Trimble Business Centre™ v3.80 (TBC) and NovAtel Inertial Explorer™ v8.60 (IE). Considering the standard deviation of the profiles (such a comparison is not shown here) and visual evaluation of processed GNSS data, more accurate results were obtained with TBC.

Alternatively, several online-PPP services were tested: APPS (n.d.), GAPS (n.d.), magicGNSS (n.d.) and CSRS-PPP (n.d.). As the Canadian CSRS-PPP was the most convenient for current data processing needs (in contrast, the 24h data files appeared to be too large for APPS) and the quality of the results was sufficient for comparison with that of the commercial software, it was selected for this study. CSRS-PPP uses precise GPS orbit and clock products provided by IGS (International GNSS Service) and Natural Resources

Canada (NRCan), whereas it estimates single station positions in static and kinematic modes (Ocalan *et al.* 2013). The CSRS-PPP position estimations are computed from code pseudorange (P) or carrier-phase (Φ) observations of the used dual frequency GNSS rover receiver. The CSRS-PPP results were then compared to those of the TBC commercial software.

The global ITRF datum was selected for kinematic processing of CSRS-PPP. The PPP service does not reveal the used GNSS-CORS reference stations, though. It appeared that when the 24h long data files were processed the PPP service gives statistically better results (as compared to commercial software) on long (extending several hundred kilometres) transit routes. Yet, it emerged that the TBC calculations are more accurate with respect to the nearest national GNSS-CORS station. An example of differences between the results of two software on a long transit route after low-pass filtering GNSS data (to be discussed later) can be seen in Figure 4. The ship was the closest to the reference stations within 12:40 and 18:10, whereas the furthest at the end of the day. Statistical differences between CSRS-PPP and TBC data processing with respect to the official NKG2015 geoid model can be seen in a table below. Due to better performance, the TBC was chosen as final data processing software for this study.

The daily GNSS data-files were cut into several sequences in a way that each single kinematic point was calculated with respect to the closest national CORS station (see Fig. 3). Precise IGS (SP3 format) ephemerides were used for the calculations. A priori error estimate as of $0.200 \text{ m} + 1.0 \text{ ppm}$ was adopted to process the vertical component of the GNSS data. Calculation results exceeding this limiting value were excluded. Discrepancies between height computations from adjacent base stations were insignificant compared to the

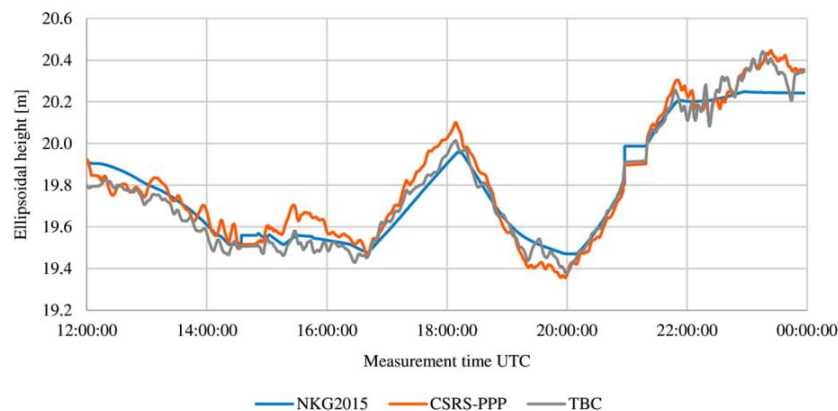


Fig. 4. CSRS-PPP and TBC calculations after filtering the GNSS-results (see below), as compared to the NKG2015 geoid model profile (after removal of the 1-dimensional offset \bar{H} from filtered data)

up-down movement of the ship. After processing all GNSS data in this way (both fixed and float solutions were aimed at), the results were recompiled into 24h long files.

A double low-pass filtering was applied for reducing the sea wave effect in GNSS data. Considering the average moving speed of the ship on transit routes, a moving median of 39 measurements was first taken:

$$\tilde{h}(i) = \text{median}(h_i [i-19, i+19]), \quad (8)$$

where h_i (blue line in Fig. 5) is a GNSS height component at time instant i and \tilde{h} (purple line in Fig. 5) median value of it in the range of the filter, i.e. the interval from 19 epochs before time instant i up to 19 epochs after the time instant i . 39 measurements (195 s) were chosen for the filtering window as this corresponds in length to the spatial resolution of the tested geoid models, which is about 1 km. Taking a median allowed to eliminate standalone gross errors in TBC calculations, as well as gross errors in GNSS measurements. From that outcome, a moving average of 39 measurements was also taken:

$$h^f(i) = \frac{1}{39} \sum_{n=i-19}^{i+19} \tilde{h}(n), \quad (9)$$

where h^f (orange line in Fig. 5) is low-pass filtered GNSS measurement at time instant i . Average was taken to further smoothen GNSS data. In the smoothing process of the 24h files the data from adjacent days were included as well.

In order to see how filtered GNSS data compares to geoid model with its spatial resolution (to find out if dense data points improve or worsen the results), further average of 39 was taken from low-pass filtering result:

$$h^a(j) = \frac{1}{39} \sum_{n=i-19}^{i+19} h^f(n), \quad (10)$$

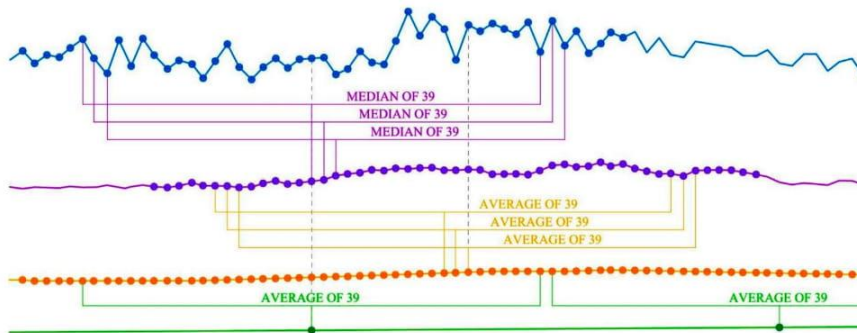


Fig. 5. Methodology of double low-pass and further averaged filtering of GNSS data (blue – raw GNSS result h_i ; purple – median values of raw GNSS result \tilde{h} ; orange – low-pass filtering result h^f ; green – averaged low-pass filtering result h^a)

where h^a (green line in Fig. 5) is averaged low-pass filtering result for a time period j (lasting 195 s, corresponding approximately to 1 km route). Note that unlike the Eq. (9), the average in Eq. (10) is not a moving one. Such a double low-pass and further averaged filtering scheme is visualised in Figure 5. The orange and green results in Figure 5 to be used for validating the participating geoid models.

Although the results coincide with geoid models, this method does not eliminate long-wavelength errors in TBC calculations (see a sample in Figure 7 from the time 5:24 to 5:29). Similar errors are seen in other software solutions, be it online-PPP services or the IE. However, spatial locations of these errors do not coincide for different software solutions.

As only one GNSS antenna was used, regrettably thus errors from the ship's attitude (roll and pitch) cannot be estimated. There is no need to know the antenna height (R_i) as only relative change of sea level surface is determined (see Eq. 1). As the ship's water-line is regulated with ballast water synchronously with the fuel consumption, there is no need for such a correction after refuelling either. Rigorously, the non-constant sea surface topography (SST) should also be considered, however, this was neglected in the current (tentative) study for the sake of simplification. It is expected that accounting for the SST could yield certain improvements in our further studies.

4. Comparison of GNSS profiles with geoid models

The most affected area by new gravimetric data lies West of Saaremaa where differences between the geoid Model 1 and Model 2 are the largest (Model 2 being generally lower than Model 1, Fig. 6). The GNSS profiles within that area (Table 1) are statistically analysed in Table 3 and Figure 7.

StDev of averaged low-pass filtering result is lower than StDev of the initial filtering result (see Tables 2 and 3), because averaging (see Fig. 5) eliminates remaining larger fluctuations from filtered data when compared to geoid models.

Note that statistics of profile (2) do not coincide in Table 2 (TBC) and Table 3 (NKG2015). This is because some of the measurements calculated by TBC were excluded by CSRS-PPP (or vice versa) and therefore the amount of processed data points differs between two

processing software. Only temporally coinciding measurements were considered for comparisons.

Table 1. General statistics of the GNSS profiles

Profile number	Measurement time	Profile length (km)	Number of low-pass filtering results	Number of further averaged results
(1)	28.06.2016	66.6	2243	58
(2)	30.06.2016	118.8	3807	98
(3)	05.07.2016	60.7	2052	53
(4)	11.07.2016	95.6	3097	79

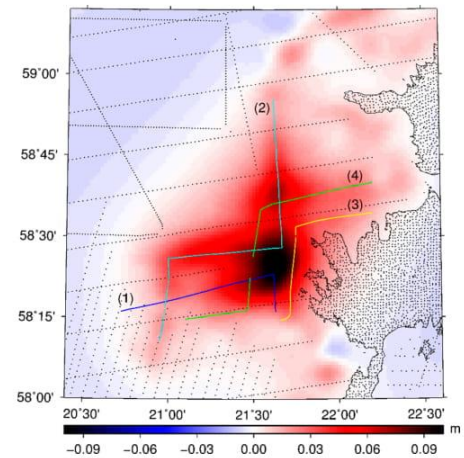


Fig. 6. Location of GNSS profiles within the area of the largest geoid model change gradient due to the newly collected JP gravity data. The black dots indicate the locations of previously existing gravity data available for the geoid modelling. The red tones denote the areas where Model 2 is lower than Model 1

Table 2. Statistics of differences between GNSS calculations using either TBC or CSRS-PPP compared to official NKG2015 geoid model

Software	Profile number	Mean (m) ¹	Min (m) ²	Max (m) ²	StDev (m)	Further averaged StDev (m)
TBC	(1)	5.905	-0.280	0.228	0.120	0.116
	(2)	6.012	-0.112	0.252	0.049	0.048
	(3)	6.112	-0.150	0.136	0.053	0.052
	(4)	6.223	-0.115	0.111	0.042	0.039
CSRS-PPP	(1)	5.957	-0.098	0.099	0.053	0.052
	(2)	5.973	-0.121	0.110	0.055	0.054
	(3)	6.126	-0.127	0.110	0.047	0.046
	(4)	6.216	-0.120	0.122	0.061	0.060

Notes: Statistics of the profile (4) analysed in Figure 3 (from 18:00 to 23:00) are high-lighted in red (see also Fig. 6 and Table 1).

¹ Mean difference between the low-pass filtered GNSS measurements and geoid height. GNSS antennae was approximately 6 m above sea surface.

² After removal of the mean difference between low-pass filtered GNSS measurements and geoid height (third column).

Table 3. Statistics of differences between GNSS measurements and geoid models within the area of the largest geoid model change gradient

Geoid model	Profile number	Mean (m) ¹	Min (m) ²	Max (m) ²	StDev (m)	Further averaged StDev (m)
NKG2015	(1)	5.905	-0.280	0.228	0.120	0.116
	(2)	6.015	-0.115	0.267	0.056	0.055
	(3)	6.112	-0.150	0.136	0.053	0.052
	(4)	6.223	-0.115	0.111	0.042	0.039
Model 1	(1)	5.309	-0.281	0.226	0.120	0.116
	(2)	5.418	-0.117	0.267	0.057	0.056
	(3)	5.514	-0.148	0.134	0.051	0.051
	(4)	5.624	-0.113	0.113	0.042	0.039
Model 2	(1)	5.353	-0.207	0.207	0.109	0.104
	(2)	5.466	-0.103	0.269	0.061	0.060
	(3)	5.558	-0.122	0.113	0.042	0.041
	(4)	5.666	-0.133	0.150	0.043	0.040

Note: Statistics of the profile (3) analysed in Figure 6 are high-lighted in red (see also Fig. 6 and Table 1).

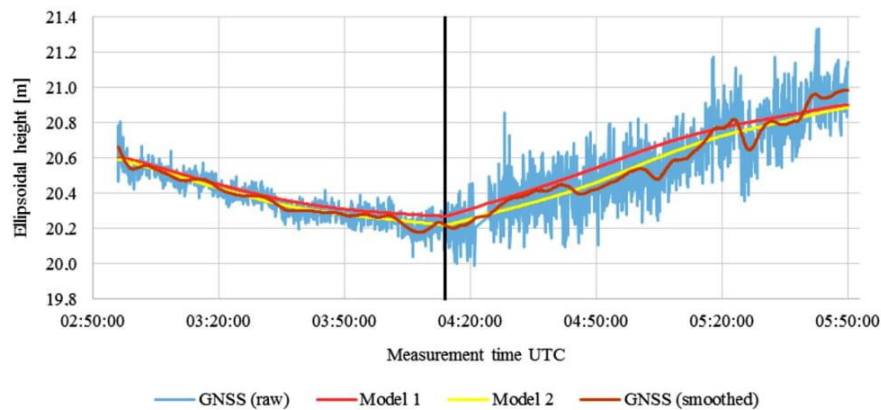


Fig. 7. An example of GNSS profile (3) compared to Model 1 and 2 geoid models (after removal of 1-dimensional offset \bar{H}). The vertical black line at 4:13 indicates the turning point of the vessel. The increase of measurements amplitude after the turn-point illustrates the effect of measurement conditions (rougher waters, most likely) on the GNSS results

As seen from Table 3, Model 1 is comparable in precision to the official NKG2015 geoid model. However, the precision of Model 2 (with the new gravimetric data collected on “Jakob Prei” during the experiment), with respect to the GNSS data, has improved at places (see Fig. 7). The largest improvement in the geoid model occurs in offshore areas with poor coverage of g -data points (see Fig. 6).

Conclusions

Ship-borne GNSS profiles prove to be an effective method to evaluate existing concurrent geoid models. For this, it is important to achieve precise GNSS height data. In the absence of close reference stations, online-PPP services are an option as they give sufficient precision for further data processing and are easy to use, requiring no previous experience in GNSS data processing.

During the study it became evident that appropriate smoothing of GNSS data is essential to assess the geoid models. It is also expected that accounting for the sea surface topography at GNSS profiles would improve the results, as well as using more than one GNSS antenna to remove errors from ships attitude.

The GNSS height profiles were used to evaluate geoid models West of Saaremaa, where the gravity data collected during the “Jakob Prei” campaign had the largest effect on the resulting geoid model. It was found that the model computed using the newly acquired gravity data agree better with the GNSS profiles.

This study can be considered as preparation for the planned marine gravity project to be carried out at the eastern end of Gulf of Finland (Narva Bay) in summer of 2017. The lessons learned will be considered

at elaborating methodology for densifying gravimetric data there and along the North-Estonian shores. Note also that instantaneous marine dynamic topography (e.g. occurring due to coastal currents and/or unidirectional wind) was neglected in the present exercise. For further studies, the Estonia adapted (by the Marine Systems Institute of TTÜ) sea surface topography model HIROMB-EST (for more details see Lagema 2012), will be tested.

Acknowledgements

This study was conducted within the frames of a Connecting Europe Facility (CEF) project “FAMOS (Finalising Surveys for the Baltic Motorways of the Sea) Odin” (VEU16013). The Estonian Maritime Agency is acknowledged for providing the hydrographic survey vessel “Jakob Prei” for the 2016 marine gravity campaign. R. Forsberg, A. V. Olesen and F. Kasenda of Danish Technical University are thanked for providing the GNSS-data and the processed gravimetric data. K. Kollo of the Estonian Land Board provided the GNSS-CORS data.

References

- Ågren, J.; Strykowski, G.; Bilker-Koivula, M.; Omang, O.; Mårdla, S.; Oja, T.; Liepinš, I.; Paršeliūnas, E.; Forsberg, R.; Kaminskis, J.; Ellmann, A.; Sjöberg, L.; Valsson, V. 2015. On the development of the new Nordic gravimetric geoid model NKG2015, in *26th IUGG General Assembly*, 22 June – 2 July 2015, Prague, Czech Republic.
- Ågren, J.; Strykowski, G.; Bilker-Koivula, M.; Omang, O.; Mårdla, S.; Forsberg, R.; Ellmann, A.; Oja, T.; Liepinš, I.; Paršeliūnas, E.; Kaminskis, J.; Sjöberg, L.; Valsson, G. 2016. The NKG2015 gravimetric geoid model for the Nordic-Baltic region, in *1st Joint Commission 2 and IGFS Meeting International Symposium on Gravity, Geoid and Height Systems*, 19–23 September 2016, Thessaloniki, Greece.

- APPS [online]. n.d. [cited 18 January 2017]. Available from Internet: <http://apps.gdgps.net/>
- Bruinsma, S. L.; Förste, C.; Abrikosov, O.; Lemoine, J.-M.; Marty, J.-C.; Mulet, S.; Rio, M.-H.; Bonvalot, S. 2014. ESA's satellite-only gravity field model via the direct approach based on all GOCE data, *Geophysical Research Letters* 41(21): 7508–7514. <https://doi.org/10.1002/2014GL062045>
- CSRS-PPP [online]. n.d. [cited 18 January 2017]. Available from Internet: <https://webapp.geod.nrcan.gc.ca/geod/tools-outils/ppp.php>
- Ellmann, A. 2002. An improved gravity anomaly grid and a geoid model for Estonia, *Proceedings of Estonian Academic Sciences, Geology* 51: 199–214.
- Ellmann, A. 2005. Two deterministic and three stochastic modifications of Stokes's formula: a case study for the Baltic countries, *Journal of Geodesy* 79: 11–23. <https://doi.org/10.1007/s00190-005-0438-1>
- Ellmann, A.; All, T.; Oja, T. 2009. Toward unification of terrestrial gravity datasets in Estonia, *Estonian Journal of Earth Sciences* 58(4): 229–245. <https://doi.org/10.3176/earth.2009.4.02>
- Ellmann, A. 2010. Validation of the new Earth Gravitational Model EGM08 over the Baltic countries, *International Association of Geodesy Symposia* 135: 489–496. https://doi.org/10.1007/978-3-642-10634-7_65
- FAMOS. 2017. *Finalising surveys for the Baltic Motorways of the Sea webpage*. [online], [cited 12 January 2017]. Available from Internet: <http://www.famosproject.eu/famos/>
- Forsberg, R.; Strykowski, G.; Solheim, D.; 2004. NKG-2004 geoid of the Nordic and Baltic Area, in *Proceedings of the IAG International Symposium "Gravity, Geoid and Satellite Gravity Missions"*, 30 August – 3 September 2004, Porto, Portugal. CD-ROM.
- GAPS [online]. n.d. [cited 18 January 2017]. Available from Internet: <http://gaps.gge.unb.ca/>
- Gruno, A.; Liibus, A.; Ellmann, A.; Oja, T.; Vain, A.; Jürgenson, H. 2013. Determining sea surface heights using small footprint airborne laser scanning, in *Proceedings SPIE 8888, Remote Sensing of the Ocean, Sea Ice, Coastal Waters, and Large Water Regions 2013*, 23 September 2013, Dresden, Germany. International Society for Optical Engineering, 88880R1–88880R13. <https://doi.org/10.1117/12.2029189>
- Héroux, P.; Kouba, J. 2001. GPS Precise Point positioning using IGS orbit products, *Physics and Chemistry of the Earth, Part A: Solid Earth and Geodesy* 26(6–8): 573–578. [https://doi.org/10.1016/S1464-1895\(01\)00103-X](https://doi.org/10.1016/S1464-1895(01)00103-X)
- Jürgenson, H.; Liibus, A.; Ellmann, A. 2008. Geoid profiles in the Baltic Sea determined using GPS and sea level surface, *Geodezija Ir Kartografija / Geodesy and Cartography* 34(4): 109–115.
- Lagemaa, P. 2012. Operational forecasting in Estonian marine waters: PhD thesis. Tallinn University of Technology, Tallinn.
- Lavrov, D.; Even-Tzur, G.; Reinking, J. 2016. Expansion and improvement of the Israeli geoid model by ship-borne GNSS measurements, *Journal of Surveying Engineering* 143(2). [https://doi.org/10.1061/\(ASCE\)SU.1943-5428.0000204](https://doi.org/10.1061/(ASCE)SU.1943-5428.0000204)
- Liibus, A.; Ellmann, A. 2015. Validation of marine geoid models by profile-wise GNSS measurements on ice surface, *Marine Geodesy* 38(4): 314–326. <https://doi.org/10.1080/01490419.2015.1037408>
- Liibus, A.; Talvik, S.; Ellmann, A.; Oja, T. 2014. Determining regional sea surface topography by GNSS surveys on ice, in *6th IEEE/OES Baltic Symposium 2014 "Measuring and Modeling of Multi-Scale Interactions in the Marine Environment"*, 26–29 May 2014, Tallinn, Estonia. IEEE, 1–8. <https://doi.org/10.1109/BALTIC.2014.6887847>
- Liibus, A.; Ellmann, A.; Kõuts, T.; Jürgenson, H. 2013. Precise Hydrodynamic Levelling by Using Pressure Gauges, *Marine Geodesy* 36(2): 138–163. <https://doi.org/10.1080/01490419.2013.771594>
- MagicGNSS [online]. n.d. [cited 18 January 2017]. Available from Internet: <https://magicgnss.gmv.com/>
- Märdla, S.; Ägren, J.; Strykowski, G.; Oja, T.; Ellmann, A.; Forsberg, R.; Bilker-Koivula, M.; Omang, O.; Paršeliūnas, E.; Liepinš, I.; Kaminskis, J. 2017. From discrete gravity survey data to a high-resolution gravity field representation in the Nordic-Baltic region, *Marine Geodesy* 40, (advance online publication). <https://doi.org/10.1080/01490419.2017.1326428>
- Märdla, S.; Oja, T.; Ellmann, A.; Jürgenson, H. 2015. Improving and validating gravity data over ice-covered marine areas, in C. Rizos, P. Willis (Eds.). *IAG 150 Years. International Association of Geodesy Symposia*, Vol. 143. Springer, 263–270. https://doi.org/10.1007/1345_2015_163
- Ocalan, T.; Erdogan, B.; Tunalıoglu, N. 2013. Analysis of web-based online services for GPS relative and precise point positioning techniques, *Boletim de Ciencias Geodesicas* 19(2): 191–207. <https://doi.org/10.1590/S1982-21702013000200003>
- Olesen, A. V.; Kasenda, F. 2016. *Marine gravity onboard Jakob Prey June/July 2016*, processing report. Danish Technical University (DTU).
- Sjöberg, L. E. 2003. A computational scheme to model the geoid by the modified Stokes formula without gravity reductions, *Journal of Geodesy* 77(7): 423–432. <https://doi.org/10.1007/s00190-003-0338-1>
- Wessel, P.; Smith, W. H. F.; Scharroo, R.; Luis, J.; Wobbe, F. 2013. Generic mapping tools: improved version released, *Eos, Transactions American Geophysical Union* 94(45): 409–410. <https://doi.org/10.1002/2013EO450001>
-
- Sander VARBLA**, master's student, Tallinn University of Technology, Department of Civil Engineering and Architecture, Road Engineering and Geodesy Research Group.
-
- Artu ELLMANN** received his MSc degree in geodesy from the Moscow State University of Geodesy and Cartography (formerly MIIGAiK) in 1993 and a PhD degree from the Royal Institute of Technology (KTH) in Stockholm in 2004. He is currently Professor in Geodesy at the Department of Civil Engineering and Architecture, School of Engineering at the TTÜ. National correspondent to the International Association of Geodesy (IAG) since 2006. His research interests include physical geodesy (gravity field and geoid modelling in particular) and remote sensing applications for engineering surveying.
-
- Silja MÄRDLA** received her MSc degree in geodesy from TTÜ, currently she is a PhD candidate and research scientist at Tallinn University of Technology focusing on gravity field and geoid modelling studies. She has also studied construction geodesy and terrestrial laser scanning related problems.
-
- Anti GRUNO**, received his MSc degree in geodesy from TTÜ, currently working Estonian Land Board Photogrammetry Department. Main task is Airborne Lidar scanning data processing.

APPENDIX B GNSS profiles compared to geoid models

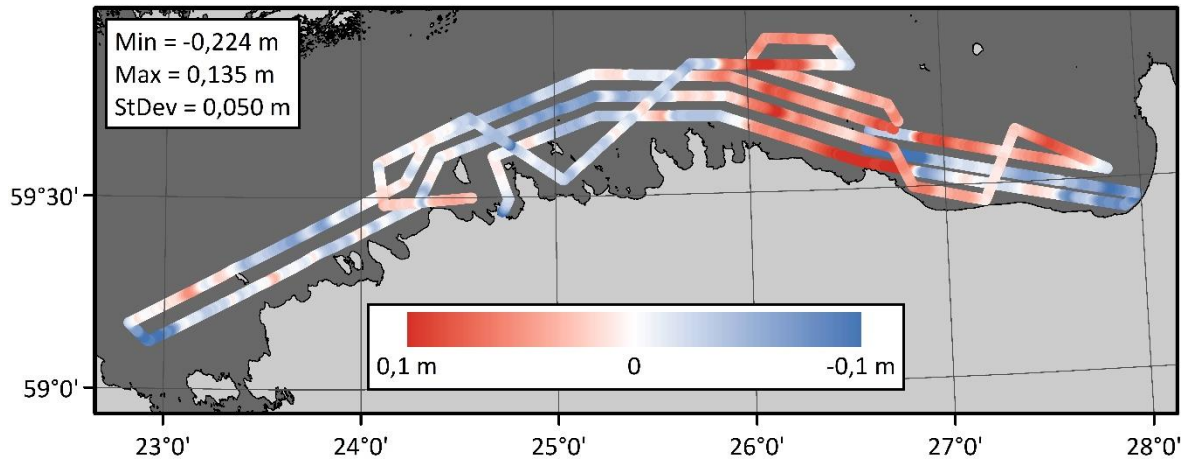


Figure B.1 EST-GEOID2011 deviations from the double low-pass filtered and corrected (DT and fuel consumption corrections; HBM-EST HDM is corrected with TGw method) TBC GNSS profile (see also Table 3.3). Assessment is conducted in BK77 height system.

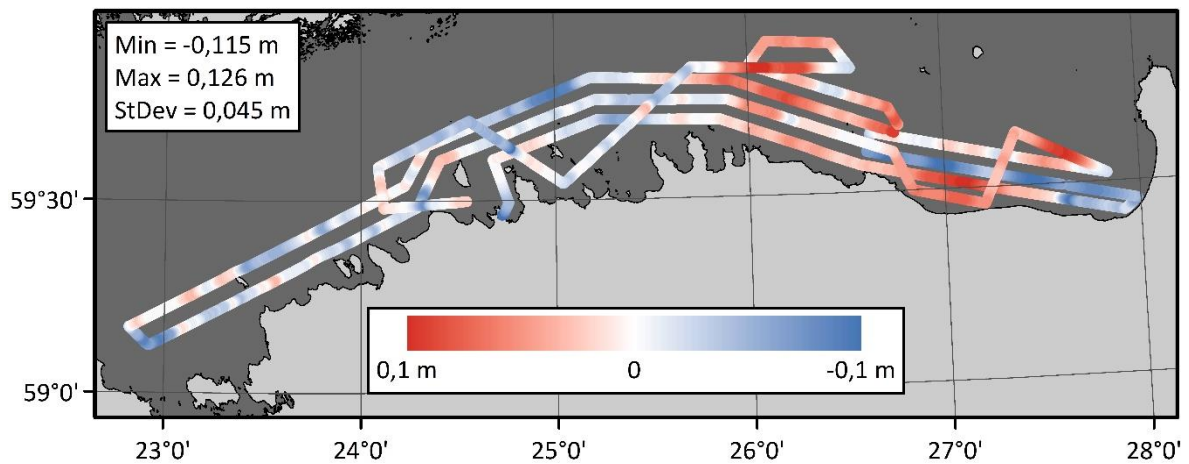


Figure B.2 EST-GEOID2011 deviations from the double low-pass filtered and corrected (DT and fuel consumption corrections; HBM-EST HDM is corrected with TGw method) NovAtel GNSS profile (see also Table 3.3). Assessment is conducted in BK77 height system.

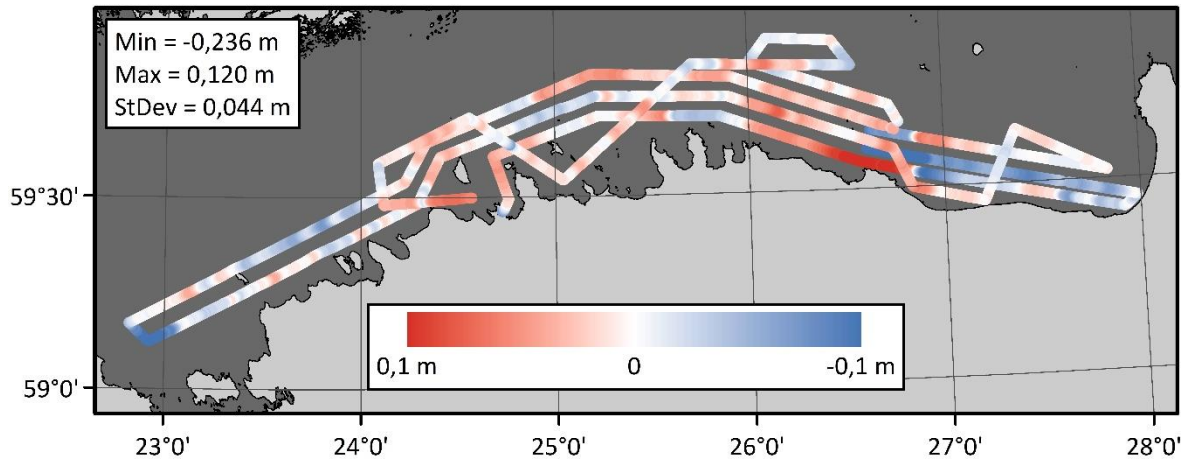


Figure B.3 EST-GEOID2017 deviations from the double low-pass filtered and corrected (DT and fuel consumption corrections; HBM-EST HDM is corrected with TGw method) TBC GNSS profile (see also Table 3.3). Assessment is conducted in EH2000 height system.

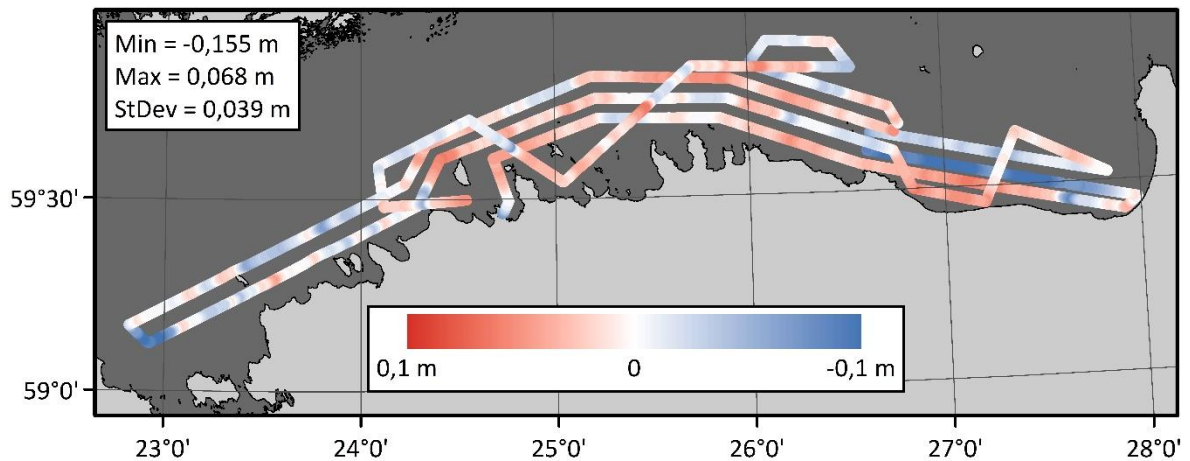


Figure B.4 EST-GEOID2017 deviations from the double low-pass filtered and corrected (DT and fuel consumption corrections; HBM-EST HDM is corrected with TGw method) NovAtel GNSS profile (see also Table 3.3). Assessment is conducted in EH2000 height system.

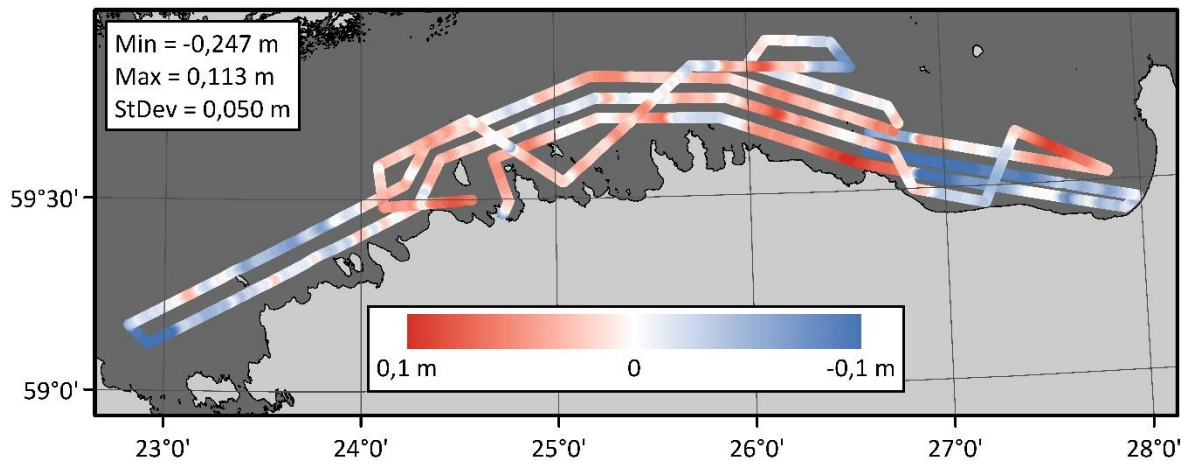


Figure B.5 NKG2015 deviations from the double low-pass filtered and corrected (DT and fuel consumption corrections; HBM-EST HDM is corrected with TGw method) TBC GNSS profile (see also Table 3.3). Assessment is conducted in EH2000 height system.

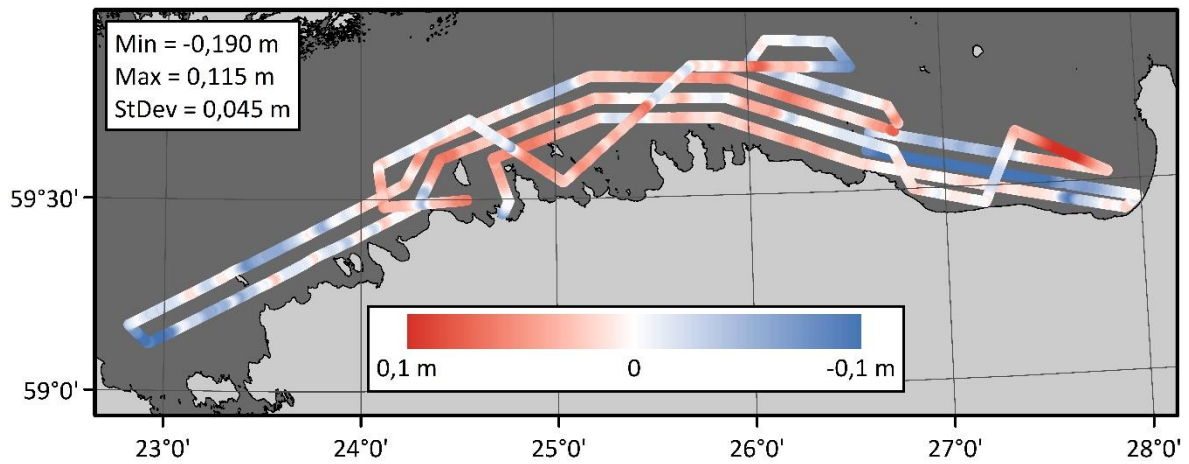


Figure B.6 NKG2015 deviations from the double low-pass filtered and corrected (DT and fuel consumption corrections; HBM-EST HDM is corrected with TGw method) NovAtel GNSS profile (see also Table 3.3). Assessment is conducted in EH2000 height system.

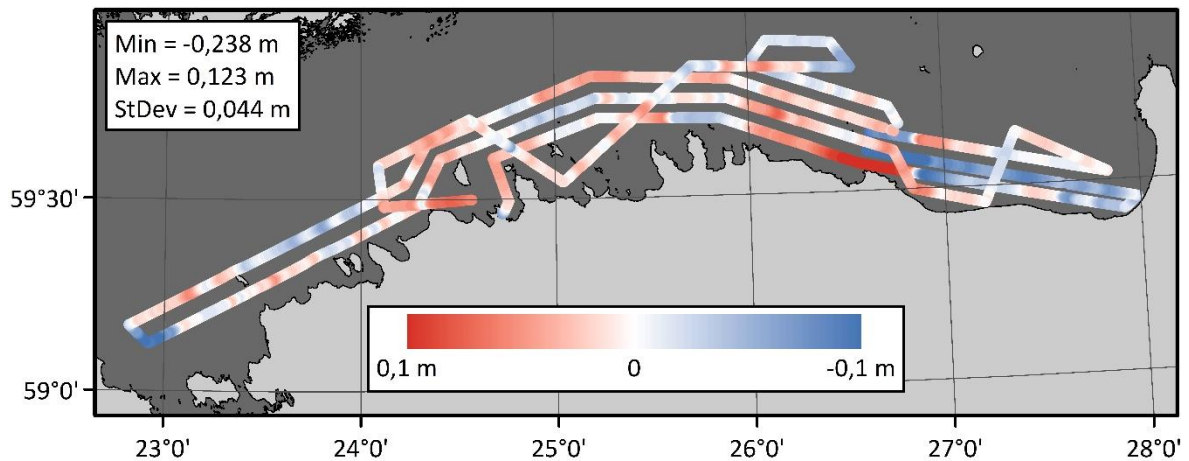


Figure B.7 FAMOS GOCO05s deviations from the double low-pass filtered and corrected (DT and fuel consumption corrections; HBM-EST HDM is corrected with TGw method) TBC GNSS profile (see also Table 3.3). Assessment is conducted in EH2000 height system.

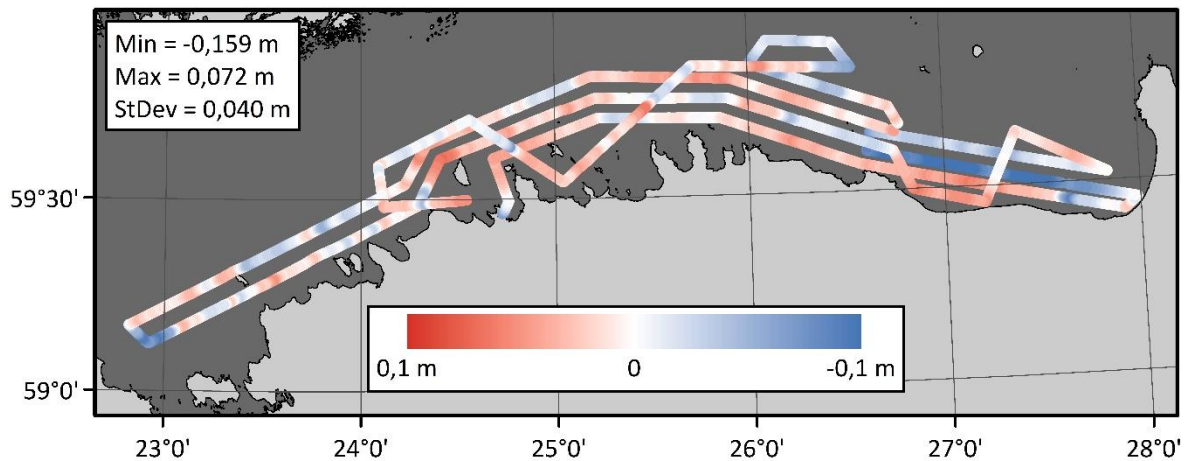


Figure B.8 FAMOS GOCO05s deviations from the double low-pass filtered and corrected (DT and fuel consumption corrections; HBM-EST HDM is corrected with TGw method) NovAtel GNSS profile (see also Table 3.3). Assessment is conducted in EH2000 height system.

APPENDIX C Comparisons of 2013 ALS data filtering results

Table C.1 Comparison between different filtering results of **ALS profile 08052013_090408**

(see Fig. 4.1). All profiles are compared to FAMOS GOCO05s geoid model. Profile length is 23,312 km. 377 profile points are included in the comparison. The smallest StDev value and deviation amplitude (maximum – minimum) are highlighted in red.

Profile type	Point cloud with noise		Cleaned point cloud	
	StDev (m)	Amplitude (m)	StDev (m)	Amplitude (m)
5x5m grid	0,6552	8,8785	0,0735	0,4069
50x50m grid	0,5930	8,0363	0,0651	0,3700
Averaging filter; Radius = 5	0,1694	1,1305	0,0380	0,2207
Averaging filter; Radius = 10	0,1240	0,6771	0,0352	0,1734
Averaging filter; Radius = 15	0,1147	0,5762	0,0350	0,1773
Exponential filter; Size = 5	0,1215	0,6643	0,0353	0,1835
Exponential filter; Size = 10	0,1103	0,5001	0,0343	0,1661
Exponential filter; Size = 15	0,1210	0,5760	0,0338	0,1633
Double low-pass filtered 5x5m grid	0,0549	0,1695	0,0325	0,1159
Double low-pass filtered 50x50m grid	0,0833	0,2470	0,0302	0,1274

Notes: Results of averaging and exponential filter are based on 5x5m grid filtering.

For double low-pass filtering results, a median of 51 profile points was taken first. From that outcome, an average of 51 profile points was then taken.

Table C.2 Comparison between different filtering results of **ALS profile 14052013_090928**

(see Fig. 4.1). All profiles are compared to FAMOS GOCO05s geoid model. Profile length is 5,146 km. 84 profile points are included in the comparison. The smallest StDev value and deviation amplitude (maximum – minimum) are highlighted in red.

Profile type	Point cloud with noise		Cleaned point cloud	
	StDev (m)	Amplitude (m)	StDev (m)	Amplitude (m)
5x5m grid	0,3756	2,9140	0,0614	0,3019
50x50m grid	0,6001	5,8451	0,0722	0,3352
Averaging filter; Radius = 5	0,1738	0,8383	0,0222	0,1029
Averaging filter; Radius = 10	0,1193	0,4772	0,0176	0,0684
Averaging filter; Radius = 15	0,1130	0,4478	0,0167	0,0624
Exponential filter; Size = 5	0,1209	0,5070	0,0173	0,0656
Exponential filter; Size = 10	0,1036	0,3545	0,0154	0,0525
Exponential filter; Size = 15	0,0963	0,3253	0,0141	0,0484
Double low-pass filtered 5x5m grid	0,0059	0,0210	0,0022	0,0092
Double low-pass filtered 50x50m grid	0,0183	0,0782	0,0054	0,0211

Notes: Results of averaging and exponential filter are based on 5x5m grid filtering.

For double low-pass filtering results, a median of 51 profile points was taken first. From that outcome, an average of 51 profile points was then taken.

Table C.3 Comparison between different filtering results of **ALS profile 14052013_091945**

(see Fig. 4.1). All profiles are compared to FAMOS GOCO05s geoid model. Profile length is 15,190 km. 246 profile points are included in the comparison. The smallest StDev value and deviation amplitude (maximum – minimum) are highlighted in red.

Profile type	Point cloud with noise		Cleaned point cloud	
	StDev (m)	Amplitude (m)	StDev (m)	Amplitude (m)
5x5m grid	0,7478	9,5476	0,0534	0,2745
50x50m grid	0,8699	11,5669	0,0466	0,3645
Averaging filter; Radius = 5	0,2876	1,6692	0,0281	0,1918
Averaging filter; Radius = 10	0,2365	1,7909	0,0267	0,1335
Averaging filter; Radius = 15	0,4007	5,6735	0,0270	0,1145
Exponential filter; Size = 5	0,3190	3,8446	0,0257	0,1261
Exponential filter; Size = 10	0,4246	5,0342	0,0253	0,1065
Exponential filter; Size = 15	0,4536	4,7647	0,0256	0,1096
Double low-pass filtered 5x5m grid	0,0747	0,3080	0,0137	0,0479
Double low-pass filtered 50x50m grid	0,0140	0,0515	0,0148	0,0543

Notes: Results of averaging and exponential filter are based on 5x5m grid filtering.

For double low-pass filtering results, a median of 51 profile points was taken first. From that outcome, an average of 51 profile points was then taken.

Table C.4 Comparison between different filtering results of **ALS profile 14052013_092746**

(see Fig. 4.1). All profiles are compared to FAMOS GOCO05s geoid model. Profile length is 17,546 km. 284 profile points are included in the comparison. The smallest StDev value and deviation amplitude (maximum – minimum) are highlighted in red.

Profile type	Point cloud with noise		Cleaned point cloud	
	StDev (m)	Amplitude (m)	StDev (m)	Amplitude (m)
5x5m grid	0,4930	5,3580	0,0504	0,2989
50x50m grid	0,4803	7,6187	0,0499	0,3076
Averaging filter; Radius = 5	0,2094	2,7463	0,0240	0,1586
Averaging filter; Radius = 10	0,2317	2,3013	0,0245	0,1423
Averaging filter; Radius = 15	0,2937	2,7604	0,0249	0,1350
Exponential filter; Size = 5	0,2426	2,3599	0,0238	0,1404
Exponential filter; Size = 10	0,3197	2,2056	0,0228	0,1177
Exponential filter; Size = 15	0,3592	2,5668	0,0216	0,1041
Double low-pass filtered 5x5m grid	0,0051	0,0182	0,0118	0,0426
Double low-pass filtered 50x50m grid	0,0173	0,0676	0,0121	0,0443

Notes: Results of averaging and exponential filter are based on 5x5m grid filtering.

For double low-pass filtering results, a median of 51 profile points was taken first. From that outcome, an average of 51 profile points was then taken.

Table C.5 Comparison between different filtering results of **ALS profile 14052013_093645**

(see Fig. 4.1). All profiles are compared to FAMOS GOCO05s geoid model. Profile length is 63,054 km. 1018 profile points are included in the comparison. The smallest StDev value and deviation amplitude (maximum – minimum) are highlighted in red.

Profile type	Point cloud with noise		Cleaned point cloud	
	StDev (m)	Amplitude (m)	StDev (m)	Amplitude (m)
5x5m grid	0,3228	5,1071	0,0463	0,3865
50x50m grid	0,3984	8,6599	0,0443	0,2742
Averaging filter; Radius = 5	0,1142	1,3174	0,0185	0,1432
Averaging filter; Radius = 10	0,0819	0,9203	0,0174	0,1236
Averaging filter; Radius = 15	0,0645	0,7560	0,0174	0,1275
Exponential filter; Size = 5	0,0773	0,8566	0,0173	0,1308
Exponential filter; Size = 10	0,0609	0,7997	0,0175	0,1339
Exponential filter; Size = 15	0,0638	0,8054	0,0178	0,1370
Double low-pass filtered 5x5m grid	0,0130	0,0650	0,0112	0,0558
Double low-pass filtered 50x50m grid	0,0131	0,0770	0,0136	0,0630

Notes: Results of averaging and exponential filter are based on 5x5m grid filtering.

For double low-pass filtering results, a median of 51 profile points was taken first. From that outcome, an average of 51 profile points was then taken.

Table C.6 Comparison between different filtering results of **ALS profile 14052013_095527**

(see Fig. 4.1). All profiles are compared to FAMOS GOCO05s geoid model. Profile length is 19,406 km. 314 profile points are included in the comparison. The smallest StDev value and deviation amplitude (maximum – minimum) are highlighted in red.

Profile type	Point cloud with noise		Cleaned point cloud	
	StDev (m)	Amplitude (m)	StDev (m)	Amplitude (m)
5x5m grid	0,1669	1,8344	0,0463	0,2633
50x50m grid	0,3239	4,9946	0,0445	0,2503
Averaging filter; Radius = 5	0,1211	1,6401	0,0261	0,1716
Averaging filter; Radius = 10	0,0999	1,4299	0,0257	0,1646
Averaging filter; Radius = 15	0,0769	1,0124	0,0259	0,1554
Exponential filter; Size = 5	0,0851	1,1336	0,0255	0,1584
Exponential filter; Size = 10	0,0568	0,6841	0,0256	0,1464
Exponential filter; Size = 15	0,0446	0,5089	0,0255	0,1395
Double low-pass filtered 5x5m grid	0,0146	0,0509	0,0209	0,0635
Double low-pass filtered 50x50m grid	0,0290	0,0919	0,0174	0,0596

Notes: Results of averaging and exponential filter are based on 5x5m grid filtering.

For double low-pass filtering results, a median of 51 profile points was taken first. From that outcome, an average of 51 profile points was then taken.

Table C.7 Comparison between different filtering results of **ALS profile 14052013_100143**

(see Fig. 4.1). All profiles are compared to FAMOS GOCO05s geoid model. Profile length is 19,778 km. 320 profile points are included in the comparison. The smallest StDev value and deviation amplitude (maximum – minimum) are highlighted in red.

Profile type	Point cloud with noise		Cleaned point cloud	
	StDev (m)	Amplitude (m)	StDev (m)	Amplitude (m)
5x5m grid	0,3870	6,2903	0,0581	0,3145
50x50m grid	0,3169	4,4581	0,0544	0,3435
Averaging filter; Radius = 5	0,0961	1,3396	0,0390	0,2703
Averaging filter; Radius = 10	0,0590	0,4907	0,0388	0,2646
Averaging filter; Radius = 15	0,0518	0,3516	0,0389	0,2655
Exponential filter; Size = 5	0,0606	0,6755	0,0387	0,2579
Exponential filter; Size = 10	0,0502	0,4326	0,0388	0,2552
Exponential filter; Size = 15	0,0561	0,4406	0,0386	0,2454
Double low-pass filtered 5x5m grid	0,0235	0,1013	0,0264	0,1135
Double low-pass filtered 50x50m grid	0,0272	0,1186	0,0220	0,0961

Notes: Results of averaging and exponential filter are based on 5x5m grid filtering.

For double low-pass filtering results, a median of 51 profile points was taken first. From that outcome, an average of 51 profile points was then taken.

Table C.8 Comparison between different filtering results of **ALS profile 14052013_101501**

(see Fig. 4.1). All profiles are compared to FAMOS GOCO05s geoid model. Profile length is 85,188 km. 1375 profile points are included in the comparison. The smallest StDev value and deviation amplitude (maximum – minimum) are highlighted in red.

Profile type	Point cloud with noise		Cleaned point cloud	
	StDev (m)	Amplitude (m)	StDev (m)	Amplitude (m)
5x5m grid	0,5771	14,2966	0,0716	0,4671
50x50m grid	0,5710	12,7634	0,0708	0,4733
Averaging filter; Radius = 5	0,2619	1,7765	0,0615	0,2478
Averaging filter; Radius = 10	0,2280	1,4750	0,0611	0,2456
Averaging filter; Radius = 15	0,2077	1,3078	0,0610	0,2424
Exponential filter; Size = 5	0,2226	1,3404	0,0608	0,2415
Exponential filter; Size = 10	0,1990	1,7928	0,0601	0,2339
Exponential filter; Size = 15	0,1908	2,0324	0,0595	0,2288
Double low-pass filtered 5x5m grid	0,1589	0,7663	0,0571	0,2006
Double low-pass filtered 50x50m grid	0,1399	0,6429	0,0568	0,2026

Notes: Results of averaging and exponential filter are based on 5x5m grid filtering.

For double low-pass filtering results, a median of 51 profile points was taken first. From that outcome, an average of 51 profile points was then taken.

Table C.9 Comparison between different filtering results of **ALS profile 14052013_133440**

(see Fig. 4.1). All profiles are compared to FAMOS GOCO05s geoid model. Profile length is 64,852 km. 1047 profile points are included in the comparison. The smallest StDev value and deviation amplitude (maximum – minimum) are highlighted in red.

Profile type	Point cloud with noise		Cleaned point cloud	
	StDev (m)	Amplitude (m)	StDev (m)	Amplitude (m)
5x5m grid	0,9231	10,2338	0,0553	0,4155
50x50m grid	0,8546	11,3280	0,0496	0,3737
Averaging filter; Radius = 5	0,4387	1,8872	0,0322	0,1688
Averaging filter; Radius = 10	0,4042	1,4233	0,0319	0,1608
Averaging filter; Radius = 15	0,3874	2,1551	0,0321	0,1667
Exponential filter; Size = 5	0,3965	1,6432	0,0318	0,1595
Exponential filter; Size = 10	0,3811	2,0714	0,0324	0,1659
Exponential filter; Size = 15	0,3815	2,2125	0,0330	0,1640
Double low-pass filtered 5x5m grid	0,3003	0,8878	0,0265	0,0897
Double low-pass filtered 50x50m grid	0,2585	0,7603	0,0233	0,0850

Notes: Results of averaging and exponential filter are based on 5x5m grid filtering.

For double low-pass filtering results, a median of 51 profile points was taken first. From that outcome, an average of 51 profile points was then taken.

Table C.10 Comparison between different filtering results of **ALS profile 14052013_135301**

(see Fig. 4.1). All profiles are compared to FAMOS GOCO05s geoid model. Profile length is 59,892 km. 967 profile points are included in the comparison. The smallest StDev value and deviation amplitude (maximum – minimum) are highlighted in red.

Profile type	Point cloud with noise		Cleaned point cloud	
	StDev (m)	Amplitude (m)	StDev (m)	Amplitude (m)
5x5m grid	0,8643	9,2787	0,0509	0,3042
50x50m grid	0,9166	10,1095	0,0479	0,3064
Averaging filter; Radius = 5	0,3784	1,9160	0,0324	0,1639
Averaging filter; Radius = 10	0,3537	1,7928	0,0314	0,1662
Averaging filter; Radius = 15	0,3703	4,3666	0,0305	0,1625
Exponential filter; Size = 5	0,3478	3,0403	0,0308	0,1558
Exponential filter; Size = 10	0,3533	4,2101	0,0296	0,1522
Exponential filter; Size = 15	0,3546	4,2384	0,0289	0,1496
Double low-pass filtered 5x5m grid	0,2145	0,7076	0,0215	0,0772
Double low-pass filtered 50x50m grid	0,2156	0,7707	0,0234	0,0843

Notes: Results of averaging and exponential filter are based on 5x5m grid filtering.

For double low-pass filtering results, a median of 51 profile points was taken first. From that outcome, an average of 51 profile points was then taken.

APPENDIX D Comparisons of 2018 ALS data filtering results

Table D.1 Comparison between different filtering results of **ALS profile 10052018_084035**

(see Fig. 4.4). All profiles are compared to FAMOS GOCO05s geoid model. Profile length is 16,802 km. 272 profile points are included in the comparison. Three smallest StDev values and deviation amplitudes (maximum – minimum) are highlighted in red.

Profile type	StDev (m)	Amplitude (m)
5x5m grid (C1)	0,0380	0,2225
50x50m grid (C1)	0,0392	0,2370
Averaging filter; Radius = 5 (C1)	0,0076	0,0400
Averaging filter; Radius = 10 (C1)	0,0065	0,0309
Averaging filter; Radius = 15 (C1)	0,0062	0,0284
Exponential filter; Size = 5 (C1)	0,0063	0,0283
Exponential filter; Size = 10 (C1)	0,0061	0,0275
Exponential filter; Size = 15 (C1)	0,0160	0,2299
Double low-pass filtered 5x5m grid (C1)	0,0077	0,0430
Double low-pass filtered 50x50m grid (C1)	0,0116	0,0630
5x5m raster (C2)	0,0359	0,1971
50x50m grid (C2)	0,0393	0,2333
Averaging filter; Radius = 5 (C2)	0,0074	0,0364
Averaging filter; Radius = 10 (C2)	0,0062	0,0287
Averaging filter; Radius = 15 (C2)	0,00576	0,0247
Exponential filter; Size = 5 (C2)	0,0060	0,0274
Exponential filter; Size = 10 (C2)	0,00575	0,0308
Exponential filter; Size = 15 (C2)	0,0159	0,2130
Double low-pass filtered 5x5m grid (C2)	0,0074	0,0389
Double low-pass filtered 50x50m grid (C2)	0,0108	0,0472

Continuation of Table D.1

Profile type	StDev (m)	Amplitude (m)
5x5m raster (C1 + C2)	0,0289	0,1944
50x50m grid (C1 + C2)	0,0289	0,1696
Averaging filter; Radius = 5 (C1 + C2)	0,0068	0,0338
Averaging filter; Radius = 10 (C1 + C2)	0,0060	0,0249
Averaging filter; Radius = 15 (C1 + C2)	0,00582	0,0242
Exponential filter; Size = 5 (C1 + C2)	0,0059	0,0238
Exponential filter; Size = 10 (C1 + C2)	0,00583	0,0282
Exponential filter; Size = 15 (C1 + C2)	0,0155	0,2197
Double low-pass filtered 5x5m grid (C1 + C2)	0,0071	0,0385
Double low-pass filtered 50x50m grid (C1 + C2)	0,0107	0,0533

Notes: For C1 + C2 results, each profile point is an average value of C1 and C2 heights at the same location.

Results of averaging and exponential filter are based on 5x5m grid filtering.

For double low-pass filtering results, a median of 51 profile points was taken first. From that outcome, an average of 51 profile points was then taken.

Table D.2 Comparison between different filtering results of **ALS profile 10052018_084640**

(see Fig. 4.4). All profiles are compared to FAMOS GOCO05s geoid model. Profile length is 22,010 km. 356 profile points are included in the comparison. Three smallest StDev values and deviation amplitudes (maximum – minimum) are highlighted in red.

Profile type	StDev (m)	Amplitude (m)
5x5m grid (C1)	0,0541	0,4040
50x50m grid (C1)	0,0381	0,2486
Averaging filter; Radius = 5 (C1)	0,0102	0,0551
Averaging filter; Radius = 10 (C1)	0,0097	0,0394
Averaging filter; Radius = 15 (C1)	0,0095	0,0382
Exponential filter; Size = 5 (C1)	0,0096	0,0388
Exponential filter; Size = 10 (C1)	0,0095	0,0369
Exponential filter; Size = 15 (C1)	0,0095	0,0363
Double low-pass filtered 5x5m grid (C1)	0,0035	0,0192
Double low-pass filtered 50x50m grid (C1)	0,0055	0,0209
5x5m raster (C2)	0,0562	0,3614
50x50m grid (C2)	0,0407	0,3140
Averaging filter; Radius = 5 (C2)	0,0104	0,0978
Averaging filter; Radius = 10 (C2)	0,0090	0,0392
Averaging filter; Radius = 15 (C2)	0,0089	0,0386
Exponential filter; Size = 5 (C2)	0,0090	0,0383
Exponential filter; Size = 10 (C2)	0,0089	0,0356
Exponential filter; Size = 15 (C2)	0,0088	0,0350
Double low-pass filtered 5x5m grid (C2)	0,0119	0,0409
Double low-pass filtered 50x50m grid (C2)	0,0043	0,0169

Profile type	StDev (m)	Amplitude (m)
5x5m raster (C1 + C2)	0,0393	0,3470
50x50m grid (C1 + C2)	0,0279	0,1665
Averaging filter; Radius = 5 (C1 + C2)	0,0098	0,0756
Averaging filter; Radius = 10 (C1 + C2)	0,0092	0,0373
Averaging filter; Radius = 15 (C1 + C2)	0,0091	0,0371
Exponential filter; Size = 5 (C1 + C2)	0,0092	0,0370
Exponential filter; Size = 10 (C1 + C2)	0,0091	0,0355
Exponential filter; Size = 15 (C1 + C2)	0,0091	0,0352
Double low-pass filtered 5x5m grid (C1 + C2)	0,0057	0,0220
Double low-pass filtered 50x50m grid (C1 + C2)	0,0039	0,0149

Notes: For C1 + C2 results, each profile point is an average value of C1 and C2 heights at the same location.

Results of averaging and exponential filter are based on 5x5m grid filtering.

For double low-pass filtering results, a median of 51 profile points was taken first. From that outcome, an average of 51 profile points was then taken.

Table D.3 Comparison between different filtering results of **ALS profile 10052018_085356**

(see Fig. 4.4). All profiles are compared to FAMOS GOCO05s geoid model. Profile length is 12,214 km. 198 profile points are included in the comparison. Three smallest StDev values and deviation amplitudes (maximum – minimum) are highlighted in red.

Profile type	StDev (m)	Amplitude (m)
5x5m grid (C1)	0,0446	0,2456
50x50m grid (C1)	0,0522	0,3827
Averaging filter; Radius = 5 (C1)	0,0115	0,0558
Averaging filter; Radius = 10 (C1)	0,0100	0,0467
Averaging filter; Radius = 15 (C1)	0,0100	0,0413
Exponential filter; Size = 5 (C1)	0,0102	0,0442
Exponential filter; Size = 10 (C1)	0,0098	0,0391
Exponential filter; Size = 15 (C1)	0,0097	0,0377
Double low-pass filtered 5x5m grid (C1)	0,0070	0,0218
Double low-pass filtered 50x50m grid (C1)	0,0146	0,0432
5x5m raster (C2)	0,0414	0,2397
50x50m grid (C2)	0,0466	0,2432
Averaging filter; Radius = 5 (C2)	0,0110	0,0537
Averaging filter; Radius = 10 (C2)	0,0095	0,0442
Averaging filter; Radius = 15 (C2)	0,0093	0,0423
Exponential filter; Size = 5 (C2)	0,0096	0,0437
Exponential filter; Size = 10 (C2)	0,0092	0,0380
Exponential filter; Size = 15 (C2)	0,0092	0,0371
Double low-pass filtered 5x5m grid (C2)	0,0074	0,0370
Double low-pass filtered 50x50m grid (C2)	0,0073	0,0289

Continuation of Table D.3

Profile type	StDev (m)	Amplitude (m)
5x5m raster (C1 + C2)	0,0311	0,1826
50x50m grid (C1 + C2)	0,0350	0,2326
Averaging filter; Radius = 5 (C1 + C2)	0,0103	0,0482
Averaging filter; Radius = 10 (C1 + C2)	0,0095	0,0446
Averaging filter; Radius = 15 (C1 + C2)	0,0095	0,0399
Exponential filter; Size = 5 (C1 + C2)	0,0097	0,0416
Exponential filter; Size = 10 (C1 + C2)	0,0095	0,0382
Exponential filter; Size = 15 (C1 + C2)	0,0094	0,0372
Double low-pass filtered 5x5m grid (C1 + C2)	0,0057	0,0269
Double low-pass filtered 50x50m grid (C1 + C2)	0,0104	0,0331

Notes: For C1 + C2 results, each profile point is an average value of C1 and C2 heights at the same location.

Results of averaging and exponential filter are based on 5x5m grid filtering.

For double low-pass filtering results, a median of 51 profile points was taken first. From that outcome, an average of 51 profile points was then taken.

Table D.4 Comparison between different filtering results of **ALS profile 10052018_085829**

(see Fig. 4.4). All profiles are compared to FAMOS GOCO05s geoid model. Profile length is 58,032 km. 937 profile points are included in the comparison. Three smallest StDev values and deviation amplitudes (maximum – minimum) are highlighted in red.

Profile type	StDev (m)	Amplitude (m)
5x5m grid (C1)	0,0998	0,6573
50x50m grid (C1)	0,0628	0,4975
Averaging filter; Radius = 5 (C1)	0,0129	0,0729
Averaging filter; Radius = 10 (C1)	0,0115	0,0998
Averaging filter; Radius = 15 (C1)	0,0112	0,0638
Exponential filter; Size = 5 (C1)	0,0116	0,1177
Exponential filter; Size = 10 (C1)	0,0112	0,0853
Exponential filter; Size = 15 (C1)	0,0110	0,0643
Double low-pass filtered 5x5m grid (C1)	0,0176	0,1010
Double low-pass filtered 50x50m grid (C1)	0,0169	0,0820
5x5m raster (C2)	0,0974	0,6888
50x50m grid (C2)	0,0644	0,4332
Averaging filter; Radius = 5 (C2)	0,0122	0,0708
Averaging filter; Radius = 10 (C2)	0,0106	0,0552
Averaging filter; Radius = 15 (C2)	0,01043	0,0518
Exponential filter; Size = 5 (C2)	0,0106	0,0541
Exponential filter; Size = 10 (C2)	0,0103	0,0531
Exponential filter; Size = 15 (C2)	0,0118	0,1204
Double low-pass filtered 5x5m grid (C2)	0,0172	0,0841
Double low-pass filtered 50x50m grid (C2)	0,0095	0,0476

Continuation of Table D.4

Profile type	StDev (m)	Amplitude (m)
5x5m raster (C1 + C2)	0,0851	0,6011
50x50m grid (C1 + C2)	0,0461	0,3330
Averaging filter; Radius = 5 (C1 + C2)	0,0118	0,0701
Averaging filter; Radius = 10 (C1 + C2)	0,0106	0,0602
Averaging filter; Radius = 15 (C1 + C2)	0,0105	0,0566
Exponential filter; Size = 5 (C1 + C2)	0,0106	0,0636
Exponential filter; Size = 10 (C1 + C2)	0,01041	0,0545
Exponential filter; Size = 15 (C1 + C2)	0,0109	0,0839
Double low-pass filtered 5x5m grid (C1 + C2)	0,0151	0,0873
Double low-pass filtered 50x50m grid (C1 + C2)	0,0121	0,0614

Notes: For C1 + C2 results, each profile point is an average value of C1 and C2 heights at the same location.

Results of averaging and exponential filter are based on 5x5m grid filtering.

For double low-pass filtering results, a median of 51 profile points was taken first. From that outcome, an average of 51 profile points was then taken.

Table D.5 Comparison between different filtering results of **ALS profile 10052018_092024**

(see Fig. 4.4). All profiles are compared to FAMOS GOCO05s geoid model. Profile length is 13,764 km. 223 profile points are included in the comparison. Three smallest StDev values and deviation amplitudes (maximum – minimum) are highlighted in red.

Profile type	StDev (m)	Amplitude (m)
5x5m grid (C1)	0,1260	0,7635
50x50m grid (C1)	0,0829	0,4124
Averaging filter; Radius = 5 (C1)	0,0133	0,0572
Averaging filter; Radius = 10 (C1)	0,0106	0,0447
Averaging filter; Radius = 15 (C1)	0,0104	0,0414
Exponential filter; Size = 5 (C1)	0,0106	0,0437
Exponential filter; Size = 10 (C1)	0,0104	0,0394
Exponential filter; Size = 15 (C1)	0,0111	0,0647
Double low-pass filtered 5x5m grid (C1)	0,0147	0,0532
Double low-pass filtered 50x50m grid (C1)	0,0101	0,0356
5x5m raster (C2)	0,1329	0,7062
50x50m grid (C2)	0,0852	0,4770
Averaging filter; Radius = 5 (C2)	0,0103	0,0529
Averaging filter; Radius = 10 (C2)	0,0061	0,0323
Averaging filter; Radius = 15 (C2)	0,0052	0,0277
Exponential filter; Size = 5 (C2)	0,0054	0,0252
Exponential filter; Size = 10 (C2)	0,0048	0,0221
Exponential filter; Size = 15 (C2)	0,0047	0,0204
Double low-pass filtered 5x5m grid (C2)	0,0143	0,0470
Double low-pass filtered 50x50m grid (C2)	0,0110	0,0350

Profile type	StDev (m)	Amplitude (m)
5x5m raster (C1 + C2)	0,1163	0,6750
50x50m grid (C1 + C2)	0,0601	0,3084
Averaging filter; Radius = 5 (C1 + C2)	0,0108	0,0528
Averaging filter; Radius = 10 (C1 + C2)	0,0078	0,0363
Averaging filter; Radius = 15 (C1 + C2)	0,0073	0,0296
Exponential filter; Size = 5 (C1 + C2)	0,0075	0,0336
Exponential filter; Size = 10 (C1 + C2)	0,0072	0,0278
Exponential filter; Size = 15 (C1 + C2)	0,0075	0,0374
Double low-pass filtered 5x5m grid (C1 + C2)	0,0133	0,0496
Double low-pass filtered 50x50m grid (C1 + C2)	0,0082	0,0251

Notes: For C1 + C2 results, each profile point is an average value of C1 and C2 heights at the same location.

Results of averaging and exponential filter are based on 5x5m grid filtering.

For double low-pass filtering results, a median of 51 profile points was taken first. From that outcome, an average of 51 profile points was then taken.

Table D.6 Comparison between different filtering results of **ALS profile 10052018_093037**

(see Fig. 4.4). All profiles are compared to FAMOS GOCO05s geoid model. Profile length is 41,106 km. 664 profile points are included in the comparison. Three smallest StDev values and deviation amplitudes (maximum – minimum) are highlighted in red.

Profile type	StDev (m)	Amplitude (m)
5x5m grid (C1)	0,1098	0,6410
50x50m grid (C1)	0,0952	0,5853
Averaging filter; Radius = 5 (C1)	0,0106	0,0657
Averaging filter; Radius = 10 (C1)	0,0073	0,0476
Averaging filter; Radius = 15 (C1)	0,0066	0,0371
Exponential filter; Size = 5 (C1)	0,0070	0,0409
Exponential filter; Size = 10 (C1)	0,0064	0,0342
Exponential filter; Size = 15 (C1)	0,0062	0,0311
Double low-pass filtered 5x5m grid (C1)	0,0203	0,1081
Double low-pass filtered 50x50m grid (C1)	0,0190	0,0846
5x5m raster (C2)	0,1105	0,6594
50x50m grid (C2)	0,0958	0,6011
Averaging filter; Radius = 5 (C2)	0,0110	0,0670
Averaging filter; Radius = 10 (C2)	0,0076	0,0445
Averaging filter; Radius = 15 (C2)	0,0069	0,0348
Exponential filter; Size = 5 (C2)	0,0072	0,0367
Exponential filter; Size = 10 (C2)	0,0067	0,0346
Exponential filter; Size = 15 (C2)	0,0065	0,0326
Double low-pass filtered 5x5m grid (C2)	0,0138	0,0566
Double low-pass filtered 50x50m grid (C2)	0,0123	0,0656

Continuation of Table D.6

Profile type	StDev (m)	Amplitude (m)
5x5m raster (C1 + C2)	0,1045	0,5706
50x50m grid (C1 + C2)	0,0730	0,4732
Averaging filter; Radius = 5 (C1 + C2)	0,0102	0,0605
Averaging filter; Radius = 10 (C1 + C2)	0,0072	0,0441
Averaging filter; Radius = 15 (C1 + C2)	0,0066	0,0358
Exponential filter; Size = 5 (C1 + C2)	0,0069	0,0385
Exponential filter; Size = 10 (C1 + C2)	0,0065	0,0338
Exponential filter; Size = 15 (C1 + C2)	0,0063	0,0317
Double low-pass filtered 5x5m grid (C1 + C2)	0,0158	0,0821
Double low-pass filtered 50x50m grid (C1 + C2)	0,0142	0,0730

Notes: For C1 + C2 results, each profile point is an average value of C1 and C2 heights at the same location.

Results of averaging and exponential filter are based on 5x5m grid filtering.

For double low-pass filtering results, a median of 51 profile points was taken first. From that outcome, an average of 51 profile points was then taken.

Table D.7 Comparison between different filtering results of **ALS profile 10052018_094208**

(see Fig. 4.4) **before removing data covering land areas**. All profiles are compared to FAMOS GOCO05s geoid model. Profile length is 27,838 km. 450 profile points are included in the comparison. Three smallest StDev values and deviation amplitudes (maximum – minimum) are highlighted in red.

Profile type	StDev (m)	Amplitude (m)
5x5m grid (C1)	0,5823	10,7770
50x50m grid (C1)	1,0430	19,0813
Averaging filter; Radius = 5 (C1)	0,7527	13,8881
Averaging filter; Radius = 10 (C1)	0,6937	12,1900
Averaging filter; Radius = 15 (C1)	0,6261	10,1424
Exponential filter; Size = 5 (C1)	0,6486	11,1551
Exponential filter; Size = 10 (C1)	0,5052	7,6930
Exponential filter; Size = 15 (C1)	0,4146	5,6135
Double low-pass filtered 5x5m grid (C1)	0,0205	0,0678
Double low-pass filtered 50x50m grid (C1)	0,0143	0,0522
5x5m raster (C2)	0,5094	7,8275
50x50m grid (C2)	0,8309	16,2040
Averaging filter; Radius = 5 (C2)	0,7924	14,9018
Averaging filter; Radius = 10 (C2)	0,7238	12,5775
Averaging filter; Radius = 15 (C2)	0,6389	10,3723
Exponential filter; Size = 5 (C2)	0,6741	11,7137
Exponential filter; Size = 10 (C2)	0,5177	7,9153
Exponential filter; Size = 15 (C2)	0,4222	5,7346
Double low-pass filtered 5x5m grid (C2)	0,0208	0,0724
Double low-pass filtered 50x50m grid (C2)	0,0187	0,0583

Continuation of Table D.7

Profile type	StDev (m)	Amplitude (m)
5x5m raster (C1 + C2)	0,5303	9,1341
50x50m grid (C1 + C2)	0,9323	17,5602
Averaging filter; Radius = 5 (C1 + C2)	0,7724	14,3931
Averaging filter; Radius = 10 (C1 + C2)	0,7087	12,3822
Averaging filter; Radius = 15 (C1 + C2)	0,6325	10,2554
Exponential filter; Size = 5 (C1 + C2)	0,6613	11,4327
Exponential filter; Size = 10 (C1 + C2)	0,5114	7,8033
Exponential filter; Size = 15 (C1 + C2)	0,4184	5,6739
Double low-pass filtered 5x5m grid (C1 + C2)	0,0203	0,0671
Double low-pass filtered 50x50m grid (C1 + C2)	0,0156	0,0512

Notes: For C1 + C2 results, each profile point is an average value of C1 and C2 heights at the same location.

Results of averaging and exponential filter are based on 5x5m grid filtering.

For double low-pass filtering results, a median of 51 profile points was taken first. From that outcome, an average of 51 profile points was then taken.

Table D.8 Comparison between different filtering results of **ALS profile 10052018_094208**

(see Fig. 4.4) **after removing data covering land areas**. All profiles are compared to FAMOS GOCO05s geoid model. Profile length is 27,838 km. 440 profile points are included in the comparison. Three smallest StDev values and deviation amplitudes (maximum – minimum) are highlighted in red.

Profile type	StDev (m)	Amplitude (m)
5x5m grid (C1)	0,1088	0,7356
50x50m grid (C1)	0,0981	0,7914
Averaging filter; Radius = 5 (C1)	0,0148	0,0911
Averaging filter; Radius = 10 (C1)	0,0126	0,0646
Averaging filter; Radius = 15 (C1)	0,0123	0,0580
Exponential filter; Size = 5 (C1)	0,0125	0,0638
Exponential filter; Size = 10 (C1)	0,01208	0,0537
Exponential filter; Size = 15 (C1)	0,0136	0,1365
Double low-pass filtered 5x5m grid (C1)	0,0207	0,0678
Double low-pass filtered 50x50m grid (C1)	0,0142	0,05217
5x5m raster (C2)	0,1084	0,6256
50x50m grid (C2)	0,0904	0,5335
Averaging filter; Radius = 5 (C2)	0,0145	0,0858
Averaging filter; Radius = 10 (C2)	0,0125	0,0653
Averaging filter; Radius = 15 (C2)	0,01214	0,0562
Exponential filter; Size = 5 (C2)	0,0124	0,0629
Exponential filter; Size = 10 (C2)	0,01195	0,05220
Exponential filter; Size = 15 (C2)	0,0138	0,1368
Double low-pass filtered 5x5m grid (C2)	0,0209	0,0724
Double low-pass filtered 50x50m grid (C2)	0,0187	0,0583

Continuation of Table D.8

Profile type	StDev (m)	Amplitude (m)
5x5m raster (C1 + C2)	0,1019	0,6504
50x50m grid (C1 + C2)	0,0673	0,4356
Averaging filter; Radius = 5 (C1 + C2)	0,0142	0,0849
Averaging filter; Radius = 10 (C1 + C2)	0,0124	0,0620
Averaging filter; Radius = 15 (C1 + C2)	0,01210	0,0552
Exponential filter; Size = 5 (C1 + C2)	0,0123	0,0616
Exponential filter; Size = 10 (C1 + C2)	0,01193	0,0518
Exponential filter; Size = 15 (C1 + C2)	0,0136	0,1365
Double low-pass filtered 5x5m grid (C1 + C2)	0,0205	0,0671
Double low-pass filtered 50x50m grid (C1 + C2)	0,0156	0,0512

Notes: For C1 + C2 results, each profile point is an average value of C1 and C2 heights at the same location.

Results of averaging and exponential filter are based on 5x5m grid filtering.

For double low-pass filtering results, a median of 51 profile points was taken first. From that outcome, an average of 51 profile points was then taken.

APPENDIX E Cross sections of 2018 ALS grids

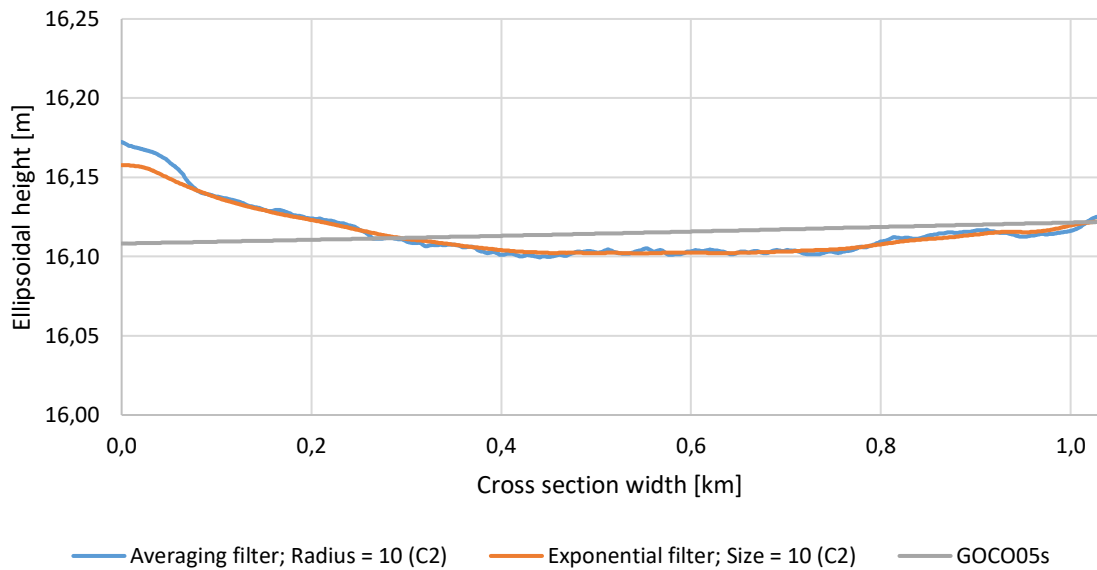


Figure E.1 First cross section of point cloud **10052018_084035** (see also Figure 4.28) compared to the FAMOS GOCO05s geoid model. For comparisons sake, FAMOS GOCO05s is lowered 0,557 m (average difference between the model and cross sections extracted from Channel 2 filtered 5x5m grids). Width of the cross section is 1,029 km.

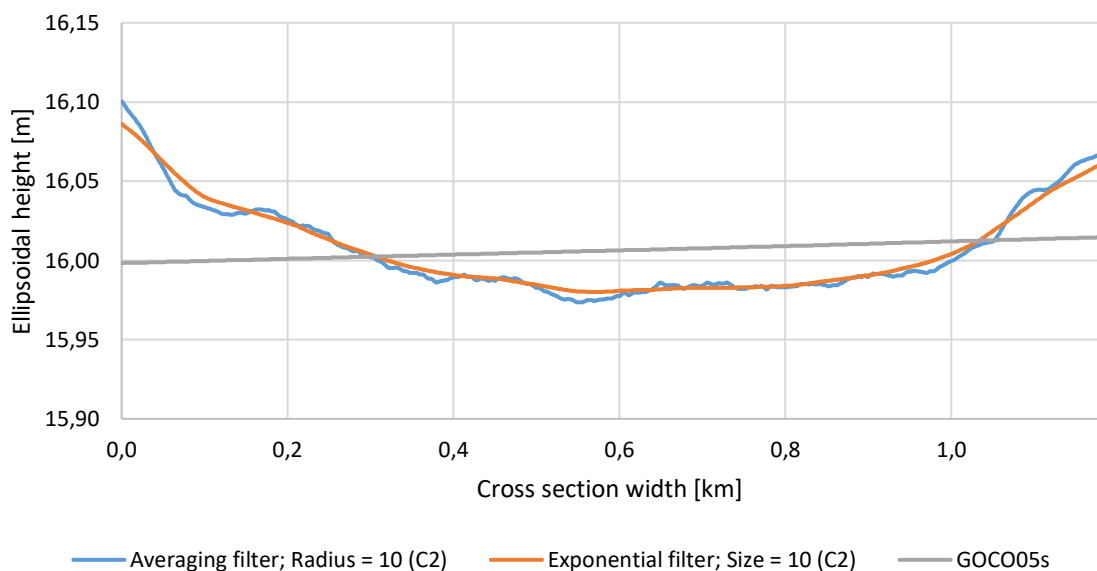


Figure E.2 Second cross section of point cloud **10052018_084035** (see also Figure 4.28) compared to the FAMOS GOCO05s geoid model. For comparisons sake, FAMOS GOCO05s is lowered 0,536 m (average difference between the model and cross sections extracted from Channel 2 filtered 5x5m grids). Width of the cross section is 1,177 km.

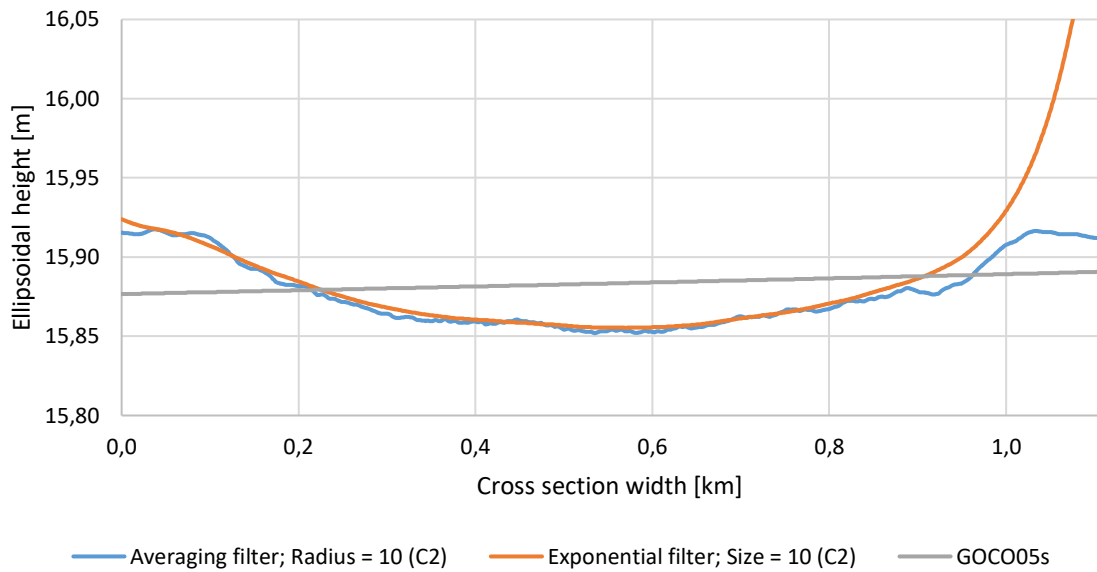


Figure E.3 Third cross section of point cloud **10052018_084035** (see also Figure 4.28) compared to the FAMOS GOCO05s geoid model. For comparisons sake, FAMOS GOCO05s is lowered 0,539 m (average difference between the model and cross sections extracted from Channel 2 filtered 5x5m grids). Width of the cross section is 1,104 km.

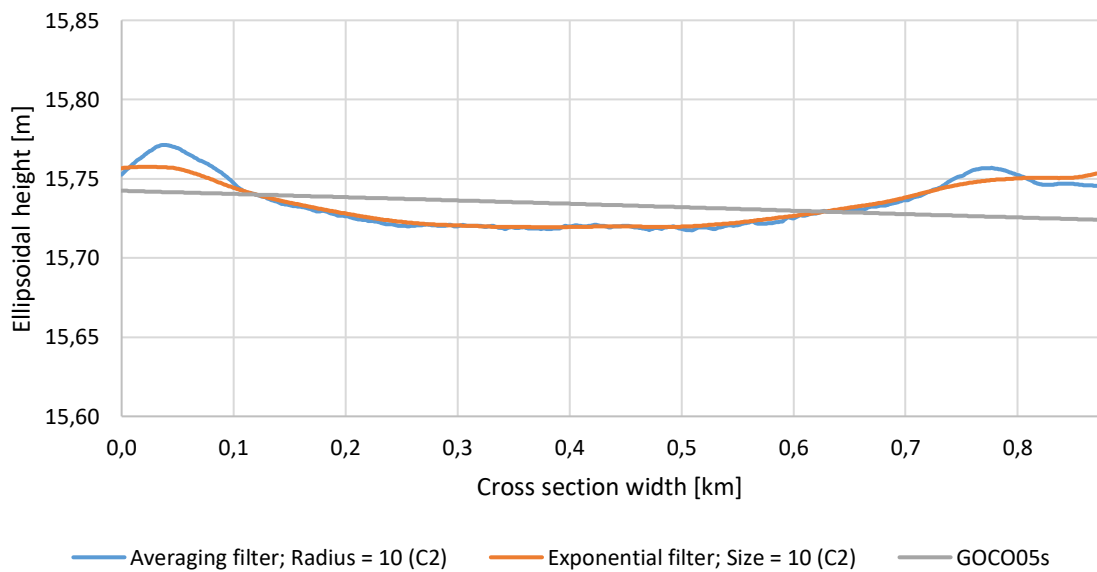


Figure E.4 First cross section of point cloud **10052018_084640** (see also Figure 4.28) compared to the FAMOS GOCO05s geoid model. For comparisons sake, FAMOS GOCO05s is lowered 0,580 m (average difference between the model and cross sections extracted from Channel 2 filtered 5x5m grids). Width of the cross section is 0,872 km.

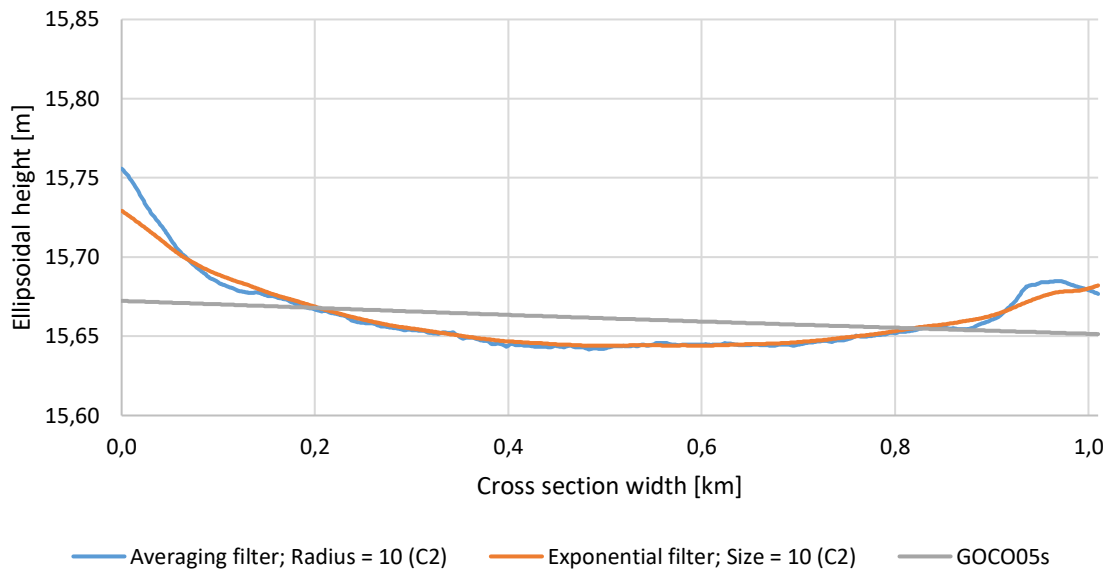


Figure E.5 Second cross section of point cloud **10052018_084640** (see also Figure 4.28) compared to the FAMOS GOCO05s geoid model. For comparisons sake, FAMOS GOCO05s is lowered 0,580 m (average difference between the model and cross sections extracted from Channel 2 filtered 5x5m grids). Width of the cross section is 1,010 km.

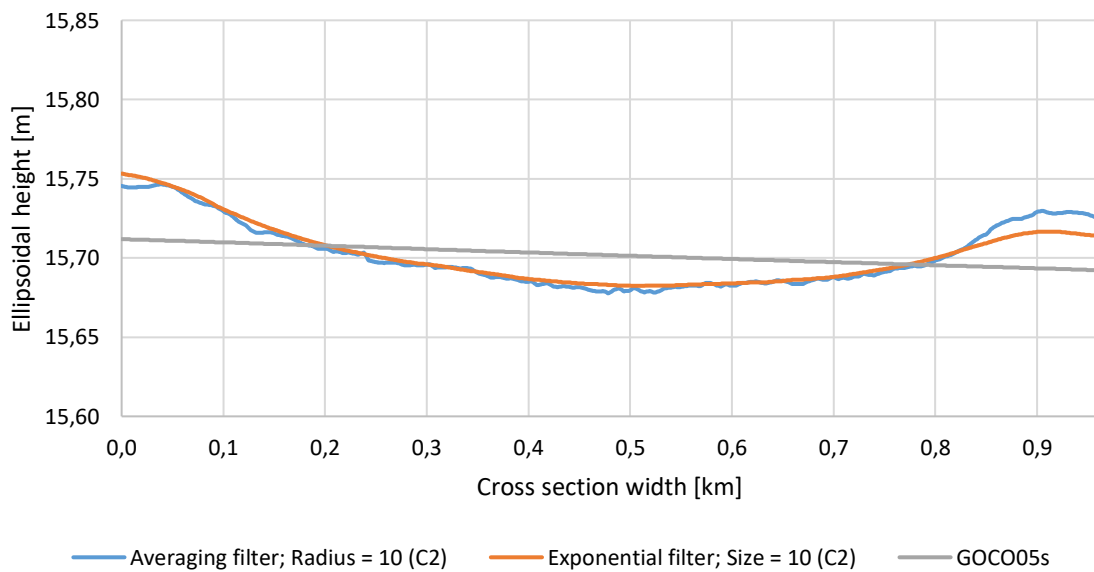


Figure E.6 Third cross section of point cloud **10052018_084640** (see also Figure 4.28) compared to the FAMOS GOCO05s geoid model. For comparisons sake, FAMOS GOCO05s is lowered 0,583 m (average difference between the model and cross sections extracted from Channel 2 filtered 5x5m grids). Width of the cross section is 0,960 km.

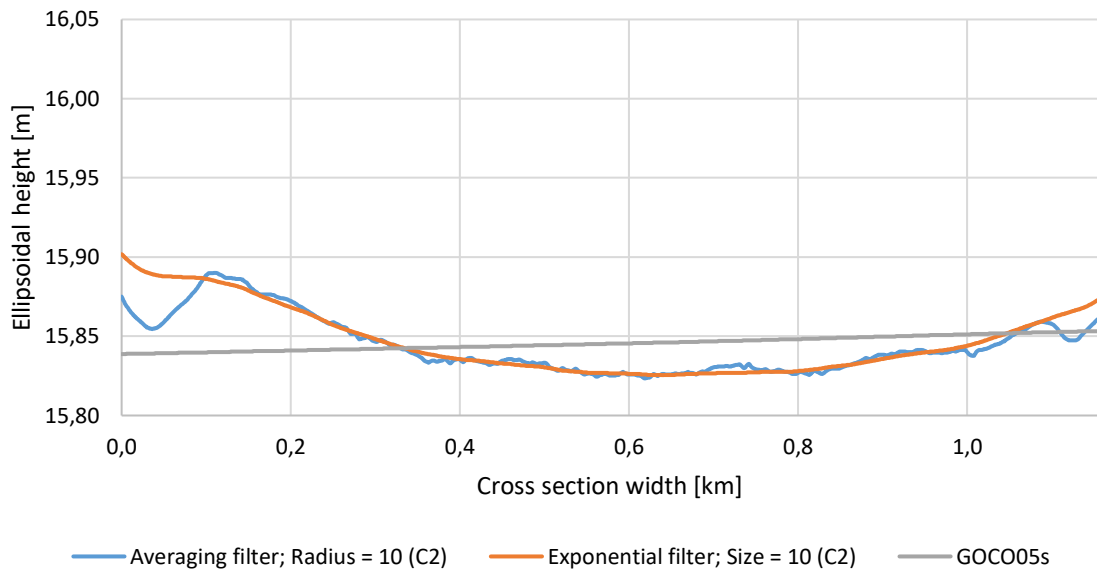


Figure E.7 First cross section of point cloud **10052018_085356** (see also Figure 4.28) compared to the FAMOS GOCO05s geoid model. For comparisons sake, FAMOS GOCO05s is lowered 0,570 m (average difference between the model and cross sections extracted from Channel 2 filtered 5x5m grids). Width of the cross section is 1,155 km.

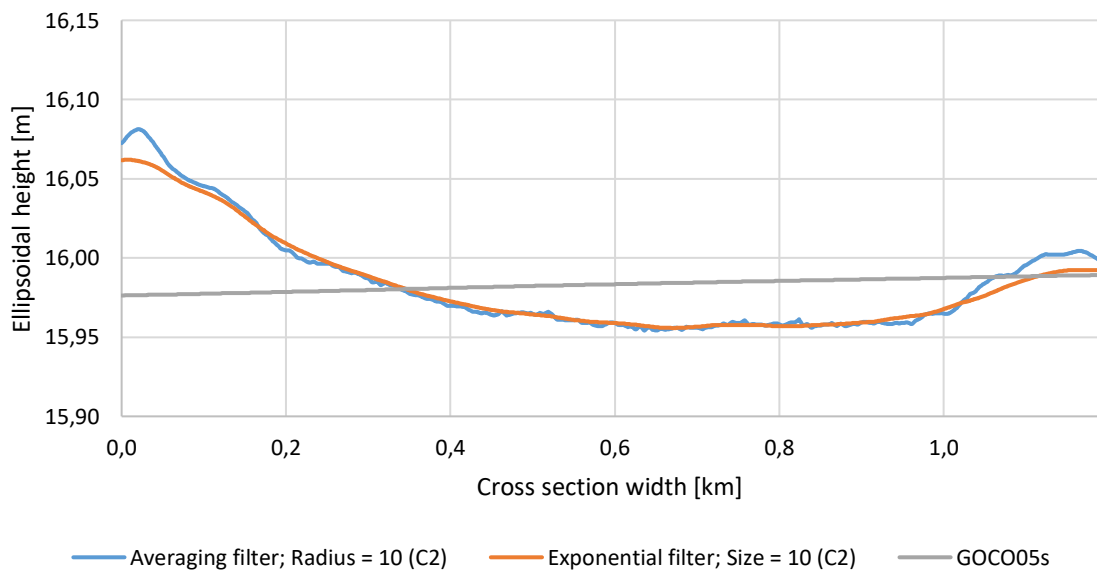


Figure E.8 Second cross section of point cloud **10052018_085356** (see also Figure 4.28) compared to the FAMOS GOCO05s geoid model. For comparisons sake, FAMOS GOCO05s is lowered 0,547 m (average difference between the model and cross sections extracted from Channel 2 filtered 5x5m grids). Width of the cross section is 1,188 km.

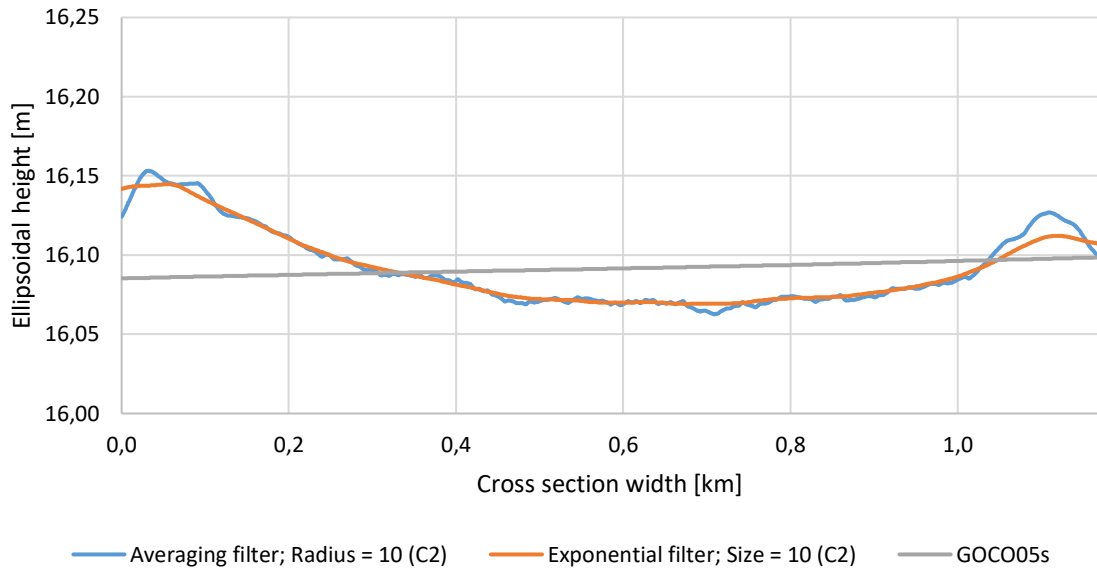


Figure E.9 Third cross section of point cloud **10052018_085356** (see also Figure 4.28) compared to the FAMOS GOCO05s geoid model. For comparisons sake, FAMOS GOCO05s is lowered 0,554 m (average difference between the model and cross sections extracted from Channel 2 filtered 5x5m grids). Width of the cross section is 1,168 km.

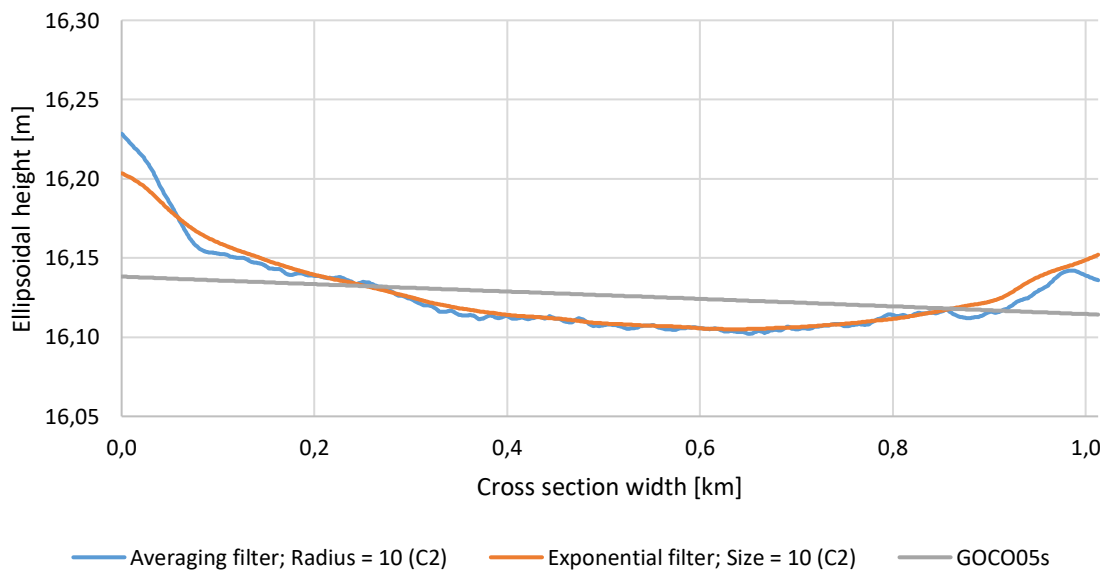


Figure E.10 First cross section of point cloud **10052018_085829** (see also Figure 4.28) compared to the FAMOS GOCO05s geoid model. For comparisons sake, FAMOS GOCO05s is lowered 0,541 m (average difference between the model and cross sections extracted from Channel 2 filtered 5x5m grids). Width of the cross section is 1,013 km.

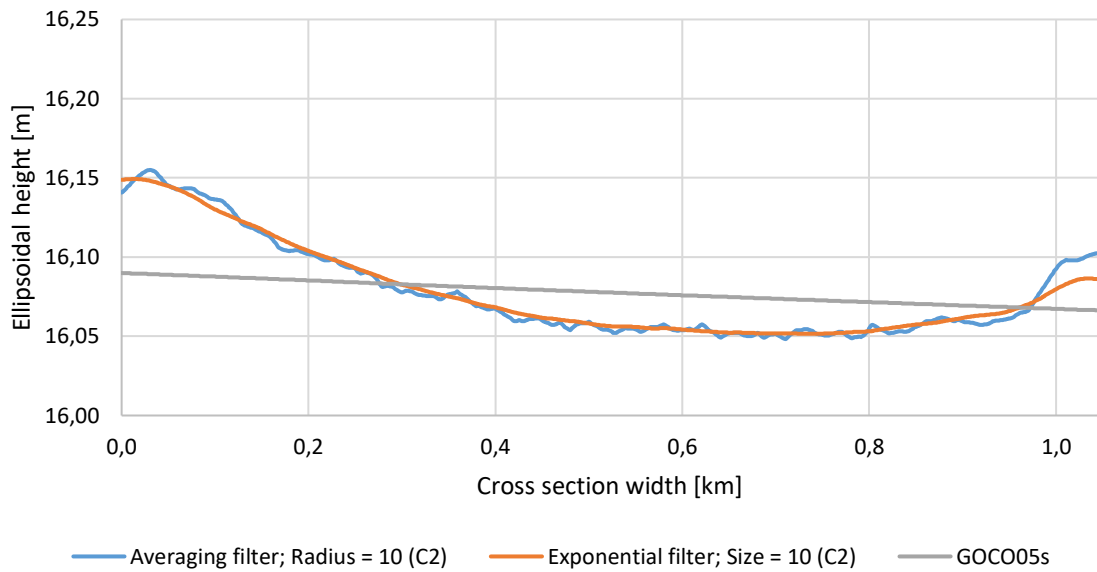


Figure E.11 Second cross section of point cloud **10052018_085829** (see also Figure 4.28) compared to the FAMOS GOCO05s geoid model. For comparisons sake, FAMOS GOCO05s is lowered 0,519 m (average difference between the model and cross sections extracted from Channel 2 filtered 5x5m grids). Width of the cross section is 1,045 km.

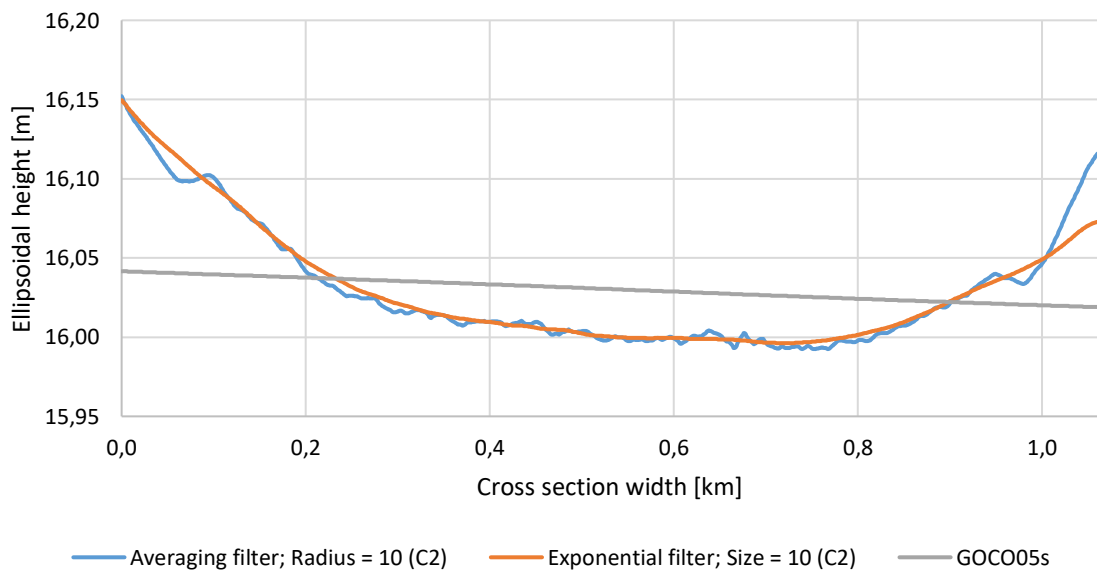


Figure E.12 Third cross section of point cloud **10052018_085829** (see also Figure 4.28) compared to the FAMOS GOCO05s geoid model. For comparisons sake, FAMOS GOCO05s is lowered 0,548 m (average difference between the model and cross sections extracted from Channel 2 filtered 5x5m grids). Width of the cross section is 1,061 km.

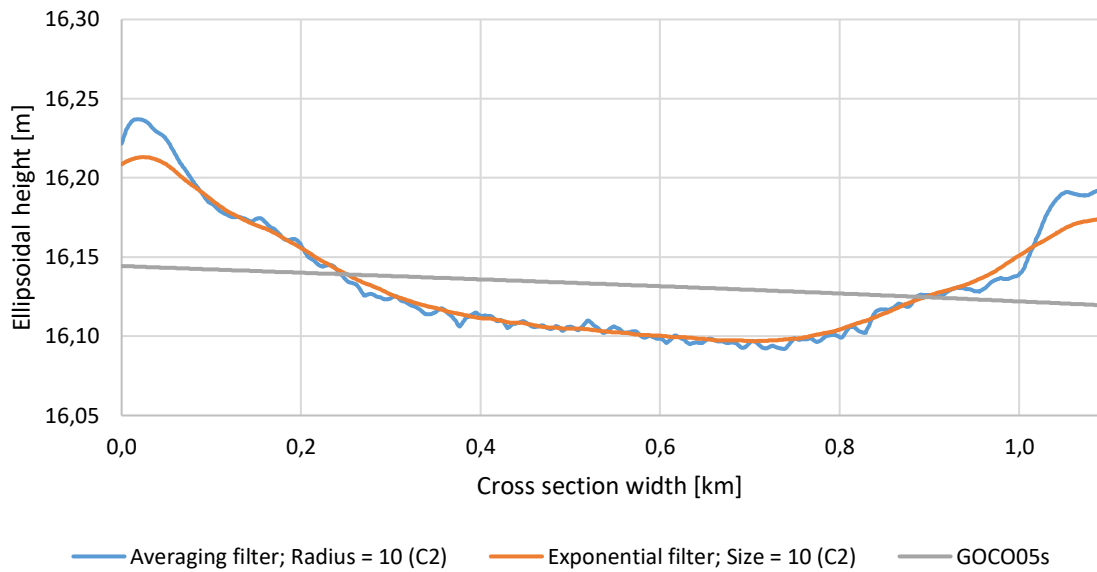


Figure E.13 First cross section of point cloud **10052018_092024** (see also Figure 4.28) compared to the FAMOS GOCO05s geoid model. For comparisons sake, FAMOS GOCO05s is lowered 0,560 m (average difference between the model and cross sections extracted from Channel 2 filtered 5x5m grids). Width of the cross section is 1,088 km.

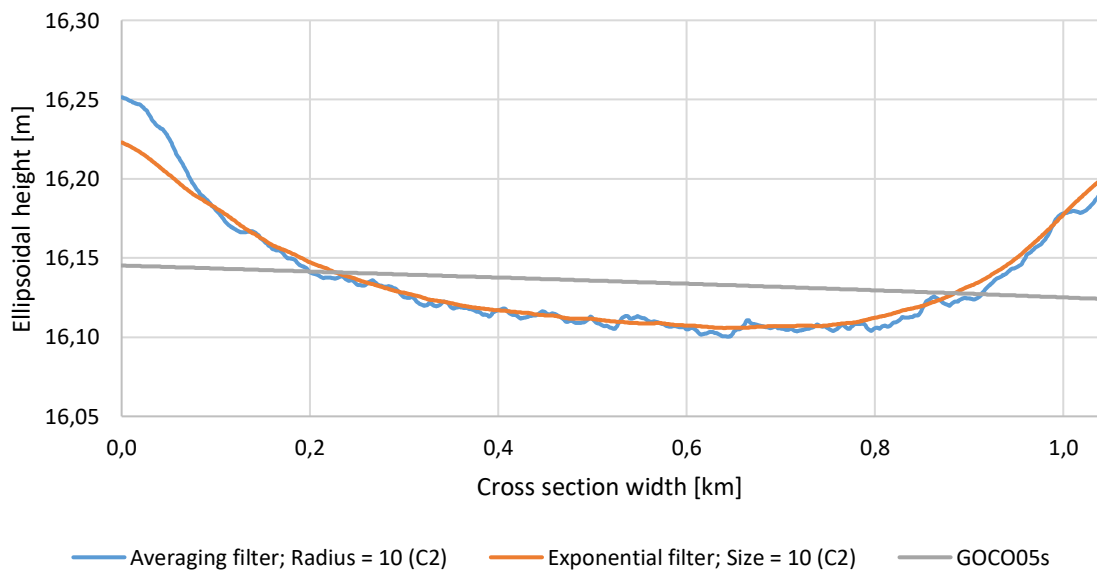


Figure E.14 Second cross section of point cloud **10052018_092024** (see also Figure 4.28) compared to the FAMOS GOCO05s geoid model. For comparisons sake, FAMOS GOCO05s is lowered 0,571 m (average difference between the model and cross sections extracted from Channel 2 filtered 5x5m grids). Width of the cross section is 1,037 km.

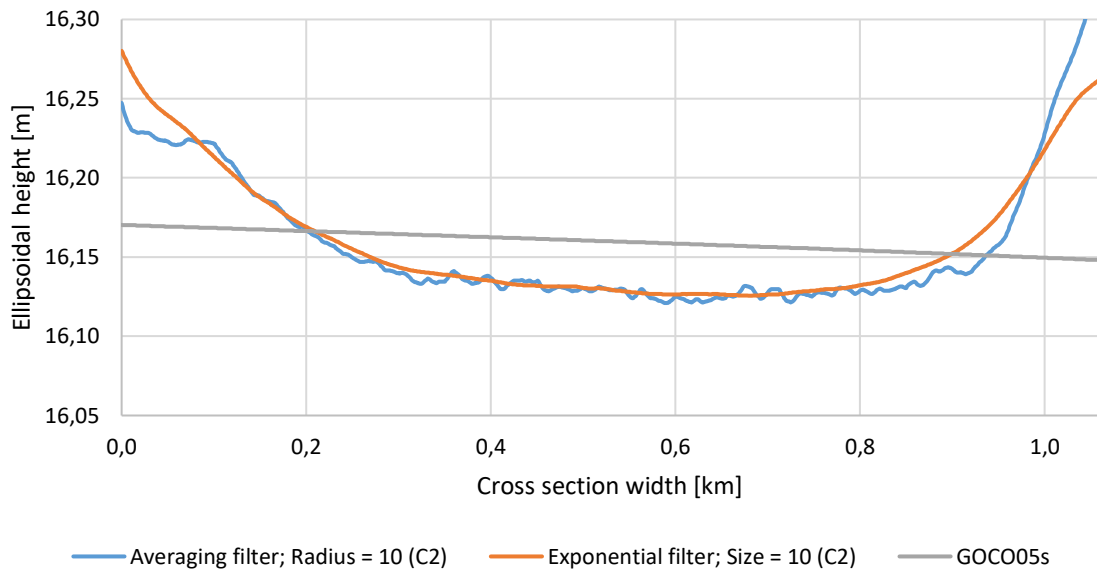


Figure E.15 Third cross section of point cloud **10052018_092024** (see also Figure 4.28) compared to the FAMOS GOCO05s geoid model. For comparisons sake, FAMOS GOCO05s is lowered 0,555 m (average difference between the model and cross sections extracted from Channel 2 filtered 5x5m grids). Width of the cross section is 1,058 km.

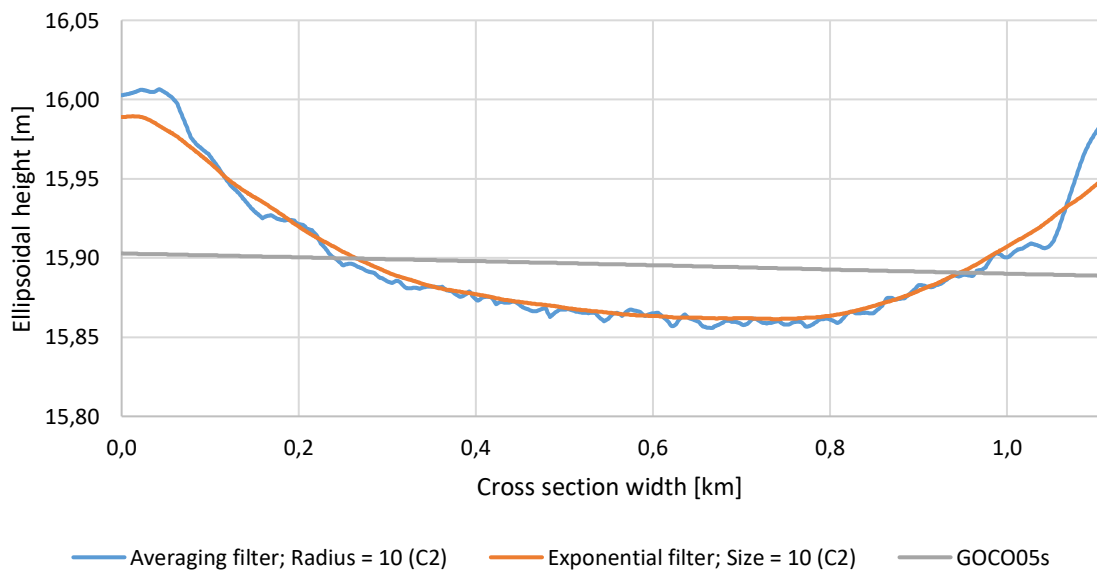


Figure E.16 First cross section of point cloud **10052018_093037** (see also Figure 4.28) compared to the FAMOS GOCO05s geoid model. For comparisons sake, FAMOS GOCO05s is lowered 0,591 m (average difference between the model and cross sections extracted from Channel 2 filtered 5x5m grids). Width of the cross section is 1,103 km.

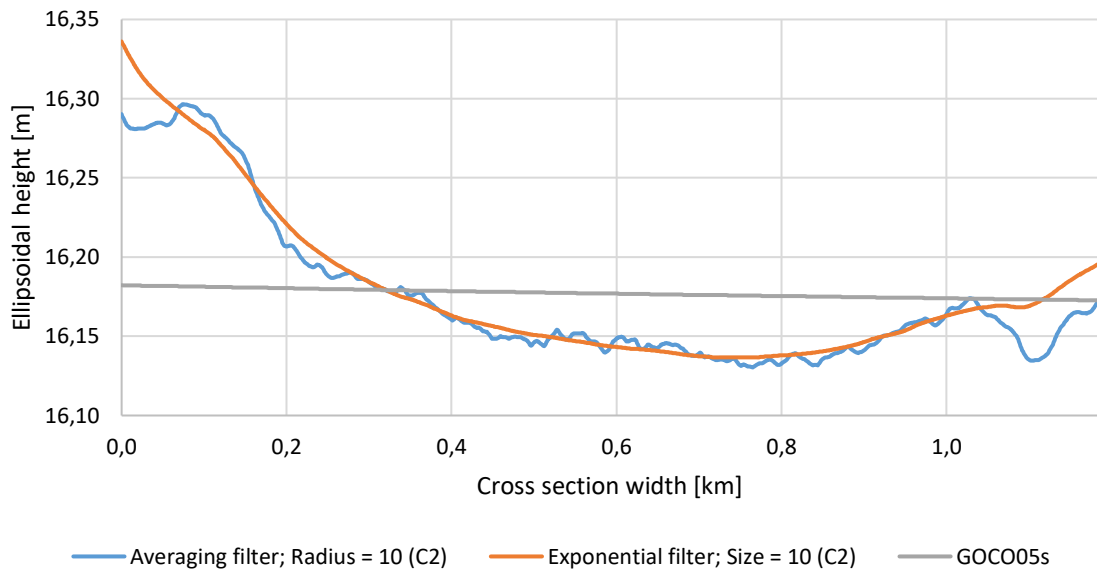


Figure E.17 Second cross section of point cloud **10052018_093037** (see also Figure 4.28) compared to the FAMOS GOCO05s geoid model. For comparisons sake, FAMOS GOCO05s is lowered 0,601 m (average difference between the model and cross sections extracted from Channel 2 filtered 5x5m grids). Width of the cross section is 1,184 km.

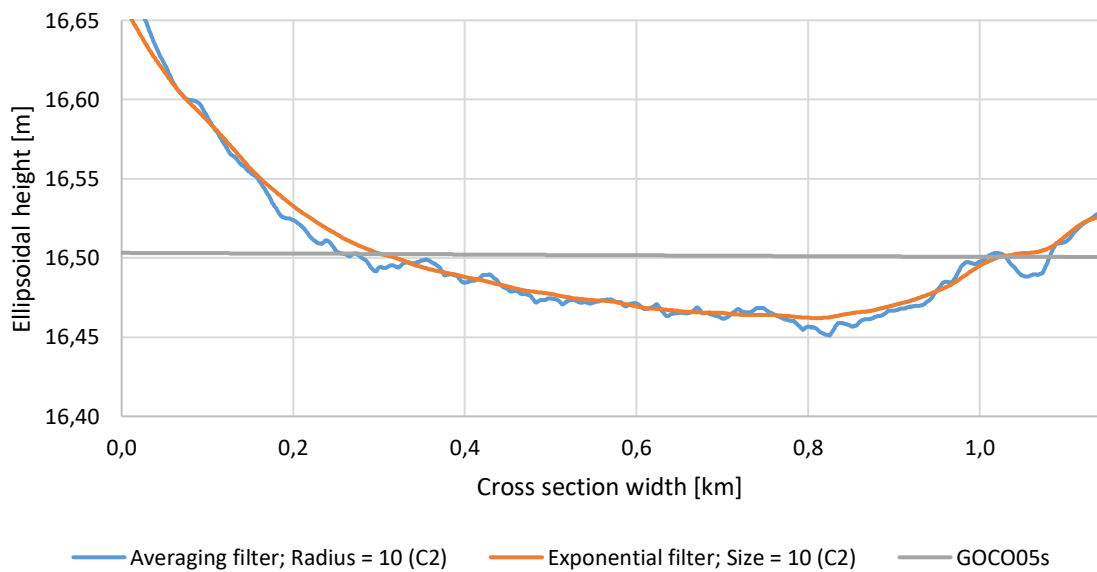


Figure E.18 Third cross section of point cloud **10052018_093037** (see also Figure 4.28) compared to the FAMOS GOCO05s geoid model. For comparisons sake, FAMOS GOCO05s is lowered 0,586 m (average difference between the model and cross sections extracted from Channel 2 filtered 5x5m grids). Width of the cross section is 1,138 km.

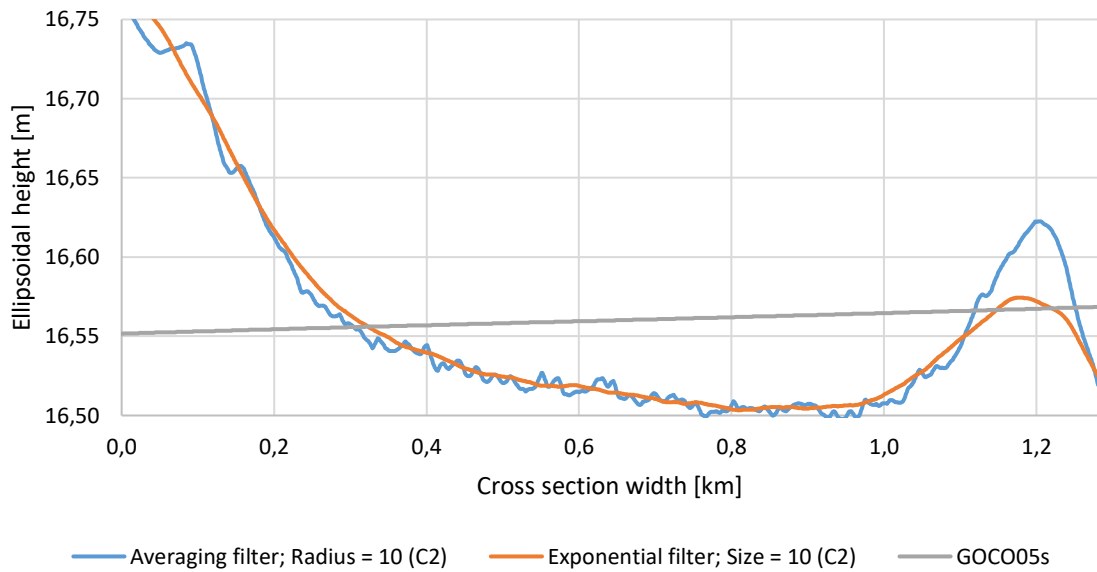


Figure E.19 First cross section of point cloud **10052018_094208** (see also Figure 4.28) compared to the FAMOS GOCO05s geoid model. For comparisons sake, FAMOS GOCO05s is lowered 0,590 m (average difference between the model and cross sections extracted from Channel 2 filtered 5x5m grids). Width of the cross section is 1,281 km.

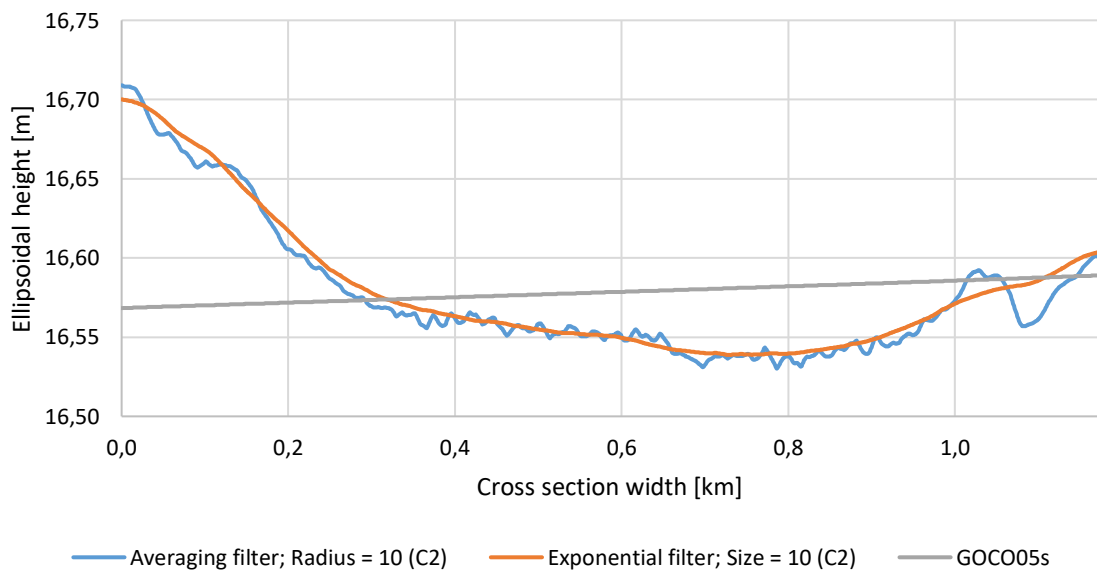


Figure E.20 Second cross section of point cloud **10052018_094208** (see also Figure 4.28) compared to the FAMOS GOCO05s geoid model. For comparisons sake, FAMOS GOCO05s is lowered 0,590 m (average difference between the model and cross sections extracted from Channel 2 filtered 5x5m grids). Width of the cross section is 1,172 km.

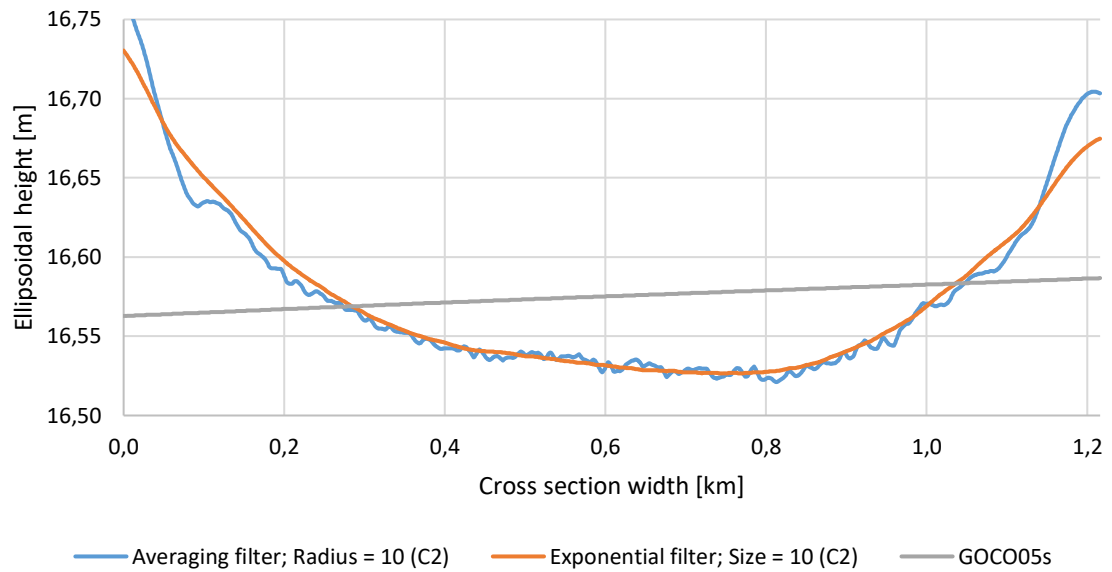


Figure E.21 Third cross section of point cloud **10052018_094208** (see also Figure 4.28) compared to the FAMOS GOCO05s geoid model. For comparisons sake, FAMOS GOCO05s is lowered 0,603 m (average difference between the model and cross sections extracted from Channel 2 filtered 5x5m grids). Width of the cross section is 1,216 km.